ISSN
2395-6992

International Journal of Engineering Research & Science

www.ijoer.com
www.adpublications.org

Volume-3 ! Issue - 3 ! March, 2017 www.ijoer.com ! info@ijoer.com

Preface

We would like to present, with great pleasure, the inaugural volume-3, Issue-3, March 2017, of a scholarly journal, *International Journal of Engineering Research & Science*. This journal is part of the AD Publications series *in the field of Engineering, Mathematics, Physics, Chemistry and scienc Research Development*, and is devoted to the gamut of Engineering and Science issues, from theoretical aspects to application-dependent studies and the validation of emerging technologies.

This journal was envisioned and founded to represent the growing needs of Engineering and Science as an emerging and increasingly vital field, now widely recognized as an integral part of scientific and technical investigations. Its mission is to become a voice of the Engineering and Science community, addressing researchers and practitioners in below areas

Chemical Engineering	
Biomolecular Engineering	Materials Engineering
Molecular Engineering	Process Engineering
Corrosion Engineering	
Civil Engineering	
Environmental Engineering	Geotechnical Engineering
Structural Engineering	Mining Engineering
Transport Engineering	Water resources Engineering
Electrical Engineering	
Power System Engineering	Optical Engineering
Mechanical Engineering	
Acoustical Engineering	Manufacturing Engineering
Optomechanical Engineering	Thermal Engineering
Power plant Engineering	Energy Engineering
Sports Engineering	Vehicle Engineering
Software Engineering	
Computer-aided Engineering	Cryptographic Engineering
Teletraffic Engineering	Web Engineering
System Engineering	
Mathematics	
Arithmetic	Algebra
Number theory	Field theory and polynomials
Analysis	Combinatorics
Geometry and topology	Topology
Probability and Statistics	Computational Science
Physical Science	Operational Research
Physics	
Nuclear and particle physics	Atomic, molecular, and optical physics
Condensed matter physics	Astrophysics
Applied Physics	Modern physics
Philosophy	Core theories

Chemistry	
Analytical chemistry	Biochemistry
Inorganic chemistry	Materials chemistry
Neurochemistry	Nuclear chemistry
Organic chemistry	Physical chemistry
Other Engineering Areas	
Aerospace Engineering	Agricultural Engineering
Applied Engineering	Biomedical Engineering
Biological Engineering	Building services Engineering
Energy Engineering	Railway Engineering
Industrial Engineering	Mechatronics Engineering
Management Engineering	Military Engineering
Petroleum Engineering	Nuclear Engineering
Textile Engineering	Nano Engineering
Algorithm and Computational Complexity	Artificial Intelligence
Electronics & Communication Engineering	Image Processing
Information Retrieval	Low Power VLSI Design
Neural Networks	Plastic Engineering

Each article in this issue provides an example of a concrete industrial application or a case study of the presented methodology to amplify the impact of the contribution. We are very thankful to everybody within that community who supported the idea of creating a new Research with IJOER. We are certain that this issue will be followed by many others, reporting new developments in the Engineering and Science field. This issue would not have been possible without the great support of the Reviewer, Editorial Board members and also with our Advisory Board Members, and we would like to express our sincere thanks to all of them. We would also like to express our gratitude to the editorial staff of AD Publications, who supported us at every stage of the project. It is our hope that this fine collection of articles will be a valuable resource for *IJOER* readers and will stimulate further research into the vibrant area of Engineering and Science Research.

Mukesh Arora

(Chief Editor)

Board Members

Dr. S.R.Boselin Prabhu

Ph.D, Wireless Sensor Networks, M.E. Network Engineering, Excellent Professional Achievement Award Winner from Society of Professional Engineers Biography Included in Marquis Who's Who in the World (Academic Year 2015 and 2016). Currently Serving as Assistant Professor in the department of ECE in SVS College of Engineering, Coimbatore.

Dr. Maheshwar Shrestha

Postdoctoral Research Fellow in DEPT. OF ELE ENGG & COMP SCI, SDSU, Brookings, SD Ph.D, M.Sc. in Electrical Engineering from SOUTH DAKOTA STATE UNIVERSITY, Brookings, SD.

Zairi Ismael Rizman

Senior Lecturer, Faculty of Electrical Engineering, Universiti Teknologi MARA (UiTM) (Terengganu) Malaysia Master (Science) in Microelectronics (2005), Universiti Kebangsaan Malaysia (UKM), Malaysia. Bachelor (Hons.) and Diploma in Electrical Engineering (Communication) (2002), UiTM Shah Alam, Malaysia

Dr. D. Amaranatha Reddy

Ph.D.(Postdocteral Fellow,Pusan National University, South Korea), M.Sc., B.Sc. : Physics.

Dr. Dibya Prakash Rai

Post Doctoral Fellow (PDF), M.Sc.,B.Sc., Working as Assistant Professor in Department of Physics in Pachhuncga University College, Mizoram, India.

Dr. Pankaj Kumar Pal

Ph.D R/S, ECE Deptt., IIT-Roorkee.

Dr. P. Thangam

BE(Computer Hardware & Software), ME(CSE), PhD in Information & Communication Engineering, currently serving as Associate Professor in the Department of Computer Science and Engineering of Coimbatore Institute of Engineering and Technology.

Dr. Pradeep K. Sharma

PhD., M.Phil, M.Sc, B.Sc, in Physics, MBA in System Management, Presently working as Provost and Associate Professor & Head of Department for Physics in University of Engineering & Management, Jaipur.

Dr. R. Devi Priya

Ph.D (CSE),Anna University Chennai in 2013, M.E, B.E (CSE) from Kongu Engineering College, currently working in the Department of Computer Science and Engineering in Kongu Engineering College, Tamil Nadu, India.

Dr. Sandeep

Post-doctoral fellow, Principal Investigator, Young Scientist Scheme Project (DST-SERB), Department of Physics, Mizoram University, Aizawl Mizoram, India- 796001.

Mr. Abilash

MTech in VLSI, BTech in Electronics & Telecommunication engineering through A.M.I.E.T.E from Central Electronics Engineering Research Institute (C.E.E.R.I) Pilani, Industrial Electronics from ATI-EPI Hyderabad, IEEE course in Mechatronics, CSHAM from Birla Institute Of Professional Studies.

Mr. Varun Shukla

M.Tech in ECE from RGPV (Awarded with silver Medal By President of India), Assistant Professor, Dept. of ECE, PSIT, Kanpur.

Mr. Shrikant Harle

Presently working as a Assistant Professor in Civil Engineering field of Prof. Ram Meghe College of Engineering and Management, Amravati. He was Senior Design Engineer (Larsen & Toubro Limited, India).

Table of Contents

Applied Biotechnology: Isolation and Detection of an Efficient Biosurfactant from *Pseudomonas* sp. Comparative Studies against Chemical Surfactants

María E. Mainez[1], Diana M. Müller[2], Marcelo C. Murguía[3*]

[1]Environment Group. Institute of Technological Development for the Chemical Industry. National Council of Scientific and Technical Research (CONICET). Güemes 3450, (3000) Santa Fe, Argentina.
[2]Laboratory of Applied Chemistry. Faculty of Biochemistry and Biological Sciences. National University of the Litoral (UNL). Ciudad Universitaria, (3000) Santa Fe, Argentina.
[3]Environment Group. Institute of Technological Development for the Chemical Industry. National Council of Scientific and Technical Research (CONICET). Güemes 3450, (3000) Santa Fe, Argentina.

***Abstract*—** *The use of biosurfactants became essential because of its multiple properties and applications. The high toxicity to the environment led to search for new alternatives such as the reduction or replacement by biological surfactants. Because of this, it is in our interest to produce biosurfactants from a non-pathogenic Pseudomonas. We obtained lower values of critical micelle concentration (CMC) from the culture broth than obtained from dodecyl sulfate sodium (SDS) and Pluronic F-68, used as pure surfactans. We found values of critical micellar concentration close to 0.15 mg/L in the purified fraction by adsorption chromatography. We determine by mass spectrometry this strain possibly produces two families of biosurfactants. Majority fraction might be formed by cyclic lipopeptides whose molecular weights could be located in the range of 1100-1200 Da. However, it is necessary perform confirmatory structural studies and to determine the specific structure of these analytes.*

***Keywords*— Biosurfactants, Critical Micellar Concentration, Mass Spectrometry, Pseudomonas, Surfactants.**

I. INTRODUCTION

Biosurfactants are a group of secondary metabolites synthesized by a great variety of micro-organisms. The properties of biosurfactants include the reduction of surface and interfacial tensions between liquids, solids and gases [1]. Due to their biodegradability and low critical micelle concentration (CMC) are ideal surfactants for environmental application [2]. These molecules have been studied extensively and now we have a good amount of information regarding their production, types and properties [3]. The principal action of these molecules will depend on its specific structure and production characteristics [4].

Biosurfactants possess a nonpolar region of long chain fatty acids and polar hydrophilic groups, such as carbohydrate, amino acid phosphate or cyclic peptides [5]. Because of this can be divided into two groups, low molecular mass this class includes phospholipids, glycolipids and lipopeptides. In general, show lower surface and interstitial tension. Another group is high molecular mass that used as emulsion stabilizing agents such as polymeric surfactants and lipoproteins [6], [3].

When are compared with synthetic surfactants, biosurfactants have several advantages, including high biodegradability, low toxicity, low irritancy, and compatibility with human skin [7], [8].

Biosurfactants not only act modifying the surface properties, but also alteration of compound bio-availability and interaction with membranes [9]. This explain their importance in the area of the therapeutic and biomedical [10], [8], [4].

Certain species of Pseudomonas are able to produce and excrete biosurfactants of great interest [11], [12]. The genomes of its species are very varied and flexible. This is reflected in their versatile secondary metabolism, which enables the production of a wide variety of organic compounds displaying a range of biological function including surfactants [13], [14]. The objective of this work is to produce biosurfactants with low values of CMC in culture supernatant and to identify the family of surfactant belong to which it belongs. It is important we to obtain these type of compounds from a non-pathogenic *Pseudomonas*. With this work, we started the studio of production of a surfactant of biological origin that can compete in the near future with synthetic surfactants.

II. MATERIALS AND METHODS

2.1 Microorganism

Bacterial strains were isolated from local soil (wild-type strain). It was identified as the genus *Pseudomonas* (strain B204). This strain was ceded for the Laboratory of Microbiology of the Faculty of Biochemistry and Biological Sciences, of the National University of the Litoral (UNL), Santa Fe, Argentina.

2.2 Production of biosurfactants from *Pseudomonas* sp.

Pseudomonas spp. was cultured, under controlled conditions of temperature and agitation, in an enriched medium similar to the published by Xia et al. (2004), pH 6.5-7.0 and using glycerol as source of carbon. Biosurfactant production was corroborated by measurements of surface tension of the culture supernatants, whose value should be between 31.5 and 37.5 mN/m. The pure cultures that comply this requirement were conditioned with a phosphate buffer and then were concentrated by ultra-filtration. The concentrated product (retentate) obtained was filtered until their sterility. Finally, it was lyophilized for storing to long term.

2.3 Extraction and quantification of biosurfactants

A technique of acidic precipitation was carried out, followed of extractions with solvents. At 3 mL of the concentrated lyophilized product was acidified to pH= 2 with 6 N hydrochloric acid and was extracted with an equal volume of chloroform/ethanol 3:1 (v/v) mixture and water as co-solvent of extraction, which was repeated three times. The phase obtained was dehydrated with anhydrous Sodium Sulfate, filtered and evaporated to dryness in rotary evaporator and finally weighed. With this data was calculated the % (w/w) and % (w/v) for estimating the yield of production for *Pseudomonas*.

Previously was performed a test of precipitation of biosurfactants and was isolated using acid precipitation. The precipitation of biosurfactants was confirmed for the increased in the tension surface of a known sample.

2.4 Thin layer chromatography (TLC)

The extraction was analyzed by thin layer chromatography (TLC), using silica gel 60 Fluka, for the biosurfactants compounds. As mobile phase was used chloroform/methanol/water 65:15:2 (v/v/v). The TLC plates were revealed with ultraviolet light and a solution of sulfuric acidic to 10% (v/v) in ethanol and were kept at 105 ºC for 5 min.

2.5 Critical micellar concentration (CMC)

A solution of lyophilized retentate of 2.4 mg/mL was prepared from which were made several dilutions in ultrapure water. The surface tension was measure at room temperature (25 °C) and it was compared with the measure of ultrapure water. The surface tension was determined by a Tensiometer Du Nouy (CSC Scientific Company, Fairfax Unites States), according to Du Nouy's ring method [15].

2.6 Analysis for mass spectrometry

The analyzes obtained by the technique of acidic precipitation were determined by electrospray ionization-mass spectrometry (ESI-MS). Negative and positive mass spectra were obtained on SQD2 single quadrupole mass spectrometer (Waters, Milford United States). The scan range used was 300 to 3000 m/z with the objective of detecting different families of biosurfactants. Methanol was used to dissolve the precipitate and was filtered with syringe filter of 0.22 μm Millipore. Were optimized the necessary parameters for to carry out then a chromatographic separation.

2.7 Isolation of majority biosurfactan by adsorption Chromatography

From of 1 g of lyophilized retentate at 45% (w/w) the biosurfactants were isolated by adsorption chromatography. A column of 30 cm long with 2 cm of internal diameter was used, to which was added 17 g of silica gel 60 to obtain a height of about 10 cm.

Chromatography was performed with a gradient of ethyl acetate: ethanol. The column wash was carried out with methanol. Chromatography was monitored by TLC in the same way as explained above. The thin layers were revealed with ultraviolet

light and a solution of sulfuric acidic to the 10% (v/v) in ethanol and were kept at 105 ºC for 5 min. For the detection of peptides, the dry plates were sprayed with a solution of 0.25% (v/v) ninhydrin in acetone.

The CMC of the fraction isolated by the column was determined in the same way as for the lyophilized retentate. In this case, it was started from an aqueous solution of 0.5 mg/mL of purified biosurfactant.

2.8 Ultra liquid performance chromatography (LC/MS) of the majority fraction

The analysis was performed in a SQD2 single quadrupole mass spectrometer (Waters) coupled to H-CLASS HPLC system (Waters, Milford United States). Ionization negative mode was used for chromatography experiments. The sample was dissolved in acetonitrile/water 1:1 (v/v) and was eluted with a water/acetonitrile gradient. The dimensions of column were 2.1 by 5 mm (ACQUITY BEH C18 1.7 µm, Waters, Milford United States), the injection volume was 3 µL and the flow rate was set to 0.3 mL/min. Spectra were taken in the m/z range of 300 to 3000 Da. The spray voltage of the mass spectrometer was 2 kV and the cone voltage 90 V. The desolvation temperature was 623 ºK and source temperature 423 ºK. The ion energy was set to 1 V. Mass Lynx (ver. 4.1) software was used for analysis and post processing.

2.9 Spectral scanning of fraction isolated of chromatography

The spectral scanning was performed of 200 to 800 nm in spectrophotometer UV-Visible (Perkin Ermer, Buenos Aires, Argentina) Lambda 20 software was used for analysis. The sample was dissolved in acetonitrile/water 4:1 (v/v).

III. RESULTS

3.1 Production, extraction and quantification of total biosurfactants

Through the values obtained from surface tension, we could ensure that we produce surfactants from nonpathogenic *Pseudomonas*. The values of surface tension (γ) measured in the culture broths were between 33 and 34 mN/m at a dilution 1/3000 (γ_{water} = 72.5 mN/m at 24 °C). The pH of broths was between 7.9 and 8.5 and their cellular concentration of 10^9-10^{10} CFU/ml. In the same dilution of retentate, the surface tension was 31 mN/m and lower values than 25 mN/m, showed the undiluted solution. The pH to the retentate was kept at 7.5. The tension superficial of undiluted permeate was around 25 mN/m, but increased to values close to water when was diluted to half.

The retentate was lyophilized and it was stored to -20 °C without losing its properties in the evaluated year. The yield of the process of lyophilized was 4.2 % (w/v).

We were able to estimate the amount of active principle released in the culture supernatant using the technique acidic precipitation. The yield of production was of 45 % (w/w) and 2% (w/v), possibly the rest consisting of proteins and the components of the culture medium. TLC plates were performed with isolated active principle and were observed in the plates two retention factor (R_f) values of 0.4 and 0.7, respectively. These showed positive reactions to sulfuric acidic reagent and in light ultraviolet.

It is important to clarify that was confirmed the precipitation of compounds of interest to pH 2 by surface tension measurements. A solution of γ = 28.5 mN/m at pH 7.5 increased the surface tension at 63 mN/m when the pH was decreased to 3.

3.2 Critical micelle concentration of the retentate (CMC)

The CMC is minimum surfactant concentration from which spontaneously begins the formation of micelles in the solution and for this reason the value of surface tension (γ) does not decrease more. The values of γ were plotted versus the values of concentration of different dilutions (Figure1) and the value of CMC of retentate was calculated from the turning point of the curve obtained. The value of CMC resulted to be 0.3 mg/mL and the surface tension was decreased to 29.6 mN/m.

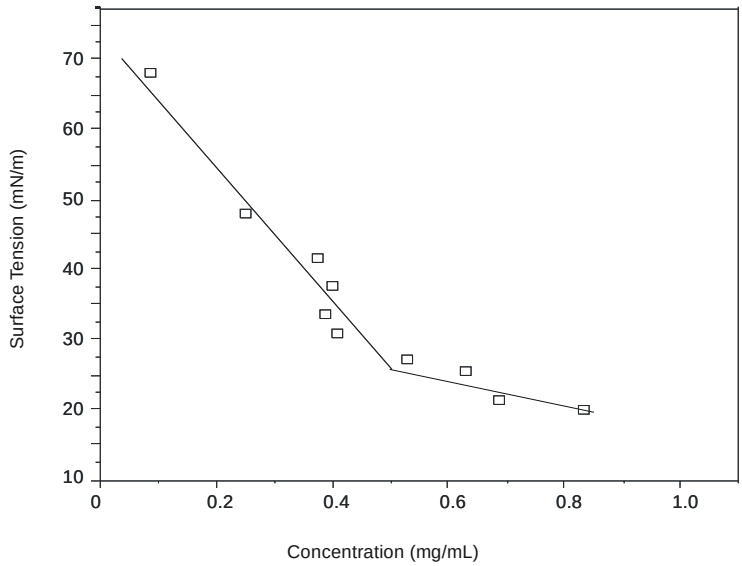

FIGURE 1. EFFECT OF RETENTATE CONCENTRATION ON SURFACE TENSION. THE INTERSECTION OF REGRESSION LINES DETERMINES VALUE OF CMC

3.3 Analysis of the product of precipitation by Mass Spectrometry

The negative-ion spectrum (Figure 2) showed a molecular ion of 1125.1 m/z of higher relative intensity. In the positive-ion spectrum this molecular ion peak appeared as 1148.8 m/z and 1170.8 indicating ions resulting from addition of one $[M+Na]^+$ and two sodium $[M+2Na]^+$ respectively. Lower molecular weight ions are also seen in the spectrum with lower relative intensity, such as masses of 502, 648 and 702 Da (Figure 2).

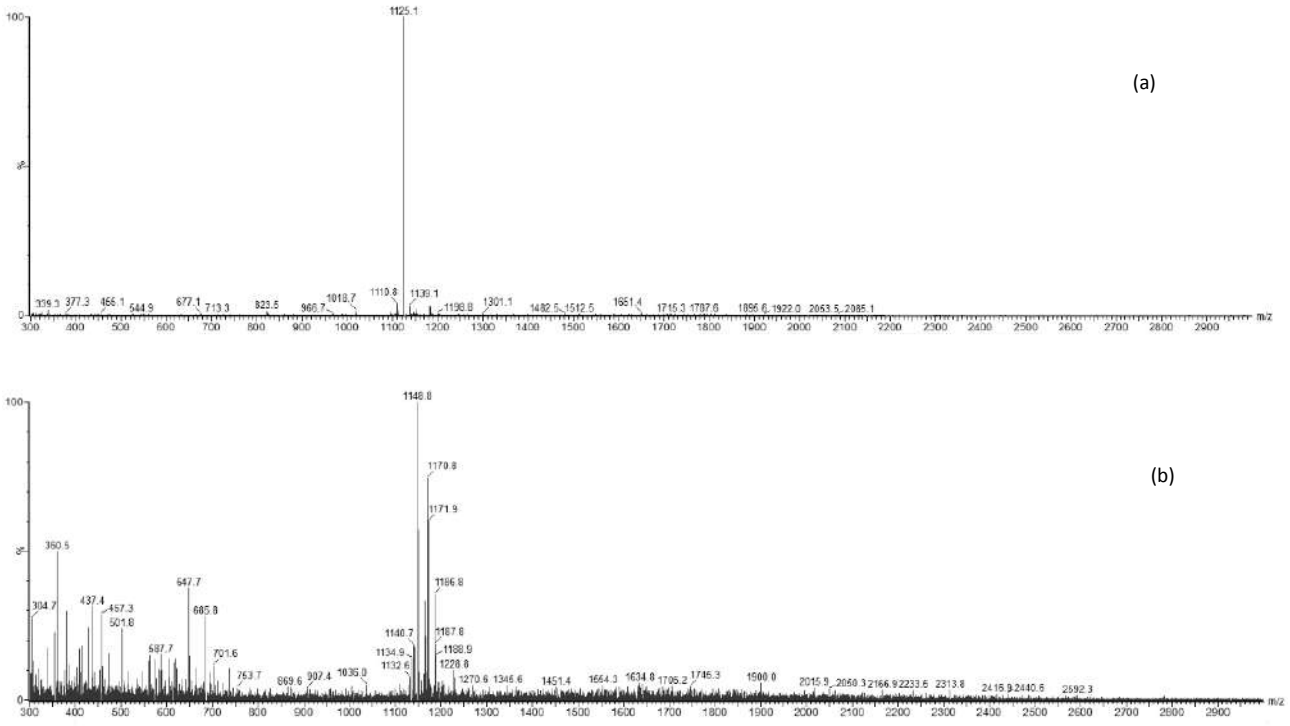

FIGURE 2. (A) ESI (-) MASS SPECTRA, AND (B) ESI (+) MASS PROFILE OF THE PRODUCT OBTAIN BY THE TECHNIQUE OF ACIDIC PRECIPITATION.

3.4 Adsorption Chromatography

The elution was achieved with a mixture of ethyl acetate/ethanol 1:1 (v/v). A fraction of 380 mg (38%) from 1 g of lyophilized retentate was obtained. The majority fraction showed a retention factor (R_f) of 0.4 in thin layer chromatography (TLC). This fraction showed positive reaction to sulfuric acidic reagent but negative reaction to ninhydrine.

CMC value was determined to confirm that isolated fraction from the column has surfactant activity. To calculate this was made a graph of surface tension versus concentration as shown in Figure 3. A value of CMC of 0.15 mg/mL was obtained. The value of surface tension at that concentration reached values of 29.6 mN/m.

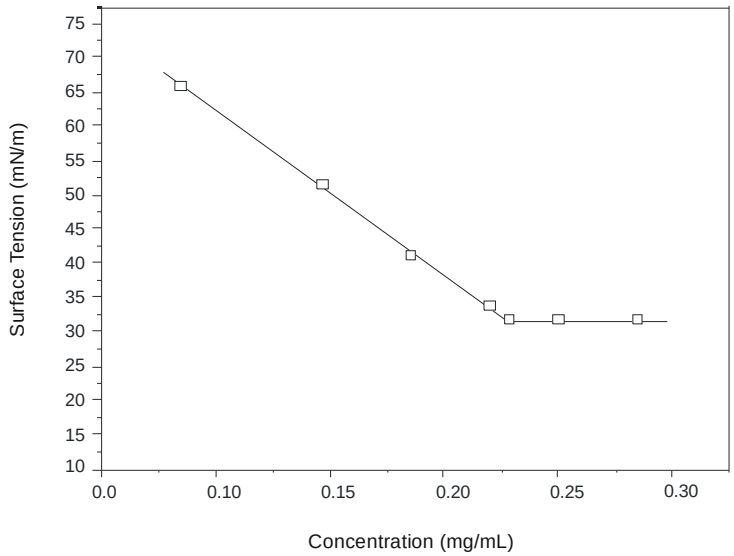

FIGURE 3. EFFECT OF ISOLATED BIOSURFACTANT CONCENTRATION ON SURFACE TENSION. THE INTERSECTION OF REGRESSION LINES DETERMINES VALUE OF CMC

3.5 Analysis by LC-MS

The majority fraction was analyzed by electrospray ionization-mass spectrometry (ESI-MS) coupled to a HPLC system. As shown in Figure 4 a series of negatively charged ions were observed in major faction isolated by adsorption chromatography. The analytes were eluted to a gradient of acetonitrile/water to 0.1% formic acid 65:35 (v/v) to 80:20 (v/v).

A retention time (RT) of 9.21 minutes was obtained by liquid chromatography-mass spectrometry LC-MS for the ion with the highest relative intensity in the form of negative ionization (Figure 4).This could be related to the deprotonated ion $[M-H]^-$ 1125.1 observed in electrospray ionization-negative ion mode (ESI-) mass spectrum, and with their corresponding sodiated ions m/z 1148.9 and 1171.8 found in electrospray ionization-positive ion mode (ESI+) mass spectrum (see Figure 2). The chromatogram showed also other less intense peaks m/z 1111; 1139 and 1154. These ions were not present in the (ESI-) mass spectrum of the product of precipitation in the Figure 2.

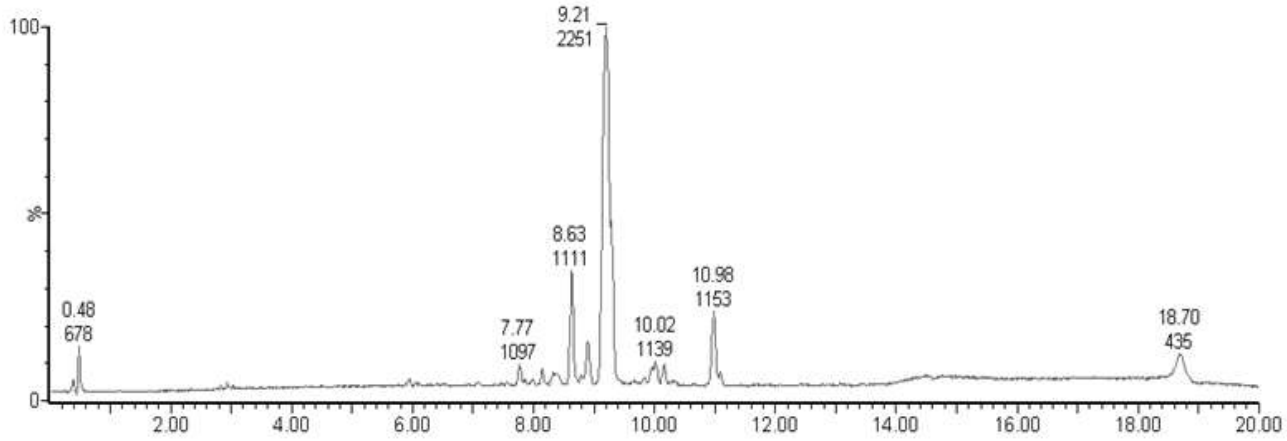

FIGURE 4. LC ESI-MS PROFILE IN NEGATIVE IONIZATION OF THE MAJOR FRACTION. THE SCAN RANGE WAS M/Z 300 TO 3000 DA.

3.6 Spectral scanning

The fraction obtained by chromatography showed a maximum of absorbance at 210 nm.

IV. DISCUSSION

The amount of surfactant needed to achieve the lowest possible surface tension is defined as the CMC, typically ranges from 1 to 200 mg/L for biological surfactants [16]. In the present study, the CMC of the crude biosurfactants and the purified majority fraction were investigated. It was possible to obtain a product with attractive surface tension values from unconcentrated culture broth. Values of CMC of dodecyl sulfate sodium (SDS) and Pluronic F-68, two chemical surfactants, were reported by O. Pornsunthorntawee et al. (2008) [17]. They found that Pluronic F-68 and SDS are able to reduce the surface tension of pure water in 42.8 and 28.6 mN/m, and the CMC values were approximately 350 and 1280 mg/L, respectively. In our case, were obtained lower values than pure chemical surfactants listed above. The retentate, reduced the surface tension of ultrapure water to 29.6 mN/m and the value of CMC was 300 mg/L. Even lower values were found for the fraction isolated by chromatography, which indicates that the compounds with greater surface activity were purified.

There are a wide variety of microorganisms have ability to produce biosurfactants, the genus *Pseudomonas* stands among them. It was reported that the strains of the genus *Pseudomonas* can produce cyclic lipopeptides and glycolipids such as rhamnolipids, these are two biosurfactants that differ in their structure and molecular weight [18]. The aim of our work is only identify the family of biosurfactants, since that in order to determine the specific structure of the compounds; it would necessary to perform Nuclear Magnetic Resonance studies and analysis of MS/MS.

Masses between 1000 and 1200 Da were observed by mass spectrometry and a maximum absorbance at 210 nm was found in the spectral scanning. This latter might indicate the presence of compounds in its structure containing peptide bonds, this could explain the high molecular weight found. The family of the compounds best known that contains hydrophobic and hydrophilic amino acids in their structure and surfactants activities are denominated cyclic lipopeptides [19]. There are two lipopeptides well described in the literature that belong to group of Viscosin, this are Viscosin and WLIP (white line-inducing principle). Its structure is very similar and both of them have a molecular weight of around of 1126 Da and 1149 Da when they form adducts with ion sodium [13], [20], [21]. The analytes observed by mass spectrometry could to form part of this family. The isolated compounds may not have free amino groups in their structure; this explains why the ninhydrin reaction was negative. This happens with Viscosin and WLIP. In contrast Viscosinamide has glutamine in its structure and the reaction of ninhydrin is positive [22].

Masses of 502, 648 and 702 Da were found, indicating that there possibly other family of compounds released to the culture broth for the strain used. These masses were described for mono and dirhamnolipids. Variations in rhamnolipid structures and their possible molecular weights are well known and are reported [23].

By acid precipitation and subsequent extraction we isolated and identified total biosurfactants. By acid precipitation technique we quantified total surfactant, and with extraction with solvents were eliminated proteins and other possible contaminants. However, in order to determine what proportion each produces, it is necessary to isolate each family of compounds. We isolate by adsorption chromatography a fraction of higher yield. The percentage of the major fraction corresponded to 84 % (w/w) of biosurfactants produced by *Pseudomonas*. In this fraction they were observed masses of 1100 to 1200 Da.

V. CONCLUSION

In the present work, we produce biosurfactants from non pathogenic *Pseudomonas*. We have obtained a possible product with surfactant activity through the addition of an ultrafiltration step in the production process, which is able to compete with a synthetic surfactant. This we demonstrate it with the CMC values achieved.

We detected two families of analytes secreted in the culture supernatant by mass spectrometry. We were able to isolate the majority fraction by adsorption chromatography; we believe that the strain used produced cyclic lipopeptides due to the molecular weights found. However, it is necessary to perform nuclear magnetic resonance studies and other structural studies that allow the detection of functional groups and confirm the above. We will continue to work on the characterization of the analytes found (biosurfactants), with possible applications as adjuvants in the agricultural sector.

ACKNOWLEDGEMENTS

The present work is partially supported by the National Council of Scientific and Technical Research (CONICET) and the National University of the Litoral (UNL) of Argentina.

REFERENCES

[1] L. Sim, O. P. Ward, and Z. Y. Li, "Production and characterisation of a biosurfactant isolated from *Pseudomonas aeruginosa* UW-1", J. Ind. Microbiol. Biotechnol., vol 19, pp. 232–238, 1997.

[2] M. Nitschke, S. G. V. A. O. Costa, and J. Contiero, "Rhamnolipid Surfactants: An Update on the General Aspects of These Remarkable Biomolecules". Biotechnol. Prog., vol 21, pp.1593–1600, 2005.

[3] S. Mukherjee, P. Das, and R. Sen, "Towards commercial production of microbial surfactants", Trends. Biotechnol., vol 24, pp. 509–515, 2006.

[4] J. D´aes, K. De Maeyer, E. Pauwelyn, and M. Höfte, "Biosurfactants in plant-*Pseudomonas* interactions and their importance to biocontrol", Environ. Microbiol. Rep., vol 2, pp. 359–372, 2010.

[5] R. Thenmozhi, A. Sornalaksmi, D. Praveenkumar, and A. Nagasathya, "Characterization of biosurfactant produced by bacterial isolates from engine oil contaminated soil", Adv. Environ. Biol., vol 5, pp. 2402–2408, 2011.

[6] M. Nitschke, and S. G. V. A. O. Costa, "Biosurfactants in food industry", Trends. Food. Sci. Technol., vol. 18, pp. 252–259, 2007.

[7] I. M. Banat, R. S. Makkar and S. S Cameotra, "Potential commercial applications of microbial surfactants", Appl. Microbiol. Biotechnol. Vol. 53, pp. 495–508, 2000.

[8] S. S. Cameotra, and R. S. Makkar, "Recent applications of biosurfactants as biological and immunological molecules", Curr. Opin. Microbiol., vol. 7, pp. 262–266, 2004.

[9] V. Singh, "Biosurfactant – Isolation, Production, Purification & Significance", Int. J. Sci. Re.s Publ., vol. 2, pp. 2250–3153, 2012.

[10] L. Rodrigues, I. M. Banat, J. Teixeira, and R. Oliveira, "Biosurfactants: Potential applications in medicine", J. Antimicrob. Chemother. Vol. 57, pp. 609–618, 2006.

[11] S. P. Lim, N. Roongsawang, K. Washio, and M. Morikawa, "Functional analysis of a pyoverdine synthetase from *Pseudomonas* sp. MIS38", Biosci. Biotechnol. Biochem., vol. 71, pp. 2002–2009, 2007.

[12] S. P. Lim, N. Roongsawang, K. Washio, and M. Morikawa, "Flexible exportation mechanisms of arthrofactin in *Pseudomonas* sp. MIS38", J. Appl. Microbiol., vol. 107, pp. 157–166, 2009.

[13] H. Gross, and J. E. Loper, "Genomics of secondary metabolite production by *Pseudomonas* spp", Nat. Prod. Rep., vol. 26, pp. 1408–1446, 2009.

[14] D. Haas, and G. Défago, "Biological control of soil-borne pathogens by fluorescent pseudomonads", Nat. Rev. Microbiol., vol. 3, pp. 307–319, 2005.

[15] W. J. Xia, Z. B. Luo, H. P. Dong, L. Yu, Q. F. Cui, and Y. Q. Bi, "Synthesis, Characterization, and Oil Recovery Application of Biosurfactant Produced by Indigenous *Pseudomonas aeruginosa* WJ-1 Using Waste Vegetable Oils", Appl. Biochem. Biotechnol., vol. 166, pp. 1148–1166, 2012.

[16] Y. Zhang, and R. M Miller, "Enhanced octadecane dispersion and biodegradation by a Pseudomonas rhamnolipid surfactant (biosurfactant)". Appl. Environ. Microbiol., vol. 58, pp. 3276-82, 1992.

[17] O. Pornsunthorntawee, P. Wongpanit, S. Chavadej, M. Abe, and R. Rujiravanit, "Structural and physicochemical characterization of crude biosurfactant produced by *Pseudomonas aeruginosa* SP4 isolated from petroleum-contaminated soil", Bioresour. Technol., vol. 99, pp. 1589–1595, 2008.

[18] J. Toribio-Jiménez, J. C. V. Aradillas, Y. Romero Ramírez, M. A. Rodríguez Barrera, J. D. González Chávez, J. Luna Guevara, and J. L. Noyola Aguirre, "*Pseudomonas* sp productoras de biosurfactantes", Tlamati, vol. 5, pp. 66–82, 2014.

[19] J. M. Raaijmakers, I. De Bruijn, and M. J. D. De Kock, "Cyclic Lipopeptide Production by Plant-Associated *Pseudomonas* spp.: Diversity, Activity, Biosynthesis, and Regulation", Mol. Plant-Microbe Interact., vol. 19, pp. 699–710, 2006.

[20] H. Rokni Zadeh, W. Li, A. Sanchez Rodriguez A, D. Sinnaeve, J. Rozenski, J. C. Martins, and R. De Mot, "Genetic and functional characterization of cyclic lipopeptide white-line-inducing principle (WLIP) production by rice rhizosphere isolate *pseudomonas putida* RW10S2", Appl. Environ. Microbiol., vol. 78, pp. 4826–4834, 2012.

[21] H. S. Saini, B. E. Barragán Huerta, A. Lebrón Paler, J. E. Pemberton, R. R. Vázquez, A. M. Burns, M. T. Marron, C. J. Seliga, A. A. L. Gunatilaka, and R. M. Maier, "Efficient Purification of the Biosurfactant Viscosin from *Pseudomonas libanensis* Strain M9-3 and Its Physicochemical and Biological Properties", J. Nat. Prod., vol. 71, pp. 1011–1015, 2008.

[22] T. H. Nielsen, C. Christophersen, U. Anthoni, and J. Sorensen, "Viscosinamide, a new cyclic depsipeptide with surfactant and antifungal properties produced by *Pseudomonas fluorescens* DR54", J. Appl. Microbiol., vol. 87, pp. 80–90, 1999.

[23] A. M. Abdel Mawgoud, F. Lépine, and E. Déziel, "Rhamnolipids: diversity of structures, microbial origins and roles", Appl. Microbiol. Biotechnol., vol. 86, pp. 1323–1336, 2010.

Combination of emodin with antibiotics against methicillin-resistant *Staphylococcus aureus* isolated from clinical specimens

Su-Mi Cha[1], Eun-Jin Jang[2], Sung-Mi Choi[3], Jeong-Dan Cha[4*]

[1,4]Department of Oral Microbiology and Institute of Oral Bioscience, Chonbuk National University, Jeonju, 561-756, Republic of Korea
[2]Department of Dental Technology, Daegu Health College, Daegu, South Korea.
[3]Department of Dental Hygiene, Daegu Health College, Daegu, South Korea

***Abstract*—** *Emodin (3-methyl-1,6,8-trihydroxyanthraquinone), a natural anthraquinone compound, is an active compound derivative isolated from the rhizome of Rheum undulatum L, an herb widely used as a laxative in traditional Korean medicine. Emodin has been reported to have a variety of biological activities, such as anti-cancer, vasorelaxation, immunosuppressive, anti-inflammatory and wound healing properties. In this study, emodin was evaluated against 20 clinical isolates of MRSA, either alone or in combination with antibiotics. The emodin exhibited strong antibacterial activity against isolates MRSA with MICs/MBCs ranged between 64-256/64-512 μg/mL, for ampicillin 64-512/128-1024 μg/mL, and for oxacillin 8-64/16-64 μg/mL. The combination of emodin plus oxacillin or ampicillin was reduced by ≥4-fold against isolates MRSA tested, evidencing a synergistic effect as defined by a FICI of ≤ 0.5. Furthermore, a time-kill study evaluating the growth of the tested bacteria was completely attenuated after 2-6 h of treatment with the 1/2 MIC of emodin, regardless of whether it was administered alone or with oxacillin (1/2 MIC) or ampicillin (1/2 MIC). In conclusion, emodin exerted synergistic effects when administered with oxacillin or ampicillin and the antibacterial activity and resistant regulation of emodin against clinical isolates of MRSA might be useful in controlling MRSA infections.*

***Keywords*— emodin, methicillin-resistant Staphylococcus aureus, minimum inhibitory concentrations, minimum bactericidal concentrations, time-kill curves, fractional inhibitory concentration.**

I. INTRODUCTION

Staphylococcus aureus is both a commensal bacterium and a human pathogen. Approximately 50% to 60% of individuals are intermittently or permanently colonized with *S. aureus* and, thus, there is relatively high potential for infections [1, 2]. Indeed, *S. aureus* is among the most prominent causes of bacterial infections in the United States and other industrialized countries. Simultaneously, it is a leading cause of bacteremia and infective endocarditis (IE) as well as osteoarticular, skin and soft tissue, pleuropulmonary, and devicerelated infections [3, 4]. Methicillin-sensitive *S. aureus* (MSSA) and methicillin-resistant *S. aureus* (MRSA) are major causes of life-threatening infections including surgical site infections, bacteraemia, pneumonia and catheter-associated infections, leading to significant morbidity and mortality [5-7]. There is a very limited antimicrobial armamentarium to treat MRSA infections, of which vancomycin (a glycopeptide) and linezolid (an oxazolidinone antibiotic) are the major antibiotics [8, 9]. Antimicrobial drugs effective for treatment of patients infected with MRSA are limited. Thus, it is important and valuable to find compounds that potentiate antimicrobial activity of antibiotics. Plant medicines are used on a worldwide scale to prevent and treat infectious diseases [10, 11]. They are of great demand both in the developed as well as developing countries for the primary health care needs due to their wide biological and medicinal activities, higher safety margin and lesser costs [12, 13]. At the same time, because of the difficulty in developing chemical synthetic drugs and because of their side-effects, scientists are making more efforts to search for new drugs from plant resources to combat clinical multidrug-resistant microbial infections [13-15].

Emodin (3-methyl-1,6,8-trihydroxyanthraquinone), a natural anthraquinone compound, is an active compound derivative isolated from the rhizome of *Rheum undulatum L*, an herb widely used as a laxative in traditional Korean medicine [16, 17]. Emodin has been reported to have a variety of biological activities, such as anti-cancer, vasorelaxation, immunosuppressive, anti-inflammatory, antibacterial activity, and wound healing properties [18-22]. Emodin is shown to significantly inhibit biofilm formation in *P. aeruginosa*, induces proteolysis of a known AHL-binding protein, and can be used as a potential QS inhibitor for the control of biofilm formation and growth [23]. Emodin from *Polygonum cuspidatum* exhibits strong

antibacterial activity against *Haemophilus parasuis in vitro*. The antibacterial mechanism of emodin to *H. parasuis* attributed to producing alterations on the physical structure and increasing cell membrane permeability [24].

In this study, the antimicrobial activities of emodin against methicillin-resistant *Staphylococcus aureus* isolated in a clinic were assessed using broth microdilution method and the checkerboard and time-kill methods for synergistic effect of the combination with antibiotics.

II. MATERIALS AND METHODS

2.1 Preparation of bacterial strains

20 isolates of methicillin-resistant *Staphylococcus aureus* isolated from the Wonkwang University Hospital, as well as standard strains of methicillin-sensitive *S. aureus* (MSSA) ATCC 25923 and methicillin-resistant *S. aureus* (MRSA) ATCC 33591 were used. Antibiotic susceptibility was determined in testing the inhibition zones (inoculums 0.5 McFarland suspension, 1.5×10^8 CFU/ml) and MIC/MBC (inoculums 5×10^5 CFU/ml) for strains, measured as described in the National Committee for Clinical Laboratory Standards (NCCLS, 1999). Briefly, the growth of bacteria was examined at 37°C in 0.95 mL of BHI broth containing various concentrations of emodin. These tubes were inoculated with 5×10^5 colony-forming units (CFU)/mL of an overnight culture grown in BHI broth, and incubated at 37°C. After 24 h of incubation, the optical density (OD) was measured spectrophotometrically at 550 nm. Three replicates were measured for each concentration of tested drugs. To rapidly identifying the methicillin-resistance, presence of *mecA* gene in MRSA isolates was detected using PCR method as the following [25].

2.2 Minimum inhibitory concentrations/minimum bactericidal concentrations assay

The antimicrobial activities of emodin against clinical isolates MRSA 20 and reference strains were determined *via* the broth dilution method [26, 27]. The minimum inhibitory concentrations (MICs) were recorded as the lowest concentration of test samples resulting in the complete inhibition of visible growth. For clinical strains, MIC_{50}s and MIC_{90}s, defined as MICs at which, 50 and 90%, respectively of the isolates were inhibited, were determined. The minimum bactericidal concentrations (MBCs) were determined based on the lowest concentration of the extracts required to kill 99.9% of bacteria from the initial inoculum as determined by plating on agar.

2.3 Checkerboard dilution test

The synergistic combinations were investigated in the preliminary checkerboard method performed using the MRSA, MSSA, and one clinical isolate strains via MIC determination [26, 27]. The fractional inhibitory concentration index (FICI) and fractional bactericidal concentration index (FBCI) are the sum of the FICs and FBCs of each of the drugs, which were defined as the MIC and MBC of each drug when used in combination divided by the MIC and MBC of each drug when used alone. The FIC and FBC index was calculated as follows: FIC = (MIC of drug A in combination/MIC of drug A alone) + (MIC of drug B in combination/MIC of drug B alone) and FBC = (MBC of drug A in combination/MBC of drug A alone) + (MBC of drug B in combination/MBC of drug B alone). FIC indices (FICI) and FBCI were interpreted as follows: ≤ 0.5, synergy; >0.5-≤1.0, additive; >1.0-≤2.0, indifference; and >2.0, antagonism.

2.4 Time-kill curves

The bactericidal activities of the drugs evaluated in this study were also evaluated using time-kill curves constructed using the isolated and reference strains. Cultures with an initial cell density of $5\text{-}8\times10^6$ CFU/ml were exposed to the MIC of emodin alone, or emodin (1/2 MIC) plus oxacillin (1/2 MIC) or emodin (1/2 MIC) plus ampicillin (1/2 MIC). Viable counts were conducted at 0, 0.5, 1, 2, 3, 4, 5, 6, 12, and 24 h by plating aliquots of the samples on agar and subsequent incubation for 24 hours at 37°C. All experiments were repeated several times and colony counts were conducted in duplicate, after which the means were determined.

III. RESULTS AND DISCUSSION

The results of the antibacterial activity showed that the emodin exhibited inhibitory activities against isolates MRSA and reference stains, MRSA ATCC33591 and MSSA ATCC25923. In Table 1, the emodin displayed varying degrees of activity against clinical isolated MRSA 1-20 with MIC in the range of 64-256 μg/mL and MBC in the range of 64-256 μg/mL. The MICs/MBCs for ampicillin were determined to be either 64/128 or 1024/2048 μg/mL; for oxacillin, either 8/16 or 64/64 μg/mL against MRSA 1-20 isolates. The range of MIC_{50} and MIC_{90} were 16-64 μg/mL and 64-256 μg/mL against MRSA 1-20 isolates, respectively. Various anthraquinones constitute an important class of phytochemicals which possess diverse

biological activities against MRSA [21, 28, 29]. A chemical structure-activity relationship study revealed that two hydroxyl units at the C-1 and C-2 positions of anthraquinone play important roles in antibiofilm and anti-hemolytic activities [28]. Emodin exhibits strong antibacterial activity against *H. parasuis in vitro* [24]. Emodin exhibits antimicrobial activity against a broad range of gram-positive, including *S. aureus*, and Mycobacterium tuberculosis as well as other microorganisms [21, 24, 30].

TABLE 1
ANTIBACTERIAL ACTIVITY OF EMODIN AND ANTIBIOTICS IN ISOLATED MRSA AND SOME OF REFERENCE BACTERIA

Samples	emodin (μg/mL)			Ampicillin	Oxacillin
	$MIC_{50<}$	$MIC_{90<}$	(1) MIC/MBC	MIC/MBC (μg/mL)	
MSSA ATCC 25923 [1]	64	256	256/512	8/16	0.25/1
MRSA ATCC 33591 [2]	32	128	128/256	1024/2048	8/16
MRSA 1[3]	8	64	64/128	512/1024	16/32
MRSA 2	16	64	64/128	128/256	16/32
MRSA 3	32	64	128/256	512/2048	8/16
MRSA 4	64	128	256/256	256/512	16/64
MRSA 5	32	128	128/256	128/256	16/32
MRSA 6	16	64	64/128	256/512	8/32
MRSA 7	16	64	64/256	128/512	16/32
MRSA 8	32	128	128/256	256/512	8/32
MRSA 9	32	256	256/512	256/512	32/64
MRSA 10	64	128	256/256	64/128	8/16
MRSA 11	32	128	128/256	128/256	16/64
MRSA 12	16	64	64/64	256/512	32/64
MRSA 13	16	64	64/128	64/128	64/64
MRSA 14	16	64	64/128	128/512	16/32
MRSA 15	32	128	128/256	64/128	16/32
MRSA 16	32	128	128/256	128/256	16/32
MRSA 17	64	256	256/256	128/256	8/16
MRSA 18	64	256	256/512	64/128	16/32
MRSA 19	16	64	64/128	128/256	16/64
MRSA 20	32	128	128/256	128/512	16/32

[1]MSSA (ATCC 25923): reference strain Methicillin-sensitive *Staphylococcus aureus.*
[2]MRSA (ATCC 33591): reference strain Methicillin-resistant *Staphylococcus aureus.*
[3]MRSA (1-20): Methicillin-resistant *Staphylococcus aureus* isolated a clinic.

Combination antibiotic therapy has been studied to promote the effective use of antibiotics in increasing *in vivo* activity of antibiotics, in preventing the spread of drug-resistant strains, and in minimizing toxicity [26, 31, 32]. The combination of oxacillin and emodin showed in a reduction in the MICs/MBCs for all bacteria, with the MICs/MBCs of 8/16 or 64/128 μg/mL for oxacillin becoming 2-8/4-16 μg/mL and reduced by ≥4-fold in most of *S. aureus* tested, evidencing a synergistic effect as defined by a FICI of ≤ 0.5 except clinic MRSA 8, 11, and 15 at MIC and clinic MRSA 1, 4, 10, 15, and 17 at MBC (Table 2). In combination with emodin, the MICs/MBCs for ampicillin were reduced by ≥4-fold in most of *S. aureus* tested, evidencing a synergistic effect as defined by a FICI of ≤ 0.5 except clinic MRSA 7, 9, and 19 at MIC and clinic MRSA 4, 7, 10, 12, and 19 at MBC by FICI of > 0.625 (Table 3). The some plant derived compounds can improve the in vitro activity of some cell-wall inhibiting antibiotics by directly attacking the same target site, that is, peptidoglycan [21, 33].

TABLE 2
SYNERGISTIC EFFECTS OF EMODIN WITH OXACILLIN IN ISOLATED MRSA AND SOME OF REFERENCE BACTERIA

Samples	Agent	MIC/MBC (μg/mL)		FIC/FBC	FICI/FBCI[2]	Outcome
		Alone	Combination[1]			
MSSA ATCC 25923[3]	Emodin	256/512	128/256	0.5/0.5	0.75/0.75	**Additive/ Additive**
	Oxacillin	0.25/1	0.0625/0.25	0.25/0.25		
MRSA ATCC 33591[4]	Emodin	128/256	32/64	0.25/0.25	0.5/0.5	**Synergistic/ Synergistic**
	Oxacillin	8/16	2/4	0.25/0.25		
MRSA 1[5]	Emodin	64/128	16/32	0.25/0.25	0.5/0.75	**Synergistic/ Additive**
	Oxacillin	16/32	4/16	0.25/0.5		
MRSA 2	Emodin	64/128	16/32	0.25/0.25	0.5/0.5	**Synergistic/ Synergistic**
	Oxacillin	16/32	4/8	0.25/0.25		
MRSA 3	Emodin	128/256	32/64	0.25/0.25	0.5/0.5	**Synergistic/ Synergistic**
	Oxacillin	8/16	2/4	0.25/0.25		
MRSA 4	Emodin	256/256	64/128	0.25/0.5	0.5/0.75	**Synergistic/ Additive**
	Oxacillin	16/64	4/16	0.25/0.25		
MRSA 5	Emodin	128/256	32/64	0.25/0.25	0.5/0.5	**Synergistic/ Synergistic**
	Oxacillin	16/32	4/8	0.25/0.25		
MRSA 6	Emodin	64/128	16/32	0.25/0.25	0.5/0.5	**Synergistic/ Synergistic**
	Oxacillin	8/32	2/4	0.25/0.25		
MRSA 7	Emodin	64/256	16/32	0.25/0.125	0.5/0.375	**Synergistic/ Synergistic**
	Oxacillin	16/32	4/8	0.25/0.25		
MRSA 8	Emodin	128/256	64/64	0.5/0.25	0.75/0.5	**Additive/ Synergistic**
	Oxacillin	8/32	2/8	0.25/0.25		
MRSA 9	Emodin	256/512	64/128	0.25/0.25	0.5/0.5	**Synergistic/ Synergistic**
	Oxacillin	32/64	8/16	0.25/0.25		
MRSA 10	Emodin	256/256	64/128	0.25/0.5	0.5/0.75	**Synergistic/ Additive**
	Oxacillin	8/16	2/4	0.25/0.25		
MRSA 11	Emodin	128/256	64/64	0.5/0.25	0.75/0.375	**Additive/ Synergistic**
	Oxacillin	16/64	4/8	0.25/0.125		
MRSA 12	Emodin	64/64	8/16	0.125/0.25	0.375/0.5	**Synergistic/ Synergistic**
	Oxacillin	32/64	8/16	0.25/0.25		
MRSA 13	Emodin	64/128	16/32	0.25/0.25	0.375/0.5	**Synergistic/ Synergistic**
	Oxacillin	64/64	8/16	0.125/0.25		
MRSA 14	Emodin	64/128	8/32	0.125/0.25	0.375/0.5	**Synergistic/ Synergistic**
	Oxacillin	16/32	4/8	0.25/0.25		
MRSA 15	Emodin	128/256	32/64	0.25/0.25	0.75/0.75	**Additive/ Additive**
	Oxacillin	16/32	8/16	0.5/0.5		
MRSA 16	Emodin	128/256	32/64	0.25/0.25	0.5/0.5	**Synergistic/ Synergistic**
	Oxacillin	16/32	4/8	0.25/0.25		
MRSA 17	Emodin	256/256	64/128	0.25/0.5	0.5/1.0	**Synergistic/ Additive**
	Oxacillin	8/16	2/8	0.25/0.5		
MRSA 18	Emodin	256/512	64/128	0.25/0.25	0.5/0.5	**Synergistic/ Synergistic**
	Oxacillin	16/32	4/8	0.25/0.25		
MRSA 19	Emodin	64/128	16/32	0.25/0.25	0.5/0.375	**Synergistic/ Synergistic**
	Oxacillin	16/64	4/8	0.25/0.125		
MRSA 20	Emodin	128/256	32/64	0.25/0.25	0.5/0.5	**Synergistic/ Synergistic**
	Oxacillin	16/32	4/8	0.25/0.25		

[1]The MIC and MBC of emodin with oxacillin
[2] the FIC/FBC index
[3]MSSA (ATCC 25923): reference strain Methicillin-sensitive *Staphylococcus aureus.*
[4]MRSA (ATCC 33591): reference strain Methicillin-resistant *Staphylococcus aureus.*
[5]MRSA (1-20): Methicillin-resistant *Staphylococcus aureus* isolated a clinic.

TABLE 3
SYNERGISTIC EFFECTS OF EMODIN WITH AMPICILLIN IN ISOLATED MRSA AND SOME OF REFERENCE BACTERIA

Samples	Agent	MIC/MBC (μg/mL)		FIC/FBC	FICI/FBCI[2]	Outcome
		Alone	Combination[1]			
MSSA ATCC 25923[3]	Emodin	256/512	64/128	0.25/0.25	0.75/0.75	**Additive/ Additive**
	Ampicillin	8/16	4/8	0.5/0.5		
MRSA ATCC 33591[4]	Emodin	128/256	32/64	0.25/0.25	0.5/0.5	**Synergistic/ Synergistic**
	Ampicillin	1024/2048	256/512	0.25/0.25		
MRSA 1[5]	Emodin	64/128	16/32	0.25/0.25	0.375/0.375	**Synergistic/ Synergistic**
	Ampicillin	512/1024	64/128	0.125/0.125		
MRSA 2	Emodin	64/128	16/32	0.25/0.25	0.5/0.5	**Synergistic/ Synergistic**
	Ampicillin	128/256	32/64	0.25/0.25		
MRSA 3	Emodin	128/256	32/64	0.25/0.25	0.375/0.3125	**Synergistic/ Synergistic**
	Ampicillin	512/2048	64/128	0.125/0.0625		
MRSA 4	Emodin	256/256	64/128	0.25/0.5	0.5/0.75	**Synergistic/ Additive**
	Ampicillin	256/512	64/128	0.25/0.25		
MRSA 5	Emodin	128/256	32/64	0.25/0.25	0.5/0.5	**Synergistic/ Synergistic**
	Ampicillin	128/256	32/64	0.25/0.25		
MRSA 6	Emodin	64/128	16/32	0.25/0.25	0.5/0.375	**Synergistic/ Synergistic**
	Ampicillin	256/512	64/64	0.25/0.125		
MRSA 7	Emodin	64/256	32/128	0.5/0.5	1.0/0.75	**Additive/ Additive**
	Ampicillin	128/512	64/128	0.5/0.25		
MRSA 8	Emodin	128/256	32/64	0.25/0.25	0.5/0.5	**Synergistic/ Synergistic**
	Ampicillin	256/512	64/128	0.25/0.25		
MRSA 9	Emodin	256/512	64/64	0.25/0.125	0.75/0.375	**Additive/ Synergistic**
	Ampicillin	256/512	128/128	0.5/0.25		
MRSA 10	Emodin	256/256	64/128	0.25/0.5	0.5/0.75	**Synergistic/ Additive**
	Ampicillin	64/128	16/32	0.25/0.25		
MRSA 11	Emodin	128/256	32/64	0.25/0.25	0.5/0.5	**Synergistic/ Synergistic**
	Ampicillin	128/256	32/64	0.25/0.25		
MRSA 12	Emodin	64/64	16/32	0.25/0.5	0.375/0.625	**Synergistic/ Additive**
	Ampicillin	256/512	32/64	0.125/0.125		
MRSA 13	Emodin	64/128	16/16	0.25/0.125	0.5/0.375	**Synergistic/ Synergistic**
	Ampicillin	64/128	16/32	0.25/0.25		
MRSA 14	Emodin	64/128	16/16	0.25/0.125	0.5/0.25	**Synergistic/ Synergistic**
	Ampicillin	128/512	32/64	0.25/0.125		
MRSA 15	Emodin	128/256	32/64	0.25/0.25	0.5/0.5	**Synergistic/ Synergistic**
	Ampicillin	64/128	16/32	0.25/0.25		
MRSA 16	Emodin	128/256	32/64	0.25/0.25	0.5/0.5	**Synergistic/ Synergistic**
	Ampicillin	128/256	32/64	0.25/0.25		
MRSA 17	Emodin	256/256	64/64	0.25/0.25	0.5/0.5	**Synergistic/ Synergistic**
	Ampicillin	128/256	32/64	0.25/0.25		
MRSA 18	Emodin	256/512	64/128	0.25/0.25	0.5/0.5	**Synergistic/ Synergistic**
	Ampicillin	64/128	16/32	0.25/0.25		
MRSA 19	Emodin	64/128	32/64	0.5/0.5	0.75/0.75	**Additive/ Additive0**
	Ampicillin	128/256	32/64	0.25/0.25		
MRSA 20	Emodin	128/256	32/64	0.25/0.25	0.375/0.375	**Synergistic/ Synergistic**
	Ampicillin	128/512	16/64	0.125/0.125		

[1]The MIC and MBC of emodin with ampicillin
[2] the FIC/FBC index
[3]MSSA (ATCC 25923): reference strain Methicillin-sensitive *Staphylococcus aureus*
[4]MRSA (ATCC 33591): reference strain Methicillin-resistant *Staphylococcus aureus*
[5]MRSA (1-20): Methicillin-resistant *Staphylococcus aureus* isolated a clinic

The efficacy of emodin administered with oxacillin or ampicillin on standard (MSSA and MRSA) and clinical isolates of MRSA (MRSA 1-20) was confirmed by time-kill curve experiment (Fig. 1-4). Cultures of each strain of bacteria with a cell density of 5-8×10^6 CFU/mL were exposed to the MIC of emodin alone or/and emodin (1/2 MIC) with oxacillin (1/2 MIC) or/and ampicillin (1/2 MIC). Interestingly, the combination of the emodin plus oxacillin or/and ampicillin exhibited a steady reduction of 5-8 × 10^6 CFU/mL to 10^3 CFU/mL within 6 h and did not recover within 24 h, as compared to that observed with emodin (MIC) alone. A powerful bactericidal effect was exerted when a combination of drugs was utilized. Although emodin has no influence on genes related to cell wall synthesis and lysis as well as β-lactamase activity and drug accumulation, emodin reduces membrane fluidity and disrupted membrane integrity [21]. This perturbation of the cell membrane coupled with the action of β-lactams on the transpeptidation of the cell membrane could lead to the enhanced antimicrobial effect [32, 33].

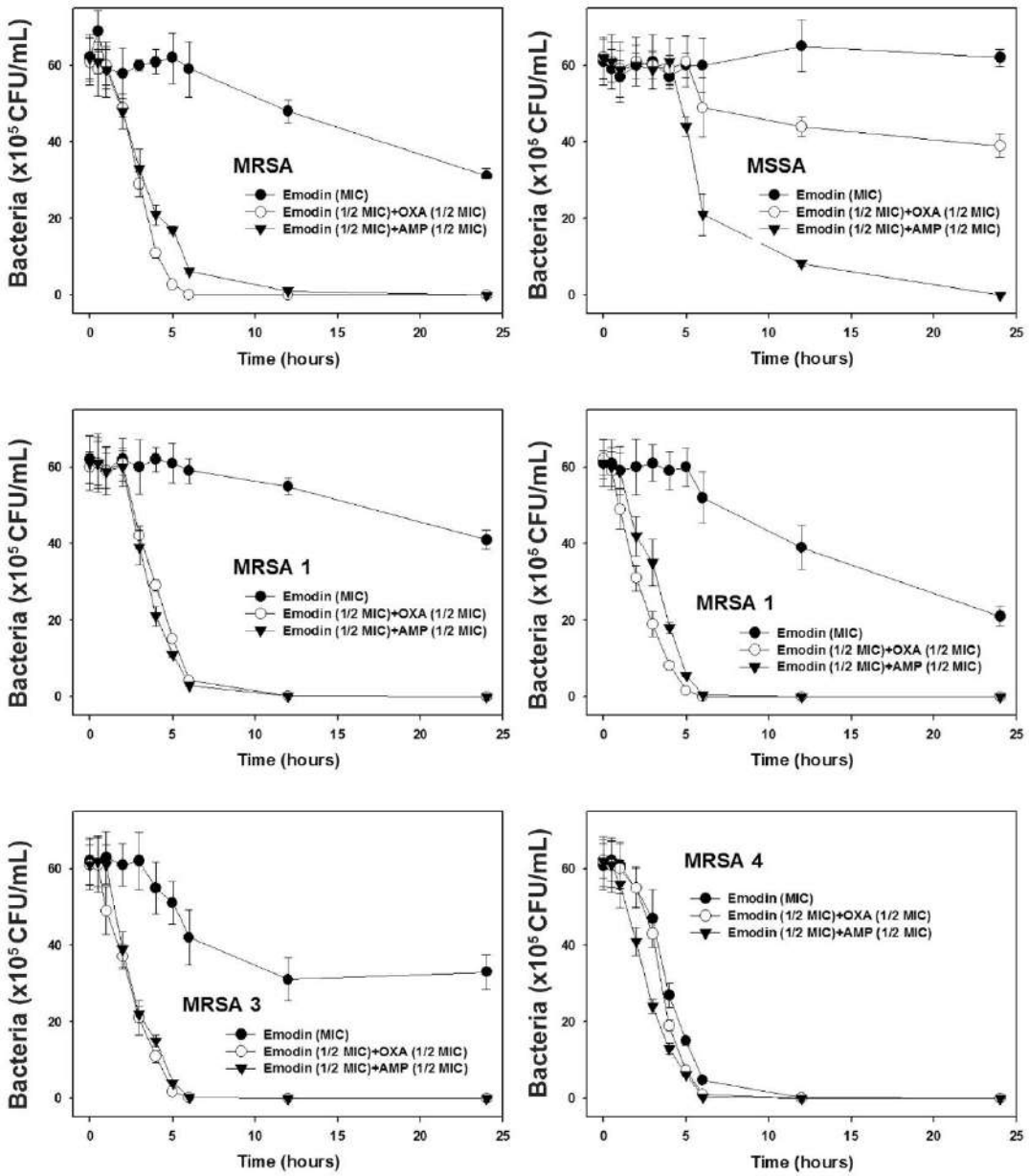

FIG. 1. TIME-KILL CURVES OF MIC OF EMODIN ALONE AND 1/2 MIC OF EMODIN WITH 1/2 MIC OF OXACILLIN OR AMPICILLIN AGAINST ISOLATES MRSA (1-4) AND METHICILLIN-SENSITIVE *S. AUREUS* (MSSA) ATCC 25923 AND METHICILLIN-RESISTANT *S. AUREUS* (MRSA) ATCC 33591 STRAINS. BACTERIA WERE INCUBATED WITH EMODIN ALONE (●) AND WITH AMPICILLIN (○) OR OXACILLIN (▼) OVER TIME. CFU, COLONY-FORMING UNITS.

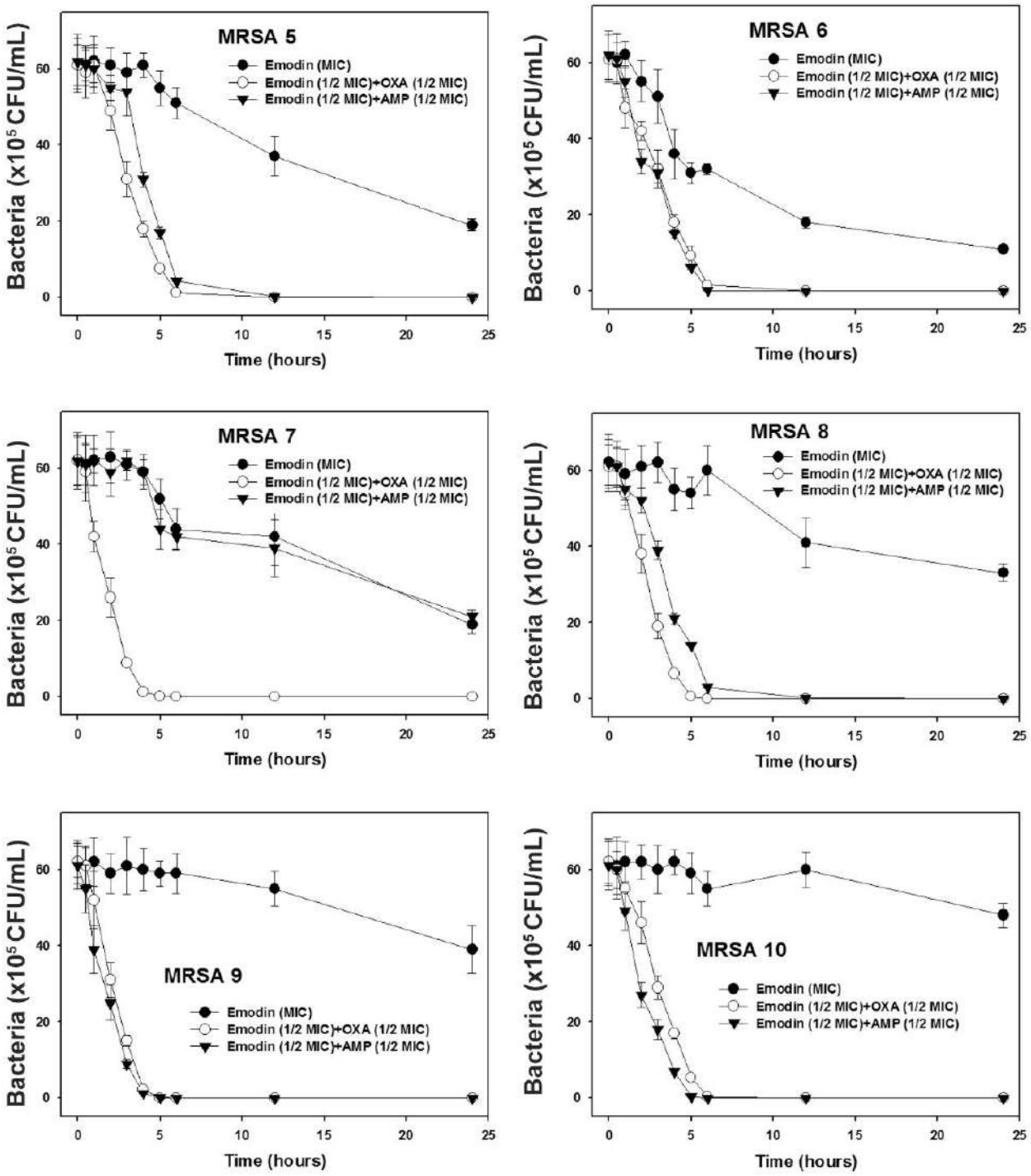

FIG. 2. TIME-KILL CURVES OF MIC OF EMODIN ALONE AND 1/2 MIC OF EMODIN WITH 1/2 MIC OF OXACILLIN OR AMPICILLIN AGAINST ISOLATES MRSA (5-10). BACTERIA WERE INCUBATED WITH EMODIN ALONE (●) AND WITH AMPICILLIN (○) OR OXACILLIN (▼) OVER TIME. CFU, COLONY-FORMING UNITS.

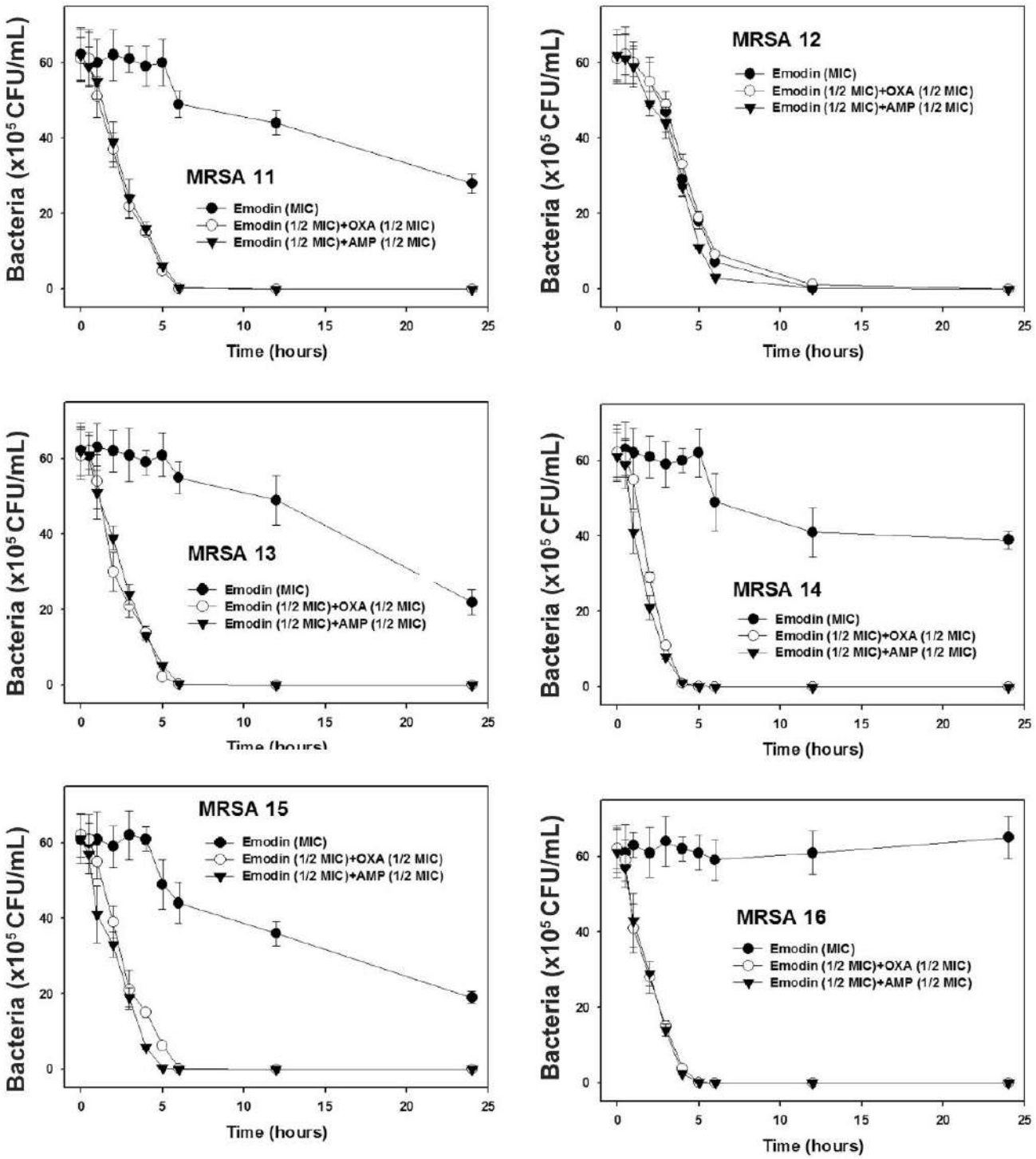

FIG. 3. TIME-KILL CURVES OF MIC OF EMODIN ALONE AND 1/2 MIC OF EMODIN WITH 1/2 MIC OF OXACILLIN OR AMPICILLIN AGAINST ISOLATES MRSA (11-16). BACTERIA WERE INCUBATED WITH EMODIN ALONE (●) AND WITH AMPICILLIN (○) OR WITH OXACILLIN (▼) OVER TIME. CFU, COLONY-FORMING UNITS.

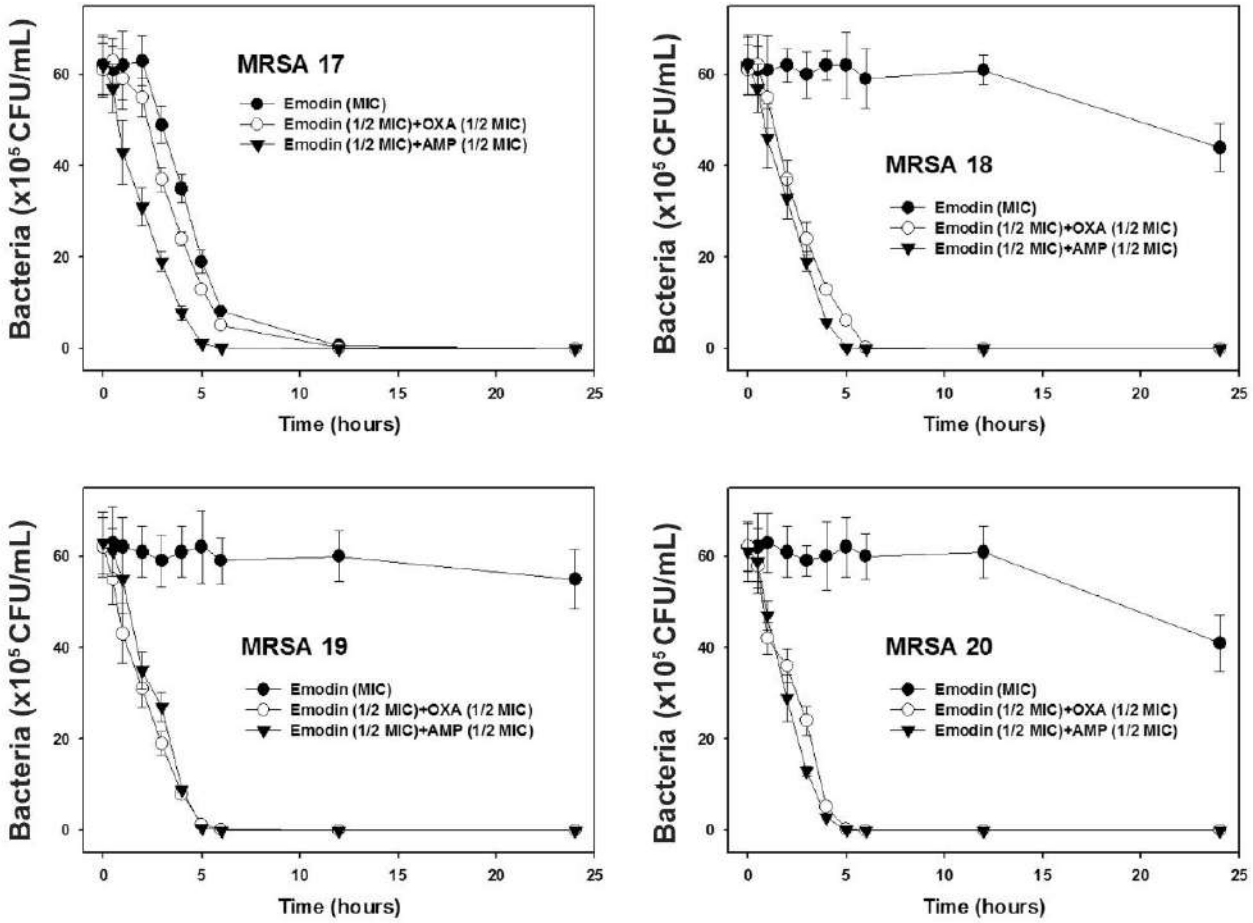

FIG. 4. TIME-KILL CURVES OF MIC OF EMODIN ALONE AND 1/2 MIC OF EMODIN WITH 1/2 MIC OF OXACILLIN OR AMPICILLIN AGAINST ISOLATES MRSA (17-20). BACTERIA WERE INCUBATED WITH EMODIN ALONE (●) AND WITH AMPICILLIN (○) OR WITH OXACILLIN (▼) OVER TIME. CFU, COLONY-FORMING UNITS.

In conclusion, our results of the antibacterial activity showed that emodin exhibited strong inhibitory activities against isolates MRSA. The combination effects of emodin with antibiotics were synergistic effect by FIC/FBC index <0.5 against most of tested clinic isolated MRSA. Emodin is expected to be recognized as natural sources for the development of new functional drugs against multi-resistant *S. aureus*, MRSA.

CONFLICT OF INTEREST STATEMENT

The authors have declared no conflict of interest.

ACKNOWLEDGEMENTS

This work was supported by a Korea Research Foundation Grant funded by the Korean Government (KRF-20110023479).

AUTHORS' CONTRIBUTION

Jeong-Dan Cha and Sung-Mi Choi have substantial contributions to conception and design and drafting and revising it. Su-Mi Cha and Eun-Jin Jang have substantial contributions to acquisition and analysis of data.

REFERENCES

[1] B. Pourakbari, G. Rezaizadeh, S. Mahmoudi, and S. Mamishi "Epidemiology of nosocomial infections in pediatric patients in an Iranian referral hospital," *J Prev Med Hyg*, vol. 53, no. 4, pp. 204-206, 2012.

[2] S. Krishna, and L. S. Miller "Host-pathogen interactions between the skin and *Staphylococcus aureus*," *Curr Opin Microbiol*, vol. 15, no. 1, pp. 28-35, 2012.

[3] B. E. Cleven, M. Palka-Santini, J, Gielen, S. Meembor, M. Kronke, and O. Krut "Identification and characterization of bacterial pathogens causing bloodstream infections by DNA microarray," *J Clin Microbiol*, vol. 44, no. 7, pp. 2389-2397, 2006.

[4] A. Zecconi, and F. Scali "*Staphylococcus aureus* virulence factors in evasion from innate immune defenses in human and animal diseases," *Immunol Lett*, vol. 150, no. 1-2, pp.12-22, 2013.

[5] S. Stefani, and P. E. Varaldo "Epidemiology of methicillin resistant staphylococci in Europe," *Clin Microbiol Infect*, vol. 9, no. 12, pp. 1179-1186, 2003.

[6] E. J. Choo, and H. F. Chambers "Treatment of Methicillin-Resistant Staphylococcus aureus Bacteremia," *Infect Chemother*, vol. 48, no. 4, pp. 267-273, 2016.

[7] S. M. Purrello, J. Garau, E. Giamarellos, T. Mazzei, F. Pea, A. Soriano, and S. Stefani "Methicillin-resistant Staphylococcus aureus infections: A review of the currently available treatment options," *J Glob Antimicrob Resist*, vol. 7, pp.178-186, 2016.

[8] J. Yue, B. R. Dong, M. Yang, X. Chen, T. Wu, and G. J. Liu "Linezolid versus vancomycin for skin and soft tissue infections," *Cochrane Database Syst Rev*, vol. 7, no. 1, pp.CD008056, 2016.

[9] C. Eckmann, D. Nathwani, W. Lawson, S. Corman, C. Solem, J. Stephens, C. Macahilig, J. Li, C. Charbonneau, N. Baillon-Plot, and S. Haider "Comparison of vancomycin and linezolid in patients with periopheral vascular disease and/or diabetes in an observational European study of complicated skin and soft-tissue infections due to methicillin resistant Staphylococcus aureus," *Clin Microbiol Infect*, vol. 21 no. Suppl 2, pp. S33-9, 2015.

[10] P. Dahiya, and S. Purkayastha "Phytochemica screening and antimicrobial activity of some medicinal plant multi-drug resistant bacteria from clinical isolates," *Indian J Pharm Sci*, vol. 74, no. 5, pp. 443-450, 2012.

[11] X. Su, A. B. Howell, and D. H. D'Souza "Antibacterial effects of plant-derived extracts on methicillin-resistant *Staphylococcus aureus," Foodborne Pathog Dis*, vol. 9, no. 6, pp. 573-578, 2012.

[12] F. Aqil, M. S. Khan, M. Osais, and I. Ahmad "Effect of certain bioactive plant extracts on clinical isolates of beta-lactamase producing methicillin-resistant *Staphylococcus aureus*," *J Basic Microbiol*, vol. 45, no. 2, pp. 106-114, 2005.

[13] J. N. Eloff "Which extractant should be used for the screening and isolation of antimicrobial components from plants?," *J Ethnopharmacol*, vol. 60, no. 1, pp. 1-8, 1998.

[14] D. E. Djeussi, J. A. K. Noumedem, B. T. Ngadjui, and V. Kuete "Antibacterial and antibiaotic-modulation activity of six Cameroonian medicinal plants against Gran-negative multi-drug resistant phenotypes," *Bmc Compem Altern*, vol. 4, no. 16, pp.124, 2016.

[15] J. Rios, and M. Recio "Medicinal plants and antimicrobial activity," *J Ethnopharmacol*, vol. 100, no. 1-2, pp. 80-84, 2005.

[16] S. Z. Choi, S. O. Lee, K. U. Jang, S. H. Chung, S. H. Park, H. C. Kang, E. Y. Yang, H. J. Cho, and K. R. Lee "Antidiabetic stilbene and anthraquinone derivatives from *Rheum undulatum," Arch Pharm Res*, vol. 28, no. 9, pp. 1027-1030, 2005.

[17] Y. Li, H. Liu, X. Ji, and J. Li "Optimized separation of pharmacologically active anthraquinones in rhubarb by capillary electrochromatography," *Electrophoresis*, vol. 21, no. 15, pp. 3109-3115, 2000.

[18] J. Lu, Y. Xu, X, Wei, Z. Zhao, J. Xue, and P. Liu "Emodin Inhibits the Epithelial to Mesenchymal Transition of Epithelial Ovarian Cancer Cells," *Biomed Res Int*, vol. 2016, pp. 6253280, 2016.

[19] S. Y. Park, M. L. Jin, M. J. Ko, G. Park, and Y. W. Choi "Anti-neuroinflammatory Effect of Emodin in LPS-Stimulated Microglia: Involvement of AMPK/Nrf2 Activation," *Neurochem Res*, vol. 41, no. 11, pp. 2981-2992, 2016.

[20] C. L. Zhang, L. N. Cong, R. Wang, Y. Wang, K. T. Ma, L. Zhao, J. Q. Si, and L. Li "Emodin-induced increase in expression of β1 subunit of BKCa channel mediates relaxation of cerebral basilar artery in spontaneously hypertensive rats," *Sheng Li Xue Bao*, vol. 66, no. 3, pp. 289-94, 2014.

[21] M. Liu, W. Peng, R. Qin, Z. Yan, Y. Cen, X. Zheng, X. Pan, W. Jiang, B. Li, X. Li, and H. Zhou "The direct anti-MRSA effect of emodin via damaging cell membrane," *Appl Microbiol Biotechnol*, vol. 99, no. 18, pp.7699-709, 2015.

[22] X. Y. Dai, W. Nie, Y. C. Wang, Y. Shen, Y. Li, and S. J. Gan "Electrospun emodin polyvinylpyrrolidone blended nanofibrous membrane: a novel medicated biomaterial for drug delivery and accelerated wound healing," *J Mater Sci Mater Med*, vol. 23, no. 11, pp. 2709-2716, 2012.

[23] X. Ding, B. Yin, L. Qian, Z. Zeng, Z. Yang, H. Li, Y. Lu, and S. Zhou "Screening for novel quorum-sensing inhibitors to interfere with the formation of Pseudomonas aeruginosa biofilm," *J Med Microbiol*. vol. 60, no. Pt 12, pp.1827-1834, 2011.

[24] L. Li, X, Song, Z. Yin, R. Jia, Z. Li, X. Zhou, Y. Zou, L. Li, L. Yin, G. Yue, G. Ye, C. Lv, W. Shi, and Y. Fu "The antibacterial activity and action mechanism of emodin from Polygonum cuspidatum against Haemophilus parasuis in vitro," *Microbiol Res*, vol. 186-187, pp. 139-145, 2016.

[25] F. Wallet, M. Roussel-Delvallez, and R. J. Courcol "Choice of a routine method for detecting methicillin-resistance in staphylococci," *J Antimicrob Chemother*, vol. 37, no. 5, pp. 901-909, 1996.

[26] M. W. Climo, R. L. Patron, and G. L. Archer "Combinations of vancomycin and beta-lactams are synergistic against staphylococci with reduced susceptibilities to vancomycin," *Antimicrob Agents Chemother*, vol. 43, no. 7, pp. 1747-1753, 1999.

[27] J. D. Cha, J. H. Lee, K. M. Choi, S. M. Choi, and J. H. Park "Synergistic Effect between Cryptotanshinone and Antibiotics against Clinic Methicillin and Vancomycin-Resistant Staphylococcus aureus," *Evid Based Complement Alternat Med*. Vol. 2014, pp. 450572, 2014.

[28] J. H. Lee, Y. G. Kim, S. Y. Ryu, and J. Lee "Calcium-chelating alizarin and other anthraquinones inhibit biofilm formation and the hemolytic activity of *Staphylococcus aureus*," *Sci Rep*, vol. 14, no. 6, pp. 19267, 2016.

[29] L. K. Omosa, J. O. Midiwo, A. T. Mbaveng, S. B. Tankeo, J. A. Seukep, I. K. Voukeng, J. K. Dzotam, J. Isemeki, S. Derese, R. A. Omolle, T. Efferth, and V. Kuete "Antibacterial activities and structure-activity relationships of a panel of 48 compounds from

Kenyan plants against multidrug resistant phenotypes," *Springerplus*, vol. 27, no. 1, pp. 901, 2016.

[30] D. Dey, R. Ray, and B. Hazra "Antitubercular and antibacterial activity of quinonoid natural products against multi-drug resistant clinical isolates," *Phytother Res*, vol. 28, no. 7, pp.1014-1021, 2014.

[31] B. Périchon, and P. Courvalin "Synersism between beta-lactams and glycopeptides against VanA-type methicillin-resistant *Staphylococcus aureus* and heterologous expression of the vanA operon," *Antimicrob Agents Chemother*, vol. 50, no. 11, pp. 3622-3630, 2006.

[32] R. Qin, K. Xiao, B. Li, W. Jiang, W. Peng, J. Zheng, and H. Zhou "The combination of catechin and epicatechin gallate from Fructus crataegi potentiates beta-lactam antibiotics against methicillin-resistant *Staphylococcus aureus* (MRSA) in vitro and in vivo," *Int J Mol Sci*, vol. 14, no. 1, pp. 1802-1821, 2013.

[33] J. G. Holler, H. C. Slotved, P. Mølgaard, C. E. Olsen, and S. B. Christensen "Chalcone inhibitors of the NorA efflux pump in *Staphylococcus aureus* whole cells and enriched everted membrane vesicles," *Bioorg Med Chem*, vol. 20, no. 14, pp. 4514-4521, 2012.

Three Level Security Technique of Image Steganography with Digital Signature Framework

Rahul Kamboj[1], Madhav Prasad Khanal[2]

[1]PG Scholar, Department of ECE, Punjab College of Engineering & Technology, Lalru, PUNJAB -140501
[2]Asst. Professor, Department of ECE, Punjab College of Engineering & Technology, Lalru, PUNJAB -140501

Abstract— *Steganography technique is more popular in recent years due to high level security involved in transferring the data. In image stegnography scheme the secret message is hidden inside a digital image by using different techniques. Least significant bit (LSB) is the commonly used technique foe embedding the information inside a cover image. A three level security scheme has been developed by using MATLAB with digital signature framework. The developed technique has a simpler approach as compared to other complex technique involved in secure transmission of data. The results are analyzed for different images using Peak Signal to noise ratio (PSNR) and the results reveals that the average PSNR value is enhanced by 15.83% compared to the reference values.*

Keywords — Image steganography, PSNR, MATLAB, LSB, Digital signature.

I. INTRODUCTION

As the usage of internet is increasing rapidly with digitization the main concern in the field of information technology (IT) and communication is security of data. Stegnography is the art and science of invisible communication. This technology conceal a message or an image within another image making it completely hidden that helps in secure transmission of information over insecure channel [1]. Image stegnography works on concept of hiding information exclusively in the form of images. Stegnography and cryptography techniques are used for security dealing with passing of secured information. Cryptography deals with maintain secrecy of content message whereas stegnography aims on maintain the secrecy of message. Data hiding method by improved LSB substitution process [2] which improves the PSNR with respect to image quality and computation work. The stego image quality can be greatly improved with minimum computational complexity by applying LSB image hiding method. The effectiveness of the proposed method is verified experimentally by achieving the balance between the security and the image quality. Exhaustive literature review of different stenographic techniques and their classification of the passed decade [3] highlighting the visual quality of the image provides a guideline for researchers and scientist. A method for hiding information on billboard display is presented [4] for online hiding of information on the output screen on the output screen of the instrument. Private marking system using symmetric key steganographic techniques and LSB techniques is used for hiding the secret information. Babloo Saha and Suchi Sharma [5] compiled research work in the field of stegnography deployed in spatial, transform and compression domain of digital images and conclude that transform domain techniques make changes in the frequency coefficients instead of manipulating the image pixels directly, leading to the minimum level of distortion thus preferred over spatial domain techniques. Framework to support the concept of image stegnography with structural design signature environment is given by Alam and Islam [6]. The experimental work by the author was conducted on smaller domain with a future plan to perform the experiment on standard data sets to test the effectiveness of framework. Arun Kumar et al. [7] proposed two simple fuzzy filters for the removal of impulse and gaussian noise in gray scale and color images. Hsien-Wei-Yang [8] proposed a reversible data hiding algorithm based on interleaving maximum-minimum histogram. In view of the above discussion the present work incorporates a MATLAB scheme for three level secure transmissions of data with digital signature framework.

II. METHODOLOGY

Following methodology is adopted for carrying out the proposed work as follows:

1. Selection of stego image-1 (SI-1) from the database.
2. Selection of cover image (CI-1) from the database.
3. Hide stego image-1 (SI-1) into cover image (CI-1) using LSB method which is modified by using MATLAB. The MATLAB program is modified in such a manner that instead changing only one bit, the program intends to change more than one bit for security purpose.
4. Apply the digital signature on the cover image-1 (CI-1) after embedding stego image into it.

5. Selection of cover image-2 (CI-2) from the database.
6. Now cover image-1 (CI-1) will act as stego image for cover image-2 (CI-2) providing three level of security.
7. Obtained image from step 6 is the final cover image to transmit.
8. Receiving of CI-2 at the receiver end.
9. Apply the reverse LSB on CI-2 to obtain CI-1.
10. Apply the digital signature on CI-1 to obtain cover image with stego image.
11. Again apply reverse LSB on CI-1 to obtain the stego image.

Now we will compare the proposed work with the work in [6] on the basis of PSNR.

2.1 Simulation Tool

MATLAB R2011a was used for simulation work and computations were done on computer with specifications as shown in Table 1.

TABLE 1
SPECIFICATIONS OF TOOL USED

Computer	Core 2 Duo or higher
RAM	3 MB
Platform	Windows 7
Other hardware	Keyboard, Mouse
Software	MATLAB 2011a

III. RESULTS AND DISCUSSION

Experimental investigation was conducted by creating different scenarios by using various set of images. The input to the MATLAB scheme was provided with three images for providing security with the help of stegnography. On running the developed scheme a window will be open from which we select the host image 1 from the data base and then a new window will open by which we select the host image 2 that will act as stego image and will hide in host image 1. Finally the last image as message image is selected that is to be encrypted, this image will hide in the host image 2 and to retrieve the message at the receiver end we apply a digital signature for decryption process to start and thus receiving the message image at the receiver end. The image quality was measured by using peak signal-to-noise ratio (PSNR). As images of different schemes are compared in terms of the PSNR which is estimated in decibel (dB) and higher PSNR value indicate a better image quality and is defined as:

$$PSNR = 10 \times \log_{10} \frac{255^2}{MSE} \tag{1}$$

Where MSE (Mean Square Error) is defined as

$$MSE = \frac{1}{wh} \sum_{i=1}^{w} \sum_{j=1}^{h} (h_{ij} - s_{ij})^2 \tag{2}$$

where w and h are the width and height of the image respectively and h_{ij} and s_{ij} are the pixel values of host and stego image at $[i, j]$ respectively..

Images used in the present work for different scenario is shown in Table 2, where the first column represents images as Host 1, second column represents the images as Host 2 and third column represents the message images taken for four different scenarios and comparative analysis of present work and reference work [6] is shown in Table 3.

TABLE 2
IMAGES USED FOR DIFFERENT SCENARIOS

Scenarios	Column 1(Host 1)	Column 2(Host 2)	Column 3(Message Image)
1			
2			
3			
4			

To compare the present results with the result of previous experimental studies the performance factor (PSNR) found in literature are summarized in Table 3. The literature review reveals that the analysis using three level securities with digital signature framework employed in the analysis has not been performed previously. So it is difficult to make direct comparison of the present study with the result obtain in previous study. However commonly used parameter for measuring image quality is peak signal to noise ratio (PSNR) is used in the present work.

TABLE 3
COMPARATIVE ANALYSIS FOR PSNR VALUES

Scenario	Host-1	Host-2	Message Image	Proposed Work	Reference Work [6]	Percentage Enhancement in PSNR Values
1	Rahul1	Bird	Objects	44.0736	38.04	15.86
2	Rahul2	Rahul1	Cameraman	44.7862	38.67	15.81
3	Rahul2	Rahul3	Rahul4	44.7875	38.57	16.12
4	Butterfly	Pepper	Rahul2	44.7858	38.79	15.45

IV. CONCLUSION

A scheme has been developed for secure transmission of high quality data with minimum distortion in the image. The developed scheme saves the computational time and reduces the complexity of the problem as compared to other techniques like DCT (Discrete cosine transform), DWT. The enhancement in the PSNR values for different scenarios from highest to lowest are: Scenario 3 (16.21%), Scenario 1 (15.86%), Scenario 2 (15.81%) and Scenario 4 (15.45%). Thus the result shows that the developed algorithm ensures higher quality of data and high encryption level.

ACKNOWLEDGEMENTS

I am greatly thankful to principal and the management of Punjab College of Engineering & Technology, Lalru, PUNJAB for motivation, encouragement and providing facility to carry out this research work.

REFERENCES

[1] Ms.G.S.Sravanthi, Mrs.B.Sunitha Devi, S.M.Riyazoddin & M.Janga Reddy "A Spatial Domain Image Steganography Technique Based on Plane Bit Substitution Method." Intertional Journal of Computer Application volume 5-No.7 October 2009.

[2] Vijay Kumar Sharma, Vishal Shrivastava, "A Steganography algorithm for hiding image in image by improved LSB substitution by minimizes detection". Journal of Theoretical and Applied Information Technology (JATIT), Vol. 36 No.1.

[3] Hussain and Mureed Hussain, "A Survey of Image Steganography Techniques. International Journal of Advanced Science and Technology" Vol. 54, May, 2013.

[4] Shashikala Channalli, Ajay Jadhav, "Steganography An Art of Hiding Data. International Journal on Computer Science and Engineering" Vol.1 (3), 2009, 137-141.

[5] Babloo Saha and Shuchi Sharma, "Steganographic Techniques of Data Hiding using Digital Images". Defense Science Journal, Vol. 62, No. 1, January 2012, pp. 11-18.

[6] Fahim Irfan Alam, Md. Mohaiminul Islam, "An Investigation into Image Hiding Steganography with Digital Signature Framework". IEEE, Vol. 6, No. 13, pp. 978-1-4799- 400, 2013.

[7] S.Arunkumar, Ravi Tej Akula, Rishabh Gupta & M.R.Vimala Devi, "Fuzzy Filters to the Reduction of Impulse and Gaussian Noise in Gray and Color Images". International Journal of Recent Trends in Engineering, Vol. 1, No. 1, May 2009.

[8] Hsien-Wei Yang, "Interleaving Max-Min Difference Histogram Shifting Data Hiding Method". Journal of software, VOL. 5, NO. 6, JUNE 2010.

A novel framework for a pull oriented product development and planning based on Quality Function Deployment

Omid Fatahi Valilai[1], Hossein Reyhani Kivi[2]

[1]Assistant Professor, Industrial Engineering, Sharif University of Technology, Azadi Street, Tehran, Iran
[2]M.Sc., Industrial Engineering, Khatam University, Molasadra street, Tehran, Iran

Abstract— *Nowadays, manufacturing organizations face with increasing pressures from the frequent changes in product type, continuous demand fluctuations and unexpected changes in customer requirements. In order to survive in this turbulent environment, manufacturing organizations must become flexible and responsive to these dynamic changes in the business environment. In this research, this papers has reviewed the current literature in the area of pull-oriented product systems and has suggested a novel framework for a pull-oriented product development system compatible with today's manufacturing environments. In the proposed framework, using the Quality Function Deployment (QFD) 4-stage matrix, a framework for product development has been proposed. The paper has used four general processes for products assembly. The framework provides capabilities for customer order analyze by a decision support system for order acceptance/rejection decision. Moreover, the accepted orders are prioritized into high and low priority orders, considering profitability of orders and a proposed assemble-to-order (ATO) production system for pull-oriented environments will handle the orders' fulfilment. The validity of proposed framework has been investigated by process analysis and simulating a scenario.*

Keywords— Product development system, Pull-oriented system, Quality Function Deployment (QFD), Assemble-to-order production (ATO).

I. INTRODUCTION

In a highly competitive environment, manufacturing organizations need a suitable production policy for the control of the production line so that the resources including machines as well as the buffer can be better utilized in conducting the manufacturing activities [1]. Manufacturing companies use different production policies to satisfy customers' demands. The most applicable production policies are Make-To-Stock (MTS), Make-To-Order (MTO), Assemble-To-Order (ATO) and Engineer-To-Order (ETO). Each policy has some specific advantages and disadvantages. Among them, MTS and MTO systems have been widely used in the production companies. In MTS companies, the customers' demands are satisfied with stocked inventories of finished products. The dominant features of such systems are short delivery time, heavy storage cost and low flexibility in responding to customized needs of customers. A substantial proportion of the research prior to 1990 in the production planning area had been aimed at the needs of MTS companies [2, 3]. On the other hand, MTO companies produce their products based on the customers' orders. Long delivery time, low storage cost and higher flexibility in responding to customers' demands are the main features of MTO systems [3, 4].

The success of an MTO system is heavily dependent on the selectivity of an order acceptance policy that seeks to maximize the average revenue per unit cost of requested capacity when demand exceeds capacity. It is noteworthy that the rejection of an order may have strategic repercussions for future customer relations, and may drastically change order arrival rates and patterns. The decision an MTO system has to make for an incoming order is whether to accept, negotiate or reject it depending on the available capacity, the profit contribution margin of the order and expected arrival times for future orders. A negotiation process of an order is only worth pursuing if accepting it may contribute significantly to generate more revenues per installed capacity and market niche development. Resorting to an order acceptance policy is thus a key decision-making problem at the interface between marketing/sales functions and production planning [5].

Unlike the make-to-stock manufacturing mode which holds finished products in stock as a buffer against demand variability, MTO production systems must hold production capacity and workin- process inventories to accept only orders of the most profitable type. The main issue is thus how to selectively accept/reject/negotiate in order to maximize cumulative profit gains. In the absence of a more elaborated policy, orders are accepted on a 'first-come-first-serve' basis. If the available capacity is not enough to process an arriving order on time, the order is rejected [6].

The build-to-order supply chain (BTO-SC) or make-to-order (MTO) system has received a great deal of attention in recent years because of the success of high-tech companies such as Dell, BMW, Compaq, and Gateway. In recent years, BTO-SCM has become prevalent among high-tech companies, including traditional manufacturing companies such as automobile companies. BTO-SC can be defined as ''the system that produces goods and services based on individual customer requirements in a timely and cost competitive manner by leveraging global outsourcing, the application of information technology and through the standardization of components and delayed product differentiation strategies" [7].

Recent years have proven a number of changes in companies' production policies and they are gradually moving more to hybrid MTS/MTO production mode. In a MTS/MTO production mode, a portion of the production system operates in a MTS mode and the remaining portion operates in a MTO mode. A proper combination of MTO and MTS can exploit the advantages of both lower inventory and short delivery time [3].

Assemble-to-order (ATO) production is a popular strategy used by firms that seek to be responsive and cost-efficient at the same time. ATO is particularly attractive when component supply lead-times are long or the supply processes are capacitated compared to final assembly. Furthermore, by pooling components stocks, an ATO strategy can reduce the cost of offering high product variety. Hence, by using this strategy a firm can shorten its response time to its customers and offer a high variety of the end product. An example of such practice is used by computer manufacturers and mail order retailers [8].

The assemble-to-order (ATO) strategy emerges in manufacturing environments where many finished products are assembled from a relatively small set of standard components and subassemblies. In a typical ATO manufacturing environment, components and subassemblies are acquired according to a forecast, while finished products are assembled only after actual customers' orders have been received. In other words, component and subassemblies are replenished in a make-to-stock (MTS) fashion, but finished products are assembled in a make-to-order (MTO) manner. Such a hybrid planning approach is particularly advantageous in situations where the assembly time of a product is considerably shorter than the procurement and/or manufacturing time of its components and subassemblies; thus, making a tradeoff between inventory holding cost, product variety, and delivery time achievable [9].

Successful and innovative product (or service) development is highly correlated with the company's success and reason for existence. It is imperative that a company's main purpose for existing is to provide goods and/or services to meet and even exceed the expectations of their customers [10]. To survive, companies need to transform themselves from production-focused to value-adding design-focused businesses [11]. Requirement understanding plays an important role in product design. Conventionally, customer needs come from questionnaires which are mainly collected by customer investigations [12]. Nowadays, QFD has been applied in a wide variety of quality control, decision-making, product design and improvement, etc. It is a customer-driven approach that can create a high level of buy-in and reach a better control of the problem [13].

Mass customization is a manufacturing approach to produce customized products based on customer requirements while maintaining the high quality and efficiency of mass production. Compared with the traditional mass production approach, mass customization can offer large variations of products to the market while leveraging the economies of scale and scope within the manufacturing capabilities of enterprises. One-of-a-kind production (OKP) is a special type of mass customization where each product is created based on requirement of an individual customer [14].

The purpose of this paper is to propose a framework for a pull-oriented product development system. In the first process, the paper has used quality house for translating customer demands into technical specifications. Customer order aanalyzed by decision support system for order acceptance/rejection decision. In sales and support product process orders are prioritized into high and low priority orders, considering profit of order. In other two processes the Production planning and manufacturing operations have been considered.

II. LITERATURE REVIEW

The literature review on pull-oriented product development issue indicates that lot attention has been paid to this issue in the production environments. Moreover, the existing research regarding this issue has been mostly focused on MTO production environments. Hendry and Kingsman [2] first emphasized on the importance of order entry stage in production environments, especially in MTO environments where the delivery date management becomes more crucial.

M.Kalantari et al [3], M. Ebadian et al [15], K.L.Choy et al [16] and S. Hemmati et al [17] presented a decision-making structure for the order entry stage in make-to-order environments. The aim of the proposed structures is to manage the arriving orders so that the MTO system just proceeds to produce those arriving orders which are feasible and profitable for the system. S. Hemmati et al [17] proposed structure composed of three phases. At the first phase, arriving orders are prioritized into high and low priority orders, considering characteristics of order and customer and utilizing technique for order performance by similarity to ideal solution (TOPSIS). At the second phase, rough-cut capacity was calculated for each order regarding priority level and so, acceptance or rejection decision is taken based on it. Finally, at the third phase, the previous phase accepted orders are evaluated based on their due dates and material arrival times and final decisions for orders are made. M. Ebadian et al [15] proposed decision support system is comprised of five steps. At the first step, the customers are prioritized based on a fuzzy TOPSIS method. Rough-cut capacity and rough-cut inventory are calculated in the second step and in case of unavailability in capacity and materials, some undesirable orders are rejected. Also, proper decisions are made about non-rejected orders. At the next step, prices and delivery dates of the non-rejected orders are determined by running a mixed-integer mathematical programming model. At the fourth step, a set of guidelines are proposed to help the organization negotiate over price and due date with the customers. In the next step, if the customer accepts the offered price and delivery date, the order is accepted and later considered in the production schedule of the shop floor, otherwise the order is rejected.

van der Laan et al [18] extend the PUSH and PULL control strategies to evaluate numerically the effects of lead-time duration and lead-time variability on total expected costs in production/inventory systems with remanufacturing. Although both strategies are non-optimal, they are relatively easy to analyze numerically and, more importantly, they are actually used in practice. The most important outcomes of the study are, that for both control strategies: (i) manufacturing lead-times have a larger influence on system costs than remanufacturing lead-times; (ii) a larger remanufacturing lead-time may sometimes result in a cost decrease; and (iii) a larger variability in the manufacturing lead-time may sometimes result in a cost decrease.

Sharma and Agrawal [1] presented a multistage serial production system. A generalized model has been developed with the use of probabilistic demand situations for the end product. The demand situations considered are binomial, exponential, lognormal and Poisson. These demand patterns are used as input parameter for various production control policies. The output values for performance parameters are obtained by simulation.

The literature available on BTO-SCM has been classified based on the nature of the decision-making areas and then sub-classified to focus on solving problems with modeling and analysis. Gunasekaran and Ngai [7] have focused mostly on the modeling aspect of the BTO-SC, but have not extended our efforts to empirical research. They have developed a unified framework for modeling and analyzing BTO-SCM and suggest some future research directions.

The objective of Ozbayrak et al [19] paper is to estimate the manufacturing and product costs by using activity-based costing (ABC) method in an advanced manufacturing system that is run under either material requirements planning (MRP) or just in time (JIT) system. ABC is a method that can overcome many of the limitations of traditional costing systems. This paper reports and discusses the implementation of the ABC alongside a mathematical and simulation model to estimate the manufacturing and product cost in an automated manufacturing system. The potential effects of manufacturing planning and control strategies implemented on financial structure of the manufacturing system are initially analyzed. ABC has been used to model the manufacturing and product costs.

Ioannou and Dimitriou [20] consider the problem of dynamically updating the manufacturing lead times estimates that are used in MRP systems. Once a new order with specific and known processing requirements enters a make-to-order manufacturing system, an exact completion time estimate is assigned to it that is based on the system's current status. The approach that is suggested addresses multi-machine, multi-product manufacturing environments with no special configuration of their resources: To this objective, simple, iterative algorithms are used to substitute the fixed lead time estimates of typical MRP systems. The results that are presented underline the significant improvement of the proposed approach over static, constant MRP lead time estimates that are as yet exclusively resorted to.

Olhager and Prajogo [21] analyze these improvement initiatives and their impact on business performance. In particular, they explore potential differences between make-to-order (MTO) and make-to-stock (MTS) firms. They use data from 216 Australian manufacturing firms. They find a clear difference of improvement focus between MTO and MTS firms. MTO firms exhibit a significant impact of supplier integration on business performance, but not for lean practices and supplier rationalization. The situation is completely reversed for MTS firms, since they have significant effects for internal lean practices and supplier rationalization, but not for logistics integration with supplier.

ElHafsi [22] study a pure assemble-to-order system subject to multiple demand classes where customer orders arrive according to a compound Poisson process. The finished product is assembled from m different components that are produced on m distinct production facilities in a make-to-stock fashion. He shows that the optimal production policy of each component is a state-dependent base-stock policy and the optimal inventory allocation policy is a multi-level state-dependent rationing policy. Using numerical experimentation, he first studies the system behavior as a function of order size variability and order size. He shows that the optimal average cost rate is more sensitive to order size variability than to order size. He also compares the optimal policy to the first-come first-serve policy and show that there is great benefit to inventory rationing. He also propose two simple heuristics and show that these can effectively mimic the optimal policy which is generally much more difficult to determine and, especially, to implement.

III. FRAMEWORK DESCRIPTION

Through the aforementioned section, the paper has achieved the requirements for framework by literature review in pull-oriented product development. So, the paper has focused on fulfilling those requirements in the proposed framework. Because of, have developed a framework in level-0 that includes four general processes (fig. 1). In review pre-order and customer process, the paper has used quality house for translating customer demands into technical specifications, and provides capabilities for customer order analyze by a decision support system for order acceptance/rejection decision. The second process (product sales and support) orders are prioritized into high and low priority orders, considering profit of order. Our third process in level-0 IDEF0 model included two QFD matrixes, this matrix are product design and process design. Furthermore, this process includes production planning, overall planning, master production scheduling (MPS) and inventory control (fig. 2). Fig. 2 is a level-1 IDEF0 model process of production planning (operation & overall plan). First stage of these processes is production planning (A21) that contains QFD second matrix. In this process, product concepts are created during this phase and part specifications are documented with product design matrix by product designers. The second process in fig. 2 is master production scheduling (MPS).

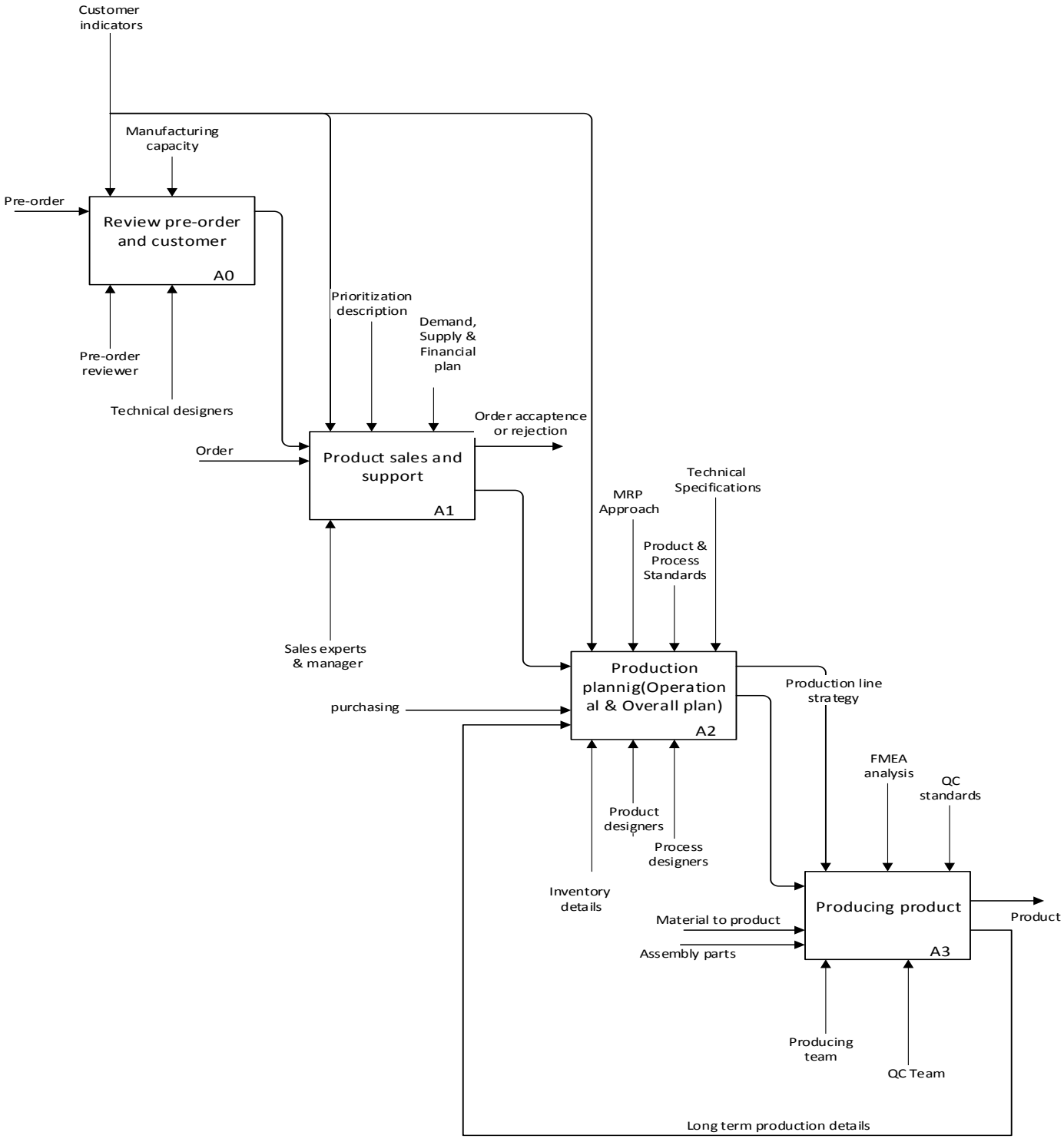

FIG. 1: FOUR GENERAL PROCESSES LEVEL-0 IDEF0 MODEL

This process include QFD third matrix. During process planning, manufacturing processes are flowcharted and process parameters (or target values) are documented. In other words, production processes will be planned according to product concepts and Production scheduling is performed. Third process of fig.2 belongs to the inventory control. In this process be done purchasing, material and assembly parts sent. Moreover, the paper has also shown the level-2 of inventory control stage in fig.3. In this level, our processes composed from raw material (A231) and assembly part (A232). The assembly part process's task is reception operation process chart (OPC) and needed parts sent.

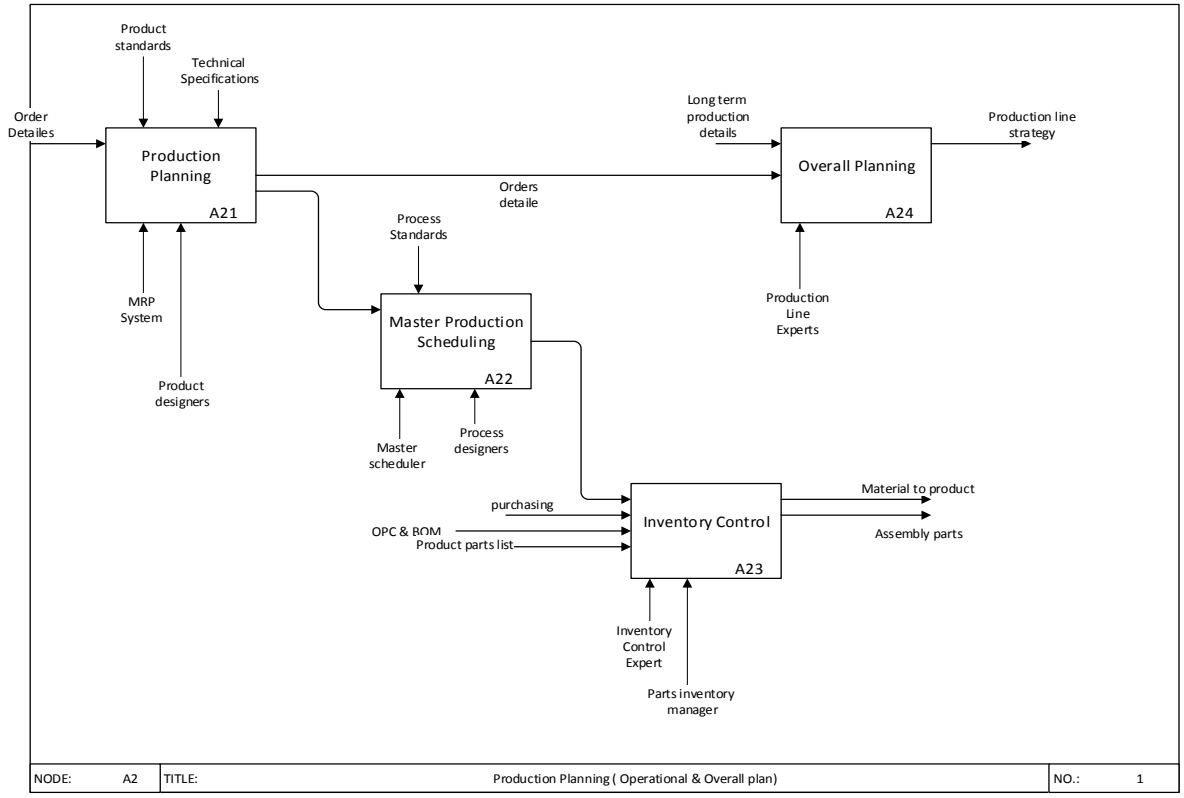

FIG. 2: PRODUCTION PLANNING LEVEL-1 IDEF0 MODEL

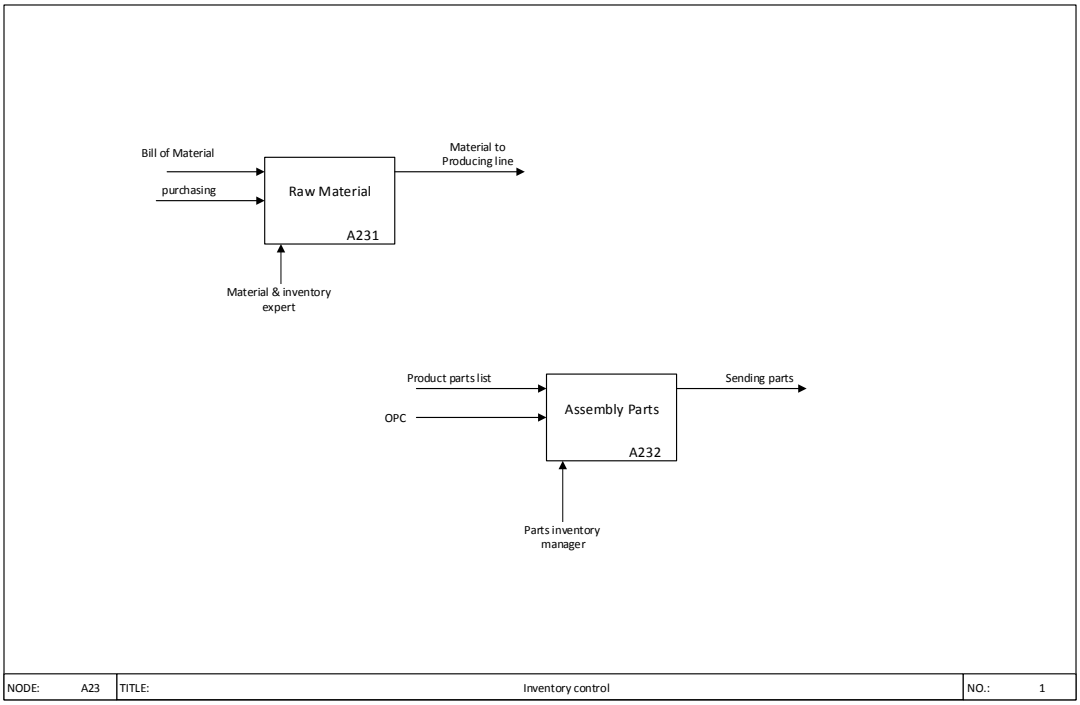

FIG. 3: INVENTORY CONTROL LEVEL-2 IDEF0 MODEL

And the raw material process's task is purchasing material and sent it to producing line. Our last level-0 processes is producing product (A3). This process contained phase 4 of QFD matrix. Finally, in this stage product assembly will be done, performance indicators are created to monitor the production process. The quality assurance department will analysis with FMEA as to which process poses the most risk and controls are put in place to prevent failures.

IV. THE USE OF QFD

In this research, the customer demands and requirements in product have been considered by using of Quality function deployment 4-stage matrix. Each of the four phases in a QFD process uses a matrix to translate customer requirements from initial planning stages through production control. Each phase, or matrix, represents a more specific aspect of the product's requirements. Relationships between elements are evaluated for each phase. Only the most important aspects from each phase are deployed into the next matrix [23].

Phase 1, Product Planning: Building the House of Quality. Led by the marketing department, Phase1, or product planning, is also called The House of Quality. Many organizations only get through this phase of a QFD process. Phase1 documents customer requirements, warranty data, competitive opportunities, product measurements, competing product measures, and the technical ability of the organization to meet each customer requirement. Getting good data from the customer in Phase1 is critical to the success of the entire QFD process.

Phase 2, Product Design: This phase2 is led by the engineering department. Product design requires creativity and innovative team ideas. Product concepts are created during this phase and part specifications are documented. Parts that are determined to be most important to meeting customer needs are then deployed into process planning, or Phase3.

Phase 3, Process Planning: Process planning comes next and is led by manufacturing engineering. During process planning, manufacturing processes are flowcharted and process parameters (or target values) are documented.

Phase 4, Process Control: And finally, in production planning, performance indicators are created to monitor the production process, maintenance schedules, and skills training for operators. Also, in this phase decisions are made as to which process poses the most risk and controls are put in place to prevent failures. The quality assurance department in concert with manufacturing leads Phase4.

In framework that presented in this research, each of the four phases in a QFD process used in the different stages of framework and the fulfillment of customer needs in the configuration and assembly of products. In this model, the paper used the first phase of QFD in the review pre-order and customer process A0 (fig.1). In this process after reaching the customer with special demands, this demands translated to technical specifications of parts with technical designers. In this process it becomes clear what the configuration of the product can be offered to customers. The paper has considered the second phase of QFD matrix in the production planning process A21 (fig.2). In this process, product designers choose the best configuration of components and parts according to technical specifications. Master production scheduling A22 (fig.2) included third phase of QFD matrix. In this phase, after identifying the product components and configuration in earlier phases, product assembly processes are considered. Required materials and parts allocated for product configuration and production scheduling. Last phase of QFD matrix considered in producing product process A3 (fig.1). In this process, manufacturing process control and product quality assurance have been considered.

V. BENEFITS OF OUR FRAMEWORK

In this section, the paper will review proposed framework and will be considered the advantage of this. The motivation of this research is meet customer requirements, a decision support system for order accept or reject, a ATO system to reduce costs of design and product manufacturing. These factors have been considered and solutions for fulfilling these requirements are proposed. For this purpose, the processes and tools that are responsive to our needs in framework are used. Despite our efforts the proposed framework will not be perfect but will have advantages to other models. So the paper pointed out the advantages of our framework to show that our proposed processes have a great effect on to achieve the objectives of product development frameworks. Of the most important one, the following items can be described:

- Benefits of Using QFD: Customer driven: The focus is on customer wants, not what the company thinks the customer wants. The "Voice of the Customer" drives the development process. Reduced development time: The likelihood of design changes is reduced as the QFD process focusses on improvements to be made to satisfy key customer requirements. Careful attention to customer requirements reduces the risk that changes will be required late in the

project life cycle. Time is not spent developing insignificant functions and features. Reduced development costs: The identification of required changes occurs early in the project life cycle. Minimizing changes following production reduces warranty costs and product support costs.

- Benefits of DSS: Helps in saving time: Research has demonstrated that decision support systems help to reduce decision cycle time for an organization. DSS provides timely information, which is then used for decision making and results in enhanced employee productivity. Improves efficiency: Another advantage of DSS is efficient decision making, resulting in better decisions. This is because use of DSS results in quick transfer of information, better data analyses, thus resulting in efficient decisions. Enhanced organizational control: Due to the use of DSS business transaction data is easily available for monitoring the performance of employees and ad hoc querying. It thus leads to enhanced understanding of business operations for the management.
- Benefits of ATO: Businesses that want the ability to make a large number of different products from common parts benefit the most from assemble to order method. They can stock the common parts and sell varied customized products to meet customer needs. Another key benefit of assemble to order method is that businesses can reduce errors in the delivery of products. For example, a business that sells computers to customers can reduce the amount of errors when choosing this method rather than the options method.
- Benefits of the FMEA: The FMEA procedure is a highly effective way to evaluate processes, services or products. It is as valuable for revealing areas needing improvement as it is for guiding the development of new processes. It is a logical, structured way to identify areas of concern while reducing development time and cost. It's also valuable when the intent is to apply a particular (typically successful) process of one product or service to another. It has proven to be an effective way to identify how to improve areas where performance might be lagging, such as sales or customer satisfaction ratings or high expense to income ratios, for example.

Furthermore, the framework has enabled the prioritization of orders into high and low priority orders, considering profit of orders that reduce the risk of lost sales lucrative orders. Also, the proposed framework has overall planning that takes long-term data from the production line. This process, provide data and offers a long-term strategy that cause increase efficiency and reduce the idle time.

VI. CONCLUSIONS

Although the bulk of research on production planning and control has taken into account the ATO systems, most of the companies have to work in a ATO environment in practice to decrease their production costs and also improve their customers service level and demands. The paper has used Quality function deployment (QFD) 4-stage matrix to meet the customer requirements. With the appearance of ATO systems, many issues have been coming up regarding the planning and scheduling of such systems. One of these issues, which have a direct impact on the customer satisfaction, is the matter of acceptance/rejection of new arriving orders to the system with respect to the resource limitations and customer importance. Other of these is an accurate translation customer demands to product features. This research has proposed a novel framework for pull-oriented product development system (ATO system) by using the QFD.

The main future research which can be considered for our study is (i) the implementation of this framework in a real production environment (ii) Prepare a case study for this framework

REFERENCES

[1] S. a. N. A. Sharma, "Selection of a pull production control policy under different demand situations for a manufacturing system by AHP-algorithm," *Elsevier,* pp. 1622-1632, 2008.

[2] B. K. L.C. Hendry, "Production planning systems and their applicability to make-to-order companies," *European Journal of Operational Research 40,* pp. 1-15, 1989.

[3] M. R. ,. M. E. Mahdokht Kalantari, "A decision support system for order acceptance/rejection in hybrid MTS/MTO production systems," *Applied Mathematical Modelling 35,* 2011.

[4] M. M. N.P. Dellaert, "Production strategies for a stochastic lot-sizing problem with constant capacity," *European Journal of Operational Research 92,* pp. 281-301, 1996.

[5] D. C. A. P. M. Zorzini, "Due date (DD) quotation and capacity planning in make-to order companies: Results from an empirical analysis," *Int. J. Production Economics 112,* p. 919–933, 2008.

[6] E. M. Facundo Arredondo, "Learning and adaptation of a policy for dynamic order acceptance in make-to-order manufacturing," *Computers & Industrial Engineering 58,* pp. 70-83, 2010.

[7] E. W. N. Angappa Gunasekaran, "Modeling and analysis of build-to-order supply chains," *European Journal of Operational Research 195,* 2009.

[8] M. ElHafsi, "Optimal integrated production and inventory control of an assemble-to-order system with multiple non-unitary demand classes," *European Journal of Operational Research 194,* p. 127–142, 2009.

[9] F. C. E. Mohebbi, "The impact of component commonalityin an assemble-to-order environment under supplyand demand uncertainty," *Omega 33,* p. 472 – 482, 2005.

[10] e. a. Zaim Selim, "Use of ANP weighted crisp and fuzzy QFD for product development," *Expert Systems with Applications,* pp. 4464-4474, 2014.

[11] W. e. a. Yan, "A stakeholder-oriented innovative product conceptualization strategy based on fuzzy integrals," *Advanced Engineering Informatics,* pp. 210-209, 2009.

[12] P. J. a. Y. L. Jin Jian, "Translating online customer opinions into engineering characteristics in QFD: A probabilistic language analysis approach," *Engineering Applications of Artificial Intelligence,* pp. 115-127, 2015.

[13] J. Z. a. Y. C. Zhong Shuya, "Determination of target values of engineering characteristics in QFD using a fuzzy chance-constrained modelling approach," *Neurocomputing,* pp. 125-135, 2014.

[14] D. X. ,. Y. T. Gang Hong, "Rapid identification of the optimal product configuration and its parameters based on customer-centric product modeling for one-of-a-kind production," *Computers in Industry 61,* p. 270–279, 2010.

[15] M. R. F. J. S. T. R. T.-M. M. Ebadian, "A new decision-making structure for the order entry stage in make-to-order environments," *Int. J. Production Economics 111,* p. 351–367, 2008.

[16] Y. L. H. C. T. P. C. K. G. H. S. K. K.L. Choy, "A hybrid scheduling decision support model for minimizing job tardiness in a make-to-order based mould manufacturing environment," *Expert Systems with Applications 38,* pp. 1931-1941, 2011.

[17] M. E. &. A. N. Hemmati Samira, "A new decision making structure for managing arriving orders in MTO environments," *Expert Systems with Applications,* pp. 2669-2676, 2012.

[18] M. S. R. D. Van der Laan Erwin, "An investigation of lead-time effects in manufacturing/remanufacturing systems under simple PUSH and PULL control strategies," *European Journal of Operational Research ,* pp. 195-214, 1999.

[19] M. A. &. A. K. T. Özbayrak M., "Activity-based cost estimation in a push/pull advanced manufacturing system," *International journal of production economics,* pp. 49-65, 2004.

[20] S. George Ioannou, "Lead time estimation in MRP/ERP for make-to-order manufacturing systems," *Int. J.ProductionEconomics139,* pp. 551-563, 2012.

[21] D. Jan Olhager, "The impact of manufacturing and supply chain improvement initiatives: A survey comparing make-to-order and make-to-stock firms," *Omega 40,* pp. 159-165, 2012.

[22] M. ElHafsi, "Optimal integrated production and inventory control of an assemble-to-order system with multiple non-unitary demand classes," *European Journal of Operational Research 194,* p. 127–142, 2009.

[23] BRIEF, PRODUCT "Quality Function Deployment", 2012: Creative Industries Research Institute.

A Car Window Segmentation Algorithm Based on Region Segmentation and Boundary Constraint

Li Xi-ying[1], Li Fa-wen[2], Zhou Zhi-hao[3], Deng Yuan-chang[4]

[1,2,3,4]Guangdong Province Key Laboratory of Intelligent Transportation Systems
[1,2,3,4]Key Laboratory of Video and Image Intelligent Analysis and Application Technology, MPS, China
[1,2,3,4]School of Engineering, Sun Yat-sen University, Guangzhou 510006, China
*Corresponding author PH: (86)20-39332772;
FAX: (86)20-39332775
Email addresses: dengych@mail.sysu.edu.cn (Yuanchang Deng)

***Abstract*—** *To enable locate and segment the window of a car accurately in complex environment, a segmentation algorithm based on region segmentation and boundary constraint is proposed. At first, multi-scale and undirected graph based on region segmentation algorithm is applied to segment the vehicle graph into some small zones and sort according to set rules; then combine and merge the small zones in sequence, The merged region with the maximum boundary smoothness is served as the candidate window; finally judge for windows by combining with geometrical parameters. The experimental results show that the algorithm is accurate in segmentation, the result of the segmentation can maintain the shape and size of the window, therefore the fitness for purpose is strong and the application prospect is wide.*

***Keywords*— graph-based segmentation region mergence, chain code, boundary smoothness, geometrical characteristics.**

I. INTRODUCTION

With the rapid development of intelligent transportation system in China, the passenger detection plays an important role in traffic safety and traffic orderly operation. For example, the construction of HOV (High Occupancy Vehicle) dedicated lane is a feasible way to improve highway capacity. To guarantee the legal and reasonable use of HOV lanes, it becomes necessary to count the passengers in the vehicle. Again, the detection for wearing condition of the driver's seat belt helps to promote the safety of driving, so it is particularly important to locate the driver's position quickly. In addition, it allows as much as possible to observe physical characteristics and driving behavior of front row driver and passenger through the windows. Therefore, as the basic procedure of passenger detection, quick and precise locating car windows can significantly improve the speed and accuracy of passenger detection.

Car window location is a challenging issue, as the conditions of lighting, camera position and etc. in actual environment are complicate and variable, which makes it difficult to precisely segment vehicle windows from its body, meanwhile, due to the color depth of the body itself, part of the body color is difficult to distinguish with the windows, making it be more difficult for the segmentation of the window. Therefore, the focus of this paper is to segment and position windows accurately in complex natural environment.

There has been some researches for vehicle window location and extraction. Based on the characteristic that the edges of vehicle windows is closely linear, Hao et al.[1] proposed a vehicle window detection method based on linear characteristic, by carrying out differential operation to the adjacent frames of video image, this method detects upper and lower boundaries of the vehicle windows by combining horizontal linear filtering with Hough transform, obtains right and left boundaries by applying template matching, this method has a better effect of vehicle window detection for video sequence image, but the locating accuracy is not high when locating the vehicle windows of pictures with non-fixed time sequence and much bigger phase difference. Li et al.[2] proposed an window location algorithm based on Hough transform, which applies Hough transform to detect the horizontal straight line, and obtains two sides of the boundary to locate the window by further combining with the integral projection, this algorithm can enable quick locating of vehicle window with simple edges and clear image, however the location fails because it is difficult to find out the line segments when there are much more edges with the image in the vehicle window and the vehicle shooting angle is away from the positive direction. As the body color consistency is high, Wang et al.[3] made full use of the feature that the color difference of window region in the HSV color model is greater than that of the body to distinguish between the windows and the body, this algorithm has much better segmentation effect to vehicles with dark color. As the shape of the vehicle window is similar to that of a isosceles trapezoid, Hou et al.[4] proposed an algorithm that the generalized Hough transform is used to map the boundary points of the image to

the parameter space, which is transformed into the clustering problem in the parameter space, and the parameters satisfying most of the boundary points are found to locate the window. Nevertheless, the calculation of this algorithm is relatively large and the results greatly affected by the size of the window. Zhang Yi et al.[5] put forward a vehicle window algorithm by combining a mean chrominance function with color block method, this method is much more complicated, and needs to know the general location of window within the whole vehicle under the different angles of vehicle picture. As the distinction of vehicle's contour as well as colors and shapes of various parts is much higher, Lu et al.[6] designed a method which first segments the vehicle image into many small regions, constructs the appearance consistency model by using the similarity of regions and position relationship, and marks the various parts of the vehicle, the construction of this algorithm model is dependent on manual marking of various parts of a vehicle, and the amount of calculation is much bigger. Based on the color difference average value of HSV color model, Wang Yunqiong et al.[7] proposed a technique for vehicle window detection, which utilizes the color difference function of the chromaticity singularity of HSV color model and locate the front window by the method of texture detection function for roof rack, the calculation amount of this technique is small and the locating speed is quick, but the effect of window detection is much worse under much stronger lighting environment. As the window detection difficulty is bigger under the influence by factors as dim lighting, indistinct motion and etc., Liu Zhifang et al.[8] applied the genetic algorithm which is constructed based on chromaticity function curves to carry out segmentation and location, this algorithm is strong in anti-noise capacity, but the algorithm is complicated and calculation amount is large. Yang H.Y et al.[9] proposed a method by combining the edge, color, energy and gradient features with least square support vector machines to carry out image segmentation. PATEL H.N et al.[10] put forward a method by using the weight of strength, color, direction and edge in the image to detect the target approximate position, enabling the segmentation of image; Wang et al.[11] applies the principle of graph segmentation, uses threshold segmentation and horizontal vertical crossover strategy to propose - peak filtering to produce trusted taillights, achieves vehicle collision brake detection by combining with SVM classifier training.

This paper puts forward a vehicle segmentation algorithm based on region segmentation and boundary constraint. By using multi-scale parameters to segment the vehicle image, this algorithm guarantees reasonable segmentation of vehicle window in conditions whether the light is strong or dim and whether the vehicle color is dark or light; then carry out restraint to the area and boundary of candidate regions and recombine them to the vehicle window region, enabling to keep actual size and shape of the window and allowing precise location and extraction of vehicle window.

II. ALGORITHM

The flow of vehicle window segmentation algorithm is shown in Fig. 1.

Step 1: Image normalization: Normalize the size of input color vehicle image to 200×220 pixels.

Step 2: Image pre-segmentation: By using the graph-based segment algorithm[12,13] to carry out segmentation to the input image, the input parameters include sigma, K and minRegion, where sigma is the Gaussian filtering parameter, K can control the size of small region obtained from segmentation, minRegion is the area threshold, the regions less than the threshold will be merged. The pre-segmentation results in different scales can be obtained by changing the value taken for K. According the order of scale parameter K from big to small, carry out vehicle window extraction of segmented image in succession for each scale.

Step 3: Obtain the initial vehicle window region: First set a reference point for mass center of the vehicle window region, find mass center of segmented small regions at the upper half of the image, sort the distance from mass center to the reference point in the order of small to big, take the small zones corresponding to minimum distance as the initial combination window regions.

Step 4: Region combination and merging: Merge the small regions into the combined vehicle window region in succession according to the order, find the area of this region at this time, if the area is smaller than the set threshold, find the boundary smoothness; if the area is bigger than the set threshold, remove this small zone.

Step 5: Obtain the candidate window region: Take the combined vehicle window region at maximum boundary smoothness, perform morphological open operation to remove the spike while smoothing the boundary of the region, and consider it as a candidate window region.

Step 6: Feature calculation and judgment: Extract area, rectangularitry, length-to-width ratio and etc. from the candidate vehicle window region, judge whether all is within the range of set threshold or not, it is the vehicle window if acceptable, if

one or more items are not acceptable, it is judged that the vehicle window is not extracted in such scale, then enter the analysis of next scale, till the exact vehicle window region is extracted.

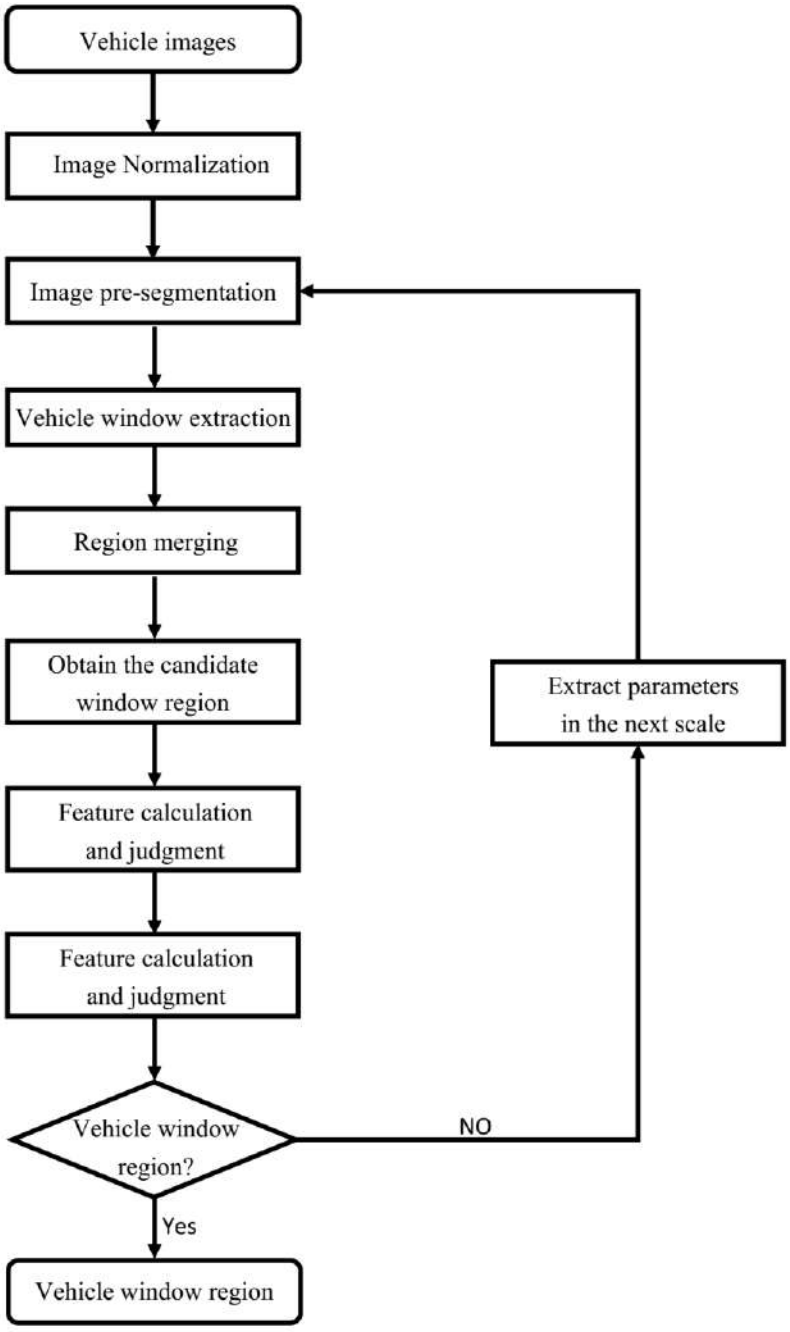

FIG. 1 FLOW OF VEHICLE WINDOW SEGMENTATION ALGORITHM

III. PRE-SEGMENTATION

Conduct pre-segmentation to the normalized image, use the graph-based image segmentation algorithm, its principle is to form an undirected graph by considering the image as vertice set and edge set, express it as G =(V, E), the single pixel is the vertex, the connection between a pair of vertices is the edge, V is the vertice set, E is the edge set. The edge has a weight of $W(v_i, v_j)$, which is the dissimilarity among the vertices, called as length of side, and defined as following equation:

$$W(v_i, v_y) = \sqrt{(r_i - r_j)^2 + (g_i - g_j)^2 + (b_i - b_j)^2} \quad (1)$$

Where r, g and b are the values of the three components of the RGB color for the vertex respectively.

Use Dif(C1 ,C2) to express the difference between two regions, which is defined as the minimum length of connection edges between two regions. The internal heterogeneity of the region is characterized by the maximum length connection edges inside the region, which is expressed as:

$$Int(C) = \max_{e \in MST(C,E)} w(e) \tag{2}$$

Where, MST(C ,E) represents the minimum spanning tree of region C. The basis of region merging:

$$Dif(C1,C2) < \min(Int(C1), Int(C2)) \tag{3}$$

As it is impossible for Int(C) to effectively estimate the local feature of regional data in the condition that the regional area is very small, which is easy to result in over-segmentation, therefore add a penalty function that is pertinent to the area, that is

$$\tau(C) = K/|C| \tag{4}$$

Where, |C| represents the area of C, K is the set point. The basis of region merging is changed to:

$$Dif(C1,C2) < \min(Int(C1)+\tau(C1), Int(C2)+\tau(C2)) \tag{5}$$

When the regional area is much smaller, the value of penalty function is significantly affected by the value of K, which always plays a major role in region merging; when the regional area is much bigger, the role of the penalty function will be reduced, the local feature of the data itself will play a major role. The larger the K value is, the greater the region of the segmentation result will be.

The image is normalized to 200×220 pixels, take sigma=0.2, min. Region=500, K=[1.8k, 1.5k, 1.3k, k, 0.7k, 0.5k, 0.2k], where k=400. As shown in Fig.2, the leftmost is the original image, the second, then the segmentation effect images from the second image from the left when K=1.8k, k, 0.2k. It is observed that the smaller the K value is, the more the number of segmented regions will become; the smaller the region area is, the much more clear the segmentation for different objects in the original image.

FIG.2 ORIGINAL IMAGE AND SEGMENTATION EFFECT

IV. VEHICLE WINDOW EXTRACTION

As the brightness and saturation in vehicle window region is much lower, the body and window of white and light color vehicle are generally easy to be distinguished and segmented, however when the light is sufficient, the persons and objects in the vehicle also become much more clear, causes the brightness or color feature in the vehicle windows to be much stronger, it always not possible to segment the vehicle window accurately no matter either the gray level or color feature is based. It is much easier to combine the body of black and dark color vehicle with the window. Therefore, the multi-scales segmentation to the vehicle image is carried out, the vehicle window extraction is performed according to the scales from small to big, till the accurate vehicle window is obtained.

4.1 Combination of vehicle window regions

The vehicle window region is always segmented into several small zones, it is necessary to combine them together for subsequent judgment. As the vehicle windows are located at the upper part of the vehicle image, just the analysis to the upper part of the image is required. The procedures for combining the segmented small zones into vehicle windows are as follows:

1) Among the segmented images, first find the centroid of various small zones, mark various small zones with centroid located at upper part of the image, express its set as “region”.

2) The width and length of the image is width and height, take the points with coordinate of [width/2, height*3/8] in the image as the mass center reference point P of the vehicle window, calculate the Euclidean distance from the mass center of region in the set to point P, and sort the regions from small to big based on this distance. If the closer the region centroid to the reference point P is, the more likely to belong to the internal window region will be, this can guarantee the combination of zones starts from the inside of the vehicle window.

3) The first small zone in the region is taken as the initial vehicle region, and written as "Re". Put the small zones in region into the Re, and combine them with the zones in Re. After certain zone is merged each time, calculate the area of Re at this moment, if the area is larger than the threshold (taking value 9500), this zone will be removed, as it possibly is the zone outside the vehicle window; the area is smaller than the threshold, it is considered as a successful combination, calculate the boundary smoothness of Re at this moment, save it in the array and save the vehicle window region at this moment. Continue to combine the subsequent small zone till the region is processed completely.

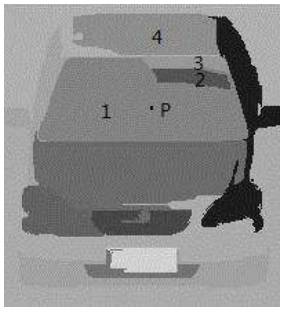

FIG.3 ZONE COMBINATION

As shown in Fig.3, the numbers in the image are the marks of zones in the region after sorting, the reference point P of centroid for zone 1 is the closest one, then comes zone 2, the rest can be done in the same manner. The zone 1 is combined with zones 2 and 3 successively, however the adding of zone 4 will cause the total area to exceed the threshold, therefore the zone 4 will not be combined.

The vehicle window region obtained by using the area to restrain the combination will not only guarantee that the vehicle window will not be combined with other part of the vehicle body, but also not miss any zone within the window region, ensuring the accuracy of final result.

4.2 Extraction of candidate vehicle window region

The shape of vehicle window is approximately trapezoidal, its boundary is consisted of approximately four straight segments, and therefore boundary of window region obtained from present algorithm should be also smooth enough. The small zones obtained by using the segmentation method in present paper are irregular in shape, when the zones are combined with the vehicle window and the boundary of the candidate window region is analyzed, if it is the closer to the actual zones of the window, its boundary will me smoother. The present paper calculates the boundary smoothness based on the extraction of region boundary chain codes.

4.2.1 Chain code

Chain code [14] refers to 8 possible directional values of the line connecting adjacent pixels, for each pixel dot, the adjacent dots will use the continuation direction to represent the directional code.

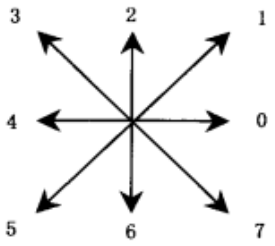

FIG.4 CHAIN CODE DEFINITION

The definition of 8 directional chain codes is as shown in Fig.4. If one is added to the chain code value, its direction is that rotates by 45° in counterclockwise direction, its direction will be rotate in counterclockwise direction with the increase of chain code values. Each pixel has only 8 adjacent dots, the chain code value will be 0 to 7, 8 in all.

The chain code of region boundary depends upon the start point and the direction of boundary follow-up. The paper takes clockwise direction. After binarizing the combined regions, it is easy to obtain the boundary sequence, and find the boundary chain code, which is expressed as Ccode.

4.2.2 Boundary smoothness

Any point on the boundary has a chain code A1 pointing this point and the chain code A2 pointing to next point. Mutual relationship of chain codes A1 and A2 is called as "relative chain code", the relative chain code will become zero when they point to same direction. If A2 is rotated relative to A1 in counterclockwise direction, the relative chain code will take values of 1 to 4 according to the size of the angles, corresponding to rotate by 45°, 90°, 135° and 180°; the relative chain code will take values of -1 to -3, corresponding to rotate by 45°, 90° and 135° along clockwise direction.

The paper defines the boundary smoothness tb to measure the degree of boundary that is composed of vehicle window tends to be straight line segment. First, calculate the generalized relative chain code Dcode:

$$Dcode=Ccode(i+3)-Ccode(i) \tag{6}$$

That is to subtract the chain code of current point from last three digits in the chain code. If the boundary is a straight line segment at this moment, Dcode is zero. The calculation of tb is as shown in equation (7):

$$tb=num(Dcode==0)/num(Dcode) \tag{7}$$

That is the ration of number of zero values in relative chain code, num() is the function for number of statistics.

The larger the tb is, indicates the more smooth the boundary will be, the smaller the degree of bumps on the border, the closer the region tends to be a regular shape (trapezoid). Take the region with maximum tb as the candidate window region, use 10×10 square structure to conduct morphological open operation, remove the long and further smooth the region boundaries as the final candidate window region.

4.3 Feature judgment

The region with maximum boundary smoothness may not be the ideal window, therefore it is still necessary to carry out final judgment to the candidate window. As the shape of window is approximate to trapezoid, and the difference among the windows of different types of cars is not big. The paper judges whether it is the window depending on the area of window region area, rectangularity extent and the ratio of length to width t.

1) By combining the area threshold in case of above-mentioned combination of region, the area of window should satisfy $5000 < area < 9500$.

2) Calculation of rectangularity

$$extent=area/areaBox \tag{8}$$

Where, areaBox is the area of smallest circumscribed rectangle of the region. The bigger the rectangularity, the closer the region is to the rectangle.

The window region is approximate to the trapezoid not a rectangle, therefore it will be acceptable is extent >0.85 is satisfied.

3) The ratio of height to width of car is about 0.5, by taking into consideration that the shooting angle of the image may reduce the height of window in the image, the present paper takes the ratio of height to width of $0.25 < t < 0.55$.

If the candidate window region meets above 3 conditions, it is considered that the window is accurately segmented; otherwise, it is considered that the extraction of window in current scale of segmentation fails, carry out the analysis of next scale till the window is accurately segmented.

V. EXPERIMENTAL RESULTS AND ANALYSIS

To verify the effectiveness of the algorithm in present paper, the front image of vehicle taken by the surveillance camera at the intersection is used for experiment. There are 720 images covering 20 types of cars with various colors in different

lighting environment. The sizes of the images are normalized to 200×220 pixels. The algorithm is realized by MATLAB r2013a, and runs under the condition of Intel 3.6G HZ and 2 GB RAM.

5.1 Experimental evaluation method

Same as Lu[6], the present paper evaluates the algorithm in two aspects: locating performance and segmentation performance.

The locating performance reflects the degree of difference of widow position coordinates obtained by present algorithm from the actual coordinates. Here the coordinates of window position refers to the coordinates of circumscribed rectangle in window region. The locating error will be measured by the average of distance between corresponding vertices of two rectangles, as it is expressed in equation (9):

$$E_{loc} = \frac{(D_{lt} + D_{rt} + D_{lb} + D_{rb})}{4} \tag{9}$$

Where, E_{loc} represents the locating error, D_{lt},D_{rt},D_{lb},D_{rb} are the distance between corresponding top left, top right, bottom left, bottom right vertices of two rectangles respectively. Finally, the locating error has to be normalized by using width of image.

The segmentation performance reflects the degree of fit between the window region and the actual window region obtained by this algorithm. This is not only related with accurate expression of the size and the shape of the window, but also related with complete extraction of image information in the window region. The segmentation performance is measured by using the Jaccard distance between the region obtained by the algorithm and actual region of the window, as it is expressed in equation (10):

$$E_{seg} = 1 - \frac{GT \cap SR}{GT \cup SR} \tag{10}$$

Where, E_{seg} represents the segmentation error, GT (ground truth) represents actual window region, SR (segmented region) is the region from segmentation.

5.2 Algorithm comparison

The algorithm in this paper will be compared with the algorithm proposed by Hao[1], the algorithm of Hao[1] is to find four boundaries of the window by combining the edge detection with Hough transform, and locate the extraction of the window.

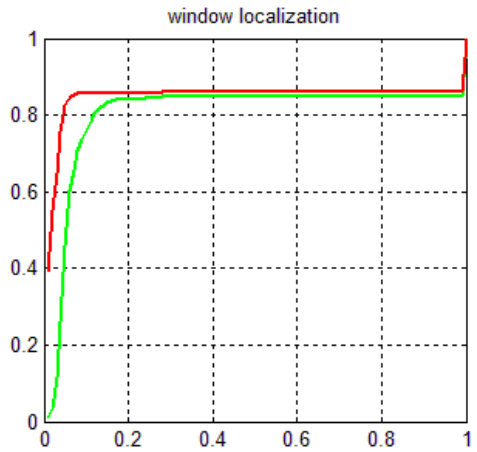

FIG.5 CUMULATIVE LOCATING ERROR

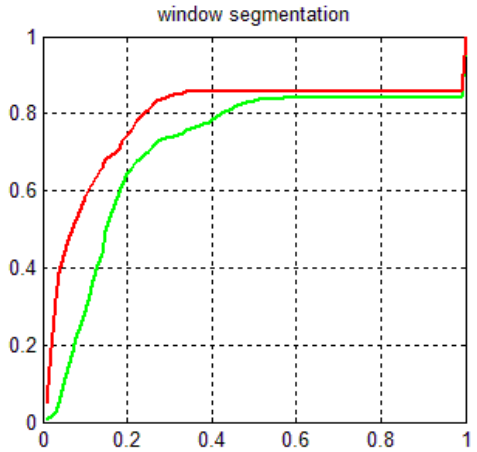

FIG.6 CUMULATIVE SEGMENTATION ERROR

In Fig.5, the horizontal axis is the locating error normalized by the width of the image, the vertical axis accounts for the proportion in the total number of images. The red line is the performance of the proposed algorithm in this paper, the green line is the performance of Hao [1] algorithm. It can be seen that the locating performance of present algorithm is better, especially prominent, the proportion of small errors is close to 40%, and this also shows that the present algorithm locating effect is good.

In Fig.6, the horizontal axis is the segmentation error, the vertical axis accounts for the proportion in the total number of images. The red line is the performance of the present algorithm, the green line is the performance of Hao[1] algorithm. The performance of present algorithm is obviously better. This is because this algorithm can only segment partial region of the vehicle window, however the segmentation results of the present algorithm can be better fit the edge of the window region.

5.3 Effect of algorithm

Some segmentation effects of the algorithm in this paper are shown in Fig.7, the abstraction of window is marked with a blue area. It can be seen that this algorithm has a good segmentation effect for various colors of vehicles. In lower half part of Fig.7, two groups at left and right are original images of vehicles and their window segmentation images under darker and stronger light conditions respectively. It can be known from the image that this algorithm can also have much better locating and segmentation effect even under the influence of different light, and shows better robustness for the test photos.

It can be known from Fig.7 that this algorithm can not only locate the position of window accurately, but also much better fit the segmented vehicle window region with edges of original vehicle window, and maintain the shape and size of the original window. This feature allows the window obtained by this algorithm can be applied in analysis of object in the window, such as detection of safety belt and number of passengers, but also further extract the window shape feature to apply for vehicle type recognition

FIG.7 ORIGINAL IMAGE OF VEHICLE AND WINDOW SEGMENTATION IMAGE

VI. CONCLUSION

This paper has analyzed the advantages and disadvantages of current vehicle window location algorithm, proposed a vehicle window segmentation algorithm based on region segmentation and boundary constraint. First the region segmentation shall be carried out for the car image according to the color feature, then the small regions will be combined and merged, finally the window region is obtained by combining the geometrical features of the vehicle window. The algorithm result not only locates the vehicle window accurately, but also keeps the shape and size of the window, which has laid a foundation for subsequent application of vehicle window image. The experiments show that the algorithm has better segmentation results for cars with different colors and different lighting conditions.

ACKNOWLEDGEMENTS

This work was supported by Science and Technology Planning project of Guangdong Province, China(NO. 2013B090200020).

REFERENCES

[1] Hao Xiaoli, Hou Dianfu. Vehicle Window Detection based Online Features[C]. International Symposium on Instrumentation & Measurement, Sensor Network and Automation (IMSNA), 2012:261-263.

[2] Li Dongmei, Hao Xiaoli. An Window Location Algorithm Based on Hough Transform [J]. China Measurement Technology, 2007, 33(3):50-53.

[3] Wang Yafu. A Window Region Identification Method and Device Based on Sobel Edge Detection [P]. China: CN104636713A, 2015.05.20.

[4] Hou Dianfu. Study in Vehicle Window Detection Technology [D]. Beijing Jiaotong University, 2011.

[5] Zhang Yi, Luo Zhongliang, Shao Peng, Chen Jiancheng. Designing and Realization on Shield Algorithm[J]. Journal of Xi'an Aerotechnical College, 2006, 24(1):12-14.

[6] Lu Wenhao, Lian Xiaochen, L.Yuille Alan. Parsing Semantic Parts of Cars Using Graphical Models and Segment Appearance Consistency[C]. Proceedings of the British Machine Vision Conference (BMVC), 2014.

[7] Wang Yunqiong, You Zhisheng. A Fast Algorithm for Localization Vehicle's Window Based on The Mean of Chromatism[J].Computer Applications and Software, 2004, 21(1):78-79.

[8] Liu Zhifang, Xu Xin, You Zhisheng, Cao Gang. Localization Vehicle's Window Based on a Genetic Algorithm[J].Application Research of Computers, 2002, 11(1):72-74

[9] YANG H Y,ZHANG X J,WANG X Y. LS-SVM-based image segmentation using pixel color-texture descriptors[J]. Pattern Analysis Applications, 2014, 17(2):341-359.

[10] PATEL H N,JAIN R K,JOSHI M V. Fruit detection using improved multiple features based algorithm[J]. International Journal of Computer Applications, 2011,13(2):1-5.

[11] Xueming Wang,Jinhui Tang,Jianwei Niu,Xiaoke Zhao. Vision-based two-step brake detection method for vehicle collision avoidance[J]. Neurocomputing, 2016,173(2):450-461.

[12] Koen E.A.van de Sande, Jasper R.R.Uijlings, Theo gevers, etal. Segmentation as Selective Search for Object Recognition[C]. IEEE International Conference on Computer Vision, 2011:1879-1886.

[13] Jiang Huaizu, Wang Jingdong, Yuan Zejian, etal. Automatic Salient Object Segmentation Based on Context and Shape Prior[C]. Proceedings of the British Machine Vision Conference (BMVC), 2011, 100.1-100.12.

[14] Tan Jianhao, Zhang Jing. Identify for the Concave-Convex of Peripherals Based on Chain code Diference[J]. Science Technology and Engineering, 2007, 7(5):769-770.

Flow production of practical and quantitative capillary driven-flow immune sensing chip using a circumferentially-grooved island micro-surface

Yusuke Fuchiwaki[1*], Kenji Goya[2], Masato Tanaka[3], Hiroki Takaoka[4], Kaori Abe[5], Masatoshi Kataoka [6], Toshihiko Ooie[7]

[1-7]Health Research Institute, National Institute of Advanced Industrial Science and Technology (AIST), 2217-14, Hayashi-cho, Takamatsu, Kagawa 761-0395, Japan
[1]CEA-LETI, Minatec Campus, 17 rue des Martyrs, 38054 Grenoble Cedex 9, France

Abstract— *Practical immunoassay chip devices are high-priority needs in point-of-care testing (POCT) for rapid diagnoses. Compared to conventional POCT microchip devices, our report describes a manufacturing process involving laser ablation, inkjet deposition, and cover film sealing that is superior to that used for practical mass production of microchip devices, and produces devices capable of sensitive and reproducible measurements using a capillary-flow-driven system at a practical point-of-care setting. To promote sensitivity and reproducibility, circular islands surrounded by 10-µm-deep grooves were prepared to provide uniformity of printed antibody spots on a capillary flow immunoassay chip. The island surface enabled dense antibody fixation due to droplet surface tension as well as antibody determination by enzyme linked immunosorbent assay (ELISA), which demonstrated greater sensitivity than that of a device using a non-island surface. The luminescence intensity of the spots of the carboxyterminal propeptide of type I procollagen (PICP) exhibited a good linear relation with PICP concentration in the range 0-600 ng·mL^{-1}, which is suitable for clinical estimation in blood.*

Keywords— Capillary driven flow, Sensing Chip, grooved Island, immunoassay chip, ELISA.

I. INTRODUCTION

Analysis of biomarkers when the patient is located is known as point-of-care testing (POCT), and needs to be a simple and rapid medical diagnostic method [1-3]. Most of the available POCT devices involve immunoassay systems, and enzyme-linked immunosorbent assay (ELISA) has been utilized as a standard analytical system due to its sensitivity and specificity [4]. Because a practical and simple POCT device must be easily available to the end user in many environments, a capillary-driven flow system is a good candidate because it does not require electrical power and is easy to operate. Indeed, a capillary-driven, flow-based immuno chromatographic assay is considered the simplest commercially available POCT device in the diagnostic market. Therefore, a capillary-driven, flow-based immunoassay system was developed for an ELISA using a piezoelectric inkjet printing system [5-7].

Practical approaches for immobilizing antibodies on a microchannel surface include microfluidic patterning [8], photolithography [9], physical entrapment [10], micro-contact printing [11, 12], and inkjet printing [5-7]. Among these approaches, printing has many advantages, such as simplicity, flexibility, low cost, minimal consumption of reagents, and simultaneous patterning of multiple reagents [13]. Many important studies have been successfully reported by printing technologies, for example, electrohydrodynamic printing [14], water-based inkjet printing [15] and printed wiring board assembly [16]. These features allow the mass production of this device [17]. Although inkjet printing can precisely deposit a drop of antibody solution at the picoliter level on a microchannel surface, a high concentration of antibodies can destabilize the ejection spray from the nozzle head due to its high viscosity, which is a problem for the development of a diagnostic immunoassay system. Accurate ELISA measurements require printing spots of identical size and equivalent amounts of antibody immobilization, which ensures reproducible determination by chemical luminescence.

To overcome the viscosity problem, a solution with a high concentration of antibodies was continuously deposited and immobilized on a circumferentially-grooved island micro surface. The island microstructure enables formation of a spherical droplet by surface tension, producing a precise antibody spot and the same amount of antibody deposition. In addition, the droplet does not adhere to the wall of the microchannel surface and the antibody spots have a uniform size, even when the ejection spray may become uneven.

For the practical mass production of circumferentially-grooved island microchannel surfaces, laser ablation offers many advantages over other micromachining techniques, such as a highly precise, fast, and non-contact fabrication process. A transparent plastic device made of a cyclic olefin copolymer (COC) is more appropriate than other conventional materials, such as silicon and glass, for this purpose because COC possesses versatile thermal and chemical surface properties. An ultraviolet (UV) pulsed laser can directly ablate and locally modify a COC surface, with the best surface quality provided by a KrF laser at 193 nm, a wavelength strongly absorbed by COC [18, 19].

The present study describes a capillary-driven, flow-based immunoassay chip that could be mass produced using a UV pulsed laser system and a piezoelectric inkjet printing system. Ultraviolet pulse lasers and inkjet printers represent mature technologies for which antibody immobilization techniques have been established. In addition, a capillary-driven flow system does not require external power or moving off-chip components. Thus, the development of stable antibody immobilization on a circumferentially-grooved island on a microchannel surface could provide a model diagnostic POCT system that is readily adaptable in many POC situations.

II. EXPERIMENTAL WORK

2.1 Reagents

The monoclonal anti-PICP antibody used was Clone PC8-7 (Takara Bio Inc., Otsu, Japan) and was supplied in a Procollagen type I C-peptide (PIP) EIA Kit (Takara). The blocking and washing solutions were purchased from Sumitomo Bakelite Co. Ltd, Tokyo, Japan. The microchip was refrigerated at a temperature of 4°C when not in use.

2.2 Equipment

The circumferentially-grooved island structure was formed using a nanosecond pulse laser (LPX-305i, Coherent Inc.), at 500 mJ and 25 W. Movement of the XYZ stages was controlled with a computer under the focused laser spot. A video microscope system allowed accurate positioning and *in situ* monitoring of the laser micromachining process.

The inkjet printing head (PulseInjector®: Cluster Technology Co., Ltd., Osaka, Japan) was a piezoelectric-driven drop-on-demand plastic head with an epoxy resin; it exhibited very low biomolecular adsorption compared with glass. The inkjet system deposited and fixed the primary antibodies (Clone PC8-7, Takara) in the spotting buffer (BSX2321, Sumitomo Bakelite Co., Ltd., Tokyo, Japan) on the microchannel surface. Combining the PulseInjector® with a dedicated driving unit (WaveBuilder®: Cluster Technology Co., Ltd., Osaka, Japan) allowed easy adjustment of the ejection drive waveform, ejection rate, and driving voltage, enabling picoliter droplets to be ejected. A derivative drive waveform produced by a function generator with a user-friendly interface provided stable ejection, and the droplets were ejected at a frequency of 1 kHz and jetting voltage of 8 V. The volume of a single discharged droplet of primary antibodies was 50 pL, and 100-1000 shots were discharged onto the surface of the microchannel to provide the optimal volume. The PulseInjector® used a 25-µm diameter ejection hole.

2.3 Microchip fabrication by laser ablation and inkjet printing

A photograph and illustration of the immunoassay chip are shown in Figure 1(a). The chip was fabricated from COC and the surface treated with a polymer solution containing *p*-nitro phenyl ester, a commercial polymer coating from Sumitomo Bakelite Co., Ltd., which binds to amino groups in proteins and immobilizes the antibodies on the microchannel surface [6, 7]. The linear channel was 100-µm deep and 300-µm wide. Sample and reagents were introduced into the respective port of the channel and capillary-driven flow was used to fill the channel (Figure 1(b)). To realize a large quantity of antibody immobilization, the island surface of the 10-µm-deep and 150-µm-wide circular groove on the channel was formed by UV nanosecond laser ablation and antibody droplets were deposited onto the surface of the microchannel using a piezoelectric inkjet system (Figure 1c). Following deposition, the microchip surface was sealed with a cover film made of 33-µm-thick polymethylmethacrylate (Toyo Ink MFG. Co., Ltd., Tokyo, Japan). All samples and reagents for the sandwich ELISA assay were infused into the microchannel from a 1.0–mm-diameter inlet reservoir using a dropper. The outlet reservoir was located on the other side of the microchannel.

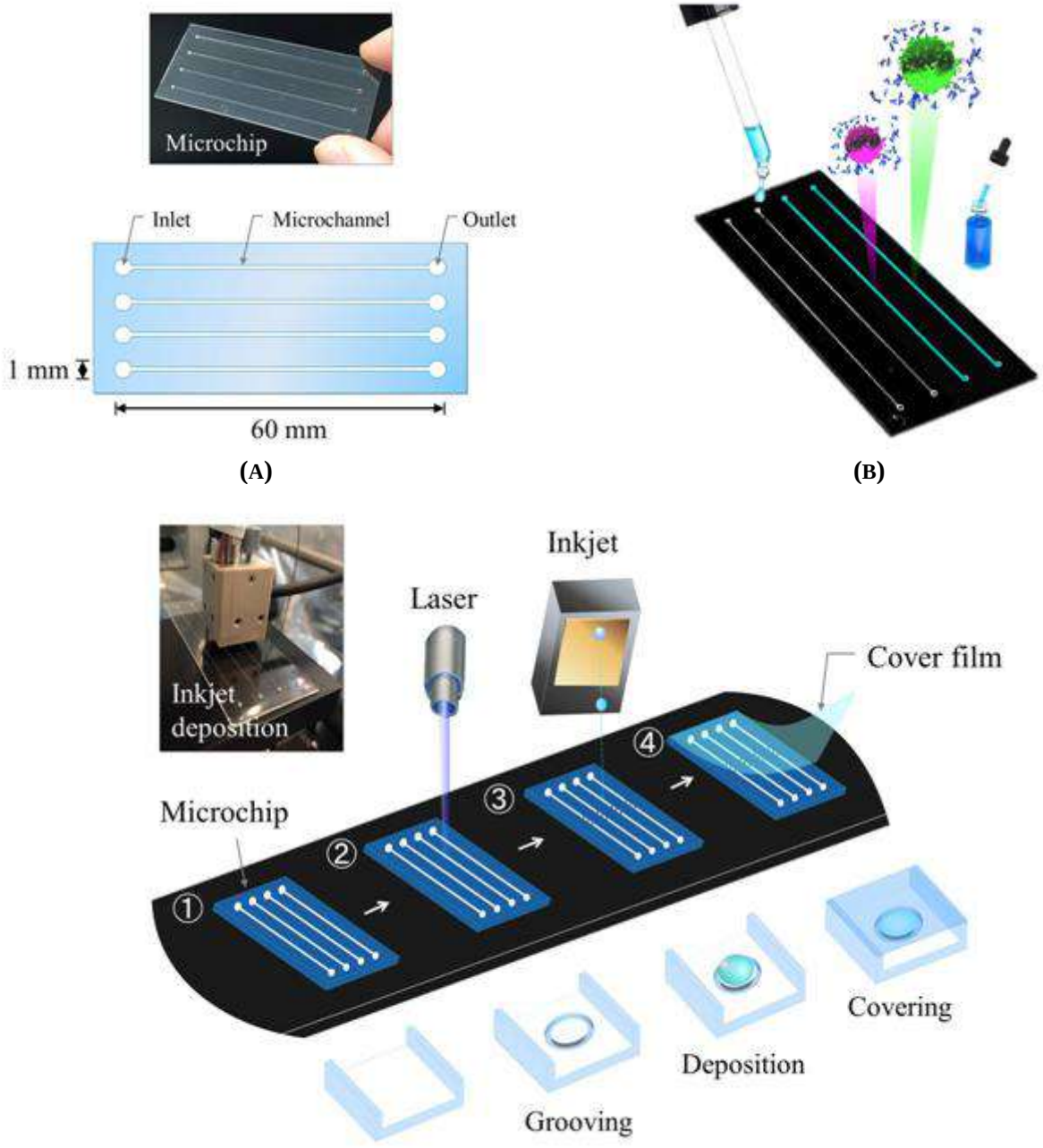

FIGURE 1: SCHEMATIC VIEW OF IMMUNOSENSING MICROCHIP SYSTEM AND CONSECUTIVE ANTIBODY PRINTING SYSTEM. (A) PHOTOGRAPH AND ILLUSTRATION OF MICROCHIP, (B) CAPILLARY-DRIVEN-FLOW SYSTEM USING DROPPER AND LUMINESCENCE DETERMINATION BY ELISA, (C) CONSECUTIVE ANTIBODY PRINTING PROCESS UTILIZING LASER PROCESSING, INKJET DEPOSITION, AND COVER FILM SEALING.

III. RESULTS AND DISCUSSION

3.1 Precise formation of printed antibody spots

Inkjet printing of antibody droplets is advantageous for on-demand manufacturing systems because it enables picoliter quantities to be deposited and reduces the total number of operations. However, depositing a greater concentration of antibody solution onto a microchannel surface with adequate reproducibility is difficult. High sensitivity demands that the primary antibodies are highly concentrated in the microchannel, but this requires a high-viscosity liquid that destabilizes ejection of the antibody droplet from the inkjet head. Such destabilizing ejection causes the droplets to adhere to the wall of the microchannel due to surface tension and has a negative effect on the uniformity of the printed spots. To avoid adherence to the microchannel wall, an island structure on the microchannel surface was formed to allow uniformly printed antibody

spots. A circumferentially-grooved island structure retains the spherical form of a large droplet due to surface tension. A circular grooved island surrounded by 10-μm-deep grooves was prepared and the uniformity of the printed antibody spots was compared for the case with and without islands (Figures 2(a,b)). Three spots were prepared on each microchannel, and 9 spots on 3 microchannels were compared. The results showed that good uniformity was obtained using islands (Figure 2(a)), but not without islands. Surface areas were calculated using Adobe Photoshop, which enables the measurement of the spots using the ruler tool. The surface area of the printed spots with the islands was 6.02 μm^2 with a relative standard deviation (RSD) of 0.9%. The surface area of spots without islands was 5.65 μm^2 with a RSD was 31.3%. This indicates that grooved-island surfaces were effective in providing uniformity of printed spots.

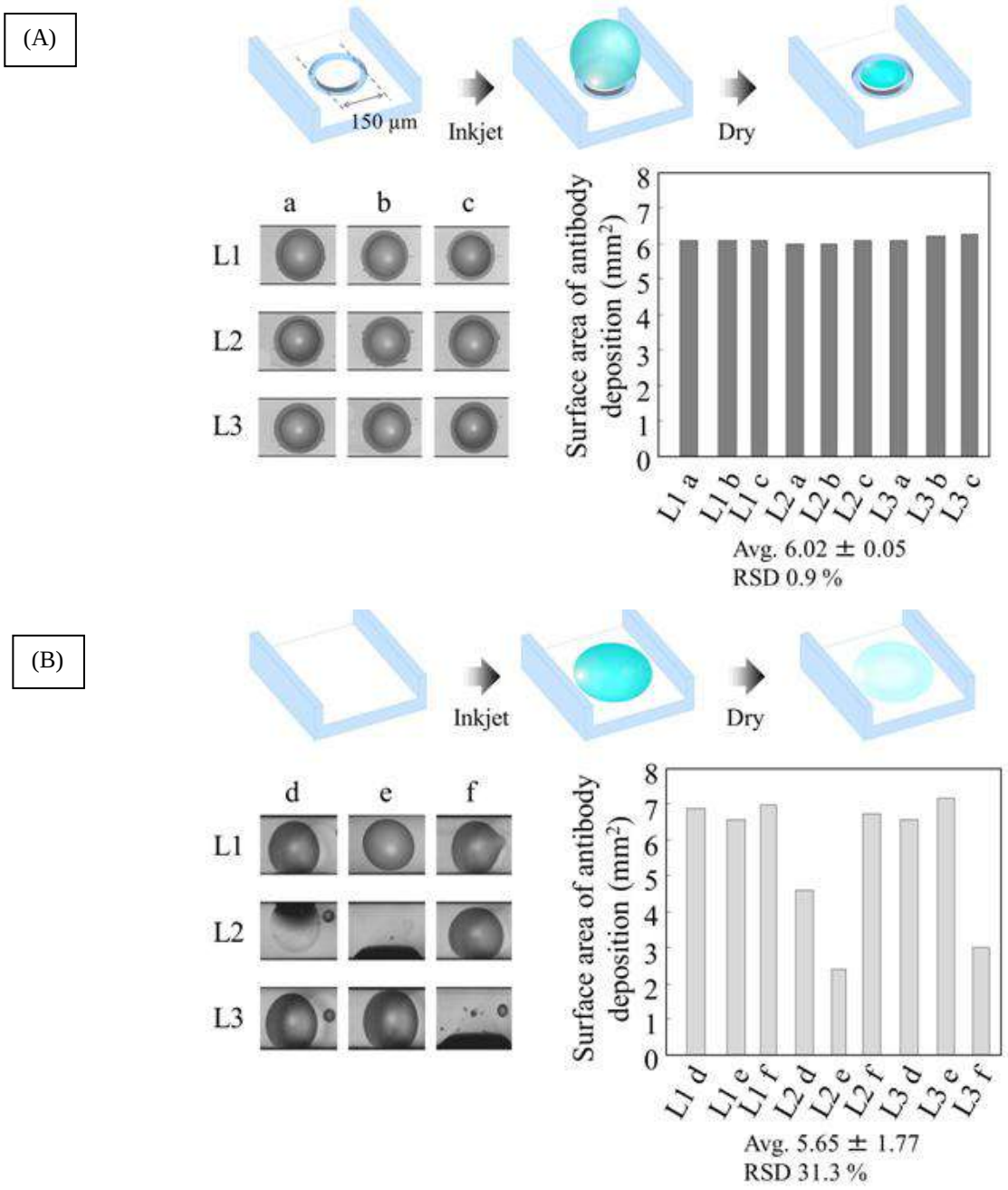

FIGURE 2: COMPARISON OF PRIMARY ANTIBODY DEPOSITION ONTO ISLAND MICROCHANNEL SURFACES AND NON-ISLAND MICROCHANNEL SURFACES. (A) IMAGE OF ANTIBODY DEPOSITION ONTO ISLAND SURFACE AND PHOTOGRAPH SHOWING ANTIBODY SPOTS, (B) IMAGE OF ANTIBODY DEPOSITION ONTO A NON-ISLAND SURFACE AND PHOTOGRAPH SHOWING ANTIBODY SPOTS.

3.2 Dense antibody deposition onto microchannel surface

The grooved-island structure should limit the spot area of antibody inkjet deposition, which allows dense primary antibody deposition and the capture of a large amount of antigen, leading to greater sensitivity. To assess this effect, Cy5 conjugated primary antibodies were prepared by the protocol specified for the Cy5® Fast Conjugation Kit (ab188288, Abcam, Tokyo, Japan), Cy5 was deposited on island and non-island surfaces, and the signal intensities were compared after 10-min incubation at room temperature (Figure 3). The resulting images were measured using a confocal laser scanning microscope (Zeiss LSM 410) equipped with a He-Ne laser (emission wavelength 633 nm) (Zeiss, Oberkochen, Germany). This laser was used to excite the Cy5 fluorophore using a FT 655 dichroic beam splitter and an RG 665 emission long pass filter.

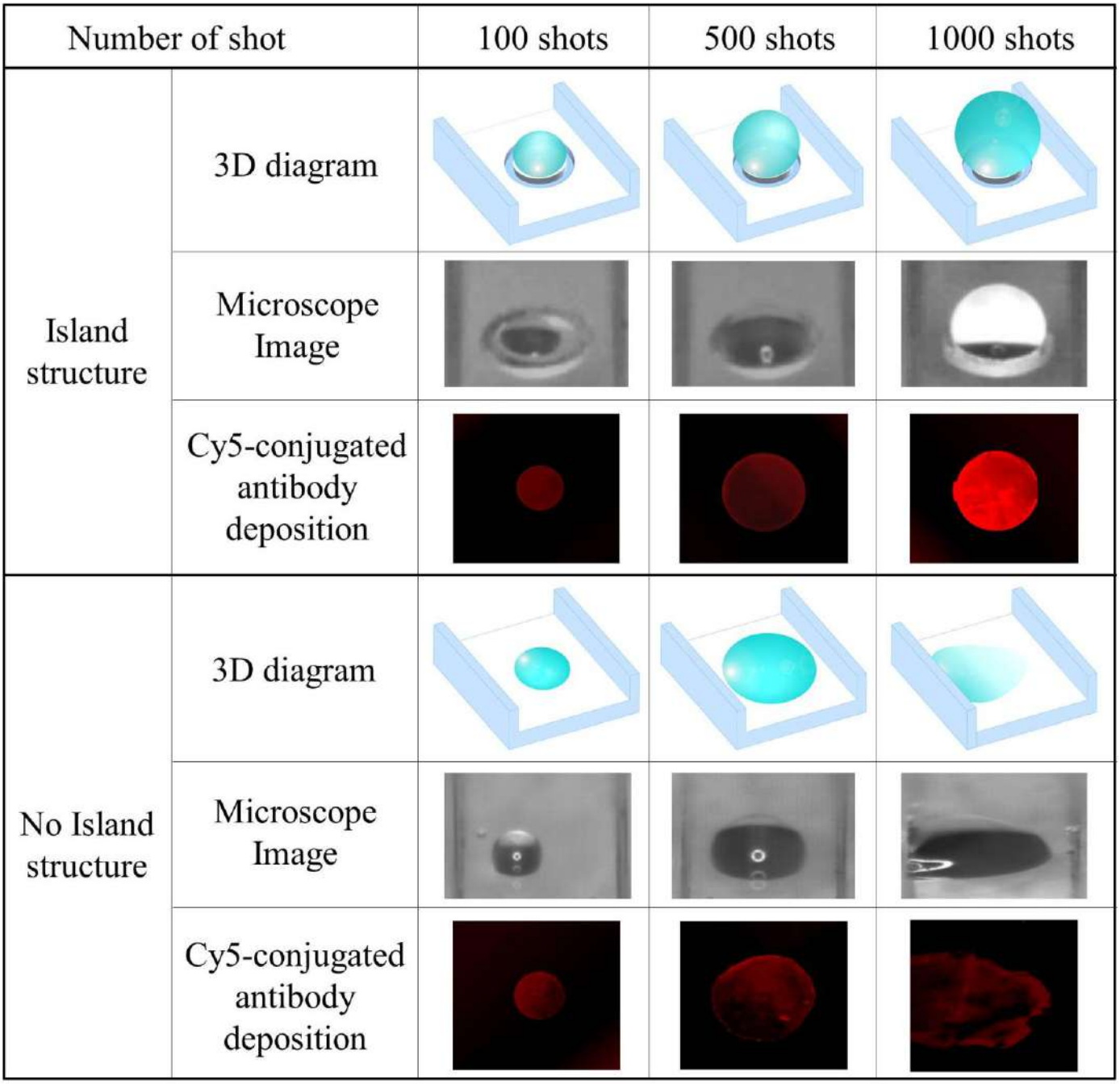

FIGURE 3: SURFACE IMAGES AFTER PRINTING AND MICROSCOPIC IMAGES OF CY5-CONJUGATED ANTIBODY ON COC MICROCHANNEL SURFACE, AND COMPARISON OF THE RELATIVE FLUORESCENCE INTENSITY AT 100, 500, AND 1000 SHOTS.

Signal intensities were compared among 100, 500, and 1000 shots. The intensities of island and non-island spots were similar until 500 shots, but those at 1000 shots were quite different. The non-island surface spots maintained a spherical form up to 500 shots but lost the spherical shape at 1000 shots because the deposited droplets adhered to the wall of the microchannel, resulting in non-uniform spots. In contrast, spots on the island surface maintained a spherical form even at 1000 shots. In addition, the intensity of the spots was highest at 1000 shots, indicating that the antibodies were densely deposited and immobilized on the island surface.

The required sensitivity and reproducibility of sandwich ELISAs necessitates dense immobilization of primary antibodies on a microchannel surface. Although a high concentration of antibody solution destabilizes the ejection stream due to viscosity, this circumferentially-grooved island provided not only uniform printed spots but also dense immobilization of antibodies.

3.3 Capillary-driven, flow-based sandwich ELISA on island surface

A capillary-driven flow system allows low volume, fast reaction time, and simple operation without external power. The potential of a sandwich ELISA on a COC microchip was investigated for rapid and accurate screening (Figures 4(a,b)) [5-7]. Sample and reagent solutions were introduced into the inlet port with a dropper, and the microchannels filled by capillary-driven flow. After filling the channel, excess solution on the inlet port was removed by contact with absorbent paper. The microchannels were emptied using the absorbent paper placed in contact with the outlet port between immunoassay steps.

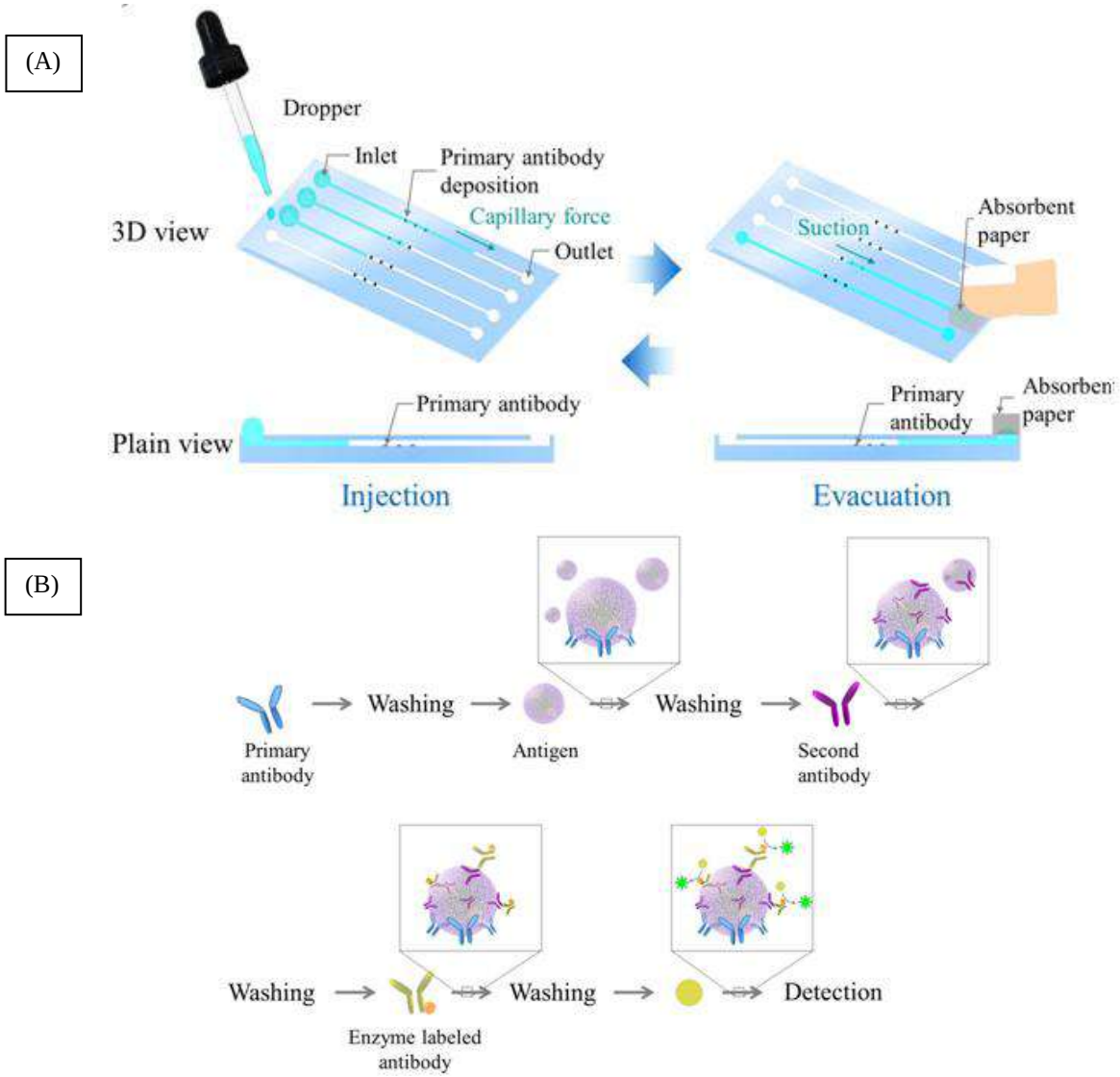

FIGURE 4: IMMUNOASSAY PROCESS BASED ON CAPILLARY-DRIVEN FLOW. (A) SCHEMATIC DIAGRAM OF IMMUNOASSAY USING A DROPPER AND ABSORBENT PAPER, (B) REACTION AND RESULTS OF A SANDWICH ELISA.

Circular islands surrounded by a 10-μm-deep groove allowed uniformity of printed antibody spots and the solutions in the microchannel could be completely replaced by capillary-driven flow. Therefore, the suitability of this approach was examined by measuring the luminescence intensity based on a sandwich ELISA on islanid and non-island surfaces at 0, 100, 500, and 1000 shots (Figures 5(a,b)). The results showed that the luminescence intensity for 5 spots at 300 mg·mL^{-1} PICP varied with the number of shots. The intensities of island and non-island spots were similar at 0, 100, and 500 shots, but were different at 1000 shots. The intensity of island spots was greater than that of non-island spots, even though both surfaces had the same amount of primary antibodies deposited. In addition, the variation in island surface spots at 500 and 1000 shots was less than that of the non-island spots. The variation was determined by the RSD, which for island surface spots was 2.37% at 500 shots and 4.08% at 1000 shots and for non-island spots was 6.86% at 500 shots and 27.2% at 1000 shots. Thus, the island surface prevents antibody droplets from adhering to the wall of the microchannel, allows a dense antibody solution to be deposited and fixed on the island surface. These results indicate that the circumferentially-grooved island surface provides high sensitivity and reproducibility compared to a non-island surface.

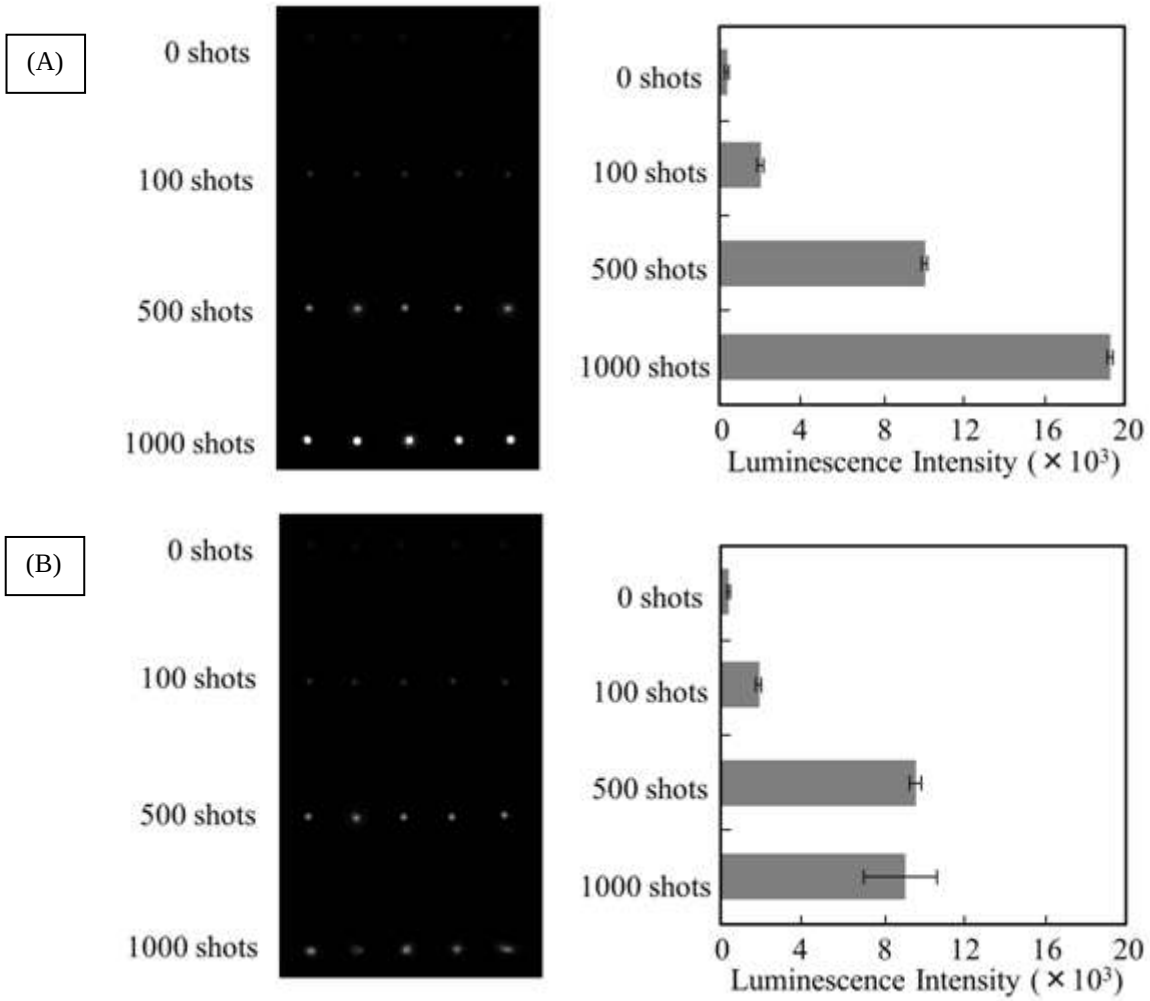

FIGURE 5: QUANTITATIVE SANDWICH ELISA USING ISLAND AND NON-ISLAND MICROCHANNEL SURFACES AT 0, 100, 500, AND 1000 SHOTS. (A) LUMINESCENCE INTENSITY OF ISLAND SURFACE SPOTS AT 0, 100, 500, AND 1000 SHOTS, (B) LUMINESCENCE INTENSITY OF NON-ISLAND SURFACE SPOTS AT 0, 100, 500, AND 1000 SHOTS.

The effects of the capillary-driven flow channel response on 0-600 ng·mL^{-1} PICP were also investigated for island and non-island surfaces (Figure 6). The luminescence intensity for both island and non-island spots increased with PICP concentration. The mean luminescence intensity for 5 different spots was plotted against PICP concentration and provided a linear relation. The intensity of island surface spots was greater overall than that of non-island surface spots. The 0-600 ng·mL^{-1} PICP concentration is adequate for clinical estimation of PICP in blood [20, 21].

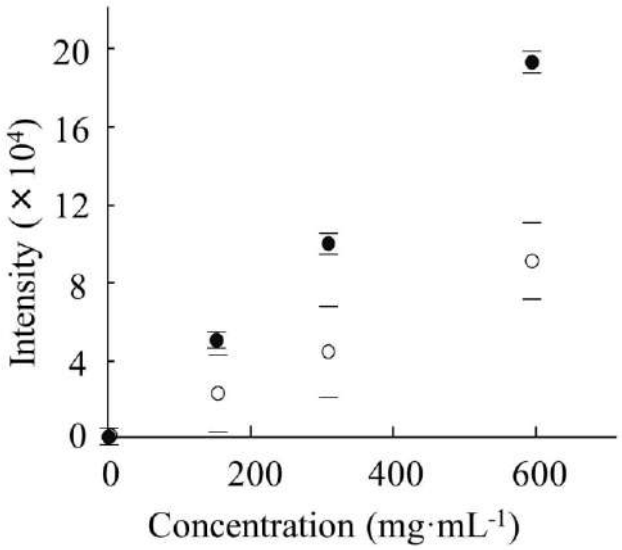

FIGURE 6: QUANTITATIVE SANDWICH ELISA USING CAPILLARY-DRIVEN FLOW CHANNEL RESPONSE FOR 0-600 ng·mL^{-1} PICP ON (●) ISLAND MICROCHANNEL SURFACES AND (○) NON-ISLAND MICROCHANNEL SURFACES.

These results demonstrated that inkjet deposition of a concentrated antibody solution onto a circumferentially-grooved island surface produced a device suitable for a capillary-driven-flow microfluidic immunoassay. Thus, this system enables sensitive and reproducible determination of PIPC concentration and is a promising methodology for a practical POC setting.

IV. CONCLUSIONS

A novel and simple approach for developing a sandwich ELISA based on a capillary-driven flow system for sensitive and reproducible measurement of PICP was developed. The circumferentially-grooved island surface allowed uniformity in printing of antibody spots onto a microchannel surface, enabling concentrated antibody solution fixation due to the droplet's surface tension. Evaluation of the precision of antibody spot printing demonstrated that the variation in the surface area of spots was 0.05% RSD on the island surface and 31.3% for spots on the non-island surface. The spots on the island surface maintained a spherical form even at 1000 shots of antibody inkjet deposition, and produced greater luminescence intensity than those on the non-island surface. In contrast, spots on the non-island surface lost their spherical form after 500 shots and had slightly reduced luminescence intensity. A concentrated antibody solution was deposited at 1000 shots on the island surface and the spot intensity in a sandwich ELISA was greater than that for the non-island surface. The intensity of 0-600 ng·mL^{-1} PICP spots showed a concentration-dependent relation and were greater overall than that for spots on non-island surfaces.

This microfluidic ELISA system using capillary-driven flow possesses many advantages for POC situations, such as simple operation, minimal sample consumption, and rapid results. The antibody immobilization process was performed consecutively using laser processing, inkjet deposition, and cover film sealing. This process is driven by mechatronic operation, which provides high throughput. This report demonstrates the potential of practical POC chip fabrication in the future.

ACKNOWLEDGEMENTS

This work was supported by a Grant-in-Aid for Scientific Research from the Ministry of Education, Culture, Sports, Science and Technology, Japan (No. 16K05833).

REFERENCES

[1] P. St-Louis, Status of point-of-care testing: promise, realities, and possibilities, Clin. Biochem 33 (2000) 427–440.

[2] D. Mark, S. Haeberle, G. Roth, F. von Stetten, R. Zengerle, Microfluidic lab-on-a-chip platforms: requirements, characteristics and applications Chemical Society Reviews 39 (2010) 1153–1182.

[3] P. von Lode, Point-of-care immunotesting: approaching the analytical performance of central laboratory methods, Clin Biochem 38 (2005) 591–606.

[4] J. Ramo´n-Azco´n, R. Galve, F. Sa´nchez-Baeza, M.P. Marco, Development of an Enzyme-Linked Immunosorbent Assay for the Determination of the Linear Alkylbenzene Sulfonates and Long-Chain Sulfophenyl Carboxylates Using Antibodies Generated by Pseudoheterologous Immunization, Analytical Chemistry 78 (2006) 71–81.

[5] Y. Fuchiwaki, Y. Yabe, Y. Adachi, M. Tanaka, K. Abe, M. Kataoka, T. Ooie, Inkjet monitoring technique with quartz crystal microbalance (QCM) sensor for highly reproducible antibody immobilization, 219 Sens. Actuators A (2014) 1–5.

[6] S. Yatsushiro, R. Akamine, S. Yamamura, M. Hino, K. Kajimoto, K. Abe, H. Abe, J. Kido, M. Tanaka, Y. Shinohara, Y. Baba, T. Ooie, M. Kataoka, Quantitative Analysis of Serum Procollagen Type I C-Terminal Propeptide by Immunoassay on Microchip, 6 PLoS ONE (2011) e18807

[7] K. Abe, Y. Hashimoto, S. Yatshushiro, S. Yamamura, M. Bando, Y. Hiroshima, J. Kido, M. Tanaka, Y. Shinohara, T. Ooie, T. Baba, M. Kataoka, Simultaneous Immunoassay Analysis of Plasma IL-6 and TNF-α on a Microchip, 8 PLoS ONE (2013) e53620

[8] Z. Yin, S.C. Tao, R. Cheong, H. Zhu, A. Levchenko, An integrated micro-electro-fluidic and protein arraying system for parallel analysis of cell responses to controlled microenvironments, Integrative Biology 2 (2010) 416–423.

[9] L.K. Fiddes, H.K.C. Chan, B. Lau, E. Kumacheva, A.R. Wheeler, Durable, region-specific protein patterning in microfluidic channels, Biomaterials 31 (2010) 315–320.

[10] K. Sato, M. Yamanaka, H. Takahashi, M. Tokeshi, H. Kimura, Microchip-based immunoassay system with branching multichannels for simultaneous determination of interferon-gamma. Electrophoresis 23 (2002) 734–739.

[11] A. Khademhosseini, K.Y. Suh, S. Jon, G. Eng, J. Yeh, A soft lithographic approach to fabricate patterned microfluidic channels, Analytical Chemistry 76 (2004) 3675–3681.

[12] T.F. Didar, A.M. Foudeh, M. Tabrizian, Patterning multiplex protein microarrays in a single microfluidic channel, Analytical Chemistry 84 (2012) 1012–1018.

[13] C. Wei, H. Qin, C. P. Chiu, Y. S. Lee, J. Dong, Drop-on-demand E-jet printing of continuous interconnects with AC-pulse modulation on highly insulating substrates, 37, Journal of Manufacturing Systems (2015) 505-510

[14] Y. Han, C. Wei, J. Dong, Droplet formation and settlement of phase-change ink in high resolution electrohydrodynamic (EHD) 3D printing, 20, Journal of Manufacturing Processes (2015) 485–491

[15] Y. Gua, A. Wua, H. Sohnb, C. Nicolettia, Z. Iqbalc, J. F. Federici, Fabrication of rechargeable lithium ion batteries using water-based inkjet printed cathodes, 20, Journal of Manufacturing Processes (2015) 198-205.

[16] S.H.G. Teng, S.S. Garimella, Manufacturing Cost Modeling in Printed Wiring Board Assembly, 17, Journal of Manufacturing Systems (1998) 87-96.

[17] F. Belachew, L. Christina, K. Liisa, J. Leena-Sisko, J. Heli, H. Leena, Patterned Immobilization of Antibodies within Roll-to-Roll Hot Embossed Polymeric Microfluidic Channels, 8 PLoS ONE (2013) e68918

[18] P. Irina-Alexandra, S. Alexandros, B. Giannis, K. Gabriella, G. Savas, Nanosecond and femtosecond UV laser ablation of polymers: Influence of molecular weight, Applied Surface Science 255 (2009) 9856–9860

[19] T. Daniel, T. Thanongsak, C. Joaquim, O. Tugrul, Nanosecond pulsed laser micromachining of PMMA-based microfluidic channels, J. Manufacturing Process 14 (2012) 435-442.

[20] A.M. Parfitt, L. S. Simon, A. R. Villanueva and S. M. Krane, Correlation with iliac bone formation rates and comparison with total alkaline phosphatase, J. Bone Miner. Res. 2 (1987) 427-436.

[21] K. Kohda, N. Ito, M. Ohwada, K. Morita, N. Watanabe, Y. Kohgo, Y. Mogi and Y. Niitsu, Diagnostic value of measurement of serum type I procollagen carboxy terminal peptides in patients with scirrhous carcinoma of the stomach. Gut 32 (1991) 624-629.

Reinforcement Q-Learning and ILC with Self-Tuning Learning Rate for Contour Following Accuracy Improvement of Biaxial Motion Stage

Wei-Liang Kuo[1], Ming-Yang Cheng[2], Hong-Xian Lin[3]

Department of Electrical Engineering, National Cheng Kung University, Tainan, Taiwan

Abstract**—***Biaxial motion stages are commonly used in precision motion applications. However, the contour following accuracy of a biaxial motion stage often suffers from system nonlinearities and external disturbances. To deal with the above-mentioned problem, a control scheme consisting of a reinforcement Q-learning controller with a self-tuning learning rate and two iterative learning controllers is proposed in this paper. In particular, the reinforcement Q-learning controller is used to compensate for friction and also cope with the problem of dynamics mismatch between different axes. In addition, one of the two iterative learning controllers is used to suppress periodic external disturbances, while the other one is employed to adjust the learning rate of the reinforcement Q-learning controller. Results of contour following experiments indicate that the proposed approach is feasible.*

Keywords—Reinforcement Learning, Q-Learning, Iterative Learning Control (ILC), Contour Following.

I. INTRODUCTION

Contour following is commonly seen in industrial processes such as machining, cutting, polishing, deburring, painting and welding. In these industrial processes, product quality depends on contour following accuracy. Generally speaking, better contour following accuracy can be achieved by reducing tracking errors and/or contour error [14]. As a matter of fact, tracking error reduction is one of the most important research topics in the contour following problems of multi-axis motion stage [1]-[4]. Due to factors such as external disturbance, system nonlinearity, servo lag and mismatch in axis dynamics, contour following accuracy of the multi-axis motion stage may not be able to meet the accuracy requirements [5]-[7].

There are many existing approaches that can be used in practice to reduce tracking error of a multi-axis motion stage [9]-[12]. For example, the commonly used multi-loop feedback control scheme with command feedforward is very effective in reducing tracking error caused by the servo lag phenomenon [8]. In addition, advanced control schemes such as sliding mode control and adaptive control can be used to reduce tracking error as well. Recently, the number of studies exploiting the paradigm of artificial neural network to improve contour following accuracy of multi-axis motion stage has risen steadily [13]-[22]. For instance, Wen and Cheng [13] proposed a fuzzy CMAC with a critic-based learning mechanism to cope with external disturbance and nonlinearity so as to reduce tracking error. Later on, Wen and Cheng [15] further proposed a recurrent fuzzy cerebellar model articulation controller with a self-tuning learning rate to improve contour following accuracy for a piezoelectric actuated dual-axis micro motion stage. In addition to tracking error reduction, the paradigm of artificial neural network has been applied to different fields such as wind power generation [24], the game of Go [22], and object grasping using robots [25]. Generally, a neural network needs to be trained before it can be used to solve a particular problem. Among different training mechanisms for neural networks, reinforcement learning is the one that has received a lot of attention recently [21]. In this paper, a control scheme consisting of a reinforcement Q-learning controller with an adjustable learning rate and two iterative learning controllers (ILC) is proposed to improve contour following accuracy of a bi-axial motion stage. In the proposed approach, the reinforcement Q-learning controller is responsible for friction compensation and also deals with the dynamics mismatch between different axes. In addition, one of the two ILCs is exploited to deal with the adverse effects due to periodic external disturbances from repetitive motions, while the other ILC is exploited to tune the learning rate of Q-learning based on current tracking error so as to further improve contour following accuracy.

The remainder of the paper is organized as follows. Section 2 gives a brief review on reinforcement learning and iterative learning control. Section 3 introduces the proposed control scheme. Experimental results and conclusions are provided in Section 4 and 5, respectively.

II. BRIEF REVIEW ON REINFORCEMENT LEARNING AND ITERATIVE LEARNING CONTROL

Since the proposed control scheme exploits the idea of reinforcement learning and iterative learning control, brief reviews on these two research topics will be provided in this section.

2.1 Reinforcement Learning and Q-Learning

In general, learning mechanisms of artificial neural networks can be divided into three types: supervised learning, unsupervised learning and reinforcement learning. Unlike the other two types of learning which either need training pairs or expected final outcome, reinforcement learning "learns" proper actions by maximizing the reward simply based on the reward/penalty resulting from previous action and current environment. Fig. 1 illustrates a typical control block diagram that employs reinforcement Q-learning.

In general, the reinforcement Q-learning controller can be expressed as:

$$Q_{t+1}(s_t, a_t) = Q_t(s_t, a_t) + \alpha_t[r_t + \gamma \max_{a_i} Q_{t+1}(s_{t+1}, a_i) - Q_t(s_t, a_i)] \tag{1}$$

Where $Q_t(s_t, a_t)$: the Q value corresponding to the state s_t and action a_t in the Q-table; s: state; a_i: action; i: action index in action space; α_t: learning rate; r: reward; γ:discount factor. $\max_{a_i} Q_{t+1}(s_{t+1}, a_i)$ is the maximum value of Q corresponding to state $s_{t+1}$and action a_i; t: time variable.

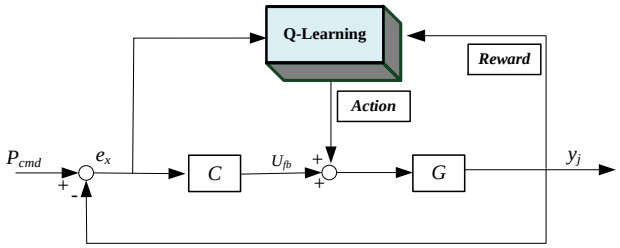

FIG. 1 A TYPICAL CONTROL BLOCK DIAGRAM THAT EMPLOYS REINFORCEMENT BASED Q-LEARNING

The probability of selecting action a_i in Q-learning is described by (2).

$$P(s, a_i) = \frac{e^{Q(s,a_i)}}{\sum e^{Q(s,a_i)}} \tag{2}$$

2.2 Iterative Learning Controller

As reported in many previous studies, ILC is effective in suppressing periodic disturbances caused by repetitive motions [17-19]. Fig. 2 is the block diagram for a control scheme consisting of a feedback controller and a control law based ILC [16]. In Fig. 2, U_{ilc} is the control force generated by ILC, L is the learning function and F is a low-pass filter. All the tracking error e_x and the control force U_{ilc} generated by ILC in the previous iteration are stored and used to update U_{ilc} in the current iteration. The total control force U_j in the jth iteration to the plant G is the sum of U_{ilc} and the feedback controller output U_{fb}.

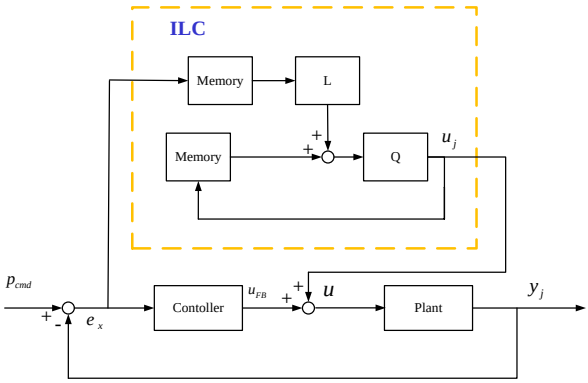

FIG. 2 BLOCK DIAGRAM FOR A CONTROL SCHEME CONSISTING OF A FEEDBACK CONTROLLER AND A CONTROL LAW BASED ILC

Based on Fig.2, the relationship between output y_j in the jth iteration and input P_{cmd} can be described as:

$$y_j = (1+GC)^{-1}G \cdot U_j + (1+GC)^{-1}GC \cdot P_{cmd} \tag{3}$$

where the total control force U_{j+1} in the j+1th iteration is updated using Eq. (4)

$$U_{j+1} = F(U_j + Le_j) + Ce_{j+1} \tag{4}$$

where e_j, and u_j are the tracking error and total control force in the jth iteration, respectively. Note that in Eq. (4), Ce_{j+1} can be regarded as the feedback control force. The control force U_{ilc} generated by ILC aims at reducing the tracking error. Namely, better performance of ILC leads to smaller tracking error so that feedback control force decreases as well.

III. THE PROPOSED REINFORCEMENT Q-LEARNING CONTROLLER WITH AN ADJUSTABLE LEARNING RATE

Fig. 3 illustrates the block diagram for the control scheme consisting of a feedback controller, a control law based ILC, and the proposed reinforcement Q-learning controller with an adjustable rate.

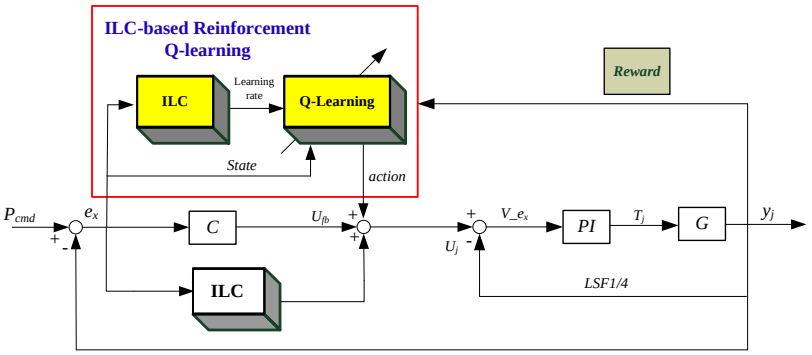

FIG. 3 BLOCK DIAGRAM FOR THE CONTROL SCHEME CONSISTING OF A FEEDBACK CONTROLLER, A CONTROL LAW BASED ILC, AND THE PROPOSED REINFORCEMENT Q-LEARNING CONTROLLER WITH AN ADJUSTABLE RATE.

In the proposed approach, the reinforcement Q-learning controller is modified as:

$$Q_{t+1}(e_t, a_t) = Q_t(\mathrm{e}_t, a_t) + L_{ilc}[\mathrm{r}_t + \gamma \max_{a_i} Q_{t+1}(\mathrm{e}_{t+1}, \mathrm{a}_i) - Q_t(\mathrm{e}_t, \mathrm{a}_i)] \tag{5}$$

Compared with Eq. (1), the learning rate α_t in the conventional Q-learning algorithm is replaced by L_{ilc} in Eq. (5), where L_{ilc} is updated using Eq. (6)

$$L_{ilc_{j+1}} = F[L_{ilc_j} + Le_j] \tag{6}$$

where L_{ilc_j+1} is the learning rate for the reinforcement Q-learning controller in the j+1th iteration. Note that in this paper, the value of L_{ilc} is constrained to be between zero and one. Moreover, in this paper, the aim is to reduce the tracking error of a multi-axis motion stage. As a result, the state s in Eq. (1) is replaced by tracking error e in Eq. (5). In addition, three possible actions — accelerate, decelerate and maintain constant velocity, and can be selected for a_t in Eq. (5) to adjust the velocity command for the motion stage. The probability of selecting action a_i in the Q-learning algorithm is rewritten as:

$$P(\mathrm{e}, a_{i,}) = \frac{e^{Q(\mathrm{e},a_i)}}{\sum e^{Q(\mathrm{e},a_i)}} \tag{7}$$

where the state is the tracking error e.

In this paper, the action space A consists of three actions

$$A = \{a_1, a_2, a_3\} \tag{8}$$

where a_1: accelerate: a_2: decelerate; a_3: maintain constant speed.

In this paper, the reward is designed to reduce tracking error. In particular, the reward is determined using Eq. (9).

$$r_{t+1} = \begin{cases} 100, & \text{if} \quad e_t - e_{t+1} < 0 \\ 0, & \text{if} \quad e_t - e_{t+1} = 0 \\ -1, & \text{if} \quad e_t - e_{t+1} > 0 \end{cases} \tag{9}$$

Fig. 4 illustrates the block diagram of the motion control scheme for a bi-axial motion stage proposed in this paper. In Fig.4, the velocity command ω_{cmd_x} for the *x*-axis consists of the control force U_{ilc_x} generated by ILC, the feedback control force U_{fb_x}, and the control force U_{RL_x} generated by the reinforcement Q-learning controller. It can be expressed as:

$$\omega_{cmd\_x} = U_{fb\_x} + U_{ilc\_x} + U_{RL\_x} \tag{10}$$

where

$$U_{fb\_x} = C \cdot e_{j+1} \tag{11}$$

$$U_{ilc\_x} = F(u_j + L \cdot e_j) \tag{12}$$

$$U_{RL\_x} = v + \Delta v \tag{13}$$

Note that the velocity command for the *y*-axis is designed similarly.

In Fig. 4, the reinforcement Q-learning controller with adjustable learning rate is responsible for friction compensation and also deals with the dynamics mismatch between the *x*-axis and *y*-axis. Fig. 4 also shows that two ILCs are employed in the proposed motion control scheme. In particular, one ILC is exploited to adjust the learning rate of the reinforcement Q-learning controller, while the other ILC is exploited to deal with the adverse effects due to periodic external disturbances so as to further reduce tracking error.

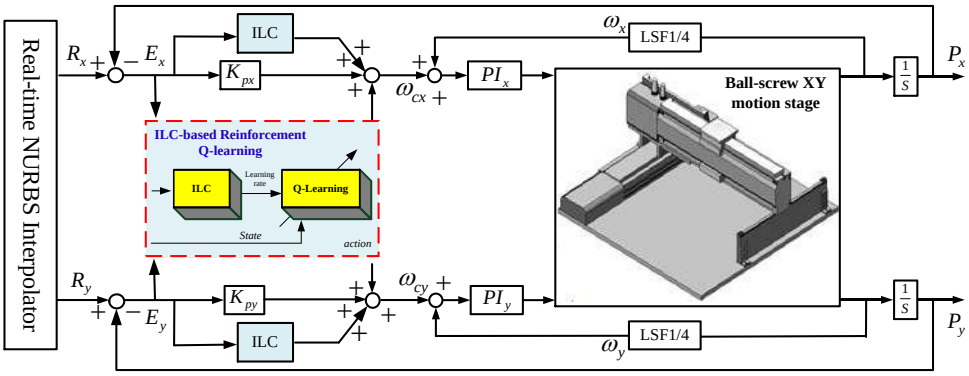

FIG. 4 THE BLOCK DIAGRAM OF THE PROPOSED MOTION CONTROL SCHEME FOR A BI-AXIAL MOTION STAGE.

IV. EXPERIMENTAL RESULTS

Fig. 5 shows a the photograph of the bi-axial motion stage used to assess the effectiveness of the proposed approach. Fig. 6 (a) shows the circle-shaped contour represented in NURBS form used in the contour following experiment. Under S-curve acceleration/deceleration motion planning, a NURBS interpolator [23] is employed to convert the circle-shaped contour into the position commands for the *x*-axis (Fig. 6(b)) and *y*-axis (Fig. 6(c)). The duration time for each circle following is 9.5 seconds. In each experiment, circle following will be performed seven times (i.e. seven iterations). In total, four different control schemes are tested in the contour following experiments. They are:

Control scheme #1: PI type feedback controller combined with an ILC.

Control scheme #2: PI type feedback controller combined with a reinforcement Q-learning controller with a fixed learning rate.

Control scheme #3: PI type feedback controller combined with an ILC and a reinforcement Q-learning controller with a fixed learning rate.

Control scheme #4: PI type feedback controller combined with an ILC and a reinforcement Q-learning controller with adjustable learning rate.

Due to the limitations in the paper length, only the experimental results of the tracking error in the *x*-axis for these four tested control schemes are shown in Fig. 7. In addition, performance indices in terms of root mean square of tracking error (RMS), average of integral of absolute tracking error (AIAE), and maximum tracking error (MAX) are listed in TABLE 1.

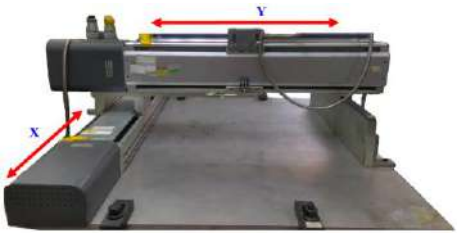

FIG. 5 PHOTOGRAPH OF THE BI-AXIAL MOTION STAGE USED IN THIS PAPER.

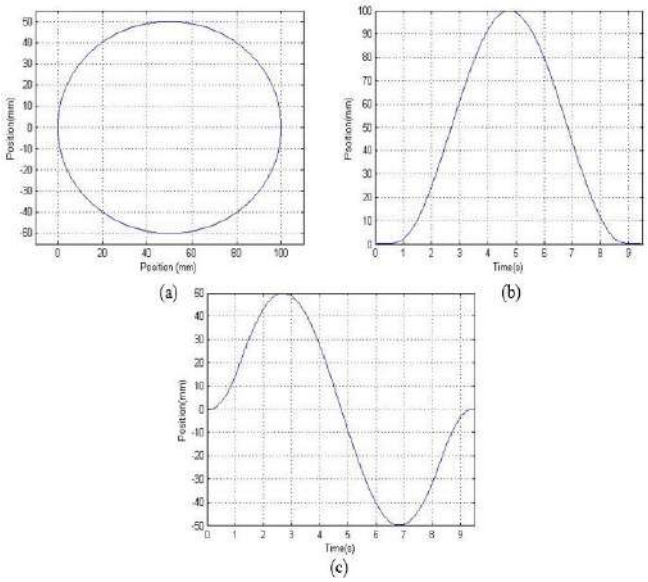

FIG. 6 (A) CIRCLE SHAPED CONTOUR REPRESENTED IN NURBS FORM (B) POSITION COMMANDS FOR X-AXIS, (C) POSITION COMMANDS FOR Y-AXIS.

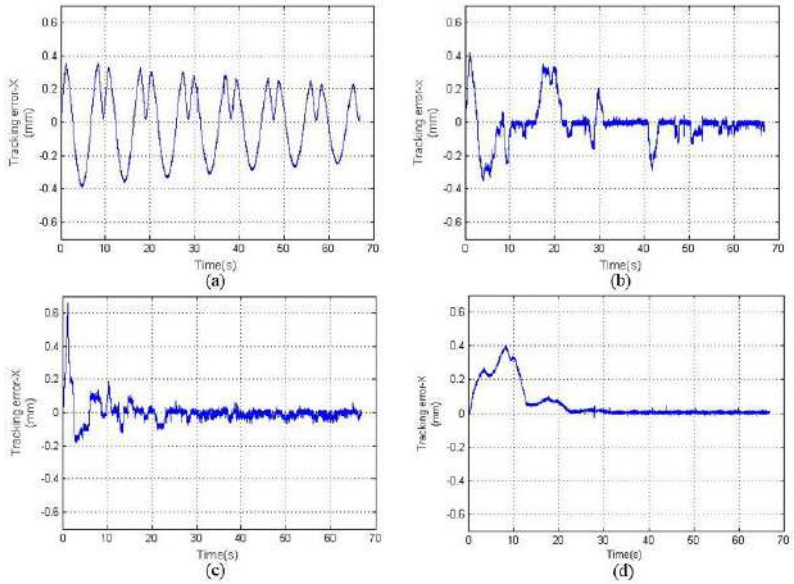

FIG. 7 EXPERIMENTAL RESULTS OF TRACKING ERROR IN THE X-AXIS (A) CONTROL SCHEME #1 (B) CONTROL SCHEME #2 (C) CONTROL SCHEME #3 (D) CONTROL SCHEME #4

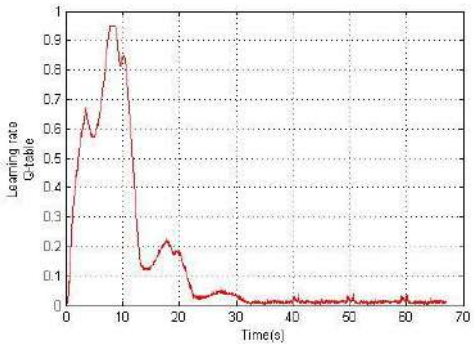

FIG. 8 THE VALUES OF THE LEARNING RATE OF THE REINFORCEMENT Q-LEARNING CONTROLLER VARIES WITH RESPECT TO TIME.

TABLE 1
TRACKING ERROR COMPARISON AMONG FOUR TESTED CONTROL SCHEMES

	Tracking error of X axis		
	RMS(μm)	AIAE(μm)	Max(μm)
Scheme #1	19.22	17.01	35.79
Scheme #2	9.48	5.16	35.08
Scheme #3	4.28	2.33	17.63
Scheme #4	2.62	1.51	9.93

Fig. 7(a) shows the tracking error of the circle following experiment using control scheme #1. Since the ILC will be activated after the 1st iteration, the tracking error for the first 9.5 seconds in Fig. 7(a) can be regarded as the results for using the PI feedback control only. Clearly, tracking error gradually decreases after the 2nd iteration, indicating that ILC indeed is effective in suppressing periodic external disturbance. Based on the experimental results shown in Fig. 7(b)~(d), the tracking error for using control schemes #2, #3 or #4 all converges much faster than that for using the control scheme #1. These facts indicate that the reinforcement Q-learning controller is indeed effective in reducing tracking error since control schemes #2, #3 or #4 all include a reinforcement Q-learning controller. In particular, the proposed control scheme (i.e. control scheme) has the best performance among the four tested control schemes.
Fig. 8 shows the values of the learning rate of the reinforcement Q-learning controller in the proposed control scheme varies with respect to time. After three iterations (after 28.5 seconds), the learning rate only changes slightly since the tracking error becomes very small after three iterations.

V. CONCLUSION

This paper has proposed a motion control scheme consisting of two ILCs and one reinforcement Q-learning controller for contour following accuracy improvement. In particular, one ILC is used to tune the learning rate of the reinforcement Q-learning controller that is mainly used to cope with system nonlinearities, while the other ILC is exploited to suppress periodic disturbance during repetitive contour following motions. Results of contour following experiments conducted on a bi-axial motion stage indicate that the proposed control scheme is feasible and outperforms other control schemes also tested in the experiment.

ACKNOWLEDGEMENTS

The authors would like to thank the MOST of Taiwan for their support of this research under Grant MOST 105-2221-E-006-105-MY3.

REFERENCES

[1] F. Hiroshi and T. Tadashi, "High-Precision Control of Ball-Screw-Driven Stage Based on Repetitive Control Using n-Times Learning Filter," IEEE Trans. Ind. Electron, vol. 61, pp. 3694–3703, 2014.

[2] Y. Li and Q. Xu, "Design and Robust Repetitive Control of a New Parallel-Kinematic XY Piezostage for Micro/Nanomanipulation," IEEE/ASME Trans. Mechatronics, vol. 17, pp. 1120–1132, 2012.

[3] C. Hu, B. Yao, Z. Chen and Q. Wang, "Adaptive Robust Repetitive Control of an Industrial Biaxial Precision Gantry for Contouring Tasks," IEEE Trans. Control Systems Technology, vol. 19, pp. 1559–1568, 2011.

[4] K.-C. Yang, and C. Hsieh, "Nanometer Positioning of a Dual-Drive Gantry Table with Precise Yaw Motion Control," J. CSME, vol. 36, no. 2, pp. 107–117, 2015.

[5] M. Tomizuka, "Zero Phase Error Tracking Algorithm for Digital Control," ASME J Dyn Syst Meas Control, vol. 109, pp. 65–68, 1987.

[6] G. Cheng, K. Peng, B.-M. Chen, and T.-H. Lee, "Improving Transient Performance in Tracking General References Using Composite Nonlinear Feedback Control and Its Application to High-Speed XY-Table Positioning Mechanism," IEEE Trans. Ind. Electron, vol. 54, pp. 1039–1051, 2007.

[7] E.C. Park, H. Lim and C.-H. Choi, "Position Control of X-Y Table at Velocity Reversal Using Presliding Friction Characteristics," IEEE Trans. Control Systems Technology, vol. 11, pp. 24–31, 2003.

[8] M. -C. Tsai, I.-F. Chiu and M. -Y. Cheng, "Design and Implementation of Command and Friction Feedforward Control for CNC Motion Controllers," IEE proceedings, Control Theory and Applications, vol. 151, Issue 1, pp. 13–20, Jan. 2004.

[9] Y. Koren, "Cross-Coupled Biaxial Computer Control for Manufacturing Systems," ASME J Dyn Syst Meas Control, vol. 102, pp. 265–272, 1980.

[10] M.-Y. Cheng and C.-C. Lee, "Motion Controller Design for Contour-Following Tasks Based on Real-Time Contour Error Estimation," IEEE Trans. Ind. Electron, vol. 54, pp. 1686–1695, 2007.

[11] K.-H. Su, and M.-Y. Cheng, "Contouring Accuracy Improvement Using Cross-Coupled Control and Position Error Compensator," International Journal of Machine Tools and Manufacture, vol. 48, pp. 1444–1453, 2008.

[12] H.-R. Chen, M.-Y. Cheng, C.-H. Wu, and K.-H. Su, "Real Time Parameter Based Contour Error Estimation Algorithms for Free Form Contour Following," International Journal of Machine Tools & Manufacture, vol. 102, pp.1–8, 2016.

[13] C.-M. Wen, and M.-Y. Cheng, "Contouring Accuracy Improvement of a Piezo-Actuated Micro Motion Stage Based on Fuzzy Cerebellar Model Articulation Controller," Control Engineering Practice, vol. 20, pp. 1195–1205, 2012.

[14] C.-Y. Chen and M.-Y. Cheng, "Velocity Field Control and Adaptive Virtual Plant Disturbance Compensation for Planar Contour Following Tasks," IET Control Theory & Applications, vol. 6, pp. 1182–1191, 2012.

[15] C.-M. Wen and M.-Y. Cheng, "Development of a Recurrent Fuzzy CMAC with Adjustable Input Space Quantization and Self-Tuning Learning Rate for Control of a Dual-Axis Piezoelectric Actuated Micromotion Stage," IEEE Trans. Ind. Electron, vol. 60, pp. 5105–5115, 2013.

[16] D.A. Bristow, M. Tharayil and A.G. Alleyne, "A Survey of Iterative Learning Control," IEEE Control Systems Magazine, vol. 26, pp. 96–114, 2006.

[17] C.-L. Chen and K.-S. Li, "Observer-Based Robust AILC for Robotic System Tracking Problem," J. CSME, vol. 30, no. 6, pp. 483–491, 2009.

[18] C.-K. Chen, C.-J. Lin, J. Hwang and C.-W. Hung, "The Iterative Learning Control of a Stewart Platform System," J. CSME, vol. 34, no. 1, pp. 21–30, 2013.

[19] K.L. Barton and A.G. Alleyne, "A Cross-Coupled Iterative Learning Control Design for Precision Motion Control," IEEE Trans. Control Systems Technology, vol. 16, pp. 1218–1231, 2008.

[20] M. Wiering and I. Martijn van Otterlo, Reinforcement Learning: State-of-the-Art. Germany: Springer-Verlag Berlin Heidelberg, 2012.

[21] R.S. Sutton and A.G. Barto, Reinforcement Learning : An Introduction. 2nd ed. London, England: in progress, 2012.

[22] D. Silver, A. Huang, C.J. Maddison, A. Guez, L. Sifre, G.V.D. Driessche, J. Schrittwieser, et al. "Mastering the Game of Go with Deep Neural Networks and Tree Search," Nature, vol. 529, pp. 484–489, 2016.

[23] M.-Y. Cheng, M.-C. Tsai and J.-C. Kuo, "Real-Time NURBS Command Generators for CNC Servo Controllers," International Journal of Machine Tools and Manufacture, vol. 42, pp. 801–813, 2002.

[24] Chun Wei, Zhe Zhang, Wei Qiao and Liyan Qu, "Reinforcement-Learning-Based Intelligent Maximum Power Point Tracking Control for Wind Energy Conversion Systems," IEEE Trans. Ind. Electron, vol. 62, no. 10, pp. 6360–6370, 2015.

[25] Sergey Levine, Peter Pastor, Alex Krizhevsky and Deirdre Quillen, "Learning Hand-Eye Coordination for Robotic Grasping with Deep Learning and Large-Scale Data Collection," unpublished.

Tool Wear and Process Cost Optimization in WEDM of AMMC using Grey Relational Analysis

B. Haritha Bai[1], G. Vijaya Kumar[2*], Anand babu. K[3]

[1]Teaching Assistant, [2]Post Doctoral Fellow, [3]Research Scholar
[1,2,3]Department of Mechanical Engineering, S. V. University, Tirupathi - 517 502, Andhra Pradesh, India

Abstract— *Wire Electrical Discharge Machining (WEDM) endorsed sensation in the production of newer materials, especially for the aerospace and medical industries. Using WEDM technology, convoluted cuts can be made through difficult-to-machine electrically conductive components with the high degree of accessible accuracy and the fine surface quality make WEDM priceless. In other hand Aluminum Metal Matrix Composites (AMMCs) are the precise materials for marine, automobile, aerospace, defense, and sports industries which are difficult to cut by conventional methods of machining. In this paper an optimal set of material and machining parameters is derived using hybrid approach called grey-fuzzy approach. For this AMMC samples are produced as per the taguchi experimental design by considering combined material and wire EDM parameters and machined using WEDM machine. The obtained responses such as kerf width, tool wear, process cost and surface roughness are optimized using grey-fuzzy approach which is obtained by combining grey relational analysis and fuzzy logic.*

Keywords— Wire EDM, AMMCs, Taguchi design, tool wear, process cost Grey-fuzzy.

I. INTRODUCTION

Aluminum Metal Matrix Composites (AMMCs) are the well-defined materials for marine, automobile, aerospace, defense, and sports industries, as they have high strength to weight ratio, and possess superior physical and mechanical properties compared to non-reinforced alloys and traditional metals. However, the presence of abrasive reinforcements in the ductile matrix causes rapid tool wear and hence tool failure. This leads to an increase in machining cost, production time and poor quality of machined components. On the other hand, some techniques such as electric discharge machining (EDM) and wire electric discharge machining (WEDM) are quite successful for machining of AMMCs. EDM has limited applications as it can be used only for drilling purpose. WEDM seems to be a better choice as it conforms to easy control and can machine intricate and complex shapes. The setting for the various process parameters required in WEDM process play crucial role in achieving optimal performance. Effective and economical WEDM of AMMCs will open new areas of applications for AMMCs.

II. LITERATURE REVIEW

Very few studies have been undertaken in WEDM of MMCs. Further, most of these studies have been done by using one-parameter-at-a-time approach, which may not explain the effects of interaction among various parameters. Some of past studies on WEDM of MMCs are follows. Sahandilya.P, Jain.P.K. & Jain.N.K [1] investigated made on consider the effect of voltage, pulse-on time, pulse-off time and wire feed rate on MRR and kerf in WEDM of SiCp/6061 AlMMC. Effect of input process parameters show that maximum value of MRR and minimum value of kerf are obtained at lower level of voltage, lower level of pulse-on time. D.Satish kumar & M. Kanthababu & V.Vajjiravelu [2] investigated WEDM of Al/SiCp MMCs in various volume fractions (5%, 10% and 15% of SiC) prepared through stir casting process considering MRR and Ra as outputs. And they concluded the microstructure of stir cast composite shows discrete localized pool/agglomeration of SiC particles indicating constrain of the process for attaining uniform microstructure. Rajesh Kumar Bhuyan, B.C.Routara, Arun Kumar Parida, A.K.Sahoo [3] investigate the effect of process parameters such as pulse on time(Ton), peak current (Ip) and flushing pressure (Fp) , metal removal rate (MRR), tool wear rate (TWR) and surface roughness (SR) during electrical discharge machining (EDM) of Al-SiC12% MMC .The experiment is followed by Central composite design (CCD) method under different combination of process parameters. K.Zakariaa, Z.Ismaila, N.Redzuana and K.W.Dalgarnob [4] investigate the effect of wire EDM cutting parameters for evaluating of Additive Manufacturing Hybrid Metal Material. Hybrid metal materials produce through Additive Manufacturing of Indirect Selective Laser Sintering. It high light those important parameters to be considered in wire cutting process of FeCuSn hybrid metal material produce by Additive Manufacturing of

Indirect Selective Laser Sintering process for fabricating the near net shape metal component. Ravindranadh Bobbili, V.Madhu, A.K.Gogia [5] investigates wire-EDM process parameters of ballistic grade aluminium alloy. Experimentation has been planned as per Taguchi technique. Three performance characteristics namely material removal rate (MRR), surface roughness (SR) and gap current (GC) have been chosen for this study. Yonghua Zhao,Masanori Kunieda, Kohzoh Abe [6] were experimentally investigated the performance of EDM slicing of SiC wafers, the fundamental characteristics of EDM of SiC single crystal. Ibrahem Maher, Liew Hui Ling, Ahmed A, D.Sarha, M. Hamdi [7] experimentally investigated the WEDM for improving process parameters. They concluded that the peak current and pulse on time are the most significant parameters affecting the cutting speed, surface roughness and heat affected zone. The wire tension has minor effect on the cutting speed and heat affected zone but it has great effect on the surface roughness. Cheol-SooLee, Eun-YoungHeo, Jong-MinKim, In-HughChoi, Dong-WonKim [8] investigated this paper presents an effective model to estimate the electrode wear of EDM. The wear amount depends on discharging environment such as material type and hole shapes. The electrode wear makes it difficult to control precise electrode feeding. Therefore, this study proposes an electrode wear estimation model. V. Chengal Reddy, N. Deepthi, N.Jayakrishna [9] studied the effect of various process parameters such as pulse on time, pulse off time, wire tension, current, upper flush and lower flush for Aluminium HE30. Vukcevic and Delijic, [10] were observed an increased interest on metal matrix composite, mostly light metal based, which have found their applications in many industry branches, among others in the aircraft industry, automotive, and armaments ones, as well as in electrical engineering and electronics, etc. M. Rosso, [11] studied applications of the metal matrix and ceramic matrix composites and their process technologies. M. Dyzia, J. OEleziona, [12] have developed and studied the mechanical properties of Aluminium matrix composites reinforced with AlN particles formed in stir casting. G. Rajyalakshmi, Dr. P. Venkata Ramaiah [13] Factors like pulse on time, pulse off time, corner servo voltage, wire feed rate, wire tension, servo feed, spark gap voltage and dielectric flow rate have been found to play a significant role in rough cutting operations for maximizations of MRR, minimization of surface roughness and minimization of spark gap in WEDM. Dewan Muhammad Nuruzzaman [14] investigated aluminium-aluminium oxide MMCs of different percentages of aluminium oxide. It is observed that density of the composite specimen increases with increase in aluminium oxide volume fraction and the density of the composites are higher for 20 ton compaction load than density obtained for 10 compaction load. H. K. Shivanand, Mahagundappa M. Benal, S. C. Sharma, N. Govindraju,[15] compared Powder Metallurgy method and stir casting method for producing the AMMC through testing of mechanical properties and conclude that stir casting method is best suitable for preparation of AMMC. Mr. Anand and S. Shivade [16] attempt was made to review the different multi-optimization method used in WEDM for optimization of process parameters such as MRR, Surface roughness, kerf width, machining time, dimensional deviation. Both the performance parameters, MRR and surface roughness are optimized in one optimal input setting using Grey relational analysis method. According to the literature survey it observed that very little work has been reported on WEDM of MMCs. Past studied not clearly concluded the list of input parameters and responses. So, there is much more scope to see effects of input parameters on outputs. Kerf width, tool wear response is not focused more. Surface roughness is mostly used which essential to measure because it states the quality of machining. Compared six and seventh series of aluminium alloys. seventh series is not used more and fifth series of aluminium alloys are also less. Coming to reinforcement materials silicon carbide is mostly used and fly ash and aluminium oxide is not used more. So this research is focused on WEDM of AMMCs which are reinforced with fly ash, aluminium oxide and silicon carbide by considering kerf width, surface roughness, tool wear and process cost as machining responses and one in each series of fifth, sixth and seventh series of aluminium alloys as base material.

III. DESIGN OF EXPERIMENTS AND PREPARATION OF ALUMINIUM METAL MATRIX COMPOSITES

In the present work nine AMMC samples are produced using stir casting furnace as per Taguchi L27 experimental design (Table. 2) which is obtained by considering material and WEDM parameters (Table 1). To produce AMMCs, First the stir casting furnace with graphite crucible is switched on and allow it to raise the temperature up to 500^{O}C then the required amount of base material is poured into the crucible and the temperature is raised up to 850^{O}C and allow it to maintain the same up to complete melting of base material. At 675^{O}C, the wetting agent Mg of 1% is added to the base material. Then the reinforcement particles are added slowly to the molten base material while the stirrer rotating. Before adding the reinforcement particles they are heated for 2 hrs upto 1000^{O}C to oxidise their surfaces. After mixing, the temperature of the slurry is raised upto 850^{O}C for getting improved fluidity and stirring is continued upto 5 minuits. Then the mixed slurry was poured in different preheated steel dies to produce the samples.

TABLE 1
INFLUENTIAL PARAMETERS AND THEIR LEVELS

S. No.	Influential parameters	Level 1	Level 2	Level 3
Material Parameters				
1	Base material (BM)	Al5052	Al6082	Al7075
2	Type of reinforcement material (RM)	SiC	Al_2O_3	Flyash
3	Percentage of reinforcement particle (PRFM)	2.5	5	10
WEDM Parameters				
4	Pulse on time(Ton)	108	110	112
5	Pulse off time (Toff)	56	58	60
6	Water pressure(wp)	3	7	10
7	Wire feed (Wf)	1	2	3
8	Servo feed (SF)	1030	1050	1070

TABLE.2
TAGUCHI DESIGN OF EXPERIMENTS

Exp. Run No	AMMC Sample No.	Material parameters			WEDM parameters				
		BM	RFM	PRFM	Ton	Toff	Wf	Wp	SF
1	1	5052	FA	2.5	108	56	1	3	1030
2		5052	FA	2.5	108	58	2	7	1050
3		5052	FA	2.5	108	60	3	10	1070
4	2	5052	SIC	5	110	56	1	3	1050
5		5052	SIC	5	110	58	2	7	1070
6		5052	SIC	5	110	60	3	10	1030
7	3	5052	Al2O3	10	112	56	1	3	1070
8		5052	Al2O3	10	112	58	2	7	1030
9		5052	Al2O3	10	112	60	3	10	1050
10	4	6082	FA	5	112	56	2	10	1030
11		6082	FA	5	112	58	3	3	1050
12		6082	FA	5	112	60	1	7	1070
13	5	6082	SIC	10	108	56	2	10	1050
14		6082	SIC	10	108	58	3	3	1070
15		6082	SIC	10	108	60	1	7	1030
16	6	6082	Al2O3	2.5	110	56	2	10	1070
17		6082	Al2O3	2.5	110	58	3	3	1030
18		6082	Al2O3	2.5	110	60	1	7	1050
19	7	7075	FA	10	110	56	3	7	1030
20		7075	FA	10	110	58	1	10	1050
21		7075	FA	10	110	60	2	3	1070
22	8	7075	SIC	2.5	112	56	3	7	1050
23		7075	SIC	2.5	112	58	1	10	1070
24		7075	SIC	2.5	112	60	2	3	1030
25	9	7075	Al2O3	5	108	56	3	7	1070
26		7075	Al2O3	5	108	58	1	10	1030
27		7075	Al2O3	5	108	60	2	3	1050

IV. EXPERIMENTATION

The experiments were conducted at ultra cut WEDM Machine (supplied by Vellore Wire Cut. Pvt. ltd) as per the taguchi design of experiments and the experimental data is recorded in the Table 3. For these experiments, brass wire is used as electrode and water as dielectric fluid.

V. IDENTIFICATION OF OPTIMUM PARAMETERS COMBINATION

Step 1: Pre-processing of Experimental Data

Data pre-processing is required where the range and unit in one data sequence may differ from the others. In data pre-processing, the original sequence is transformed to a comparable sequence. Depending on the quality characteristic of a data sequence, there are various methodologies of data pre-processing are available.

For quality characteristic of the "larger – the - better", the original sequence can be normalized as

$$x^*_i(k) = \frac{x^o_i(k) - \min x^o_i(k)}{\max x^o_i(k) - \min x^o_i(k)} \quad (1)$$

For quality characteristic of the "smaller – the - better" the original sequence, can be normalized as

$$x^*_i(k) = \frac{\max x^o_i(k) - x^o_i(k)}{\max x^o_i(k) - \min x^o_i(k)} \quad (2)$$

Where $i = 1\ldots, m;\ k = 1\ldots, n$. m is the number of experimental data items and n is the number of parameters. $x^o_i(k)$ Denotes the original sequence, $x^*_i(k)$ the sequence after the data pre-processing, max $x^o_i(k)$ the largest value of $x^o_i(k)$, min $x^o_i(k)$ the smallest value of $x^o_i(k)$, and x^o is the desired value. For the experimental values of, tool wear and process cost, smaller-the-better is applicable. Hence, its experimental values are normalized using Eqs1&2 as shown in Table 3.

TABLE 3
EXPERIMENTAL RESULT AND NORMALIZED VALUES OF EXPERIMENTAL RESULTS

Exp. No	Experimental results		Normalized values of experimental Results	
	Tool wear	Process Cost	Tool wear	Process cost
1	0.018	633.76	0.3043	0.6652
2	0.01	519.94	0.6521	0.7828
3	0.014	533.65	0.4782	0.748
4	0.018	477.10	0.3043	0.8271
5	0.025	395.013	0	0.9119
6	0.018	569.51	0.3043	0.7316
7	0.015	698.01	0.4347	0.5988
8	0.011	705.15	0.6086	0.5915
9	0.018	1277.726	0.3043	0
10	0.013	567.53	0.5217	0.7336
11	0.009	394.61	0.6956	0.9123
12	0.012	346.43	0.5652	0.962
13	0.019	781.30	0.2608	0.5128
14	0.013	822.94	0.5217	0.4698
15	0.013	987.93	0.5217	0.2993
16	0.015	408.89	0.4347	0.8975
17	0.016	658.75	0.3913	0.6394
18	0.009	510.02	0.6956	0.7937
19	0.019	569.12	0.2608	0.732
20	0.014	394.61	0.4782	0.9123
21	0.016	414.84	0.3913	0.8194
22	0.014	352.18	0.4782	0.9561
23	0.002	309.74	1	1
24	0.014	568.32	0.4782	0.7328
25	0.013	470.60	0.5217	0.8338
26	0.012	600.17	0.5652	0.9996
27	0.015	561.82	0.4347	0.7394

TABLE 4
GREY RELATIONAL COEFFICIENTS AND GREY RELATIONAL GRADE

S.No	Grey Relational Coefficients		Grey Relational Grade
	Tool wear	Cost	
1	0.6216	0.429	0.5253
2	0.4399	0.389	0.41445
3	0.5111	0.4	0.45555
4	0.6216	0.376	0.4988
5	1	0.3541	0.67705
6	0.621	0.4059	0.51345
7	0.534	0.455	0.4945
8	0.451	0.458	0.4545
9	0.6216	1	0.8108
10	0.4893	0.405	0.44715
11	0.4182	0.354	0.3861
12	0.4693	0.3419	0.4056
13	0.6572	0.4936	0.5754
14	0.4893	0.5155	0.5024
15	0.4893	0.6255	0.5574
16	0.5349	0.3585	0.4467
17	0.5609	0.4388	0.49985
18	0.4182	0.3864	0.4023
19	0.6572	0.4058	0.5315
20	0.511	0.354	0.4325
21	0.5609	0.3789	0.4699
22	0.5111	0.3433	0.4272
23	0.333	0.33	0.3315
24	0.5111	0.4055	0.4583
25	0.4893	0.3748	0.43205
26	0.4693	0.4167	0.443
27	0.5349	0.4033	0.4691

Step II: Determine the grey relational coefficient

After data pre-processing, the grey relation coefficient $\xi_i(k)$ for the k^{th} performance characteristics in the i^{th} experiment can be determined using the Eq.3

$$\xi_i(k) = \frac{\Delta_{\min} + \zeta \Delta_{\max}}{\Delta_{oi}(k) + \zeta \Delta_{\max}} \quad (3)$$

Where, Δ_{oi} is the deviation sequence of the reference sequence and the comparability sequence?

$$\Delta_{oi} = \| x^*_o(k) - x^*_i(k) \|$$

$$\Delta_{\min} = \min_{\forall j \in i} \min_{\forall k} \| x^*_o(k) - x^*_j(k) \|$$

$$\Delta_{\max} = \max_{\forall j \in i} \max_{\forall k} \| x^*_o(k) - x^*_j(k) \|$$

$x^*_o(k)$ denotes the reference sequence and $x^*_i(k)$ denotes the comparability sequence. ζ is distinguishing or identification coefficient and its value is between '0' and '1'. The value may be adjusted based on the actual system requirements. A value of ζ *is* the smaller and the distinguished ability is the larger. $\zeta = 0.5$ is generally used. The Grey Relational coefficients of tool wear and process cost are shown in the Table.4.

Step III: Determination of Grey relational grade

The grey relational grade is defined as

$$\gamma_i = \frac{1}{n} \sum_{k=1}^{n} \xi_i(k) \quad (4)$$

The grey relational grade γ_i represents the level of correlation between the reference sequence and the comparability sequence. If the two sequences are identical, then the value of grey relational grade is equal to 1. The grey relational grade values are calculated for each factor at each level and the optimal level for each factor is identified based on their individual grey relational grade values. The optimal level of any influential factor has highest grey relational grade (GRG) value among their considered levels. Grey relational Grade is shown in the Table 4.

TABLE 5
GRG FOR EACH LEVEL OF INFLUENTIAL FACTORS

GRG for each level of influential factors								
Level	**BM**	**RM**	**PRFM**	**TON**	**TOFF**	**WP**	**WF**	**SF**
1	0.538267	0.452006	0.440128	0.486072	0.486511	0.454544	0.478250	0.492272
2	0.469211	0.504611	0.474700	0.496894	0.460150	0.490283	0.478006	0.490739
3	0.443894	0.494756	0.536544	0.468406	0.504711	0.506544	0.495117	0.468361
Delta	0.094372	0.052606	0.096417	0.028489	0.044561	0.052000	0.017111	0.023911
Rank	2	3	1	6	5	4	8	7

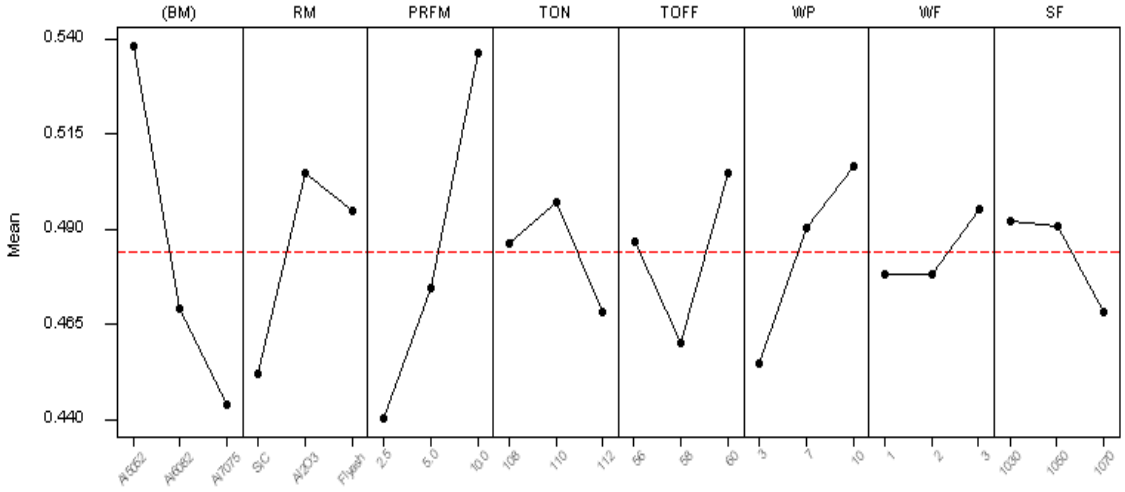

FIG 1: GRG FOR EACH LEVEL OF INFLUENTIAL FACTORS

Step V Obtaining optimal combination of influential factors

After determining the GRG, the effect of each parameter is separated based on GRG at different levels. The mean values of GRG for each level of the influential factors and the effect of influential factors on multi responses in rank wise are summarized in Table 6 Basically, larger GRG means it is close to the product quality. Thus, a higher value of the GRG is desirable. From the Table 6 and fig 1, the optimal combination of influential factors is BM1RM2PRM3TON2TOFF3WP3WF3SF1. This means Base material at level 1 ie; 5052, Reinforcement material at level 2 ie; AL2O3 Percentage of Reinforcement material at level 3 ie; 10, TONat level 2 ie; 112, TOFF at level 3 ie; 60, WP at level 3 ie; 10, WF at level 3 ie; 3, SF at level 1 ie; 1050.

VI. CONFORMATION TEST

For the obtained optimal combination, confirmation test has been conducted and compared the results with initial set of parameters. These results are satisfactory as the responses for optimal combination shows better performance.

TABLE 6
COMPARISON OF RESPONSES BETWEEN AMMC WITH INITIAL COMBINATION AND OPTIMAL COMBINATION

Combination	Combination of Controllable Parameters	Tool wear	Process cost	GRG
Initial set		0.018	476	0.5812
Optimal set	BM1RM2PRM3TON2TOFF3WF2WP3SF1	0.008	350	0.7902
Gain	N/A	0.01	126	0.2090
% of Gain	N/A	55.55	26.47	35.96

VII. CONCLUSIONS

After analyzing the data of obtained influential factors combination, it is concluded that PRFM, BM and RM are the most significant parameters which influence th multi responses WP and TOFF are the medium influenced parameters on multi responses TON, SF and WF are influenced lastly the multi responses. Also grey relational grade of the optimal combination is increased about 35.96%

REFERENCES

[1] **Shandilya. P, Jain. P. K, Jain. N. K "**Wire electric discharge of metal matrix composite**".** Damm International scientific book, 2011. pp. 383-400.

[2] **D. Satishkumar, M. Kanthababu, V. Vajjiravelu** "Investigation of wire electrical discharge machining characteristics of Al6063/SiCp composites." International Journal of advanced manufacturing technology." October 2011. 56:975–986.

[3] **3.Rajesh Kumar Bhuyan, B.C.Routara, Arun Kumar Parida, A.K.Sahoo** "Parametric optimization of Al-SiC12% metal matrix composite machining by EDM." 5th International & 26th All India Manufacturing Technology, Design and Research Conference (AIMTDR 2014) December 12th–14th, 2014.

[4] **K. Zakaria, Z. Ismaila , N.Redzuana and K.W. Dalgarnob** "Effect of wire EDM cutting parameters for evaluating of Additive Manufacturing Hybrid Metal Material." 2nd International Materials, Industrial, and Manufacturing Engineering Conference, MIMEC2015, 4-6 February 2015, Bali Indonesia 532 – 537.

[5] **Ravindranadh Bobbili, V. Madhu, A.K. Gogia** "Multi response optimization of wire-EDM process parameters of ballistic grade aluminium alloy." Engineering Science and Technology, an International Journal 18 (2015) 720e726.

[6] **Yonghua Zhaoa, Masanori Kuniedaa, Kohzoh Abeba** "Study of EDM cutting of single crystal silicon carbide." Science Direct Precision Engineering 38 (2014) 92– 99.

[7] **Ibrahem Maher, liew Hui Ling** "Improve WEDM performance at different machining parameters." IFAC(2015) 105-110.

[8] **Cheol-Soo Lee, Eun-YoungHeo, Jong-MinKim, In-HughChoi,Dong-WonKim** "Electrode wear estimation model for EDM drilling." Robotics and Computer-Integrated Manufacturing 36(2015)70–75.

[9] **V. Chengal Reddya, N. Deepthib, N.Jayakrishna** "Multiple Response Optimization of Wire EDM on Aluminium HE30 by using Grey Relational Analysis." Materials Today: Proceedings 2 (2015) 2548 – 2554.

[10] **Vukcevic, M. and Delijic, K. "**Some New Directions in Aluminum Based PM Materials for Automotive Applications" Materials in Technological, 2002 36, pp101-105.

[11] **M. Rosso** "Ceramic and metal matrix composites: Routes and properties" Journal of Materials Processing Technology 175 (2006) 364–375.

[12] **M. Dyzia, J. OEleziona** "Aluminium matrix composites reinforced with AlN particles formed by in situ reaction" Archives of Materials Science and Engineering Volume 31, Issue 1, May 2008, Pages 17-20.

[13] **G. Rajyalakshmi** "Simulation, Modelling and Optimization of Process parameters of Wire EDM using Taguchi –Grey Relational Analysis." ISSN: 2278-7844 2012 IJAIR.

[14] **Dewan Muhammad Nuruzzaman** "Fabrication and Mechanical Properties of Aluminium-Aluminium Oxide Metal Matrix." International Journal of Mechanical & Mechatronics Engineering IJMME-IJENS Vol:15 No:06.

[15] **Mr. Anand and S. Shivade1** "A review on advanced multi-optimization methods for WEDM." International Journal of Scientific Research Engineering & Technology (IJSRET) Volume 2 Issue 7 pp 435-439 October 2013.

The Effect of welding method and heat treatment on creep resistance of Inconel 718 sheet welds

Zenon A. Opiekun[1], Agnieszka Jędrusik[2]

Rzeszów University of Technology, Department of Foundry and Welding, Al. Powstańców Warszawy, Poland

Abstract— *The paper presents results of a study on the effect of welding technique and heat treatment on structure and creep resistance of welded joints made on thin (0.5–1.2 mm) Inconel 718 sheet with the use of GTAW and laser method without filler metal. Technological high-temperature creep tests consisted in measuring the time to rupture for sheet metal without and with welded joints under constant stress σ = 150 MPa and at constant temperature t_c = (860 ± 2)°C.*

Sheet metal joints made with the use of GTAW method and laser-welded are characterized with a three-zone macrostructure, including the weld with size of dendritic grains depending on welding method, the heat-affected zone (HAZ), and the base material (BM). For GTAW method, with increasing sheet metal thickness, the observed values of parameter λ_{2s} (distance between axes of second-order branches of dendritic grains) decrease from about 12 µm to 8 µm, and similarly, in case of laser welding, λ_{2s} values decrease from about 9.6 µm to 5 µm with increasing sheet metal thickness.

Thin sheet Inconel 718 in as-delivered condition high-temperature creep-tested have the time to rupture on the level of 12 h at elongation of about 48%. Similar time-to-rupture values characterize the joints made by laser welding. GTAW joints are characterized by about 30% shorter time to rupture and elongation less by about 45%.

The microstructure change induced by heat treatment (solution treatment and two-stage ageing) resulted in significant increase of creep resistance properties of both base metal and laser-welded joints. The time to rupture of heat-treated specimens of thin Inconel 718 sheet and laser-welded joints creep-tested at 860°C ± 2°C under stress of 150 MPa was about 19.5 h with elongation ranging from 23% to 33%.

Keywords— Inconel 718, GTAW, laser welding, heat treatment, microstructure, high-temperature creep.

I. INTRODUCTION

Inconel 718, a nickel-based alloy, belongs to a large group of heat-resisting and creep-resisting metallic materials used to manufacture a variety of welded structures, especially in aircraft industry where they are used for exhaust components in PW400 and CF6 jet engines [1–4]. The alloy shows good weldability and can be heat-treated by precipitate strengthening [5–9]. Components made of thin Inconel 718 sheet can work at high temperatures which in case of combustion chambers can reach 1300°C [2, 8].

In operating conditions, welded structures with components made of the alloy are subject to both high temperatures and large stresses. In view of the above, creep-resisting properties of welded joints in such structures are of great importance.

The sources of concentrated heat streams used to weld Inconel 718 sheet include: electric arc in GTAW welding method [10–12] and a beam of monochromatic light in case of laser welding.

The paper concerns the effect of the two welding methods used for welding thin Inconel 718 sheet [13, 14] and heat treatment on structure and the time to rupture of obtained joints measured in high-temperature creep test.

II. MATERIAL AND METHODOLOGY

The material used in the study was thin Inconel 718 alloy sheet with thickness 0.5 mm, 0.9 mm, and 1.2 mm. Chemistry of each material type was determined with the use of emission spectrometer Q4 TASMAN (Bruker). Table 1 summarizes average chemical composition of the examined sheet metal samples.

TABLE 1
CHEMISTRY OF 0.5-mm, 0.9-mm, AND 1.2-mm THICK INCONEL 718 SHEET SPECIMENS USED IN THE STUDY (AVERAGE FROM 5 MEASUREMENTS FOR EACH SHEET THICKNESS).

Sheet thickness (mm)	Alloy components (% wt.)										
	Cr	Fe	Nb	Mo	Ti	Al	Si	C	B	N	Ni
0.5	17.30	16.20	5.20	2.45	1.0	0.55	0.16	0.050	0.022	0.040	balance
0.9	17.20	16.30	5.25	2.50	1.20	0.57	0.17	0.061	0.021	0.038	balance
1.2	17.28	16.15	5.30	2.38	1.18	0.54	0.14	0.059	0.023	0.041	balance

For the purpose of the study, sheet alloy specimens were prepared with joints arc-welded by means of GTAW methods and with joints obtained with the use of monochromatic light beam generated by TruLaser Robot 5020 (TRUMPF). Heat treatment of thin sheet metal specimens with welded joins was carried out in Nabertherm N 61/H electric chamber furnace according to schematic diagram shown in Fig. 1.

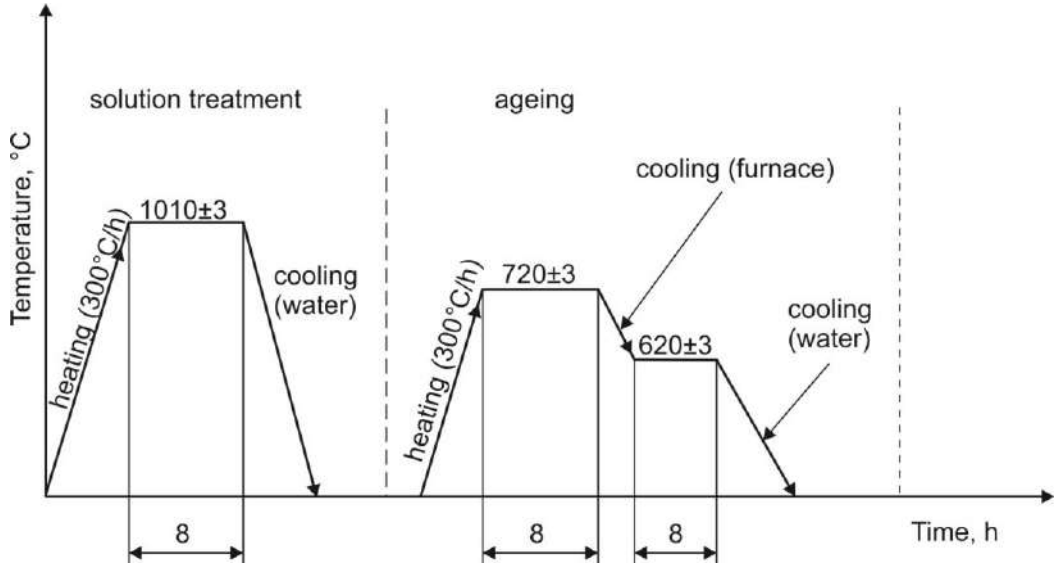

FIG. 1 — SCHEMATIC DIAGRAM REPRESENTING THE COURSE OF HEAT TREATMENT APPLIED TO THIN INCONEL 718 SHEET WITH GTAW AND LASER JOINTS.

The sheet metal was arc-welded in argon atmosphere according to GTAW method or laser-welded. Based on results of visual inspection, the best welds were identified and corresponding parameters of welding were adopted in further analysis. The best GTAW joints were obtained when welding parameters were I = 20 A/80 ms, 30 A/80 ms, and 40 A/80 ms for 0.5-mm, 0.9-mm, and 1.2-mm thick sheet metal, respectively. The welding rate V_{GTAW} = 200 mm/min was the same for all sheet grades, with arc length τ_A = 3 mm; diameter of non-consumable electrode (W + 2%Y_2O_3) sharpened at angle 45° was Ø = 2.4 mm, and consumption of argon with purity 99.95% Ar was 8 L/min.

Similarly, the following parameters were adopted for further studies concerning laser welding of thin Inconel 718 sheet: welding rate V_L = 300 mm/min; focal length f_l = 340 mm; laser power P = 690 W, 780 W, and 990 W for 0.5-mm, 0.9-mm, and 1.2-mm thick sheet metal, respectively.

Examination of creep resistance of welded joints in thin Inconel 718 sheet consisted in determining their time to rupture in the course of technological high-temperature creep tests under conditions of constant stress σ = 150 MPa and constant temperature t_c = (860 ± 2)°C [15]. For the purpose of this study, specimens (Fig. 2) with Ø8 mm holes in the holder portion were prepared. The specimens were fixed in holders by means of Ø8 mm mandrels (Fig. 3). Holders and mandrels were made of creep-resisting cobalt-based alloy MAR-M509 [16].

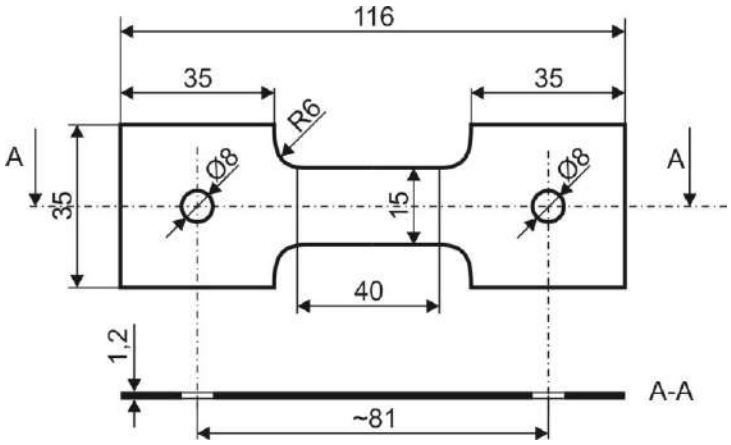

FIG. 2 — AN EXAMPLE SPECIMEN USED FOR HIGH-TEMPERATURE CREEP RESISTANCE TESTS.

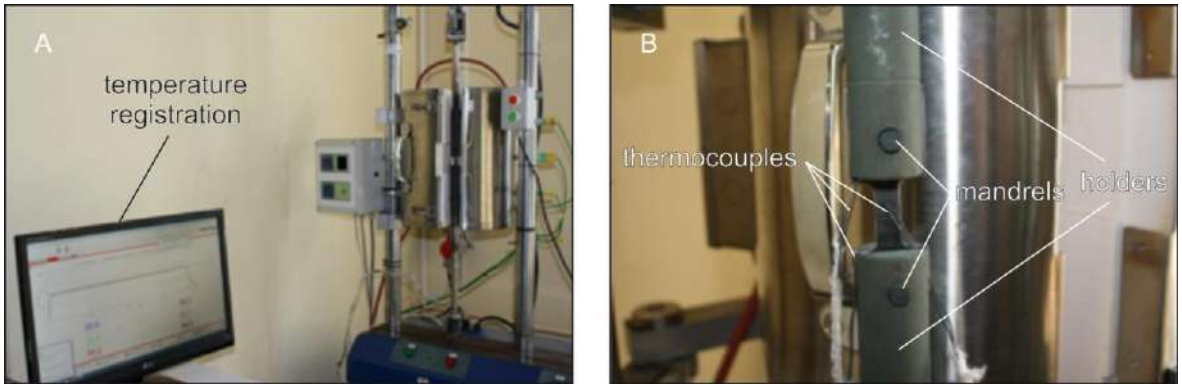

FIG. 3 — WPM ZST 3/3 CREEP TESTING MACHINE. A — A VIEW OF OPEN FURNACE WITH SPECIMEN MOUNTED IN HOLDERS BY MEANS OF MANDRELS; B — THE INSTALLED THERMOCOUPLES.

The creep tests were carried out as per standard [17] on WPM ZST3/3 (VEB Werkstoffprüfmaschinen Leipzig) creep testing machine equipped with three-zone LAB TEMP (Thermocraft Incorporated, USA) heating furnace operating at maximum temperature of 1200°C. 3 specimens were prepared and tested for each of the welding methods and each sheet metal thickness, for material both without and after heat treatment.

Fig. 3 shows a view of the creep testing machine with mounted specimen and three thermocouples attached along its length.

2.1 Preparation of metallographic sections for structural examination

Metallographic inspection (examination of microstructure and macrostructure) of welded joints made on 0.5-mm, 0,9-mm, and 1.2-mm thick sheet was carried out on metallographic sections prepared before and after heat treatment. The sections were obtained by means of mechanical polishing of transverse sections of the joints and etching with Kalling's reagent. Images were taken by means of Neophot 2 metallographic optical microscope equipped with advanced image acquisition and analysis system Multiscan V.08 and scanning electron microscope (SEM) VEGA 3 (Tescan) coupled with X-ray microanalysis adapter INCA x-art (Oxford).

III. RESULTS

3.1 Metallographic examination

Metallographic examination included observations of macrostructure and microstructure of welded joints made on thin Inconel 718 sheet specimens in as-delivered condition (not treated thermally) and after heat treatment. Revealing the macrostructure of joints was necessary to asses its shape, adjust the technological processes of GTAW and laser welding, and check the welds for possible presence of hot cracks.

3.2 Macrostructure of welded joints on sheet metal in as-delivered condition and after heat treatment

Examples of macrostructure observed in welded joints on thin Inconel 718 sheet in as-delivered condition made with the use of electric arc and laser are presented in Figs. 4–6, while Fig. 7 shows the microstructure after heat treatment.

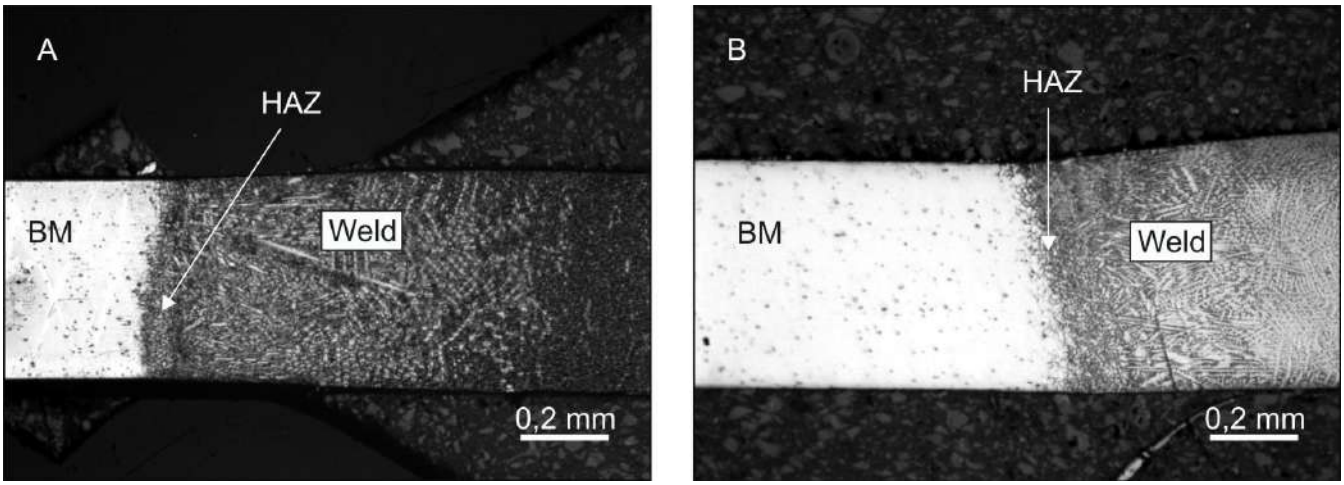

FIG. 4 — MACROSTRUCTURE OF A JOINT ON 0.5-mm THICK SHEET METAL MADE WITH: A —ELECTRIC ARC; B — LASER. VISIBLE ARE: THE WELD, HEAT-AFFECTED ZONE (HAZ), BASE MATERIAL (BM).

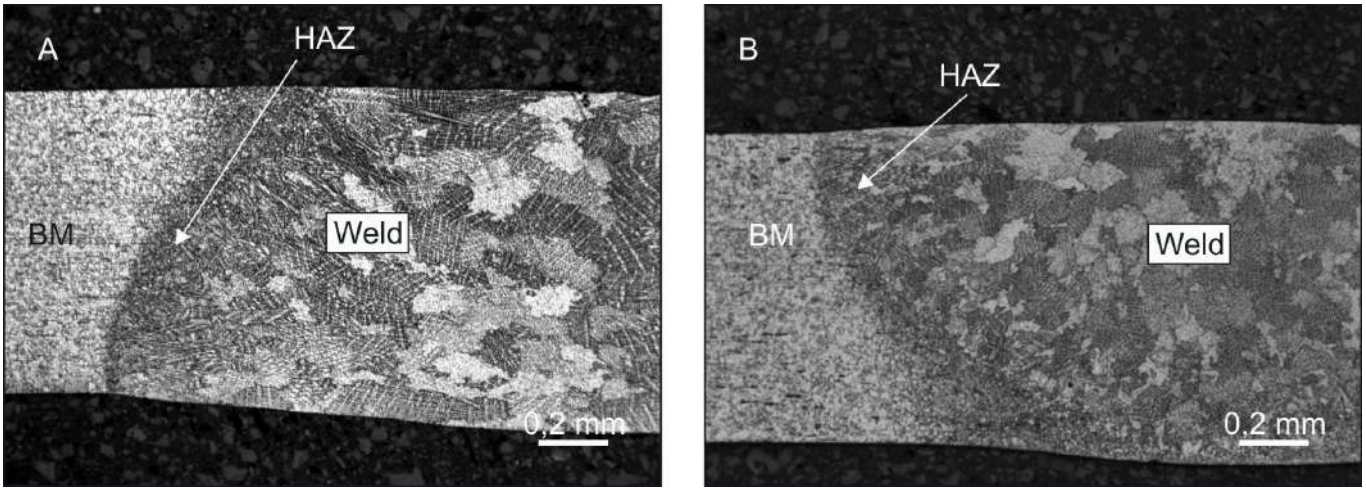

FIG. 5 — MACROSTRUCTURE OF A JOINT ON 0.9-mm THICK SHEET METAL MADE WITH: A — ELECTRIC ARC; B — LASER. VISIBLE ARE: THE WELD, HEAT-AFFECTED ZONE (HAZ), BASE MATERIAL (BM).

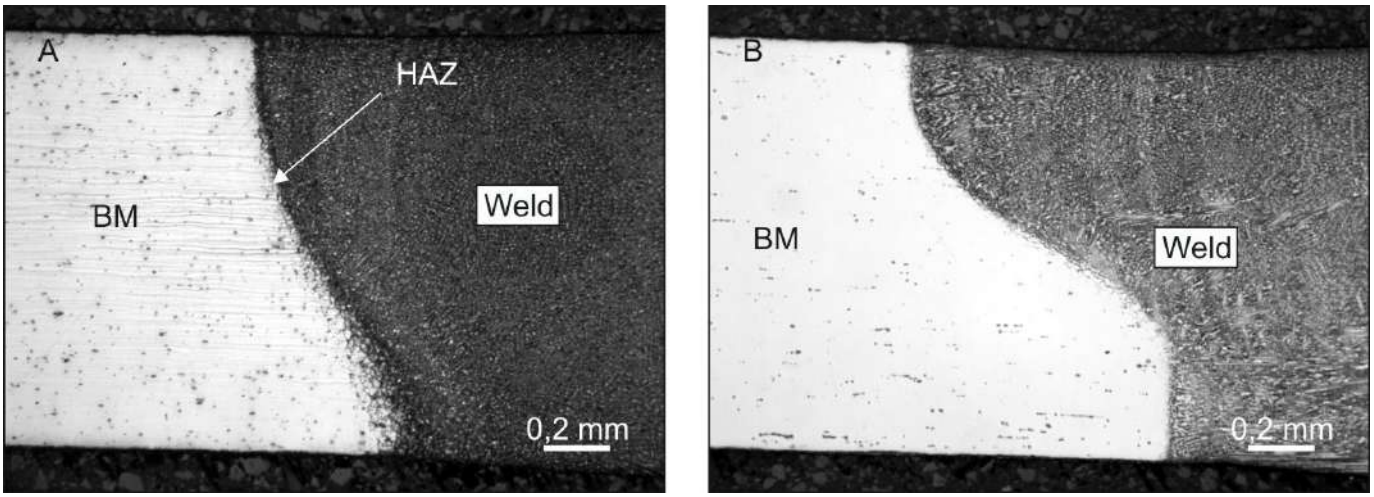

FIG. 6 — MACROSTRUCTURE OF A JOINT OF 1.2-mm THICK SHEET METAL MADE WITH: A — ELECTRIC ARC; B — LASER. VISIBLE ARE: THE WELD, HEAT-AFFECTED ZONE (HAZ), BASE MATERIAL (BM).

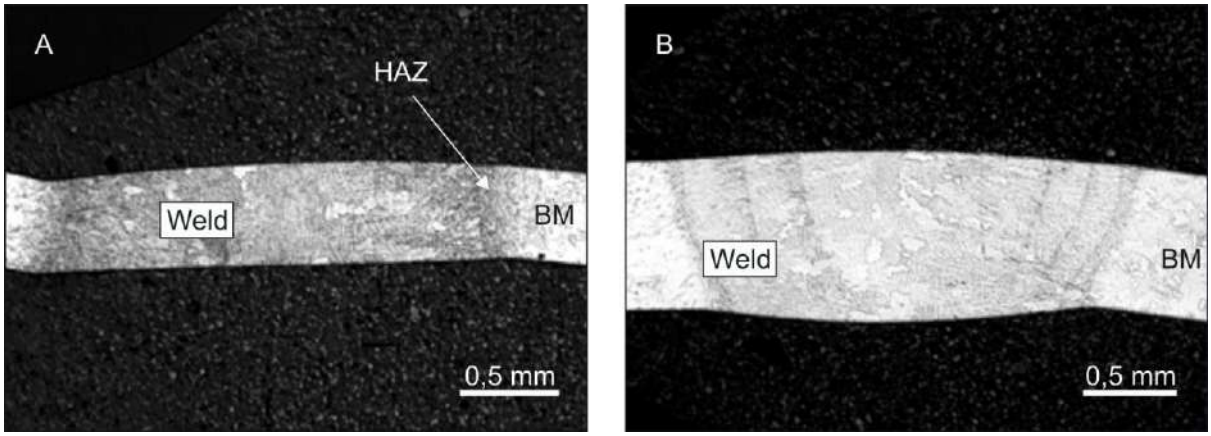

FIG. 7 — MACROSTRUCTURE OF A LASER-WELDED JOINT OF: A — 0.5-mm; B — 0.9-mm THICK SHEET METAL AFTER HEAT TREATMENT. VISIBLE ARE: THE WELD, HEAT-AFFECTED ZONE (HAZ), BASE MATERIAL (BM).

In thin sheet metal joints obtained with the use of different sources of concentrated heat streams, i.e. electric arc and laser light beam, one can distinguish between three characteristic structures: the weld, the heat-affected zones (HAZs), and the base material (BM).

Grains in welded joints have different morphology (shape and size) depending on welding method and parameters. Also the heat-affected zones of welded joints have different widths and grain sizes depending on the used welding methods and welding parameters such as current intensity, laser power, and welding rate.

3.3 Microstructure of welded joints on sheet metal in as-delivered condition and after heat treatment

Example result of microstructure examination of welded joints made on thin Inconel 718 sheet are presented in Figs. 8–11 for the material in as-delivered condition and in Fig. 12 for heat-treated specimens.

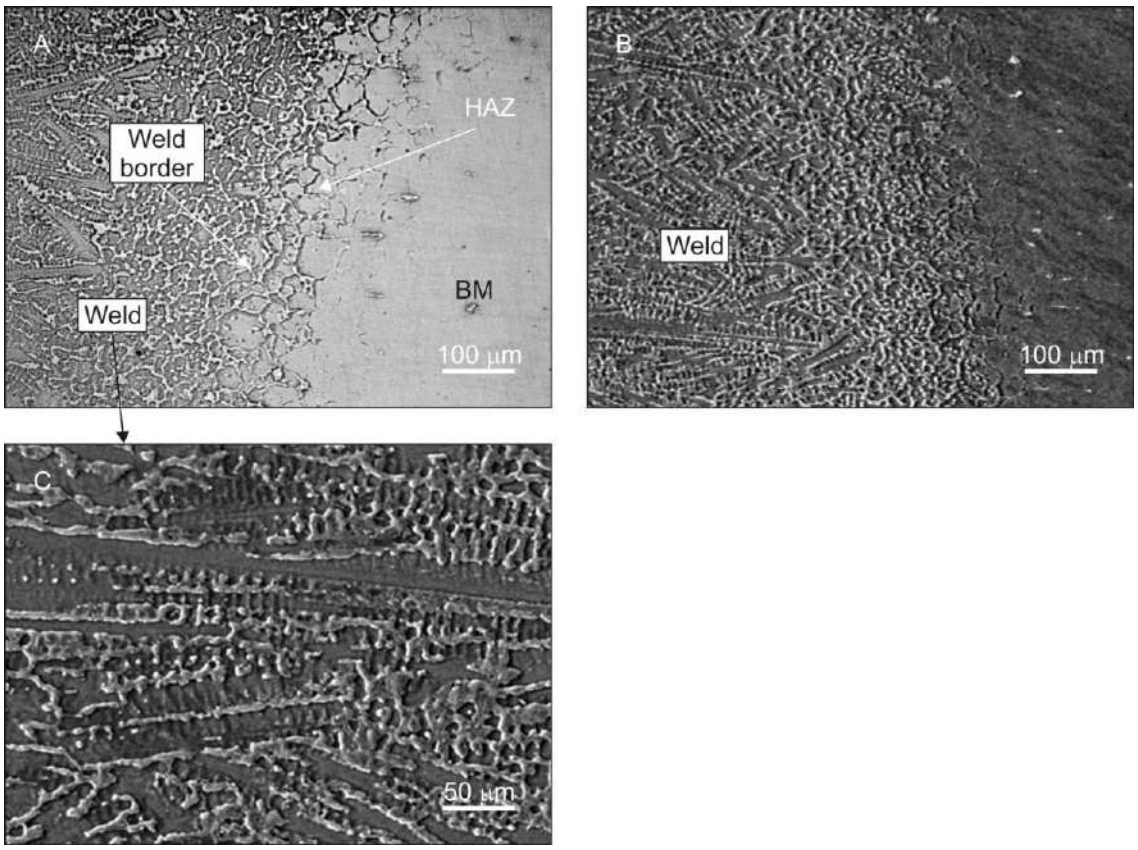

FIG. 8 — MICROSTRUCTURE OF AN ARC-WELDED JOINT OF 0.5-mm THICK SHEET METAL. A — OPTICAL MICROSCOPE; B, C — SEM.

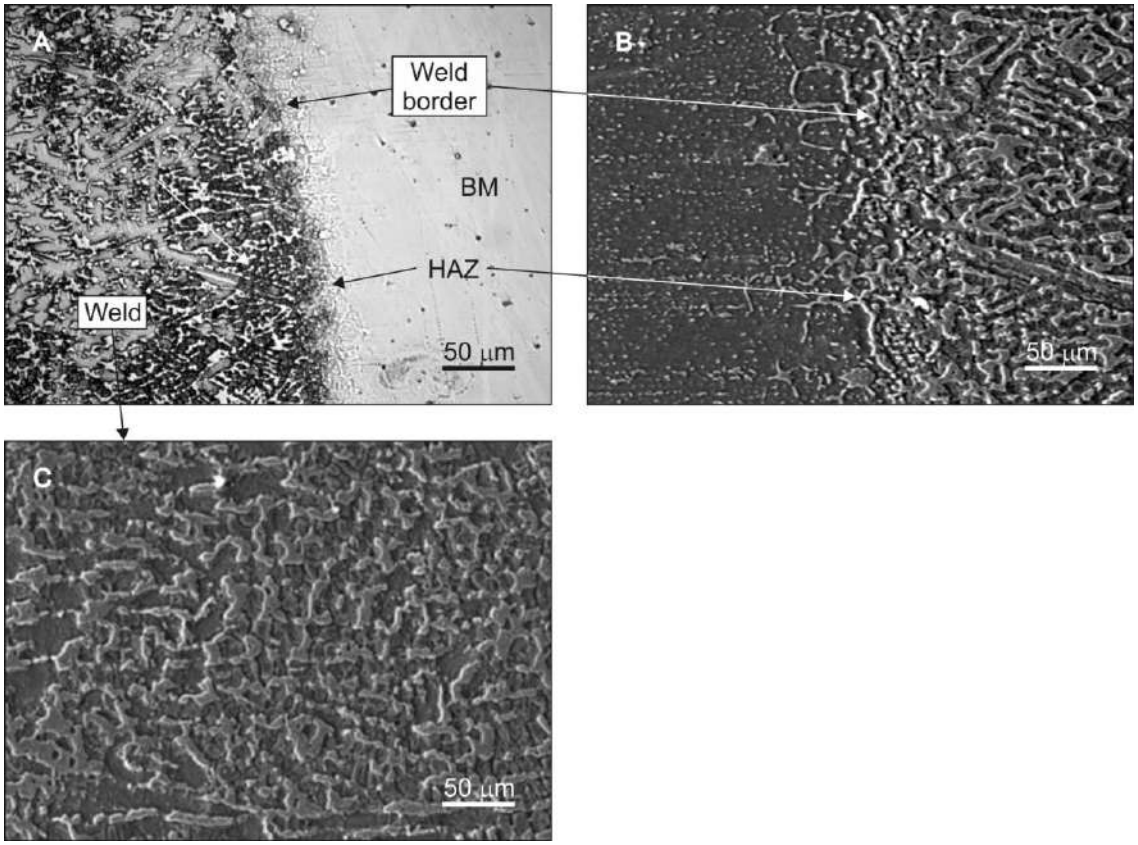

FIG. 9 — MICROSTRUCTURE OF A LASER-WELDED JOINT OF 0.5-mm THICK SHEET METAL. A — OPTICAL MICROSCOPE; B, C — SEM.

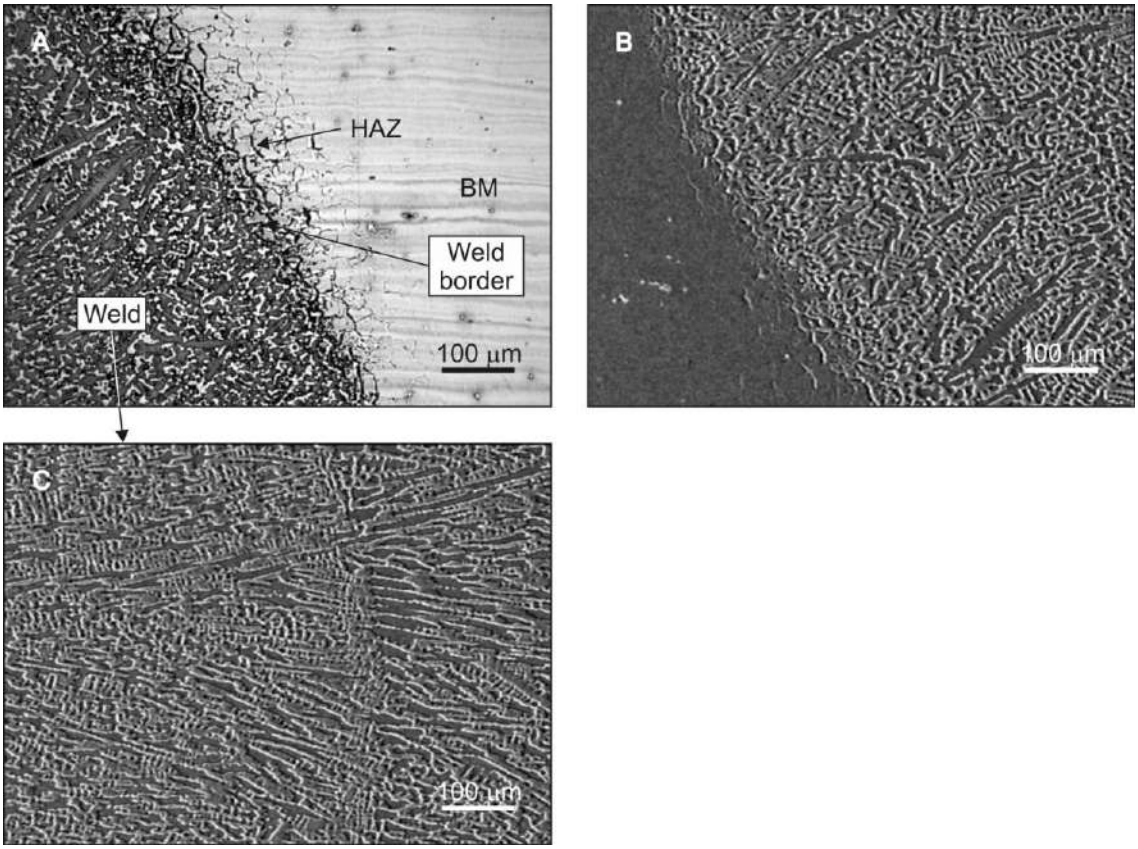

FIG. 10 — MICROSTRUCTURE OF AN ARC-WELDED JOINT OF 1.2-mm THICK SHEET METAL: A — OPTICAL MICROSCOPE; B, C — SEM.

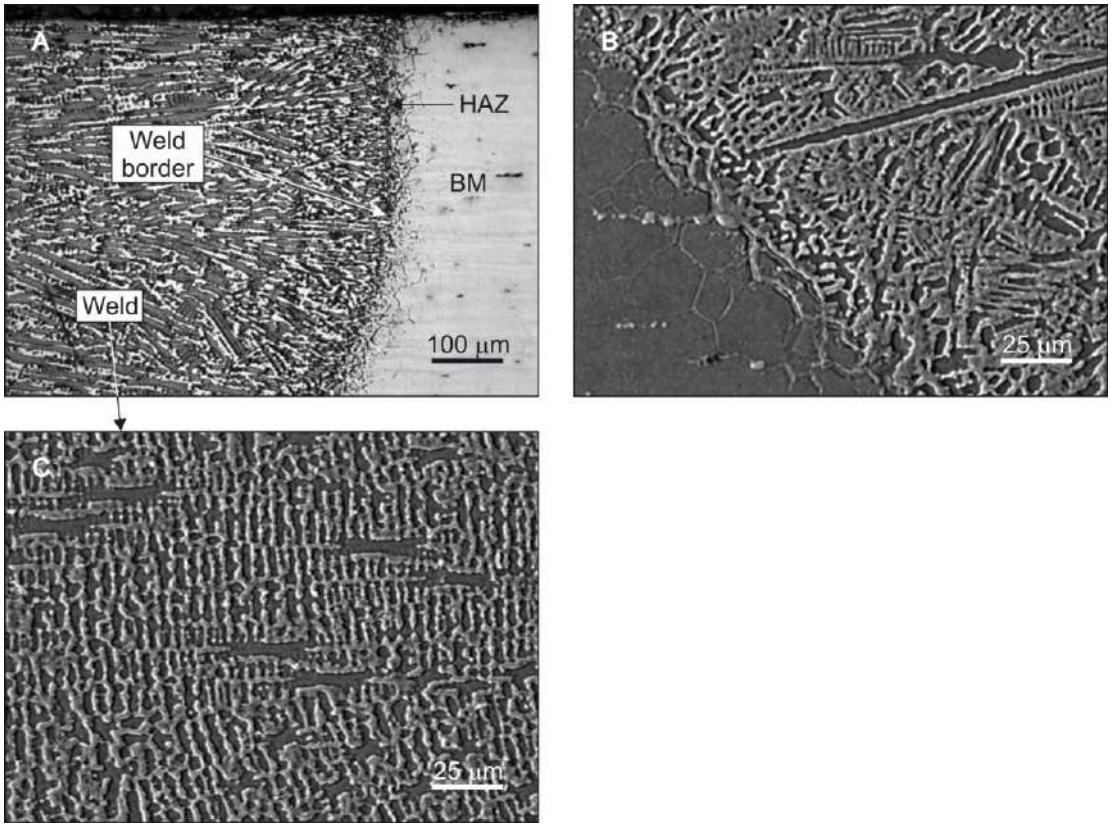

FIG. 11 — MICROSTRUCTURE OF A LASER-WELDED JOINT OF 1.2-mm THICK SHEET METAL. A — OPTICAL MICROSCOPE; B, C — SEM.

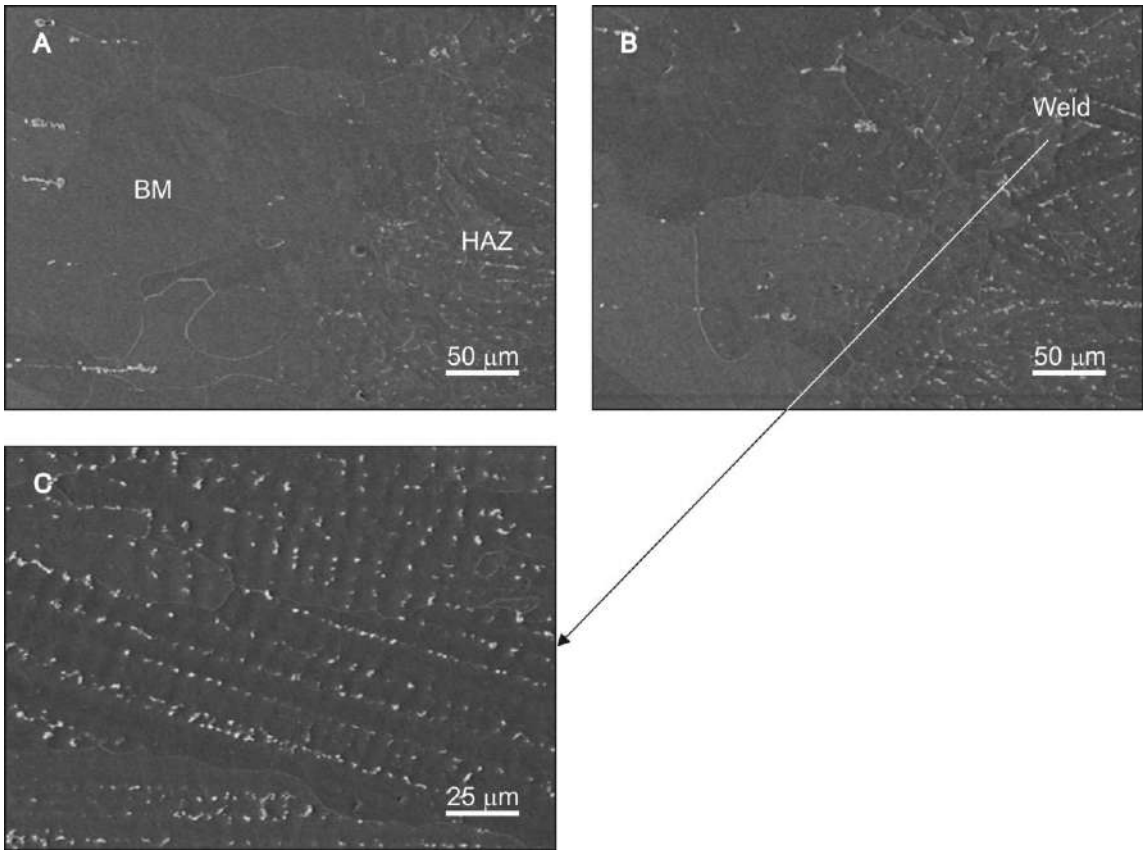

FIG. 12 — SEM IMAGES OF MICROSTRUCTURE OF A LASER-WELDED JOINT OF 1.2-mm THICK SHEET METAL

IV. X-RAY MICROANALYSIS

Example results of X-ray chemistry microanalysis carried on in micro-areas of welded joints on Inconel 718 sheet in as-delivered condition and after heat treatment are presented in Figs. 13 and 14, respectively.

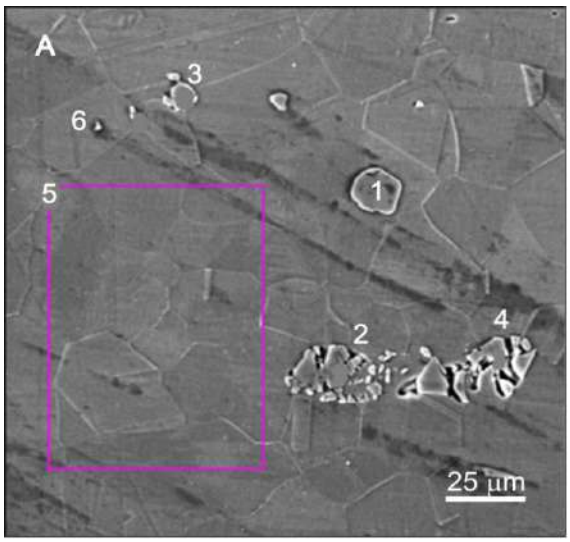

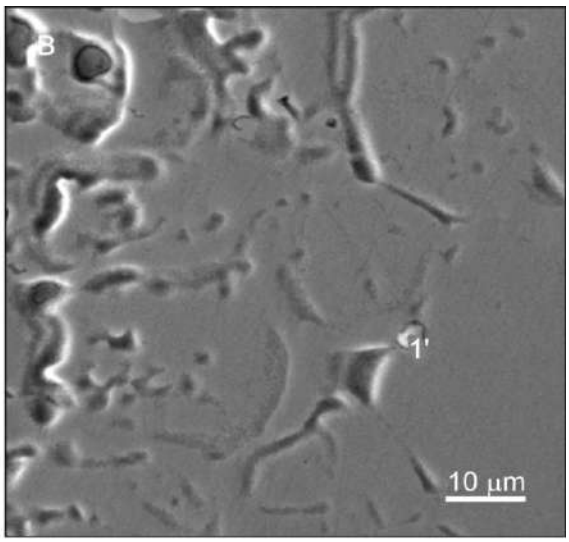

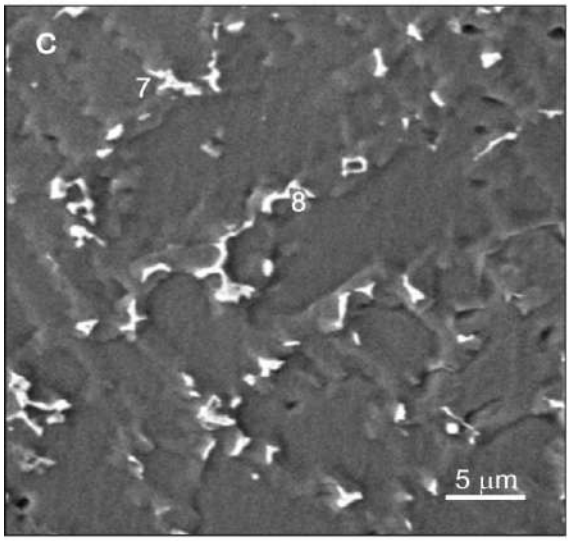

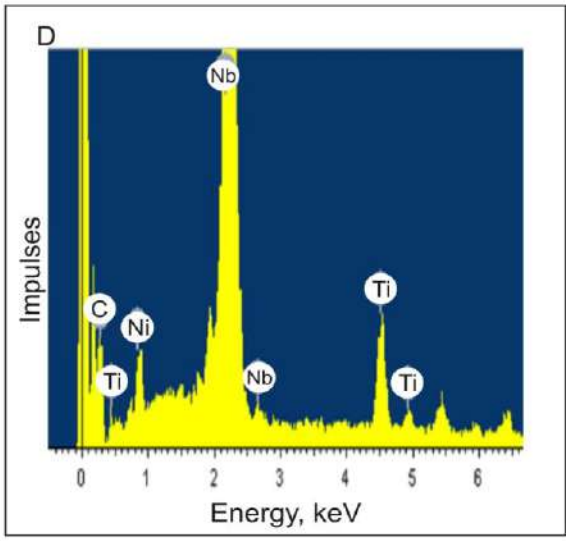

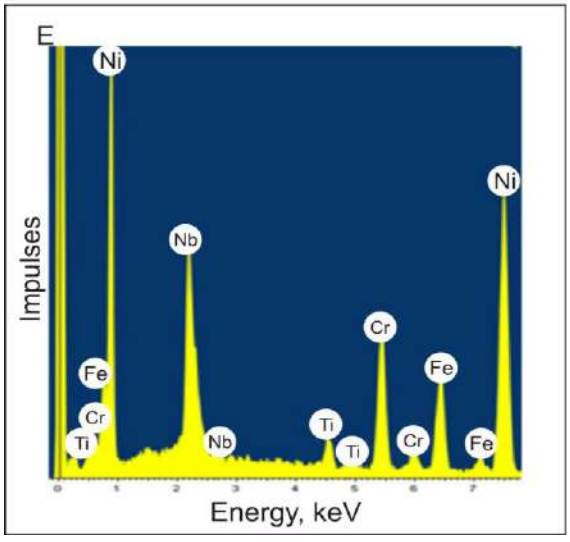

Micro-area No.	Element content (% wt.)						
	C	Ni	Nb	Cr	Fe	Ti	Mo
1	20.20 (64.0)*	1.70 (1.30)	70.80 (29.0)	—	—	7.30 (5.70)	—
1′	19.5	1.80	74.36	—	—	4.34	—
2	—	56.33	4.50	19.43	18.63	1.11	—
3	—	56.97	3.91	19.23	18.88	1.02	—
4	—	55.73	3.67	20.17	19.25	1.18	—
5	—	60.28	4.34	16.85	15.20	0.90	2.43
6	—	55.88	3.92	20.02	18.96	1.22	—
7	19.80	1.60	71.25	—	—	6.90	—
8	—	57.9 (55.7)	—	20.8 (22.7)	20.4 (20.6)	0.9 (1.0)	—
* Figures in parentheses denote element content in atomic %							

FIG. 13 — MICROSTRUCTURE OF: A — BM; AND B, C —GTAW JOINT OF 0.9-mm THICK SHEET METAL IN AS-DELIVERED CONDITION WITH MARKED X-RAY MICROANALYSIS AREAS NOS. 1–8. ENERGY SPECTRA OF X-RAYS SCATTERED FROM: D — MICRO-AREA NO. 1; AND E — MICRO-AREA NO. 8. THE TABLE SUMMARIZES RESULTS OF X-RAY MICROANALYSIS.

Microstructure of Inconel 718 sheet in as-delivered condition reveals large grains of phase γ with carbides of MC type reach in niobium and titanium (Nb, Ti)C precipitated unevenly inside and on borders of the grains. Moreover, structure of the sheet metal contains irregular intermetallic phases rich in nickel, chromium, iron, niobium, and titanium. These are probably topologically close-packed (TCP) phases (σ phases). These phases correspond to compositions Ni(Cr, Fe, Nb) and Ni(Cr, Fe, Nb, Ti).

The seams in the joints welded both with electric arc and laser are characterized with dendritic structure. In welded joints of sheet metal in as-delivered condition, irregular eutectic composed of intermetallic phases (σ phases) and MC-type carbides is located on boundaries of phase γ dendritic grain branches.

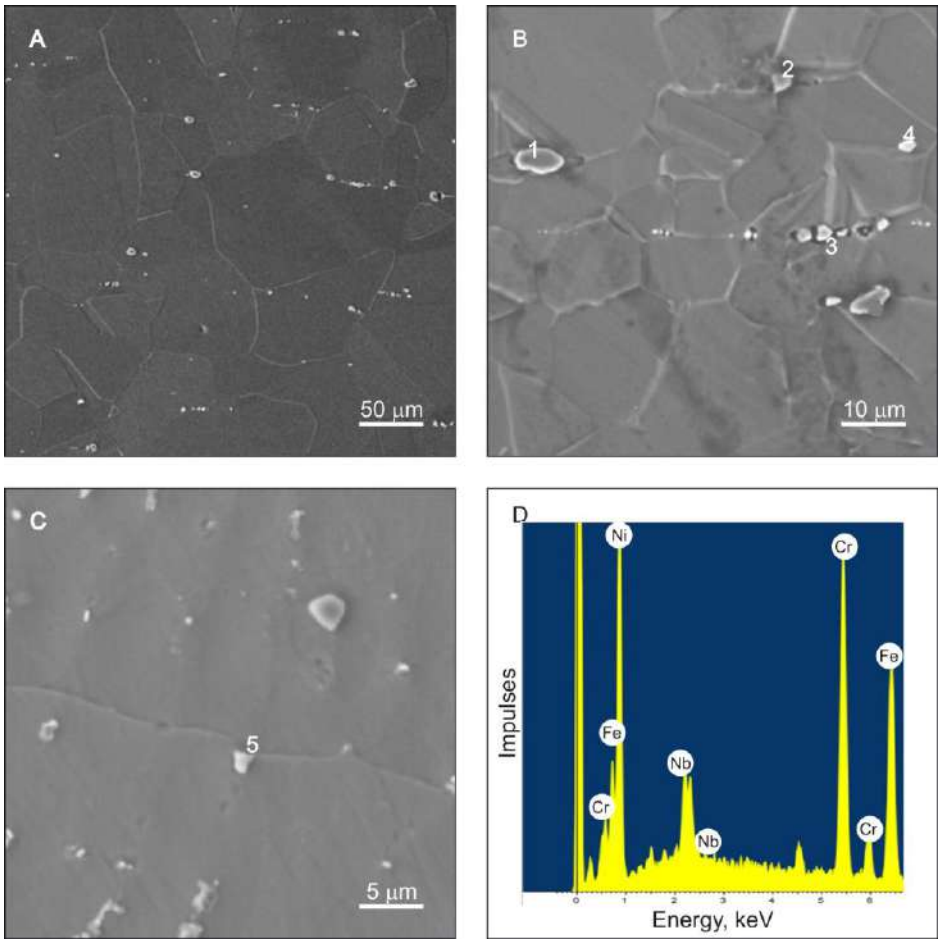

Micro-area No.	Element content (% wt.)						
	C	Ni	Nb	Cr	Fe	Ti	Al
1	19.25 (58.60)*	2.85 (1.70)	69.74 (34.56)	—	—	8.16 (5.14)	—
2	—	50.50	3.50	18.05	16.99	1.15	0.64
3	—	56.80	4.57	19.71	18.92	—	—
4	—	55.74	4.07	19.98	19.27	0.94	—
5	—	53.2	19.8	12.7	12.1	2.2	-

* Figures in parentheses denote element content in atomic %

FIG. 14 — MICROSTRUCTURE OF: A, B — BM; AND C — LASER WELDED JOINT OF 1.0-mm THICK HEAT-TREATED SHEET METAL WITH MARKED X-RAY MICROANALYSIS AREAS NOS. 1–5. D — ENERGY SPECTRUM OF X-RAYS SCATTERED FROM MICRO-AREA NO. 3. THE TABLE SUMMARIZES RESULTS OF X-RAY MICROANALYSIS.

In heat-treated sheet metal, the base material comprises equiaxial large grains of phase γ with regularly distributed (especially on grain boundaries) rounded MC-type carbides and residues of unsolved intermetallic phases (Fig. 14). Welded joints of heat-treated sheet metal have dendritic structure. It can be seen that irregular eutectic is almost completely dissolved in solid γ solution. On boundaries of phase γ grains' second-order branches there are finer rounded σ phases Ni(Nb, Cr, Fe, Ti) and spherical MC-type carbides rich in niobium.

4.1 High-temperature creep test

High-temperature creep tests were carried out at constant temperature on specimens prepared specifically for the purpose of this study out of Inconel 718 sheet with thickness 0.5 mm, 0.9 mm, and 1.2 mm (Fig. 2) with the use of creep testing machine (Fig. 3). Creep tested were specimens with welds made using GTAW method and with laser, untreated and heat-treated. Figs. 15 and 16 show example specimens ruptured in high-temperature creep tests.

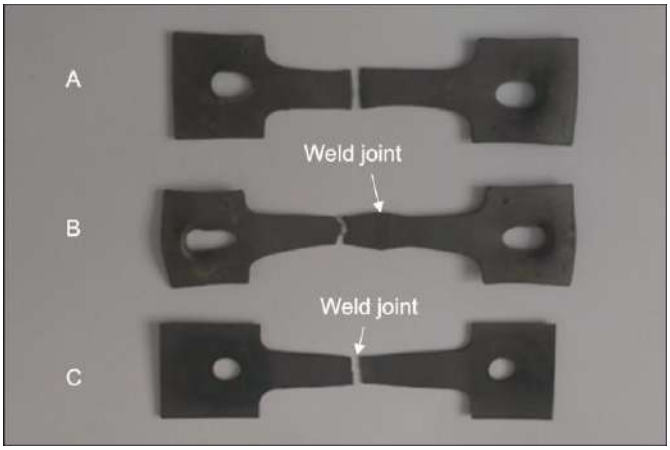

FIG. 15 — EXAMPLE SPECIMENS OF 1.0 mm SHEET ALLOY IN AS-DELIVERED CONDITION RUPTURED AFTER HIGH-TEMPERATURE CREEP TEST. A — BM; B — LASER-WELDED JOINT; C — GTAW JOINT.

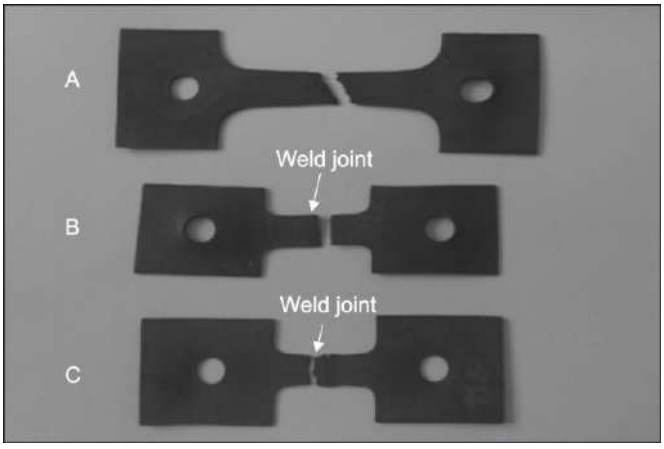

FIG. 16 — EXAMPLE SPECIMENS OF 1.0 mm SHEET ALLOY, HEAT-TREATED AND RUPTURED IN HIGH-TEMPERATURE CREEP TESTS. A — BM; B — LASER-WELDED JOINT; C — GTAW JOINT.

Table 2 shows results of high-temperature creep test, and Fig. 17 presents values of the time to rupture for specimens of sheet metal in as-delivered condition, heat-treated, welded by means of GTAW method and laser-welded in the form of a bar graph.

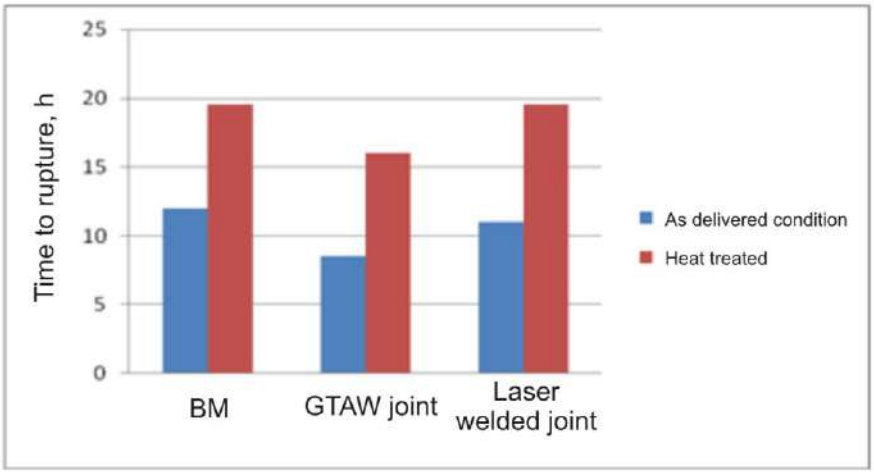

FIG. 17 — THE TIME TO RUPTURE MEASURED IN HIGH-TEMPERATURE CREEP TEST OF INCONEL 718 SHEET SPECIMENS. TEST CONDITIONS: T = 860°C, σ = 150 MPa.

The obtained results indicate that thin Inconel 718 sheet in as-delivered condition demonstrates a significantly shorter time to rupture in high-temperature creep tests than the heat-treated material. The welding method has significant effect on the time to rupture in the adopted high-temperature creep test conditions in case of sheet metal in both as-delivered condition and heat treated. Welded joints made with laser show the time to rupture values almost twice as high as those obtained for electric arc welding in argon atmosphere. Joints in Inconel 718 sheet specimens made with laser and heat treated demonstrate creep resistance similar to this of the base material (heat-treated sheet metal subject to high-temperature creep test).

When creep-tested at high temperatures, heat-treated Inconel 718 sheet specimens with GTAW joints got ruptured in the area of welded joints, just like those welded with the same method but in as-delivered condition. The joints made with the use of electric arc are characterized with lower creep resistance, and the time to rupture demonstrated by them in the high-temperature creep test has the value by about 30% lower than the time to rupture observed for sheet metal in as-delivered condition. GTAW joints of heat-treated sheet alloy show higher values of the time to rupture in the creep tests. The time to rupture value for sheet metal welded by means of GTAW and heat treated is similar to this characterizing base material without heat treatment (in as-delivered condition).

V. CONCLUSIONS

The initial material selected for the study were three grades of thin (0.5-mm, 0.9-mm, and 1.2-mm thick) sheet metal in as-delivered condition, rolled out of nickel-based Inconel 718 alloy. The material contained about 17% Cr, 16% Fe, 5.0% Nb, 2.5% Mo, 1.0% Ti, 0.60% Al, and 0.05% C. Total content of other elements such as Si, Mn, B, and N did not exceed 0.25%.

The microstructure of sheet metal reveals equiaxial grains of phase γ with dimensions of about (100 ± 15) μm with a small quantity of irregular phases σ and spherical carbides of MC-type sparsely distributed in the matrix. Intermetallic (TPC-type) phases σ have complex and diversified chemical composition (Fig. 13). These phases contain Nb and can be therefore described as Ni(Cr, Fe, Nb, Ti). There are also phases without Nb, Ni(Cr, Fe, Ti), as well as those without Ti, Ni(Cr, Fe, Nb). Carbides of MC type sparsely distributed in structure of the sheet metal contain mainly Nb and Ti and small quantities of nickel. They can be described as (Nb, Ti)C.

Thin Inconel 718 sheet in as-delivered condition with such microstructure shows good tensile strength on the level of about (850 ± 30) MPa at high plasticity, and elongation on the level of (30 ± 3)% [15]. The creep resistance of sheet metal in as-delivered condition determined by means of the time to rupture measured in high-temperature creep tests at temperature 860°C and under stress 150 MPa was 12 h at elongation of 48%.

Structure change induced by thermal treatment of Inconel 718 sheet consisting in solution treatment starting from temperature 1010°C/8 h/H_2O and two-stage ageing at temperatures 720°C/8 h and 620°C/8 h resulted in significant improvement of their strength properties. Tensile strength on the level of 1240 MPa was obtained with elongation similar to this measured for sheet metal in as-delivered condition [15].

Heat treatment (solution treatment and ageing) of Inconel 718 alloy sheet resulted in changes of morphological features characterizing its microstructure.

Mixtures σ-phase with diversified chemical composition irregularly distributed in the alloy's microstructure (Fig. 13) were almost entirely dissolved in solid solution of phase γ. Unsolved phase σ remaining in microstructure of Inconel 718 occurs on the form of fine rounded particles (Fig. 14). Similarly, MC-type carbides rich in niobium and titanium remaining in the alloy's microstructure have spherical shapes and are present in the form of fine particles on boundaries of γ phase grains.

It has been found that the current intensity I on the level of 80 A and the welding rate V_s = 200 mm/min were GTAW parameters most favorable from the point of view of thermal efficiency η_c and HAZ size. Such parameters of Inconel 718 sheet welding allowed to obtain good welded joints (Figs. 4–7) with minimum HAZ widths ranging from about 50 μm to 100 μm (Figs. 10–12).

Limited heat efficiency of laser light beam means that higher power levels must be used when welding thin Inconel 718 alloy sheet. Good joints on 0.7–0.9 mm thick sheet were obtained for laser with power of 400 W and welding rate of the order of 25 mm/s. For such laser welding parameters, the welded joints had virtually no HAZ (Figs. 4B, 5B, and 6B) or widths of their HAZs did not exceed 40 μm (Figs. 9 and 11).

The seams in the joints welded both with electric arc and laser reveal dendritic structure. Value of the structural parameter λ_{2s} characterizing dendritic grains of the joints depends on the welding method and decreases with increasing sheet metal thickness. In case of GTAW, increase of sheet metal thickness from 0.5 mm through 0.9 mm to 1.2 mm is accompanied by reduction of λ_{2s} parameter value from 12 μm through 10 μm to 8 μm. Similarly, in case of laser-welded joints, with sheet metal thickness increasing from 0.5 mm to 1.2 mm, λ_{2s} values decrease from 9.6 μm to 5μm.

Boundaries of second-order branches of dendritic grains observed in welded joints on sheet metal in as-delivered condition made with the use of both GTAW and laser method are the locations where irregular eutectic (Fig. 13A) composed of σ phase and MC-type carbides can be found. Heat treatment (solution treatment and ageing) of welded sheet metal joints resulted in almost complete dissolution of σ phases and disappearance of irregular eutectic. On boundaries of joint grains' second-order branches there are fine rounded MC-type carbides surrounded with residues of σ phase (Fig. 14C).

A measure of creep-resisting properties of thin sheet Inconel 718 in as-delivered condition, heat-treated and welded with the use of GTAW and laser method is the time to rupture at adopted high-temperature creep conditions (Table 2, Fig. 17). The obtained results in combination with conclusions drawn from of microstructure examination of welded joints before and after heat treatment show that the use of laser welding allows to increase the time to rupture of heat-treated joints by nearly 62% in comparison with BM in as-delivered condition and by about 80% with respect to the time to rupture observed in GTAW joints made on sheet in as-delivered condition.

Specimens of sheet metal in as-delivered condition welded with the use of laser method and heat treated get ruptured outside the welded joint areas (Fig. 15B and 16B). It can be therefore concluded that laser-welded joints demonstrate higher creep resistance than the base material.

REFERENCES

[1] Ruedl E., 1975 *Phase transformation in the alloy Hastelloy B, Materials Research Bulletin* 10, 16-22

[2] Agarwal D.C., 2002 *Chronology of Developments in Ni-Mo Alloys:* The Last 70 Years, Corrosion 58, 27-29

[3] Bloom D.S, Putnam J.W., Grant. N., 1952: Trans. AIME, *Journal of Metals 194*, 1, 626

[4] Lancaster J., 1992: *Handbook of structural welding: processes, materials and methods used in the welding of major structures, pipelines and process plant*, Abington Publishing, Cambridge, 56-58

[5] Hong J. K., Park J. H., Park N. K., Eom J. S., Kim M. B., Kang G. Y., 2008: *Microstructures and mechanical properties of Inconel 718 welds by CO2 laser welding*, Journal of Materials Processing Technology, 1132-1138

[6] Gozlan. E., Bamberger. M. S., Dirnfeld. F., Prinz. B., Klodt. J., 1991: *Topologically close-packed precipitations and phase diagrams of Ni-Mo-Cr and Ni-Mo-Fe and of Ni-Mo-Fe with constant additions of chromium*, Materials Science and Engineering A, 141,85

[7] Durand-Charne M., 1997: *The microstructure of superalloy*, Institut National Polytechnique de Grenoble, 48-52

[8] Yukawa N., Hida M., Imura T., Kawamura M., Mizuno Y., 1972: *Structure of Chromium Rich Cr-Ni, Cr-Fe, Cr-Co and Cr-Ni-Fe Alloy Particles Made By Evaporation In Argon*, Metallurgy Transaction 3, 47

[9] Klein J. H., Brooks C. R., Stansbury E. E., 1970: *The establishment of long-range order in NiCr using electron microscopy*, Physica Status Solidi 38, 831

[10] Dupont J. N., Michael J. R., and Newbury B. D., 1999: *The weldability of an advanced corrosion-resistant alloy in investigated and linked to microstructural development in the fusion zone.* Welding Journal 78(12): 708-s to 415-s

[11] Savage W. F., and Lundin C. D., 1965: *The Verestraint test.* Welding Journal 44(10): 433-s to 442-s

[12] Savage W. F., and Lundin C. D., 1966: *Application of the Verestraint technique to the study of weldability.* Welding Journal 45(11):497-s to 503-s

[13] Broks J. A., and Thompson A. W., 1991: *Microstructural deveplomen*t *and solidification craking suspectibility of austenic stainless steel welds.* International Materials Reviews 36: 16-44

[14] Knorowski G. A., Cieslak M. J., Headley T. J., Roming A. D., and Hammelter W. F., 1989: *Inconel 718: a solidification diagram.* Metallurgical Transactions A 20 A:2149-2158

[15] Jędrusik A., 2015: *„Technology of cutting, cleaning nad laser welding of thin sheet metal made of nickel alloy Inconel 718"* Doctor thesis, Rzeszow University of Technology

[16] Opiekun Z., 2011: *Temperature influence of ceramic form on the structure of cobalt alloy MAR-M509 castings.* Acta Metallurgica Sinica (English letters) 24(1) 23-33

[17] E-139-00 *Standard Test Methods Conducting Creep. Creep-Rupture, and Stress-Rupture Test of Metallic Materials.*

Standardization of the Central Console of Police Vehicles – An Outline of the Diagnosed Needs

Piotr ŁUKA[1], Andrzej URBAN[2]

[1]PhD Piotr Łuka, head of the Social Security Faculty of the Security and Public Order at the Police Academy in Szczytno.

[2]Associate Professor, PhD Eng. Andrzej Urban, Associate Professor at the Social Security Faculty of the Security and Public Order at the Police Academy in Szczytno.

Abstract— *The authors bring closer the results of social studies conducted on a group of respondents - policemen using police cars during their everyday duty. The study seeks to answer the question: how to improve the daily duty and integrate the devices that are used for the everyday activities by the law enforcement services which contribute to safety or public order? It also seeks information and guidance concerning the actions to be taken in the future for the devices installed in police cars to be the most ergonomic and safest for their users.*

Keywords— Safety, traffic, device integration, police car.

I. INTRODUCTION

The publication is the result of the social studies performed during the project implemented in the field of defense and security under tender No. 7/2015 funded by the National Centre for Research and Development entitled "Development of police vehicles classification depending on their purpose and standardization of the central console of vehicles in the scope of arrangement and installation of ICT systems and control devices of special purpose signals" No. DOB-BIO7/04/02/2015. The project is implemented by a scientific consortium composed of the Police Academy in Szczytno - project leader, the Automotive Industry Institute from Warsaw and the company Marvel Sp. z o. o. from Lodz. The beneficiary of the effects of research and development in this project are to be the services reporting to the Minister of the Interior and Administration. The assumptions established in the project fit in well with the current priorities of the Chief of Police [1] for the years 2016-2018. One of the seven priorities established by the Polish Police Headquarters include: improving the quality of the tasks performed by police officers and the employees of the Police by providing the optimal duty / work conditions. One of the specific tasks indicated for the implementation in this regard by the Polish Police Headquarters is equipping the Police with computer and communications hardware (including mobile devices and enabling the use of the functionality of information systems used by the Police) and transport equipment.

II. MATERIALS & METHODS

The project implementation began in December 2015 and has been lasting for 36 months. The main objective of the project is to develop a directory of vehicles and to prepare documentation for the modification of the central console and the electrical system of the vehicles (depending on the classification) with respect to the standardization and enabling the installation of communications and ICT equipment at the locations adapted for this purpose along with the implementation of the document for use in proceedings when purchasing vehicles [3]. One of the results of the project was conducting surveys. The aim of this study was to collect reviews from the users of Police vehicles and draw conclusions for further exploration prospects.

Based on the available data, it was found that the Polish Police operates a total of 21 794 vehicles. This number includes 13 821 passenger vehicles (including 6 145 marked and 7676 unmarked units). Outside the indicated category, the Police also uses SUVs, pick-ups, utility vehicles, off-road RD-Video vehicles, van-type vehicles, trucks, buses and special purpose vehicles [2]. In order to obtain information about the preferences of the users of the Police vehicles with respect to the need for the modification of the central console of the field units of the Police, a study was conducted using the method of diagnostic survey. The study was carried out from April to June 2016. It was participated by a total of 354 police officers from the garrisons in Malopolska, Wielkopolska, Warmia-Mazury and the policemen during training and vocational training at the Police Academy in Szczytno. The policemen during training were the representatives of all the of the Polish Police garrisons. For the purpose of the study, a research tool was developed in the form of a questionnaire consisting of 22 questions.

The study used a questionnaire prepared by the employees of the Police Academy in Szczytno and the Automotive Industry Institute in Warsaw. The study was preceded by obtaining the approval of the Chief of Police. The main purpose of the study was to find out user reviews concerning the Police vehicles with respect to the solutions functioning in them, as well as their assessment and preferences concerning the planned future solutions. Participants responded to a series of questions relating in particular to the vehicle's type and purpose which are the most commonly used in the Police and the type of additional devices in the vehicles. Further questions concerned the safety and efficiency of the operations related to the use of the devices installed in the vehicles. The policemen also commented on the location of the installation of the equipment, assessing the aptness of the location in the vehicle. The policemen were also asked what kind of other, not currently installed in the Police vehicles, devices should be there in the future. One of the important questions was also the one concerning the need for the integration of the devices in the vehicles and those used as part of their duties.

The study showed that the policemen (in prevention, crime units) mostly use passenger marked vehicles (44% respondents) and passenger unmarked vehicles (30% respondents).

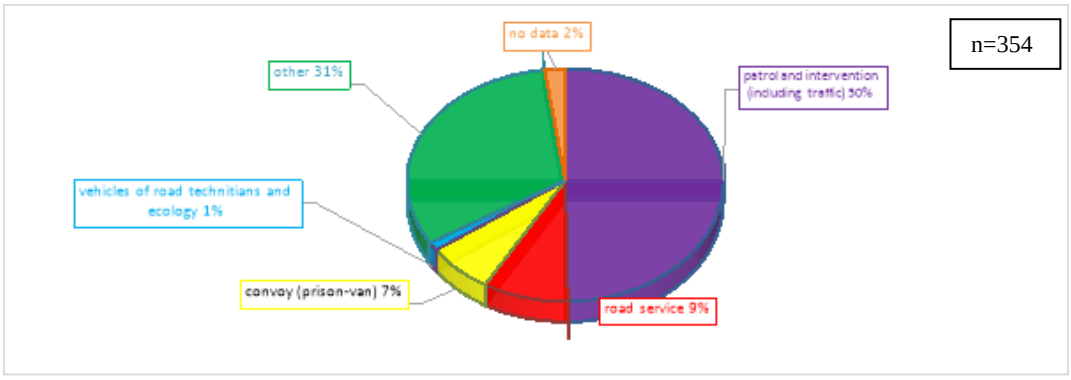

DIAGRAM 1. INTENDED USE OF THE MOST COMMONLY USED VEHICLES.
[Source: own research carried out under the project No. DOB-BIO7/04/02/2015]

Patrol and intervention vehicles are the most frequently used in everyday duty (Diagram 1) of the respondents - 50%. Another category of the vehicles that were used the most frequently were the traffic ones - 9% of the respondents and convoy vehicles - 7% of respondents. 1% of the respondents indicated the vehicles of road technicians and ecology. 31% of the respondents indicated "other" as the most commonly used vehicles.

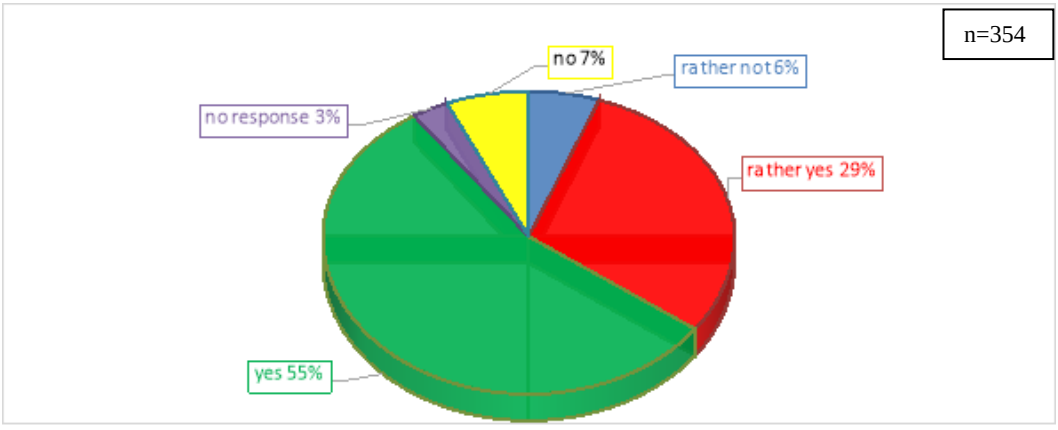

DIAGRAM NO. 2. IS THE INTEGRATION OF THE OPERATION OF THE DEVICES INSTALLED IN THE VEHICLE IN ONE CONTROL PANEL (TOUCH SCREEN) JUSTIFIED?
[Source: own research carried out under the project No. DOB-BIO7/04/02/2015]

The question of whether the integration of the operation of the devices installed in the vehicles in one control panel was justified (Diagram 2) was answered "yes" by 55% of the respondents and "rather yes" by 29%. A total of as many as 84% of the responding policemen claimed that such a solution was justified. The results confirmed the validity of the undertaken development work aimed at integrating the devices used by officers during their daily duty. On the other hand, 13% disagreed. 7% percent claimed strongly that the integration was not needed, and 6% expressed the view that it was rather unnecessary.

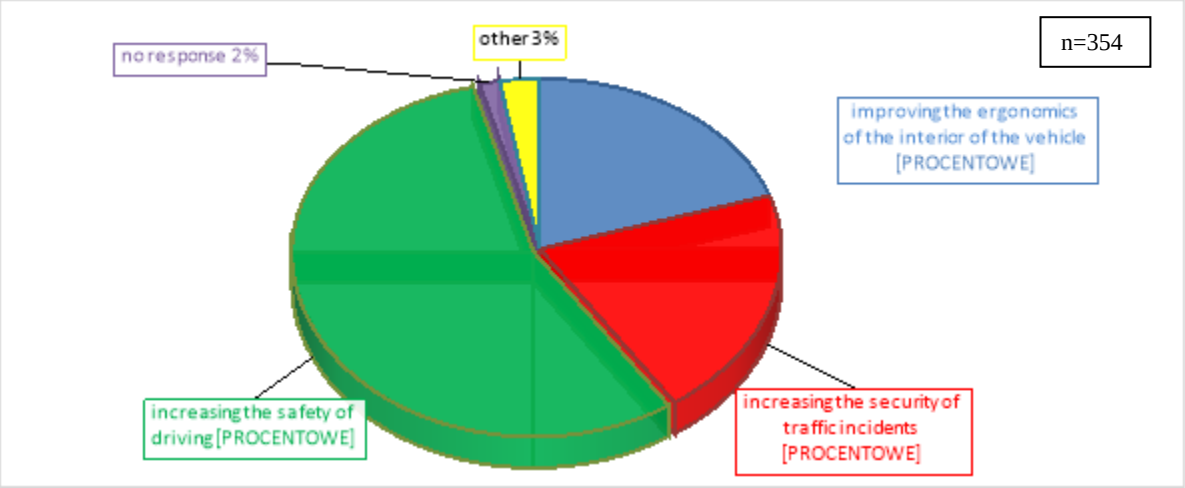

DIAGRAM 3. WHAT IS THE RATIONALE BEHIND THE INTEGRATION OF THE OPERATION OF THE DEVICES INSTALLED IN THE VEHICLE IN A SINGLE CONTROL PANEL?
[Source: own research carried out under the project No. DOB-BIO7/04/02/2015]

Justifying the need for integrating the operation of the devices in vehicles (Diagram 3), the respondents most often indicated, as the most important, the need for increasing their safety while driving (55% of respondents). It was followed by the need for the integration of operating the devices in the vehicle (20% of respondents), as justified by increasing the safety of the users of vehicles during traffic incidents or improving the ergonomics of the interior of the vehicle.

Typically, Police vehicles are equipped with radio stations and devices for operating light and sound signals. The respondents were asked questions concerning the safe use of the devices while performing duties (Diagrams 4 and 5).

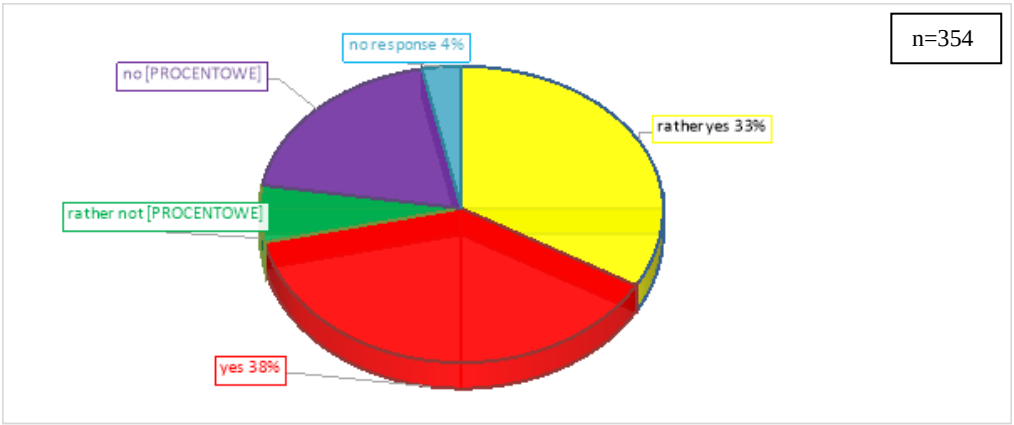

DIAGRAM 4. SAFE OPERATING DEVICES FOR OPERATING LIGHT AND SOUND SIGNALS DURING THE PERFORMANCE OF DUTIES
[Source: own research carried out under the project No. DOB-BIO7/04/02/2015]

The users of Police vehicles were also asked about the possibility (due to the location) of the safe and efficient operation of the light- and sound-signal control devices during driving the vehicle (Diagram 4). The responses show that 19% of the users said that the devices did not enable safe and efficient use while driving. Another 6% of the respondents also had doubts about the proper installation of the devices, checking the answer "rather not". In total, 24% of the respondents had reservations about the installation of the devices. 71% of the respondents felt that the location enabled safe and efficient operation. The analysis of this distribution of responses raises concerns. Almost every fourth vehicle user points to the lack of the safe and efficient use of the light- and sound-signal control devices. The results force conducting research to undertake further studies concerning the use of simulators and the Eye Tracker System.

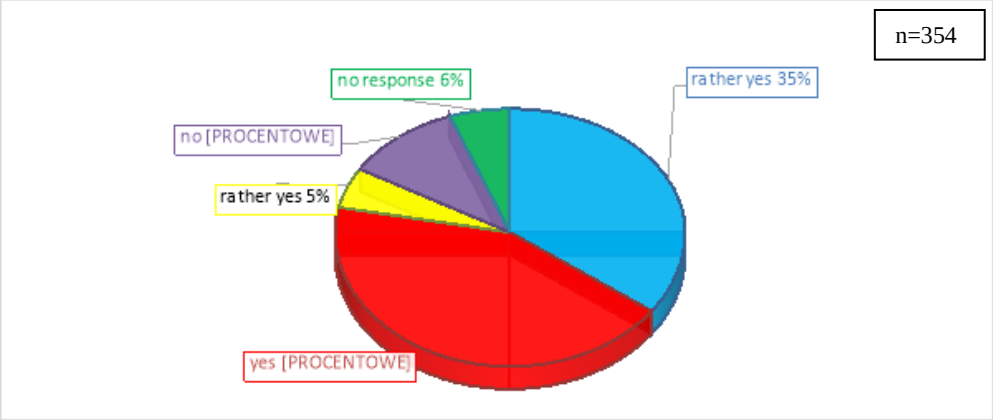

DIAGRAM 5. SAFETY OF THE USE OF A RADIO STATION DURING THE PERFORMANCE OF DUTIES
[Source: own research carried out under the project No. DOB-BIO7/04/02/2015]

The question concerning the possibility (due to the location) of the safe and efficient operation of a radio station during driving the vehicle (Diagram 5) was responded by a total of 16% of the respondents with the claim that the radio station did not enable simultaneous safe and efficient use of it while driving. On the other hand, a total of 78% of the respondents felt that the location of the radio station enabled safe and efficient use (43% of respondents replied "yes", and 35% "rather yes").

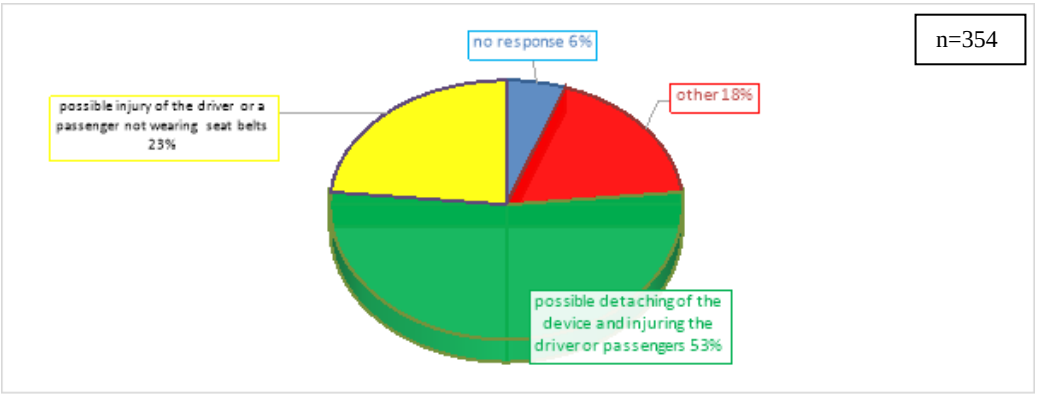

DIAGRAM 6. RISK ASSOCIATED WITH THE CURRENT LOCATION OF LIGHT- AND SOUND-SIGNAL CONTROL DEVICES
[Source: own research carried out under the project No. DOB-BIO7/04/02/2015]

The respondents were also asked about the risks of the current location of the light- and sound-signal control device in the vehicles they use (Diagram 6). It turned out that as many as 53% of the respondents fear the possible detaching of the device and injuring the driver or passengers. Another 23% of the respondents believe that the injury of the driver or a passenger not wearing seat belts is possible. The result indicates the need for the verification of the current rules and practices of the installation of such devices in Police vehicles.

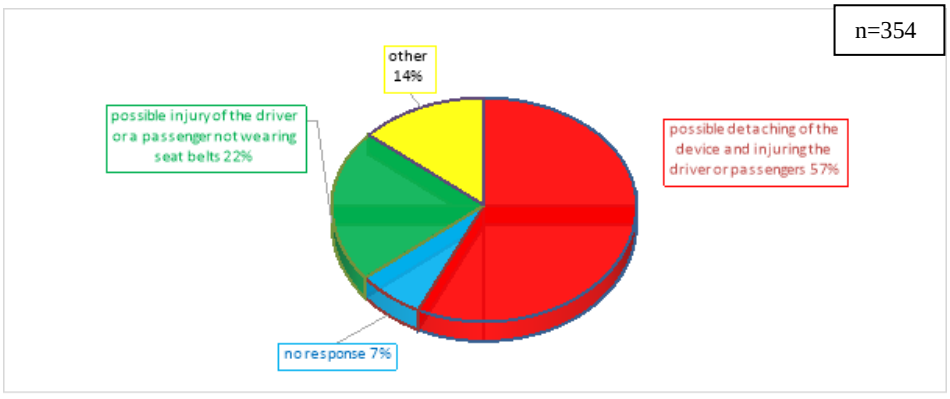

DIAGRAM 7. RISK ASSOCIATED WITH THE CURRENT LOCATION OF A RADIO STATION
[Source: own research carried out under the project No. DOB-BIO7/04/02/2015]

Similarly to the question described in Diagram 6, the respondents were asked about the risks associated with the current location of the radio station in their vehicles (Diagram 7). It turned out that as many as 57% of the respondents fear the possible detaching of the device and injuring the driver or passengers. On the other hand, 22% of the respondents believe that the injury of the driver or a passenger not wearing seat belts is possible. Conclusions from the analysis of the responses are the same as with respect to the question relating to the installation of the light- and sound-signal control device.

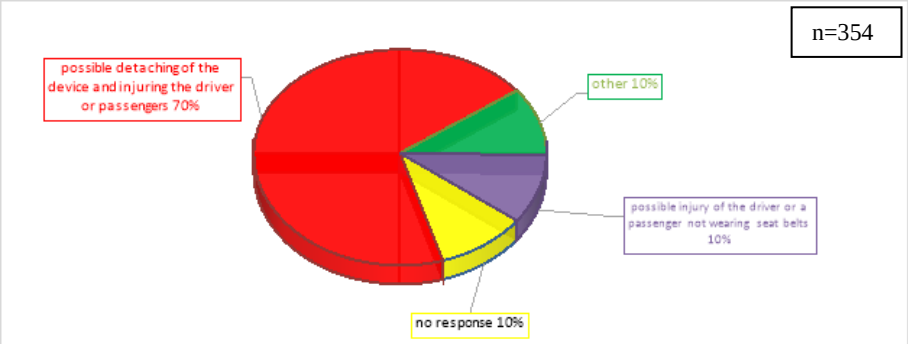

DIAGRAM 8. RISK ASSOCIATED WITH THE CURRENT DVR LOCATION
[Source: own research carried out under the project No. DOB-BIO7/04/02/2015]

The responses to the question concerning the risks associated with the current DVR location (Diagram 8) are even worse. In this case, 70% of the respondents indicated their concern about the possible detaching of the device and injuring the driver or passengers. 10% of the respondents also indicated the possible injury of the driver or a passenger not wearing seat belts.

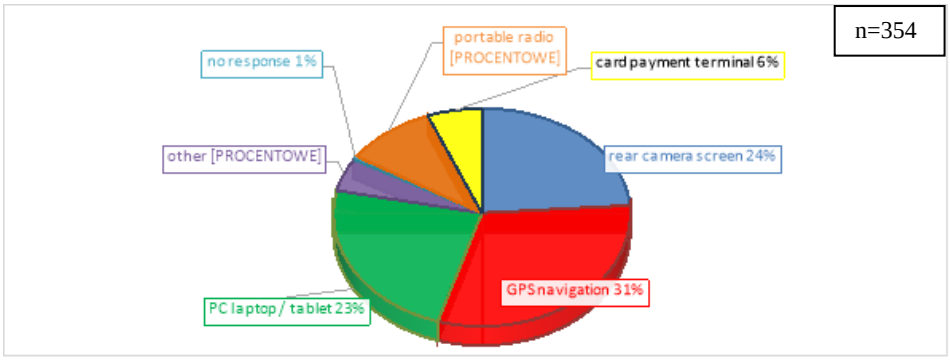

DIAGRAM 9: WHAT DEVICES, OTHER THAN THE CURRENTLY INSTALLED IN THE VEHICLES, SHOULD BE THERE IN THE VEHICLES / ON THE CONSOLE OF THE VEHICLES?
[Source: own research carried out under the project No. DOB-BIO7/04/02/2015]

Responding to the question concerning other devices than the currently installed in the vehicles that should be there in the vehicles / on the console of the vehicles in the future (Diagram 9), the respondents most frequently pointed to the need for GPS navigation (31%), the rear camera screen (24%), a portable computer (23%), a portable radio (6%) and a card payment terminal (6%) in their vehicles.

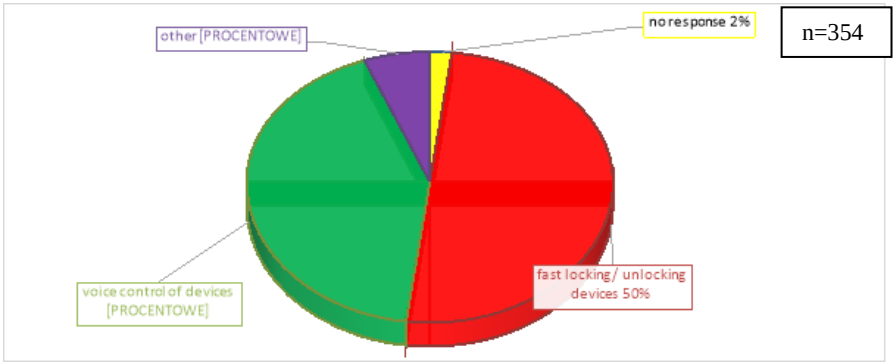

DIAGRAM 10. WHAT OTHER DESIRED FUNCTIONALITY SHOULD BE THERE ON THE CONSOLE OF POLICE CARS?
[Source: own research carried out under the project No. DOB-BIO7/04/02/2015]

Responding to the question concerning other desired functionalities of the devices installed on the console of police cars (Diagram 10), the respondents most frequently pointed to fast locking / unlocking devices (50% of the respondents), and the voice control of devices (43% of the respondents).

III. CONCLUSION AND EXPLORATORY PERSPECTIVE

On the basis of the research material collected, referring it to the previously established research assumptions, it can be concluded that it is justified to design the modifications of the central console and the electrical system of vehicles with respect to their standardization and enabling the installation of communications and ICT equipment in appropriate locations. It is indicated in the needs signaled in the field research conducted on the users of the Police vehicles. Particularly noteworthy are the ones that have been exposed in the paper, relating to the safety and, subsequently, the ergonomics and the possibility of efficient operating duty vehicles. The needs diagnosed on the basis of the users' reviews will be, in the later stages of the research, confronted with the technical capabilities in the field of the safe and ergonomic installation of devices in the vehicles. Account will be taken of the limitations of the current standards and regulations, and the requirements specified by vehicle manufacturers and the manufacturers of the equipment installed in the vehicles. Noteworthy and worthy of further research is the information collected from the users of the vehicles (Diagrams 4 and 5) reading that operating such additional devices as a radio or a light- and sound-signal control console, as assessed by some of the respondents, increases the risk of road accidents during the use of the devices while driving. In turn, diagrams 6, 7 and 8 show the concerns of policemen related to the possible detaching of the device and injuring the driver or passengers. The result suggests the need for the verification of the current rules and practices of the installation of such devices in duty vehicles.

REFERENCES

[1] Priorities and priority tasks of the Chief of Police for the years 2016-2018 approved by the Chief of Police (http://bip.kgp.policja.gov.pl/kgp/priorytety-kgp).

[2] Agreement No. DOB-BIO7/04/02/2015 on the execution and financing of the project implemented in the field of defense and security under tender No. 7/2015 entitled "Development of police vehicles classification depending on their purpose and standardization of the central console of vehicles in the scope of arrangement and installation of ICT systems and control devices of special purpose signals".

[3] Statistical data obtained from the Logistics Bureau of the Polish Police Headquarters, as at 31.12.2015.

Microfluidics and Sensors for DNA Analysis

Vishal M Dhagat[1*], Faquir C Jain[2]

Department of Electrical & Computer Engineering, University of Connecticut 371 Fairfield Way; U-4157
Storrs, Connecticut 06269-4157 USA

Abstract— *The manipulation of fluids in microchannels has been studied extensively due to its vast array of applications including genome sequencing, single cell detection, cost and time reduction with electronic microdevices. Microfluidics has the potential to influence subject areas from chemical synthesis and biological analysis to optics and information technology. The review paper introduces the advancement of microfluidics in DNA analysis. Wherever possible commercially available device information is also provided to emphasize the importance of that particular technology and its scope. It will briefly introduce you to different types of biosensor technology currently researched and one example that make the conceptual design into a reality.*

Keywords— Biosensor, DNA, Electrical, Microfluidics, PDMS.

I. INTRODUCTION

Microfluidics drives the advance technology to perform biological and chemical experiments at micro and nanometer scale, at affordable cost with minimal material consumption and optimal results. In microfluidic devices fluidic components are miniaturized and integrated together, leading to a realization of an entire "lab on a chip," in the same way that a microelectronic circuit is a whole computer on a chip [1]. There has been keen interest in achieving the full potential of this approach and, consequently, the development of many microfluidic devices and fabrication methods. Elastomeric materials such as polydimethylsiloxane (PDMS) have excellent alternatives to the silicon and glass used in new devices fabricated by MEMS (microelectromechanical systems) processes. Simplified device fabrication and the possibility of incorporating densely integrated microvalves into designs have helped microfluidics to expand into a ubiquitous technology that has found applications in many diverse fields.

Microfluidics is the science and technology of systems that process or manipulate small (10^{-9} to 10^{-6} liters) amounts of fluids, using channels with dimensions less than tens to hundreds of micrometers. Applications of microfluidic technologies offer many useful capabilities: the ability to use minuscule quantities of samples and reagents and to carry out separations and detections with high resolution and sensitivity; low cost; short times for analysis; and small footprints for the analytical devices [2]. Microfluidics exploits its most prominent characteristic, small size and less distinct characteristics of fluids in microchannels. It offers new capabilities in the control of concentrations of molecules in space and time. Microfluidics is a key to advancing molecular sensor based on bioassays including immunoassay, cell separation, DNA amplification and analysis [2]. It processes a vast number of parallel experiments rapidly with the tiny amount of reagents and chemicals. A reduction in size to the micrometer scale will usually not change the nature of molecular reactions, but laws of scale for surface per volume, molecular diffusion, and heat transport enable dramatic increases in throughput. The research for drugs demands robust and fast methods to find, refine and test a likely drug with relatively low cost. The discovery of a unique molecule with new qualities out of a nearly unlimited number of possibilities is laborious, time-consuming and relies heavily on technological resources that are available for handling small liquid volumes, automation, and high-through-put processing and analysis [1]. Initially, the concept of microfluidics solely dedicated to significantly reducing sample consumption and increasing efficiency in separation methods such as electrophoresis, but eventually low costs of mass production of microchips and automation of reaction systems for commercial use. At the time of review, there are many commercially available microfluidic devices made by prominent companies like Agilent Technologies, Evotec Technologies, Hitachi, and Fluidigm Technology [2].

II. MICROFLUIDIC DEVICE FABRICATION

Microfluidic devices are fabricated using standard photolithographic techniques using the replica molding method because it allows for simple, low-cost prototyping of microchannels. For rapid prototyping, polydimethylsiloxane-covered cover glasses are suitable for sealing devices. PDMS is spun onto a cover slip to a thickness of several microns and allowed to cure. The PDMS comes into contact with the chip containing trenches [3]. Fig. 1 shows typical processing steps of the microfluidic device fabrication.

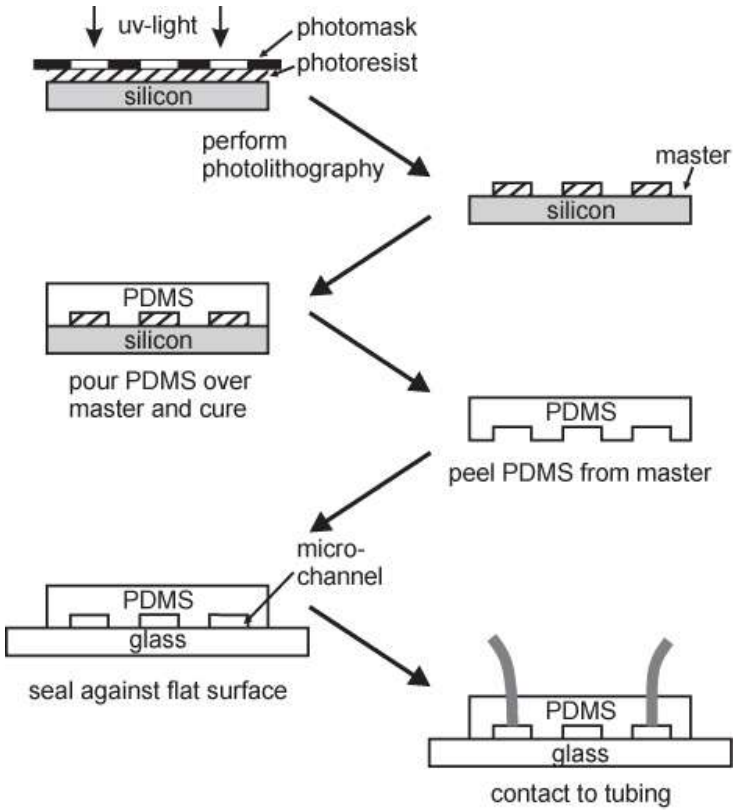

FIG. 1. MICROFLUIDIC DEVICE FABRICATION PROCESS [3]

III. DEOXYRIBONUCLEIC ACID (DNA)

Deoxyribonucleic Acid is one of the most used scientific terms in biotechnology. DNA is a biopolymer consisting of repeating units, i.e., four types of nucleotides, adenine (A), thymine (T), guanine (G), and cytosine (C). Each nucleotide is comprised of nucleobases and sugars as shown in fig. 2. These nucleobases are linked to ester bonds between the sugar and the phosphate groups, the backbone of DNA polymers. DNA double helix structure is a direct result of two DNA polymers with complementary base sequences paired following the Watson-Crick rule, A-T, and G-C. DNAs are the carriers of genetic information encoded by the sequence of four nucleotides, which transmits to RNA that directs protein synthesis process [4]. Each base pair is 3.4 Angstroms apart, and because each base pair is rotated 36 degrees on the previous pair, the helix repeats every 34 Angstroms. The average size of a protein-coding gene is 30 kbp, and the average mass of a base pair is 650 Da. The longest gene in the human genome is Titin (80 791 bp) while the most extended piece of synthetic DNA is the Mycoplasma genitalium bacterial genome (582 970 bp). Because of the negatively charged phosphate ions in the backbone, DNA has an overall negative charge [5].

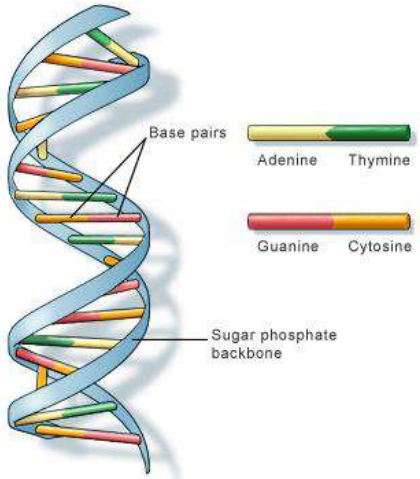

FIG. 2. DNA DOUBLE HELIX STRUCTURE FORMED WITH SUGAR-PHOSPHATE BACKBONE [4].

IV. MICROFLUIDICS FOR DNA ANALYSIS

Detection of single cells or individual DNA strands is necessary for specific diseases. Particular DNA mutations or cell disorders can now be detected using DNA analysis. There are several fundamental techniques used for DNA analysis including detection, amplification, and separation. Further advancement in the field to push for higher specificity and selectivity and the faster reaction time is ongoing. Microfluidic technologies enable one with a precise actuation of fluids and manipulation of bioparticles (e.g. DNA, RNA, proteins, and cells) at the micro scale. Fluid flow in ultra low dimensions of micrometers is laminar and precisely controlled by adjusting the flow rate. This distinct property gives rise to more efficient and accurate mass delivery to cells in controlled time and space. Also, because microfluidic platforms have scalable sizes with most biological macromolecules, cells, and blood vessels, they provide unique functionality for the design and remodeling of precise scaffolds, which mimic the physiological microenvironment [6]. DNA amplification is an essential step for DNA analysis. Micro Polymerase Chain Reaction (Micro-PCR) is used to perform DNA amplification. Micro-PCR offers many advantages including less use of reagents, rapid cooling/heating rates, decreased power consumption, and portability. PCR microfluidic devices allow simultaneous multiple reactions to occur while reducing the risk of contamination and increasing efficiency. Electrophoresis is a method of separating macromolecules such as DNAs, Proteins, and cells by charge and size. Capillary electrophoresis on microfluidic chip devices can increase throughput and streamline the process that was conventionally time-consuming. A microfluidic channel is ranging from five to two hundred microns in diameter filled with a conducting buffer solution. The potential difference creates a current through the channel. Once current begins to flow, charged particles begin to flow. Because the rate of their flow is dependent on their charge, the DNA fragments are distributed by charge along the microchannels in a way similar to a conventional gel electrophoresis. Each well connects to an electrode. A voltage is selectively applied to each pair of wells to perform sample injection and separation.

V. COMMERCIAL DEVICES

5.1 The Fluidigm BioMark System

The Fluidigm BioMark System is the first commercial system for digital PCR-based on integrated microfluidic microchips with integrated chambers and valves for partitioning samples. Quake et al. at the California Institute of Technology developed the microfabrication technique in 1998. It is one of the many microfluidic systems produced that utilizes the NanoFlex valve on an integrated microfluidic chip for single cell gene expression profiling using digital PCR, genotyping, mutant detection, as well as real-time PCR. Fig. 3 shows the Fluidigm BioMark System.

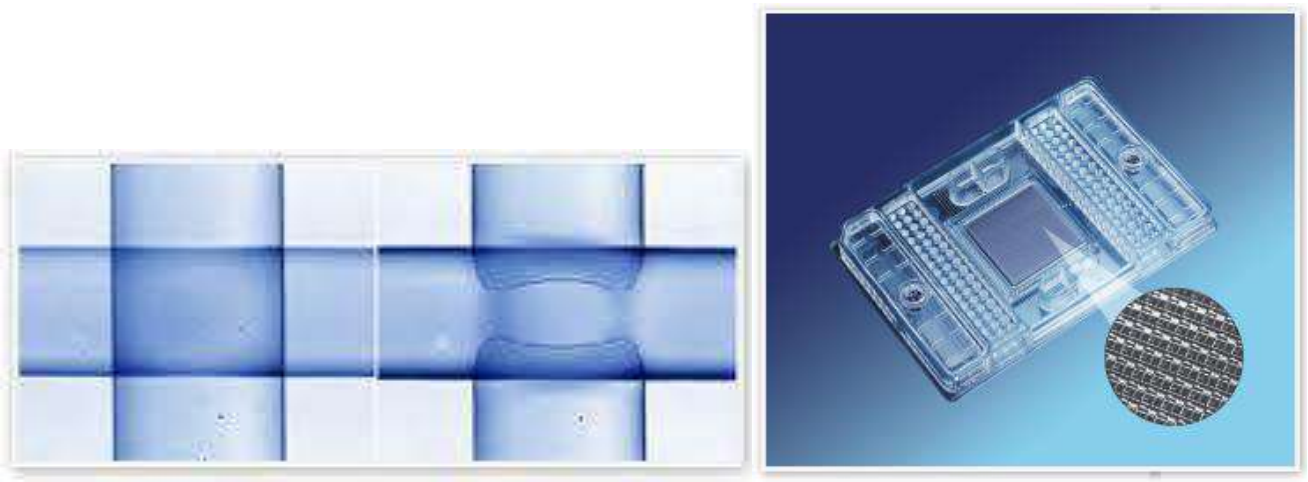

FIG. 3. THE FLUIDIGM BIOMARK SYSTEM WITH NANOFLEX VALVE [7].

5.2 Agilent LabChip

Agilent 2100 device is one of the most widely used commercial chip-based DNA analysis devices. They are manufactured from PDMS using soft lithography. The system uses interchangeable chips that interface with a bench-top device that acts as the power supply for electrophoresis and also contains the optical detection system. Fig. 4 shows the Agilent LabChip with its detailed processing steps.

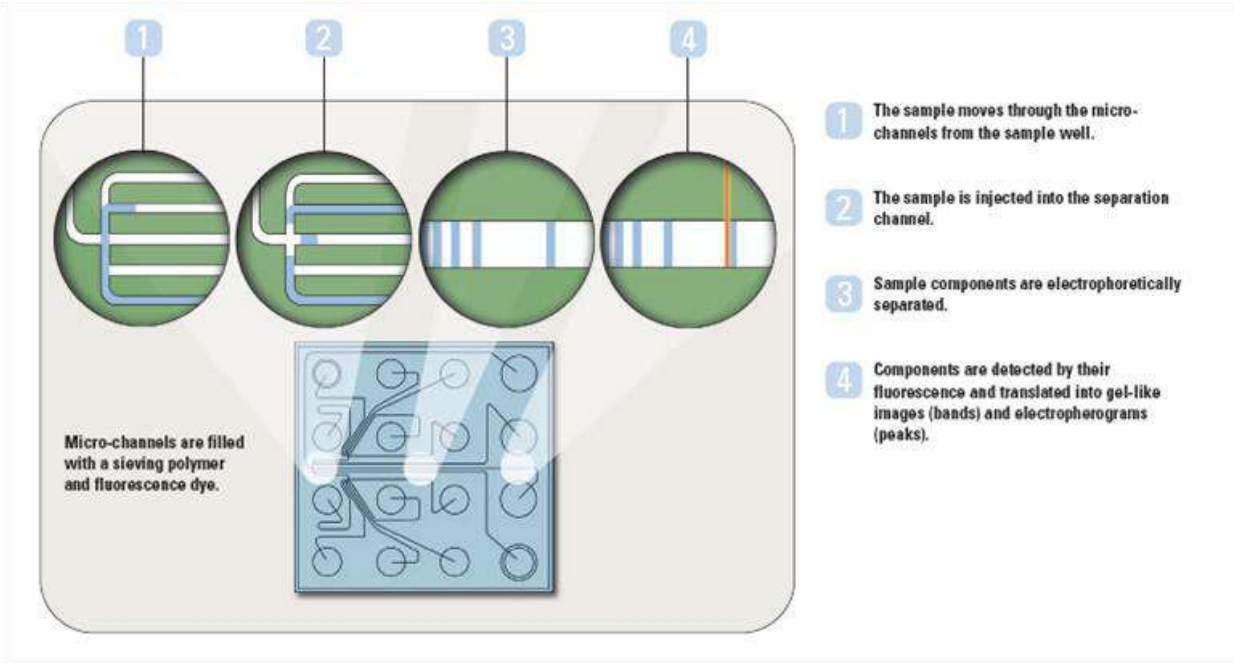

FIG. 4. AGILENT LABCHIP IS SHOWN WITH THE PROCESSING STEPS [8].

VI. DNA SENSOR METHODS

DNA sensors ought to detect, record, and indicate a physical or chemical property, with potential capability for further processing. DNA biosensor is a "compact logical device or unit incorporating a biological or biologically derived sensitive 'recognition' element integrated or associated with a physicochemical transducer [4]. Fig. 5 shows a typical structure of a biosensor. A sensor can be broken down into three elements: (1) recognition element, (2) transducer and (3) amplifier/processor. Recognition refers to binding of target molecules in our case the DNA. Binding of DNA induces the sensing effect, or the physical or chemical changes, due to a detection event. Desired characteristics for this stage include:

1. Selectivity – Only the target DNA generates sensing effect
2. Sensitivity – Large sensing effect with a small amount
3. Resolution – A good indication of the amount of captured DNA
4. Dynamic Range – Not saturated with a large quantity of DNA

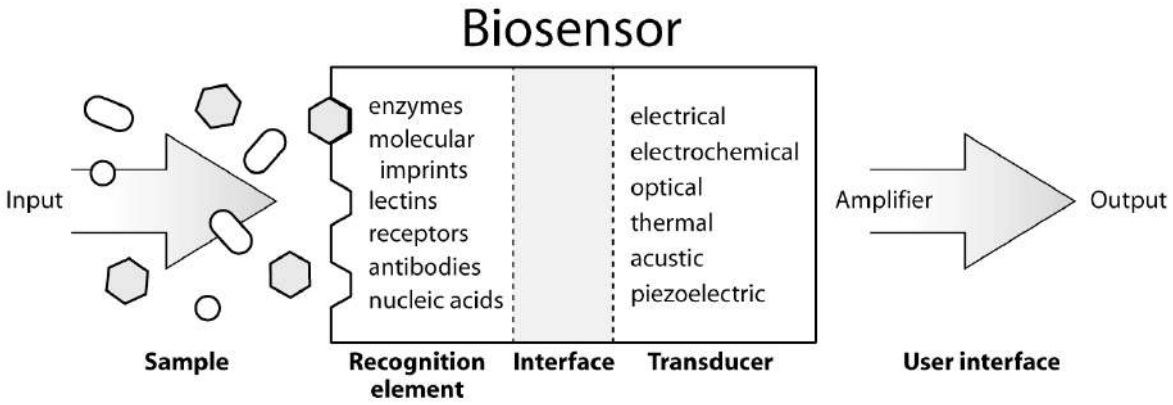

FIG. 5. THE CONFIGURATION OF A BIOSENSOR SHOWING BIO-RECOGNITION, INTERFACE, AND TRANSDUCTION ELEMENTS [4].

Transduction refers to the conversion of the detection event into a useful, measurable signal that is usually an electrical signal of either voltage or current [4]. Most transducers are physical sensors that convert the sensing effect of molecular binding into measurable electrical signals. The signal from the transducer has to be measured or recorded and interpreted as the

quantity of molecular activity. High levels or signal processing may be needed to retrieve meaningful data in most cases. Signal processing is performed mostly done by digital processors and computers [5]. Sensors through signal transductions convert the detection event into a measurable signal. Chemical, physical and biological quantities transformed into a detectable signal, mostly an electrical signal. DNA sensors fall into three types, namely optical transduction, electrical transduction, and mechanical transduction [5].

VII. OPTICAL BIOSENSOR

Optical biosensors are a powerful detection and analysis tool that has large applications in biomedical research, health- care, pharmaceuticals, environmental monitoring, and homeland security. They are immune to electromagnetic interference; capable of performing remote sensing, and can provide multiplexed detection within a single device. There are two screening protocols in optical biosensing: fluorescence-based detection and label-free detection [5]. A surface plasmon wave (SPW) is a charge density oscillation that occurs at the interface of two media with dielectric constants of opposite signs, such as a metal (gold or silver) and a dielectric. There are four basic methods to excite the SPR, as shown in Fig. 6: prism coupling, waveguide coupling, fiber optic coupling, and grating coupling. In the prism coupling configuration (Fig. 6(A)), the incident light is totally reflected at the prism–metal interface and generates an evanescent field penetrating into the metal layer. At the resonant angle or resonant wavelength, the propagation constant of the evanescent field matches that of the SPW, and as a result, the photon will have couple into the SPW [5].

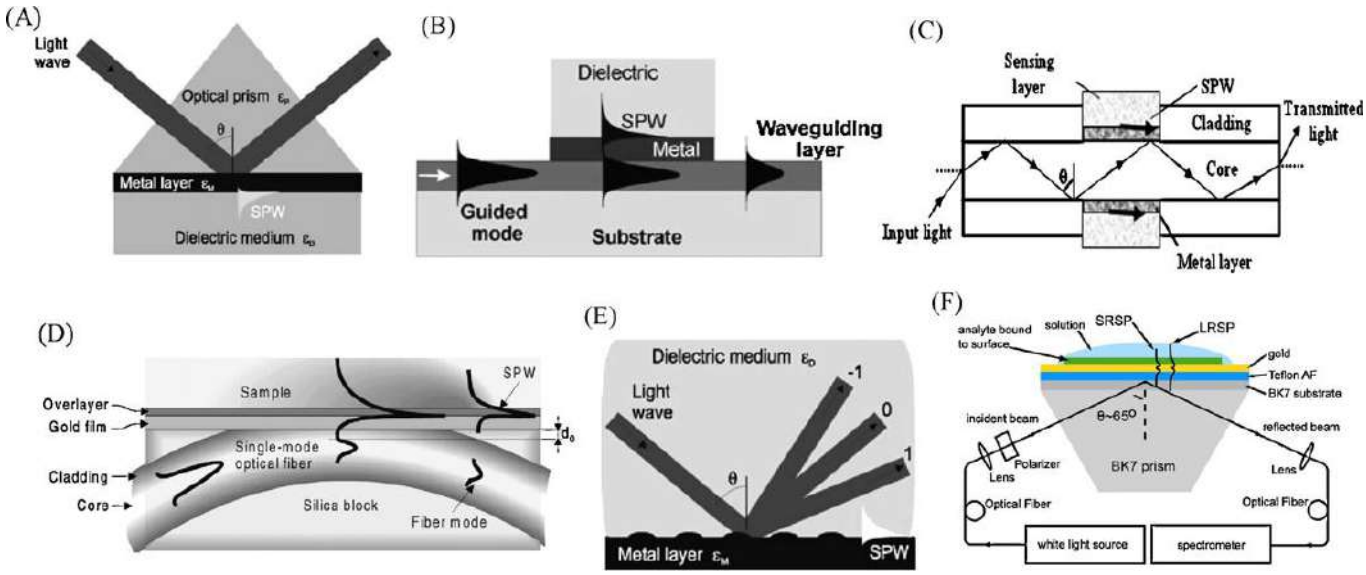

FIG. 6. VARIOUS SPR SENSOR CONFIGURATIONS. (A) PRISM COUPLING, (B) WAVEGUIDE COUPLING, (C) OPTICAL FIBER COUPLING, (D) SIDE-POLISHED FIBER COUPLING, (E) GRATING COUPLING AND (F) LONG-RANGE AND SHORT-RANGE SURFACE PLASMON [5].

The following research demonstrates a Localized Surface Plasmin Resonance (LSPR) Biosensor. The major discovery reported is that triangular silver nanoparticles fabricated by nanosphere lithography do indeed function as unexpectedly sensitive and selective nanoscale affinity biosensors. LSPR Nano sensors as shown in fig 7. possess at least two unique characteristics modified by changing nanoparticle size and shape: (1) modest refractive sensitivity on the order of 1 part in 102 and (2) a short-range, sensing length scale determined by the characteristic decay length of the local electromagnetic field. These two factors combine to yield an areal mass sensitivity of ~100-1000 pg/mm2, which is only a factor of 100 poorer than the best propagating SPR sensitivities. LSPR Nano sensors retain all of the other desirable features of SPR spectroscopy [6].

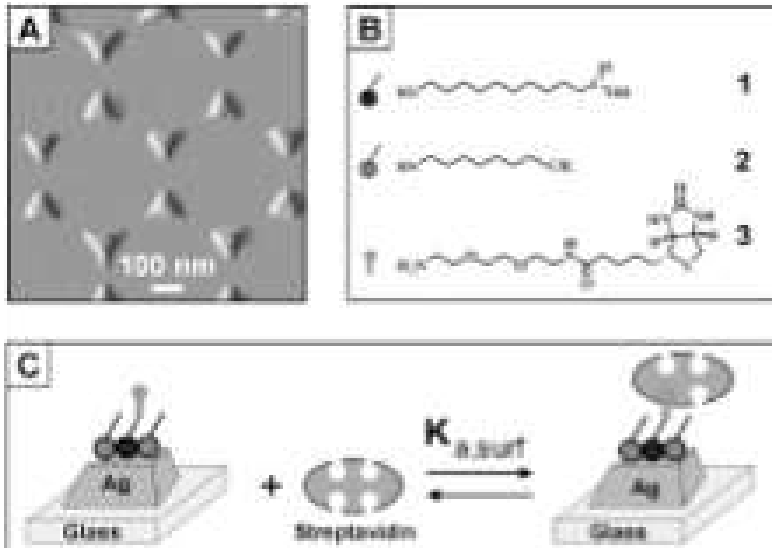

FIG. 7. LSPR NANOBIOSENSOR: (A) AFM IMAGE OF THE AG NANOPARTICLES. (B) SURFACE CHEMISTRY OF THE AG NANOBIOSENSOR. (C) SCHEMATIC REPRESENTATION OF SA BINDING TO A BIOTINYLATED AG NANOBIOSENSOR [6].

VIII. MECHANICAL BIOSENSOR

Mechanical interactions are fundamental to biology. Mechanical forces of synthetic origin determine motility and adhesion on the cellular scale and govern transport and affinity on the molecular level. Biological sensing in the mechanical devices provides unique opportunities to measure forces, displacements and mass changes from cellular and subcellular processes. A basic design of the cantilever chip is shown in fig. 8. Nanomechanical systems are particularly well matched in size with molecular interactions, and provide a basis for biological probes with single-molecule.

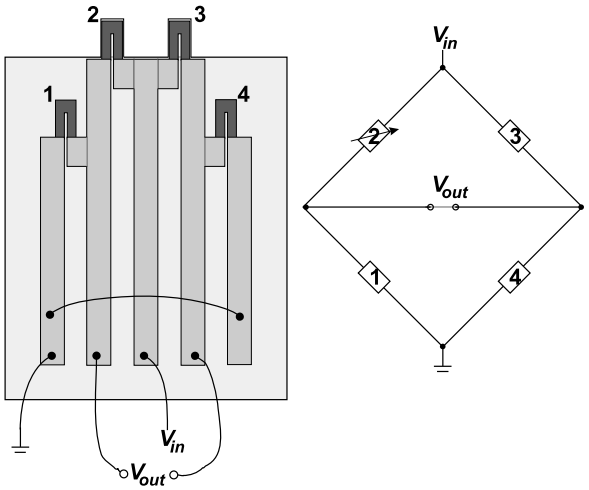

FIG. 8. THE BASIC DESIGN OF THE CANTILEVER CHIP WITH FOUR INTEGRATED PIEZORESISTORS PLACED IN AN ON-CHIP WHEATSTONE BRIDGE [9].

The following research presents a cantilever-based biochemical sensor with piezoresistive read-out as shown in figure 8, optimized for measuring surface stress. The resistors and the electrical wiring on the chip are encapsulated in Low-Pressure Chemical Vapor Deposition (LPCVD) silicon nitride so that the chip is well suited for operation in liquids. The wiring is titanium silicide, which in contrast to conventional metal wiring—is compatible with the high-temperature LPCVD coating process [9]. The 1/f noise is found from the measured spectral noise density shown in Fig. 9. The lowest curve is for no applied voltage and reflects the Johnson noise, whereas the other three curves show 1/f noise for three different supply voltages.

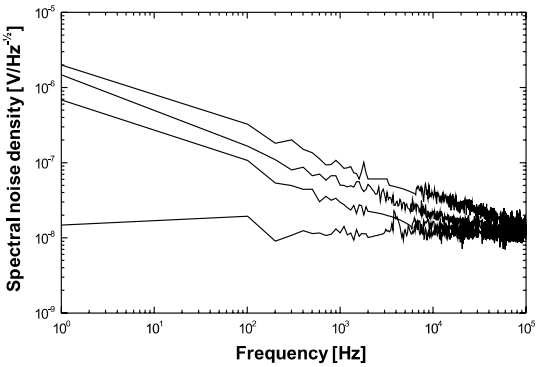

FIG. 9. SPECTRAL NOISE DENSITY CURVES AT DIFFERENT VOLTAGES [9].

IX. ELECTRICAL BIOSENSOR

Biosensors are electronic devices that produce electric signals as the result of biological interactions. A biosensor includes a natural receptor linked to an electronic transducer in such a way that biochemical activity converted into electrical activity [6]. The electronic component of the biosensor measures voltage (potentiometric), current (amperometric), light, sound, temperature, or mass (piezoelectric) [6].

The motivation of the thrombin FET biosensor came from this paper recently published, which uses functionalized nanotubes as a detection scheme. The ability to precisely control the size, shape and surface functionality of organic/inorganic materials is a necessity for contemporary developments in the fields of catalysts, batteries, electronic devices, drug delivery systems, and so forth. Recently, nanometer-sized particles with controlled shapes have aroused burgeoning interest because of the beneficial properties as a result of their high surface area and small dimensions. Over the last decade, in particular, numerous studies on the synthesis and physical properties of carbon nanotubes (CNTs) have been carried out and, in turn, have opened new avenues for advanced device applications. One notable example is the CNT-based biological sensing system [10]. A schematic representation of a nanotube sensor and corresponding sensitivity plot is shown in fig. 10.

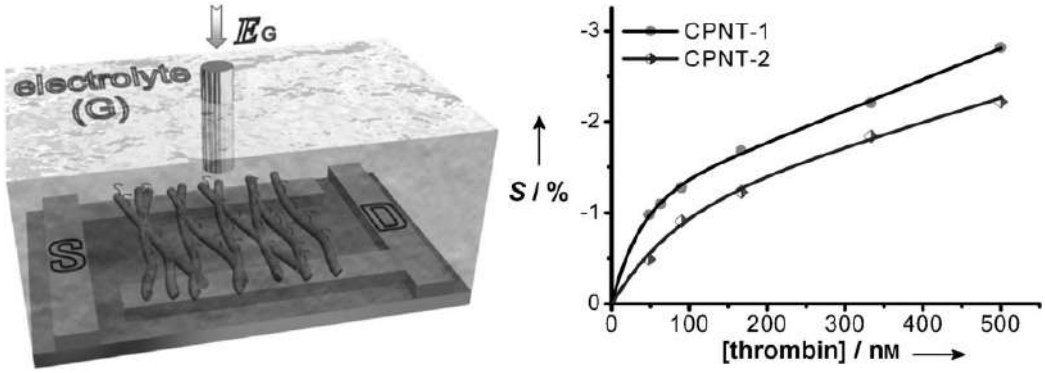

FIG. 10. SCHEMATIC REPRESENTATION OF CPPY NANOTUBE SENSOR AND GRAPH SHOWING SENSITIVITY OF THE SENSOR [10]

CPPy nanotubes with controlled chemical functionalities covalently immobilized onto the microelectrode substrate for high-quality electrical contact between polymer transducers and metal electrodes. Consecutively, thrombin aptamers readily tethered onto the nanotubes by covalent linkages with- out sophisticated surface treatment. Thus, this fabrication approach might present an efficient route for the construction of sensor platforms that based on nanoscale polymer transducers conjugated with molecular recognition elements. The FET-type sensors based on A CPPy nanotubes constructed by using liquid-ion gating. The recognition ability of thrombin aptamers, combined with the inherent charge transport property of CPPy nanotubes yielded a direct and label-free electrical readout [10].

Following research presents a novel silicon field effect transistor-based electrochemical sensor tailored to sense the protein thrombin. This novel device structure employs site-specific self-assembled silicon oxide-cladded silicon quantum dots (SiOx-Si QDs) as the gate material, replacing the conventional metal gate electrode. A functionalization process of QDs on the field effect transistor gate region proposed [11], where a single-stranded DNA (ssDNA) thrombin aptamer is covalently

attached to the QD surface, which specifically binds to thrombin as shown in figure 11. The sensing operation of the QD-gated FET operates by increasing the threshold voltage. This increase in threshold voltage was experimentally observed, in addition to the corresponding decrease of the MOSFETs drain current [11].

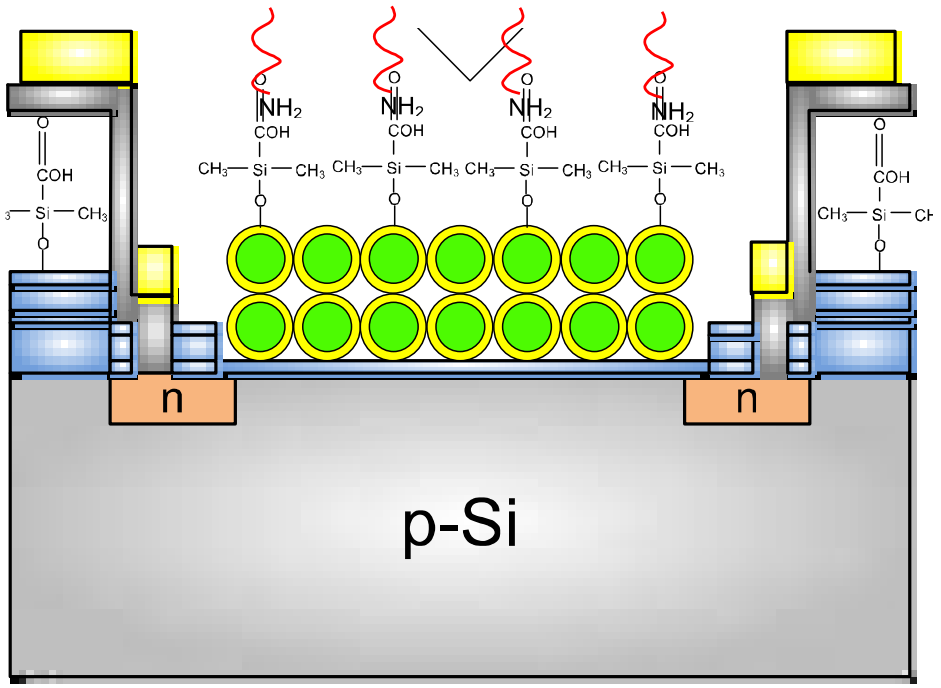

FIG. 11. QUANTUM DOT GATE FIELD EFFECT TRANSISTOR THROMBIN BIOSENSOR [11]

Figure 12 below shows the ID-VG and ID-VD transfer characteristics, respectively, of the fabricated transistor having a W/L ratio of 10µm / 26µm. As evident from the features, the substitution of the conventional metal gate electrode with site-specific self-assembled SiOx-cladded Si quantum dots atop a 40Å thermally grown gate insulator demonstrates the feasibility of configuring a QD gate FET as a biosensing device.

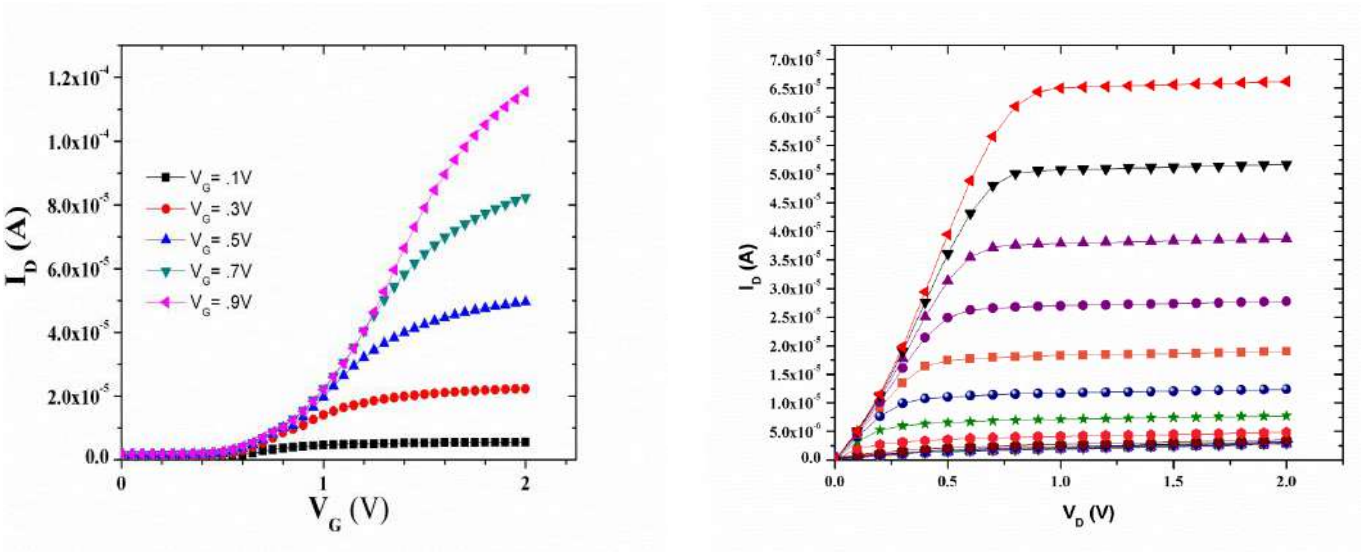

FIG. 12. ID-VG AND ID-VD TRANSFER CHARACTERISTICS OF THE LIQUID TOP-GATED QUANTUM DOT FET [11].

As evident from Figure 13, there is a definite increase in threshold voltage as higher Thrombin concentration is present at the gate, according to the threshold voltage equation for an NMOS transistor.

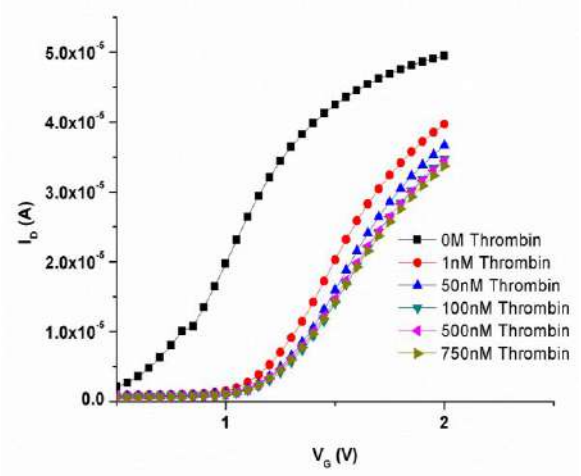

FIG. 13. ID-VG TRANSFER CHARACTERISTICS OF THE SSDNA THROMBIN APTAMER FUNCTIONALIZED QDG GET WITH ADDITIONS OF THROMBIN PROTEIN [11]

X. CONCLUSION

Microfluidics offers revolutionary new capabilities for the future of DNA sensing. The manipulation of small volumes of fluid with precise dynamic control over concentrations provides the key to advancement. The paper gives a detailed insight into the world of novel biosensors and it's feasibility. It also introduces the audience to the importance of microfluidics and its application in DNA sensing technologies. Commercially available devices for DNA separation and analysis are explored. Nanotechnology enables development of vast types of sensors to analyze metabolites that in turn drives the diagnostic methods in medicine and research.

REFERENCES

[1] Whitesides, G. M. (2006). The origins and the future of microfluidics. *Nature*, *442*(7101), 368-73. doi:10.1038/nature05058

[2] Dittrich, P. S., & Manz, A. (2006). Lab-on-a-chip: Microfluidics in drug discovery. *Nature Reviews. Drug Discovery*, *5*(3), 210-218. doi:10.1038/nrd1985

[3] Tegenfeldt, J. O., Prinz, C., Cao, H., Huang, R. L., Austin, R. H., Chou, S. Y., . . . Sturm, J. C. (2004). Micro- and nanofluidics for DNA analysis. *Analytical and Bioanalytical Chemistry*, *378*(7), 1678-1692. doi:10.1007/s00216-004-2526-0

[4] Chambers, J. P., Arulanandam, B. P., Matta, L. L., Weis, A., & Valdes, J. J. (2008). Biosensor recognition elements. *Current Issues in Molecular Biology*, *10*(1-2), 1. doi:10.21775/cimb.010.001

[5] Fan, X., White, I. M., Shopova, S. I., Zhu, H., Suter, J. D., & Sun, Y. (2008). Sensitive optical biosensors for unlabeled targets: A review. *Analytica Chimica Acta*, *620*(1-2), 8-26. doi:10.1016/j.aca.2008.05.022

[6] Haes, a. J., & Van Duyne, R. P. (2002). A nanoscale optical biosensor: Sensitivity and selectivity of an approach based on the localized surface plasmon resonance spectroscopy of triangular silver nanoparticles. *Journal of the American Chemical Society*, *124*(35), 10596-10604. doi:Article

[7] Fluidigm. (2014). Www.fluidigm.com. Retrieved from https://www.fluidigm.com/products/biomark-hd-system

[8] Agilent. (2014). Http://Www.genomics.agilent.com/. Retrieved from http://www.genomics.agilent.com/en/Bioanalyzer-System/2100-Bioanalyzer-Instruments/?cid=AG-PT-106&tabId=AG-PR-1001

[9] Rasmussen, P. A., Thaysen, J., Hansen, O., Eriksen, S. C., & Boisen, A. (2003). Optimised cantilever biosensor with piezoresistive read-out. *Ultramicroscopy*, *97*(1-4), 371-376. doi:10.1016/S0304-3991(03)00063-9

[10] Yoon, H., Kim, J., Lee, N., Kim, B., & Jang, J. (2008). A novel sensor platform based on aptamer-conjugated polypyrrole nanotubes for label-free electrochemical protein detection. *Chembiochem : A European Journal of Chemical Biology*, *9*(4), 634-641. doi:10.1002/cbic.200700660

[11] Croce, R. A., Jr. (2012). Functionalization and characterization of nanomaterial gated field-effect transistor-based biosensors and the design of a multi-analyte implantable biosensing platform Available from Available from Dissertations & Theses @ University of Connecticut; ProQuest Dissertations & Theses Global. (1239427597).
(http://ezproxy.lib.uconn.edu/login?url=http://search.proquest.com.ezproxy.lib.uconn.edu/docview/1239427597?accountid=14518). doi:1239427597

Effect of Solid Particle Density on Hydraulic Performance of a Prototype Sewage Pump

Xiao-Jun Yang[1], Yu-Liang Zhang[2], Zhen-Gen Ying[3], Yan-Juan Zhao[4]

[1,2,3]College of Mechanical Engineering, Quzhou University, Quzhou 324000, China
[4]College of Information Engineering, Quzhou College of Technology, Quzhou 324000, China

Abstract**—** *A frozen rotor method based on a mixture multiphase flow model, an RNG k–ε dual-equation turbulence model, and a SIMPLE algorithm is used to perform a numerical simulation of steady flow in a sewage pump that transports solid and liquid phase flows. The method is also utilized to analyze the effect of solid-phase particle density on the hydraulic performance of the sewage pump and predict the wear degree of the overflow components. Results of the study indicate that with the increasing density of solid particles, the head curve of the pump initially decreased and then increased, that is, the head curve had the minimum value. Additionally, the efficiency curve of the pump increased, decreased, and then increased again, indicating an insignificant overall change. Meanwhile, the pump shaft power showed a monotonic upward trend. When the solid-phase density is less than, equal to, and greater than the liquid-phase density, solid-phase concentration on the blade pressure surface shows a distribution law more than, equal to, and less than 10%, respectively. With the increase in density of the delivered solid particles, solid-phase concentration on the blade pressure surface shows a decreasing trend.*

Keywords**— sewage pump, particle density, frozen rotor method, numerical calculation.**

I. INTRODUCTION

Sewage pumps consist of both solid- and liquid-phase flow pumps and are key equipment for urban channel cleanout. Many scholars at home and abroad have carried out in-depth and meticulous research on sewage pumps and have achieved productive results. Engin et al considered a centrifugal pump with a semi-closed impeller as the object of study to compare the performance of the pump in delivering water, sand, and other media with different hardness. They likewise provided a conclusion regarding the relationship between particle size and pump performance. The deviation between predicted and measured values of the solid- and liquid-phase head of delivery was –20~+15% [1]. Gandhi et al. carried out an experimental study on the performance of a centrifugal pump with a closed impeller in delivering water, mortar, and a solid–liquid mixture of zinc tailings. When the solid concentration was smaller than 20%, the relationship between the pump head and the flow could be confirmed through the relational expression of the water's working conditions. When the solid concentration was higher than 20%, the effect of solid particles on the pump performance should be considered [2]. Yuan et al. carried out a numerical simulation of solid–liquid two-phase turbulence inside a non-overloaded mud pump [3]. Findings suggested that backflow occurred in the inlet and velocity slip between two phases, and turbulent kinetic energy and dissipation rates reached their peaks at the junction of the pressure surface and the suction surface. Li et al. conducted an experimental study on the effect of solid particle properties, including concentration and particle size, on the external characteristics of centrifugal pumps[4]. Under the working condition of small flow, efficiency value increased slightly, the stable working area decreased, and the optimal efficiency point moved to the small flow direction. Zhang et al. performed a numerical research on solid–liquid two-phase flow field in a low specific speed centrifugal pump by means of numerical calculation [5]. The obvious jet flow-wake structure occurred near a volute tongue, and it was more obvious with the increase of volume fraction. Zhang et al. made a numerical simulation of the start-up characteristics of a high specific speed centrifugal pump for solid–liquid two-phase flow by means of a dynamic grid [6]. Harry et al. carried out an experimental study on a centrifugal pump blade made of high chromium white iron and aluminum alloy through a Coriolis experiment [7] to obtain different wear modes on the centrifugal pump blade as it delivers mud. Veselin et al. put forward a new wear prediction method based on a fast experiment and mathematical analysis [8] to substitute a costly and time-consuming traditional slurry pump wear test with weak applicability. The error between the predicted results and the experimental results was less than 3%. Pagalthivarthi et al. studied the effects of operational parameters, pump flow and velocity, particle diameter, different geometries, curve of tongue, and width of volute on erosion wear on particles through a numerical calculation [9]. Dong et al. conducted a study and found that particle size and shape, liquid velocity, and other flow parameters had a great impact on erosion pit on the surface of wet parts, and that the degree of distortion and maximum stress of the pit increased with the increase of particle size [10]. Li et al. revealed the impact of internal flow characteristics on the wear characteristics of solid–liquid two-phase centrifugal pump [11].

Therefore, studying the internal flow of the pump to provide a theoretical basis for realizing a high-performing and stable-operating pump design is needed. The present study aims to conduct a numerical simulation and analysis on solid-liquid two-phase flow pump to analyze the impact of the density of solid-phase particles on sewage pump performance, including the hydraulic performance of sewage pump and wear degree of wet parts.

II. PUMP MODEL AND CALCULATION METHOD

2.1 Pump model and computational grid

The pump model used for the computation was a medium specific speed centrifugal pump, with a specific speed of n_s=129.3. Its basic performance parameters were as follows: flow rate Q=50m^3/h, head H=20.54m, velocity n=2900r/min, shaft power P_a=3.54kW, efficiency η=79.5% and net positive suction head $NPSH_C$=2.59m. The main dimensions of the pump were as follows: inlet diameter D_j=76mm, hub diameter d_h=0mm, impeller outlet diameter D_2=137mm, impeller outlet width b_2=14mm, blade outlet angle β_2=30°, blade number Z=6, blade wrap angle =104.5°, volute base circle diameter D_3=145mm, and volute inlet width b_3=30mm.

2.2 Computational grid

The commercial software UG was used to create a 3D model of the internal computing area. The appropriate extension of the straight-tube suction chamber was made to eliminate the influence of the given inlet speed. An appropriate extension of the pump outlet was also carried out to better calculate convergence. As shown in Fig.1, the commercial grid partitioning software GAMBIT2.3.16 was used to create a grid division of the computational domain. Tetrahedral meshes were adopted in the impeller rotation region and volute static region, with mesh numbers 435,530 and 597,127 respectively. Hexahedral meshes were used in the suction chamber and outlet extension, with mesh numbers of 152,827 and 54,944 respectively. The total mesh number of the overall computational domain was 1,240,428. This number was not enough to simulate the micro flow in the boundary layer of simulation but was sufficient for the macro flow and macro characteristic capturing in the pump. Mesh quality checking revealed that the equiangular slope and equidimensional slope of the mesh were not more than 0.83.Mesh quality was good at around 30 near wall Y+.

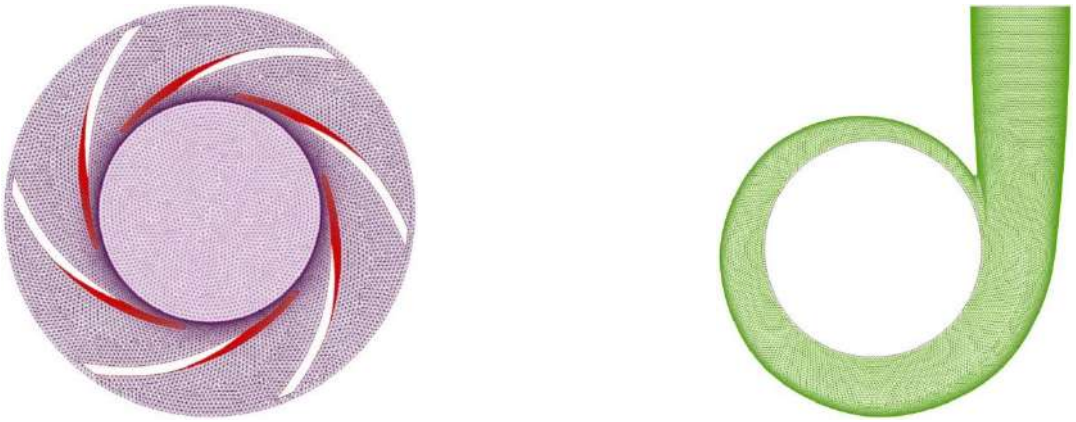

(A) IMPELLER AREA **(B) VOLUTE AREA**

FIG.1 COMPUTATIONAL MESH

2.3 Governing equations

The 3D unsteady turbulent flow of incompressible fluid in a centrifugal pump can be described by Reynolds-averaged equations.

$$\begin{cases} \dfrac{\partial \overline{u}_i}{\partial x_i} = 0 \\ \rho \dfrac{\partial \overline{u}_i}{\partial t} + \rho \overline{u}_j \dfrac{\partial \overline{u}_i}{\partial x_j} = \rho F_i - \dfrac{\partial \overline{p}}{\partial x_i} + \mu \dfrac{\partial^2 \overline{u}_i}{\partial x_j \partial x_j} - \rho \dfrac{\partial}{\partial x_j}\left(\overline{u_i' u_j'}\right) \end{cases} \tag{1}$$

Where prefers to fluid density, and $-\rho\overline{u_i' u_j'}$ refers to mean Reynolds stress.

Unsteady turbulent flow calculation used in the present study used the RNG k–ε two-equation model to close the mean Reynolds stress. RNG k–ε turbulent model, which considers the rotation and swirling flow in the mean flow, can better process the flow with high strain rate and great streamline curvature.

2.4 Multiphase flow model

This study aims to make a 3D turbulent flow calculation of incompressible viscous fluid by using the commercial code FLUENT software based on a finite volume method. The multiphase flow model in numerical computation used the algebraic slip mixture model [12] based on Euler's method to complete the calculation of solid–liquid two-phase flow. In the calculation, the particles were treated as quasi fluid.

2.5 Solution settings

The dynamic and static coupling between rotor and stator in numerical calculation was achieved by means of the frozen rotor method. Velocity inlet and free output were respectively used as the boundary conditions of the inlet and outlet. No-slip boundary condition was applied on all solid walls considering viscosity, and standard wall function was used in near-wall low Reynolds number region to deal with the problem from the high Reynolds number turbulence model. The coupling between velocity and pressure was calculated by using SIMPLE algorithm. First-order upwind scheme was used for the spatial discretization of the convection term. The central difference scheme with two-order accuracy was used for the spatial discretization of diffusion terms. The linear standard format was used for spatial discretization of the source terms considering that solid particles were uniform spherical particles with unchanged physical properties. The convergence criterion of each control equation was 0.0001.

2.6 Computational scheme

To explore the effect of solid-phase properties on hydraulic transport performance as the sewage pump delivers solid–liquid two-phase flow, the following computational scheme was formulated:

Under a designed flow rate (Q=50m^3/h) with10%solid-phase concentration and 0.10mmparticle diameter, numerical calculation was conducted for a solid–liquid two-phase flow field under five conditions when the particle densities were 500, 1000, 1500, 2000,and 2500kg/m^3.

III. ANALYSIS OF RESULTS

3.1 External characteristics

Pump inlet and outlet pressures and the external characteristics under five particle densities obtained from the numerical calculation are shown in Figs.2 and 3. In Fig. 2, the densities of solid particles in delivering solid–liquid two-phase flow were 500, 1000, 1500, 2000, and 2500kg/m^3. The values of total pressure at pump inlet were-0.259,-0.281, -0.302, -0.323, and -0.358kPa, respectively, and the values of total pressure at pump outlet were 128.582, 133.377, 138.662, 146.071, and 153.524, respectively. With the increase of the density of solid particles, the total pressures of the pump inlet and of the pump outlet showed a trend of monotonic decline and rising. The calculation result of external characteristics in Fig.3 shows that when the densities of solid particles in solid–liquid two-phase flow were 500, 1000, 1500, 2000, and 2500kg/m^3, the calculated heads were 14.00, 13.80, 13.66, 13.74, and 13.81, respectively, and the calculated efficiencies were 47.02%, 47.17%, 47.097%, 47.36%, and 47.49%,respectively. The calculated shaft powers were 3.850, 3.982, 4.145, 4.344, and 4.551kW, respectively. With the increase of the density of solid particles, the pump head curve showed an initially decreasing then increasing trend and reached the minimum value of 13.66m when the density of solid particles was 1500kg/m^3.The pump efficiency curve showed an initially increasing then decreasing trend. Nevertheless, the absolute value of the overall change was not significant. At the same time, pump shaft power showed a monotonic upward trend.

Previous research has shown that under the assumption of non-viscous and non-granular force, the equation met by solid-liquid two-phase flow in the impeller is deduced theoretically. Based on the conclusion, the pump head delivering two-phase flow was lower than the head delivering liquid-phase flow when the particle density was more than the liquid-phase density. On the contrary, the pump head increased. The calculation results in this study proved that the conclusion is completely correct.

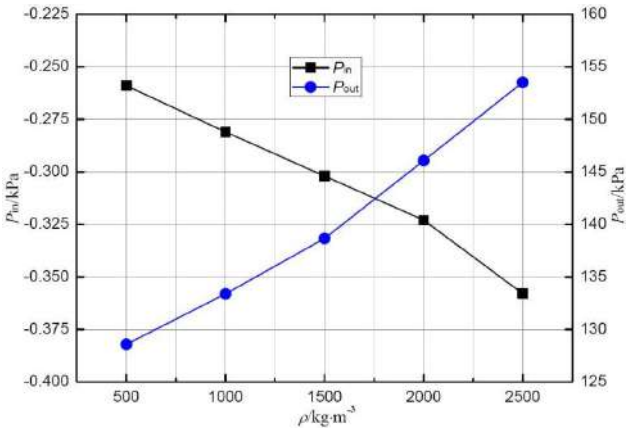

FIG.2 EFFECTS OF PARTICLE DENSITY ON PUMP INLET AND OUTLET PRESSURES

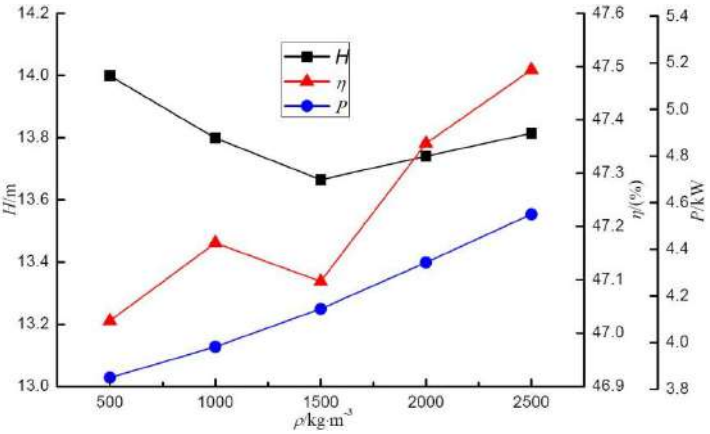

FIG.3 EFFECTS OF PARTICLE DENSITY ON THE EXTERNAL CHARACTERISTICS OF THE PUMP

3.2 Pressure surface characteristics

The effects of the density of solid particles obtained from the numerical calculation on the performance parameters of blade pressure surface are shown in Fig.4. Fig. 4(a) shows the influence of total pressure distribution along the blade. The total pressure on the blade pressure surface increased with the increase of the semi diameter. Findings also showed that the second half of the blade pressure surface was the main point of the increase in pressure. Meanwhile, with the increase of the density of solid particles, total pressure on the blade pressure surface showed a gradual increasing trend. The corresponding densities of solid particles were 500, 1000, 1500^3, 2000, and 2500kg/m^3. In the front of the blade pressure surface, the total pressures were 11.488, 10.490, 7.918, 6.820, and 6.419kPa, respectively. When the relative length of the middle of blade was 0.5, total pressures were 162.641, 161.726, 160.032, 163.475, and 167.60kPa.In the tailing of the blade pressure surface, total pressures were 202.057, 207.212, 209.95, 215.042, and 221.334kPa. In the tailing of the blade pressure surface, total pressure drop occurred due to the influence of jet-wake flow.

Fig. 4(b) shows the obtained distribution of solid-phase concentration on the blade pressure surface. Under different densities of delivering particles, the solid-phase concentration on the blade pressure surface showed a completely opposite distribution status. In the case of particle density (500 kg/m^3), the density of solid-phase concentration was smaller than the density of delivering medium water (1000kg/m^3). The solid-phase concentration on the blade pressure surface was more than 10% because when particle density is lighter than water, particles suspend in the water medium. Under centrifugal force and blade force, solid particles suspended in the water medium gather on the blade pressure surface, causing solid-phase concentration to significantly increase from the front edge of the blade. Findings indicated that, in this case, the blade pressure surface bore more severe dynamic attacks and wears. However, in consideration of the small density of solid particles, wear degree will be further studied. In the front edge, middle, and tailing of the blade pressure surface, instantaneous solid concentrations were 10.382%, 16.544%, and 12.257%, respectively. When the delivered solid-phase density was 1000kg/m^3, solid-phase density was completely equal to water density, and solid phase was equal to water medium. These factors were completely mixed together and suspended. Therefore, the calculation result showed that the solid-phase density on the overall blade pressure surface is always about 10%, which is equal to the calculated solid-phase density of the incoming flow. Findings revealed that the wear on the blade pressure surface was completely similar. In three cases, the densities of solid particles were 1500, 2000, and 2500kg/m^3. Starting from the front edge of the blade pressure surface, the concentration of solid-phase particles gradually decreased and dynamically stabilized. Solid-phase concentration was smaller than 10%, which indicated that, in these three cases, the wear on the blade pressure surface was not severe. Large densities of particles also entailed large inertial force of particles. Although particle concentration was not high, a greater degree of wear still occurred. This finding needs further confirmation. In the three cases presented, the instantaneous solid-phase concentrations in the front edge of the blade pressure surface were 9.878%, 10.048%, and 10.187%,respectively.In the middle of the blade pressure surface, instantaneous solid-phase concentrations were 6.15%, 4.48%, and 3.343%, respectively. In the tailing of the blade pressure surface, instantaneous solid-phase concentrations were 8.275%, 7.536%, and 6.908%, respectively. With the increase in density of delivering solid particles, solid-phase concentrations on the blade pressure surface showed a gradual declining trend. This finding indicated that the degree of wear increasingly lessened, which was mainly related to the inertial

force of solid particles. If the inertial force was greater, the ability of particles to escape from the restraint of the blade pressure surface would be stronger; otherwise, it would be weaker.

In terms of vorticity [Fig.4(c)], the densities of solid particles in five cases were 500, 1000, 1500, 2000,and 2500kg/m^3,respectively.At position 0.2, which was relatively long from the front edge of the blade pressure surface, the obtained vorticity values were 4723.99, 5467.7, 5922.38, 6000.75,and 6016.79s^{-1}; at position 0.5, the obtained vorticity values were 4998.75,6544.94,7552.63,7804.41,and 7883.16s^{-1},respectively; and at position 0.8, the obtained vorticity values were 8780.93, 9692.48, 10462.4,10838.3,and 10958s^{-1},respectively. With the increase in density of delivering particles, the vorticity value on the blade pressure surface showed an increasing trend.

For turbulent kinetic energy [Fig.4 (d)], turbulent dissipation rate [Fig.4(e)], and turbulence intensity [Fig.4(f)], the changing characteristics were generally consistent. In five cases, the densities of delivering solid particles were 500, 1000, 1500, 2000,and 2500kg/m^3,respectively.At position 0.5, which was relatively long from the front edge of the blade pressure surface, turbulent kinetic energies were 4.36109, 3.18985, 2.20454, 1.66049,and 1.28034m^2·s^{-2},respectively; turbulent dissipation rates were 22872.9, 14340.3, 8247.05, 5389.18,and 3650.25m^2·s^{-3},respectively; and turbulence intensities were 1.636%, 1.395%, 1.164%, 1.015%, and 0.897%. With the increase in density of delivering solid particles, the turbulence effect on blade pressure surface decreased gradually, and flow was more stable. However, in terms of any kind of delivery concentration, turbulent kinetic energy, turbulent dissipation rate, and turbulence intensity, the minimum value from the front edge gradually decreased and then increased.

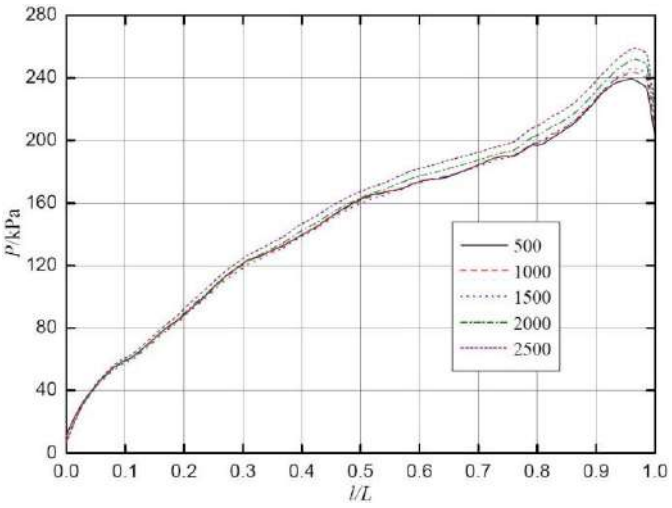

(A)TOTAL PRESSURE

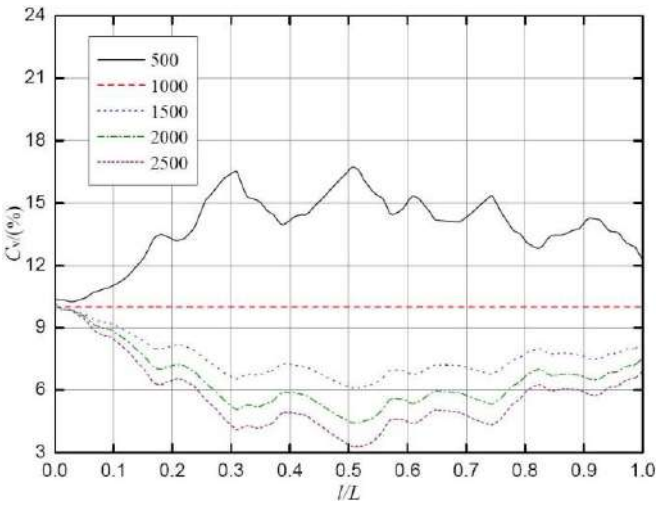

(B)SOLID-PHASE CONCENTRATION

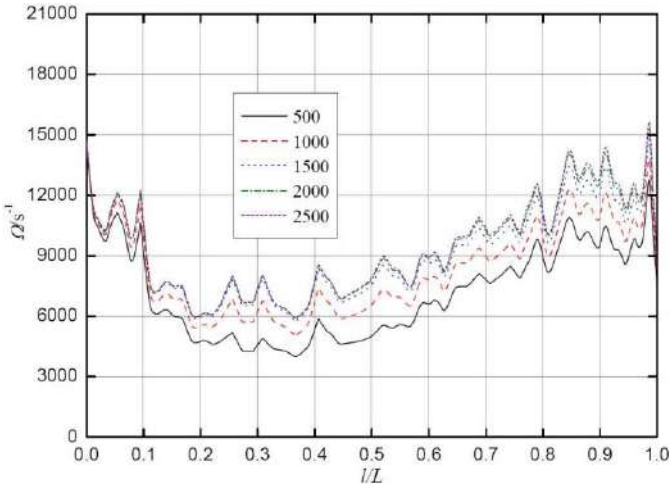

(C)VORTICITY

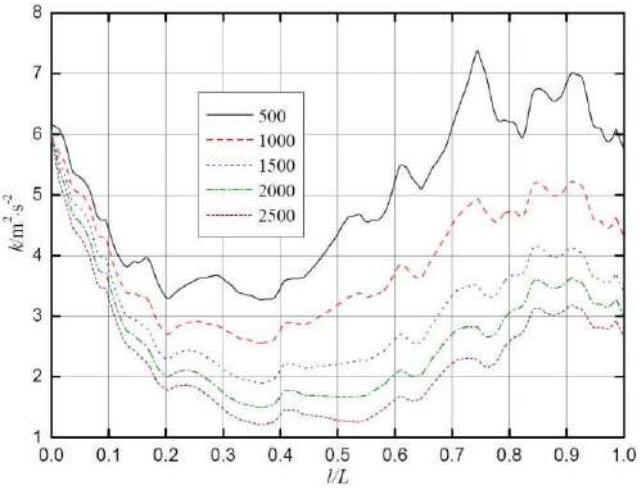

(D)TURBULENT KINETIC ENERGY

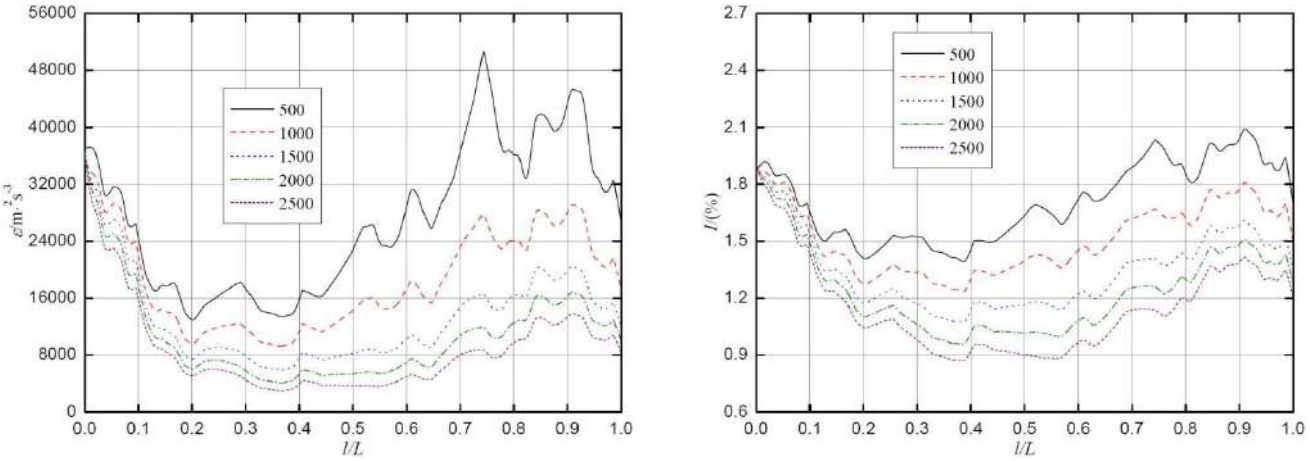

(E)TURBULENT DISSIPATION RATE **(F)TURBULENCE INTENSITY**

FIG.4 EFFECTS OF PARTICLE DENSITY ON THE PERFORMANCE PARAMETERS OF BLADE PRESSURE SURFACE(kg/m^3)

3.3 Suction surface characteristics

The effect of the density of solid particles obtained from the numerical calculation on the performance parameters of the blade suction surface is shown in Fig.5. Fig.5 (a) shows the influence of total pressure on the distribution along the blade. For any density of delivered solid particles, total pressure increased from the front edge of the suction surface with the constant increase of the blade's semi-diameter. At the place near the outlet of the suction surface, a sudden drop phenomenon occurred similar to the previous occurrence. In five cases, the densities of delivering solid particles were 500, 1000, 1500, 2000,and 2500kg/m^3, respectively. At position 0.10, which was relatively long from the front edge of the blade suction surface, the obtained total pressures were -5.459, -6.553, -7.449, -8.192, and -9.021kPa, respectively. At position 0.40, the obtained total pressures were 35.215, 35.728, 35.469, 35.593, and 35.880kPa, respectively. In the scope of 0.4, which was in the first half of the blade suction surface, the effect of the variation in the solid particle densities on the rise of total pressure was not significant. In the scope apart from this site, the total pressure on the blade suction surface showed an increasing trend with the increase in the density of delivering solid particles, in which the density of solid particles mainly affected the second half of the blade suction surface. At position 0.70, the obtained total pressures were 125.945, 142.46, 160.267, 176.806, and 190.735kPa, respectively. At position 0.90, the obtained total pressures were up to 208.003, 235.989, 269.077, 306.533, and 339.416kPa, respectively.

The effect of the density of delivering solid particles obtained from the numerical calculation on the distribution of solid-phase concentrations on the blade suction surface are shown in Fig. 5(b). In terms of the medium with the 1000 kg/m^3density of delivering particles, the solid-phase concentration on the blade suction surface obtained from the calculation was 10%. Apparently, the reason for this finding was that the solid-phase density was the same as the liquid-phase density. When both of these factors had the same density, the solid phase was equal to the liquid phase, free and uniformly distributed. However, in the following four cases, the densities of solid particles were 500, 1500, 2000,and 2500kg/m^3 before and after the position that was relatively0.25 long from the front edge of the blade suction surface; the distribution laws of solid-phase concentration were completely opposite. Before position 0.25, the solid-phase concentrations on the blade suction surface showed a declining trend with the increase of the density of solid particles, and after position 0.25, solid-phase concentrations on the blade suction surface showed an increasing trend with the increase of the density of solid particles. For example, at position 0.10, the solid-phase concentrations on the blade suction surface in the above four cases were 11.229%, 8.724%, 7.963%, and 7.338%, respectively; and at position 0.80, the solid-phase concentrations on the blade suction surface in the above four cases were 5.868%, 19.458%, 28.393%, and 32.351%, respectively. In the middle and late parts on the blade suction surface, solid-phase concentrations on the blade suction surface gradually reduced when the density of solid particles was smaller than that of water. This finding indicated that the degree of wear also constantly decreases. Under the condition that the density of solid particles was greater than water density, solid-phase concentrations on the blade suction surface gradually increased. This result indicated that the degree of wear constantly increases. However, in the small part from the front edge of the blade suction surface, the changing trends of both these factors were opposite, revealing that the degrees of wear were also opposite.

Fig.5(c) shows the vorticity distribution on the blade suction surface in cases of different densities of delivering solid particles. Vorticity distribution characteristics in five kinds of delivering density were basically the same, showing a gradually declining trend from the front edge of the blade suction surface. Furthermore, the effect of different densities on vorticity values was not significant.Figs.5(d), 5(e), and5(f) show the respective distributions of turbulent kinetic energy, turbulent dissipation rate, and turbulence intensity along the blade suction surface under different densities of delivering solid particles. Generally, these factors had similar changing characteristics, namely, increasing with the increase of the densities of delivering solid particles. Three parties reflected time-averaged characteristics of turbulence.

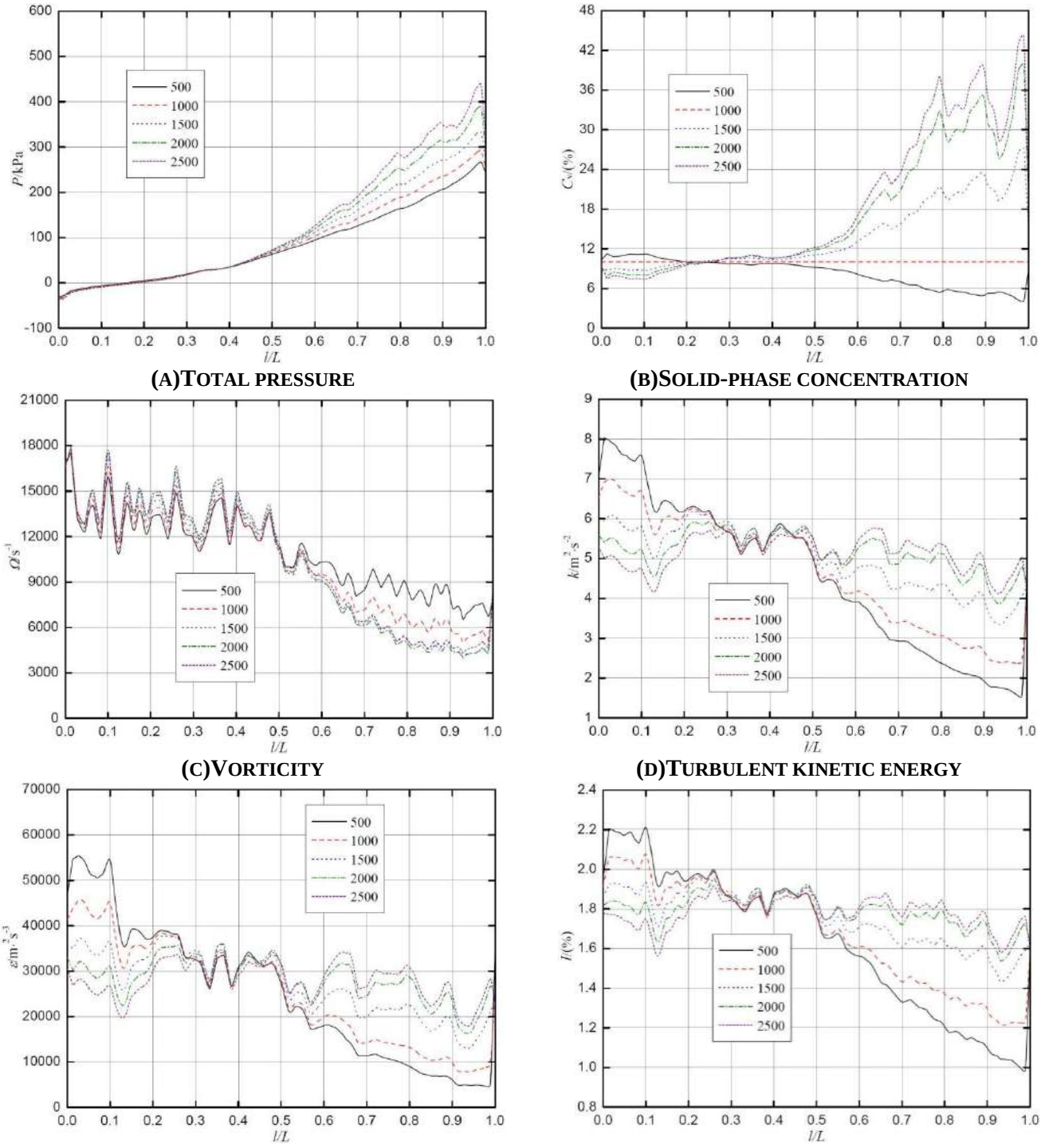

(A)TOTAL PRESSURE **(B)SOLID-PHASE CONCENTRATION**

(C)VORTICITY **(D)TURBULENT KINETIC ENERGY**

(E)TURBULENT DISSIPATION RATE **(F)TURBULENCE INTENSITY**

FIG.5 EFFECTS OF PARTICLE DENSITIES ON THE PERFORMANCE PARAMETERS OF BLADE SUCTION SURFACE(kg/m^3)

3.4 Particle concentration on the blade pressure surface

Fig. 6 shows the distribution of particle concentration on the blade pressure surface in five densities of delivering solid-phase particles. The figure illustrates that when particle density (500 kg/m^3) is smaller than liquid-phase (water) density, the solid-phase concentrations on two sides of the blade pressure surface are considerably higher; when the density of solid-phase particles (1000 kg/m^3) was equal to liquid-phase density, the distribution of solid-phase concentration on the blade pressure surface was more uniform. This result is clearly related to their similar densities. In three cases where the densities of delivering solid-phase particles were 1500, 2000, and 2500kg/m^3, with the increase of the density of delivering solid particles, the distribution area of solid-phase concentration on the pressure surface shrank to the inlet. This finding indicated that the wear area and the wear degree on the blade pressure surface decreased.

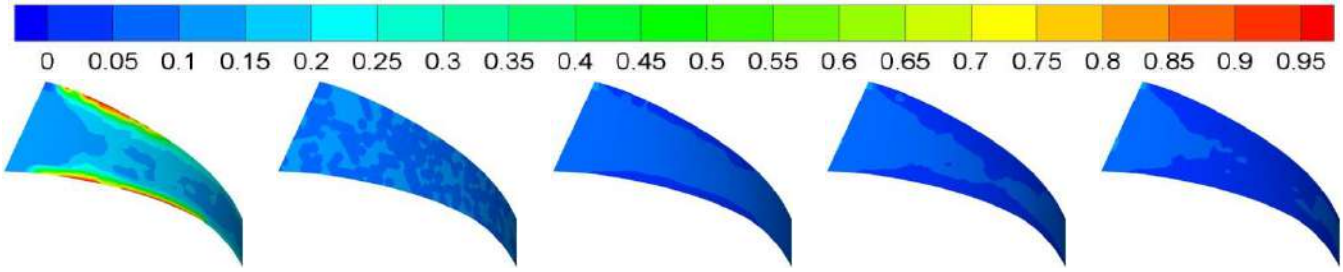

(A) 500 (B)1000 (C)1500 (D)2000 (E)2500

FIG.6 DISTRIBUTION OF THE PARTICLE CONCENTRATIONS ON THE BLADE PRESSURE SURFACE UNDER DIFFERENT PARTICLE DENSITIES (kg/m^3)

3.5 Particle concentration on the blade suction surface

Fig. 7 shows the distribution of particle concentration on the blade suction surface in five densities of delivering solid-phase particles. When particle density (500 kg/m^3) was smaller than the liquid-phase (water) density, the solid-phase concentration on the first half of the blade suction surface was higher than that on the second half of the blade suction surface. The wear was more serious. When the density of solid-phase particles (1000 kg/m^3) was equal to liquid-phase density, the distribution of solid-phase concentration on the blade suction surface was more uniform. Therefore, the degree of wear was also consistent. In three cases where the densities of delivering solid-phase densities were 1500, 2000, and 2500kg/m^3, the density of particles was apparently greater than the liquid-phase density. With the increase of the density of delivering solid particles, solid-phase volume fraction on the second half of the suction surface was higher. This finding indicated that the degree of wear on the blade suction surface was constantly increasing.

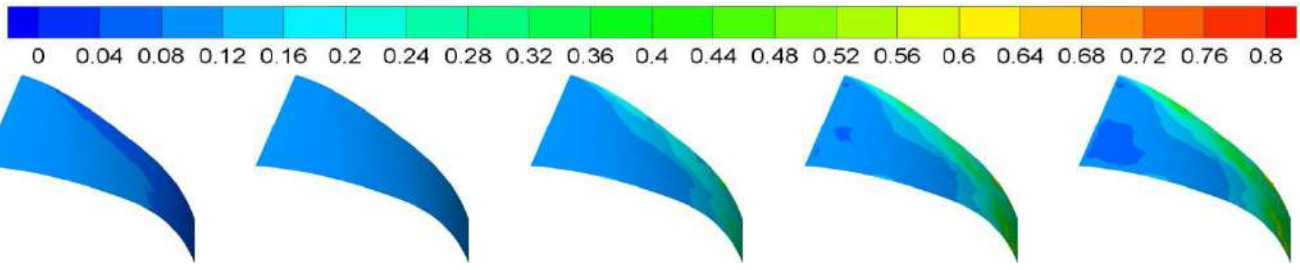

(A) 500 (B)1000 (C)1500 (D)2000 (E)2500

FIG.7 DISTRIBUTION OF PARTICLE CONCENTRATIONS ON THE BLADE SUCTION SURFACE UNDER DIFFERENT PARTICLE DENSITIES (kg/m^3)

3.6 Particle concentration on volute surface

Fig. 8 shows the distribution of particle concentration on volute surface under five different densities of delivering solid-phase particles. When the density of delivering solid particles (1000 kg/m^3) was equal to the liquid-phase density (1000 kg/m^3), solid-phase volume fraction on volute surface was very uniform. The degree of wear in this case was the same. However, when the particle density was smaller or greater than the liquid-phase density (500, 1500, 2000, and 2500 kg/m^3), the solid-phase volume concentration on volute surface was more or less non-uniform. The degrees of wear on volute surface under these four cases were not the same.

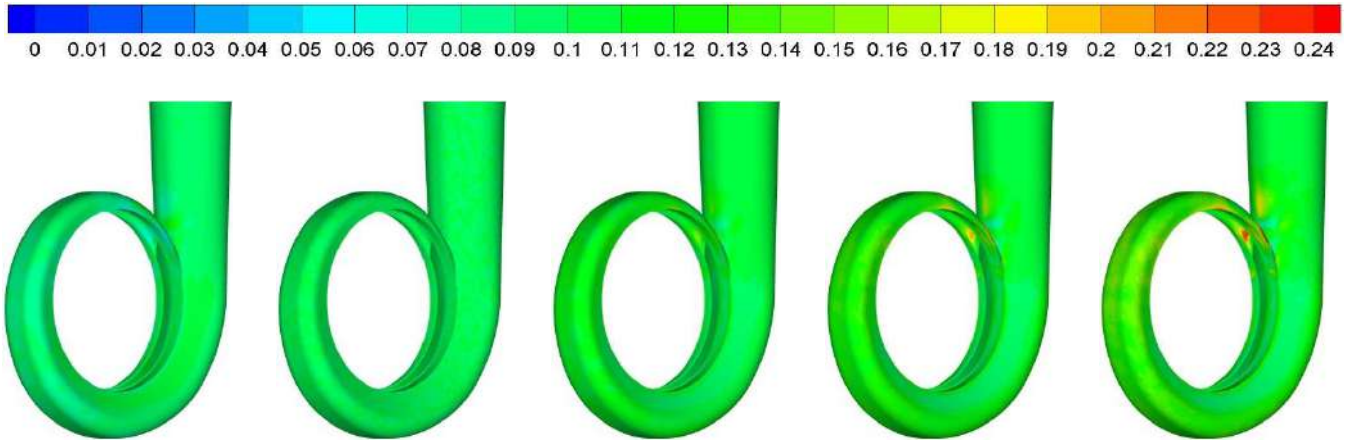

(A) 500 (B)1000 (C)1500 (D)2000 (E)2500

FIG.8 DISTRIBUTION OF PARTICLE CONCENTRATIONS ON VOLUTE SURFACE UNDER DIFFERENT PARTICLE DENSITIES (kg/m^3)

IV. CONCLUSION

1) With the increase of the density of solid particles, the total pressure of both the pump inlet and the pump outlet showed a trend of monotonic decline. Pump calculation head curve showed a trend of first declining and then rising, reaching the minimum value of 13.66m when the density of solid particles was 1500kg/m^3.The pump efficiency curve showed a trend of initial rise and decline and then rise, but its change was not significant. The pump shaft power showed a trend of monotonic rise.

2) When particle density was smaller than, equal to, and greater than liquid-phase concentration, solid-phase concentration on the blade pressure surface showed the distribution laws more than, equal to, and smaller than 10%, respectively. With the increase in the density of solid particles, solid-phase concentration on the blade pressure surface showed a gradually declining trend. These findings indicated that the wear and tear was getting smaller and smaller.

3) In the middle and late half of the blade suction surface, when the density of solid particles was smaller than that of water, solid-phase concentration on the blade suction surface gradually decreased. This result indicated that the wear and tear was constantly smaller and smaller. In the case where the density of solid particles was greater than water density, solid-phase concentration on the blade suction surface increased gradually. This finding indicated that the wear and tear constantly increased. However, in a small part from the front edge of the blade suction surface, the change trends of both were opposite. This finding showed that the degree of wear was opposite.

ACKNOWLEDGEMENTS

The work was supported by the Zhejiang Provincial Science and Technology Project (No.2015C31129, No.2016C31127), Academic Foundation of Quzhou University (No.XNZQN201508).

REFERENCES

[1] Engin T, Gur M. Performance characteristics of centrifugal pump impeller with running tip clearance pumping solid-liquid mixtures[J]. Journal of Fluids Engineering, 2001, 123(3): 532-538.

[2] Gandhi B K, Singh S N, Seshadn V. Effect of speed on the performance characteristics of a centrifugal slurry pump[J]. Journal of Hydraulic Engineering, 2002, 128(2): 225-233.

[3] Yuan Shouqi, Zhang Peifang, Zhang Jinfeng. Numerical simulation of 3-D dense solid- liquid two- phase turbulent flow in a non-clogging mud pump[J]. Chinese Journal of Mechanical Engineering, 2004, 17(4):623-627.

[4] Li Yi, Zhu Zuchao, He Weiqiang, et al. Numerical simulation and experimental research on the influence of solid phase characteristics on centrifugal pump performance[J]. Chinese Journal of Mechanical Engineering, 2012, 25(6): 1184-1189.

[5] Zhang Yuliang, Li Yi, Cui Baoling, et al. Numerical simulation and analysis of solid-liquid two-phase flow in centrifugal pump[J]. Chinese Journal of Mechanical Engineering, 2013, 26(1): 53-60.

[6] Zhang Yuliang, Li Yi, Zhu Zuchao, et al. Computational analysis of centrifugal pump delivering solid-liquid two-phase flow during startup period[J]. Chinese Journal of Mechanical Engineering, 2014, 27(1): 178-185.

[7] Harry H T, Graeme R A. Experimental study on erosive wear of some metallic materials using Coriolis wear testing approach[J]. Wear, 2005, (258): 458-469.

[8] Veselin B. Erosive wear model of slurry pump impeller[J]. Journal of Tribology, 2010, 132(2): 021602.1～5.

[9] Pagalthivarthi K V, Gupta P K, Tyagi V, et al. CFD prediction of erosion wear in centrifugal slurry pumps for dilute slurry flows[J]. Journal of Computational Multiphase Flows, 2011, 3(4): 225-245.

[10] Dong Xing, Zhang Hailu, Wang Xinyong. Finite element analysis of wear for centrifugal slurry pump[C]. The 6th International Conference on Mining Science & Technology, 2009, (1): 1532-1538.

[11] Li Yi, Zhu Zuchao, He Zhaohui, et a1. Abrasion characteristic analyses of solid-liquid two-phase centrifugal pump[J]. Journal of Thermal Science, 2010, 20(3): 283-287.

[12] Sanyal J, Vasquez S, Roy S, et al. Numerical simulation of gas-liquid dynamics in cylindrical bubble column reactors [J]. Chemical Engineering Science, 1999, 54(21):5071-5083.

New Finite Element for modeling connections in 2D small frames - Static Analysis

Chadi Azoury[1], Assad Kallassy[2], Ibrahim Moukarzel[3]

[1]Mechanical Engineering Department, Lebanese University, Lebanon
[2]Civil Engineering Department, Lebanese University, Lebanon
[3]Faculty of Engineering, Lebanese University, Lebanon

Abstract *— The paper presents a proposal to create a new one-dimensional (1-D) finite element that can substitute for the three-dimensional (3-D) finite model of connection elements in static analysis. The study is conducted on a simple small frame. First, a 3-D model is constructed, followed by the construction of an equivalent two-dimensional (2-D) one. At the final stage, the results of the static analysis of many proposed 1-D element models are compared with the results of the 2-D model. With a special treatment of the connection elements, the results of the analysis of the new 1-D finite element models agree well with the results of the 2-D model.*

Keywords: Structures, Finite element methods, Condensation, Timoshenko beam, Connection element, and Small frames.

Notations

E	Young's elastic modulus
v	Poisson coefficient
ρ	density
I	moment of inertia
E I	flexural beam stiffness = E × I
t	frame thickness
K(*n*×*n*)	stiffness matrix of order *n*
L(*n*×*m*)	rectangular matrix with *n* rows and *m* columns
EB	Euler-Bernoulli
sh	shear deformation
FE	finite element
DOF	degree-of-freedom

I. INTRODUCTION

To perform a static analysis of a frame, 3-D finite elements are usually used in the meshing process. A large number of elements are required, which in turn requires a large number of DOF and consequently, a great deal of work. The main objective consists of developing a 1-D model made up of simple 1-D elements to replace the 3-D model made up of tetrahedral prisms or brick elements. To perform a static analysis, the calculation of the stiffness matrix is required.

In order to find the best 1-D finite meshing element, 3-D meshing is used, and 2-D and 1-D models are consecutively constructed.

All calculations are done by using ANSYS Version 16.2 and MATLAB Version 7. A simple frame is used in the calculations.

II. TEST STRUCTURE

Our test structure will be of this form:

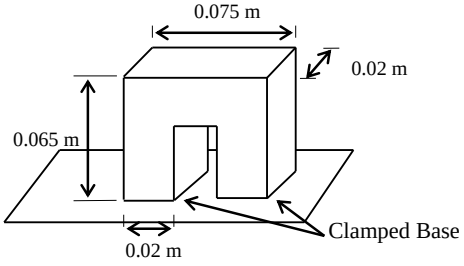

FIGURE 1: TEST STRUCTURE

The beam section of the test structure is rectangular (0.02×0.02 m^2). The mechanical characteristics are: Poisson coefficient $\nu = 0.31$, density $\rho = 78000$ N/m^3, and elastic modulus E = 184 GPa. The test structure is clamped at its base and consists of 5 structural elements shown in Figure 2.

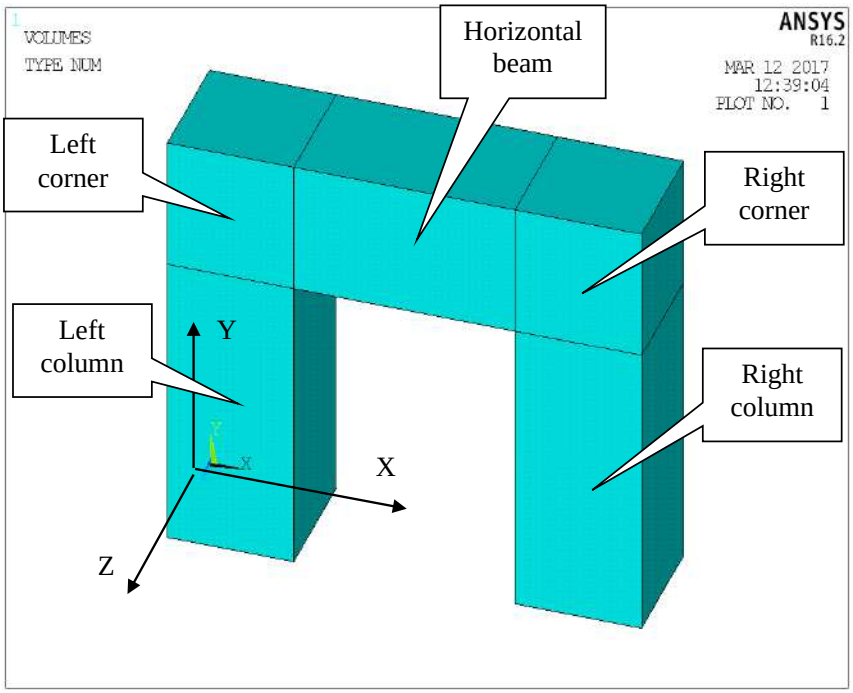

FIGURE 2: TEST STRUCTURE CONSTRUCTED IN ANSYS® R16.2

Different types of elements are used in the meshing processes. In static analysis, the comparison between different models is based on the deformation in the XY plan of the structure. These models are compared in 2 load cases illustrated in

Figure 3:

- Case 1: a body load of 78000 N/m^3 along the vertical axis of the horizontal beam
- Case 2: a body load of 78000 N/m^3 along the horizontal axis of the left column

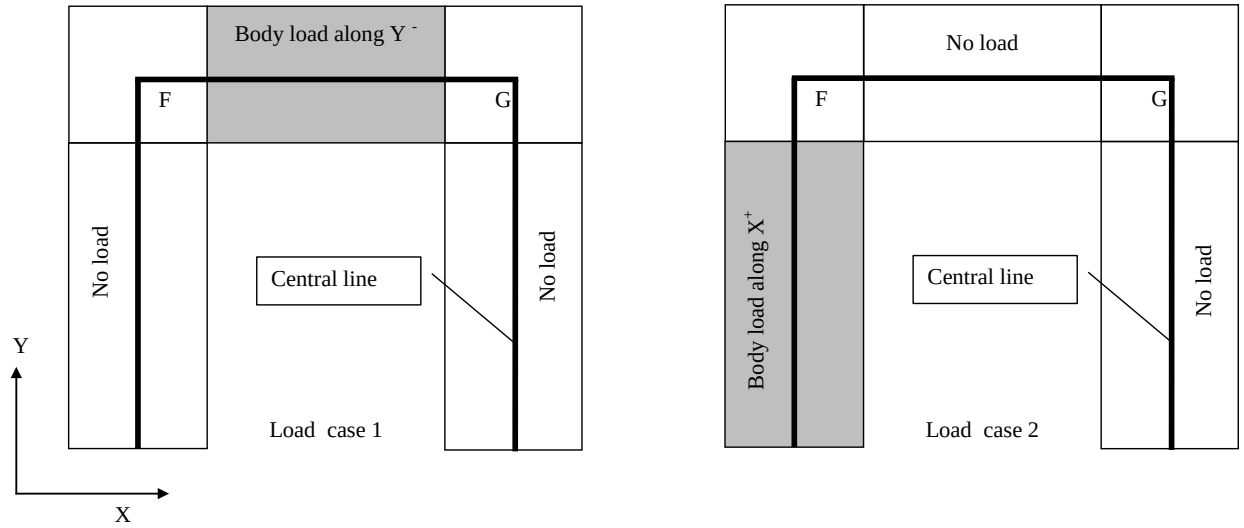

FIGURE 3: TEST STRUCTURE WITH LOAD CASES 1 AND 2

III. 3D AND 2D MODELING

The 3D model of the test structure is meshed using H8 volumetric finite elements with 8 nodes. Each column is modeled using 8×8×16 = 1024 elements and each corner includes 8×8×8 = 512 elements. The horizontal beam is modeled using 8×8×16 = 1024 elements. In total, it is equal to 4096 elements with 5265 nodes (see Figure 4).

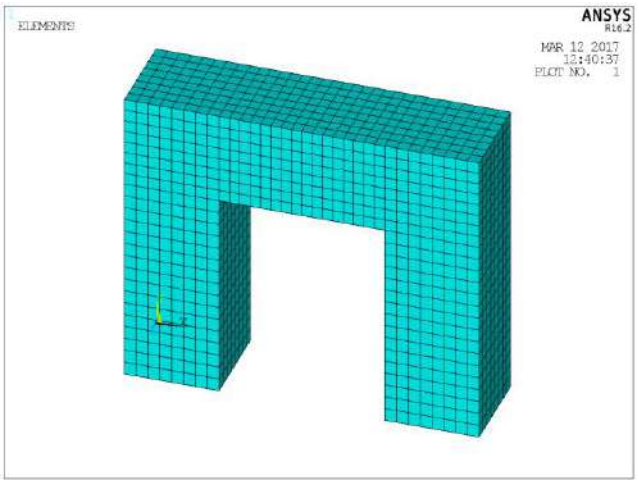

FIGURE 4: 3D TEST STRUCTURE MODELLED USING H8 FINITE ELEMENTS

Figures 5 and 6 show the total displacement contours of the frame under load case 1 and 2.

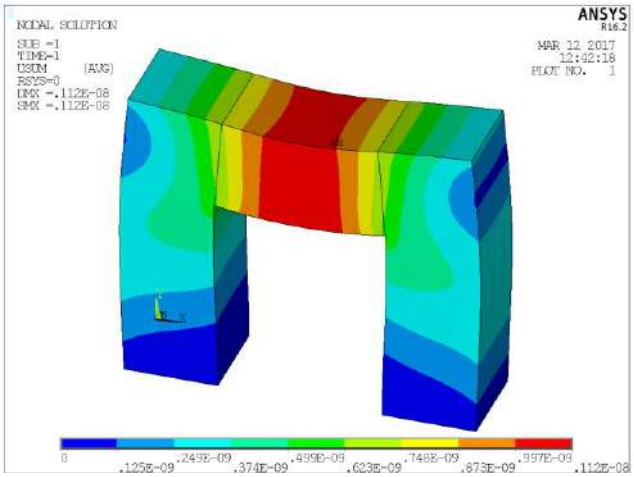

FIGURE 5: THREE-DIMENSIONAL DEFORMED TEST STRUCTURE UNDER LOAD CASE 1

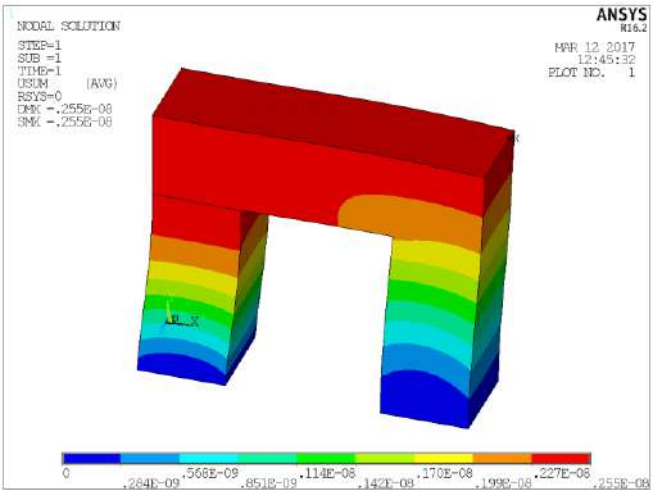

FIGURE 6: THREE-DIMENSIONAL DEFORMED TEST STRUCTURE UNDER LOAD CASE 2

The test structure is then modeled in two dimensions. A Q4 plane element with a thickness t = 0.02 m and having 4 nodes is used. Each column is modeled using 8×16 = 128 elements. Each corner includes 8×8 = 64 elements. The horizontal beam is modeled using 8×16 = 128 elements. The total is 512 elements with 585 nodes (see Figure 9a).

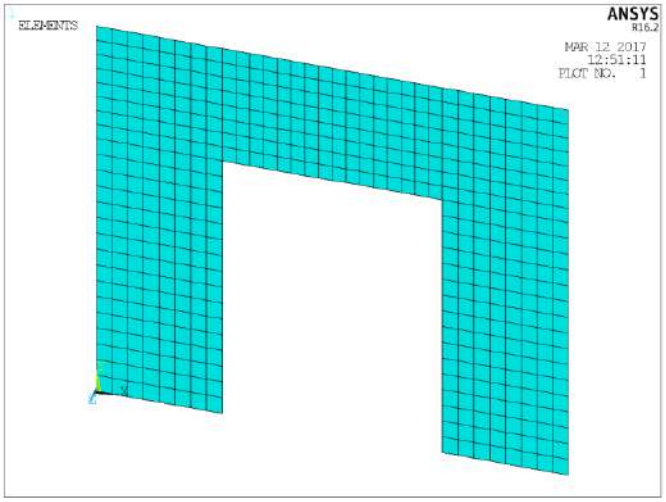

FIGURE 7: 2D TEST STRUCTURE MODELED USING Q4 PLANE FINITE ELEMENTS

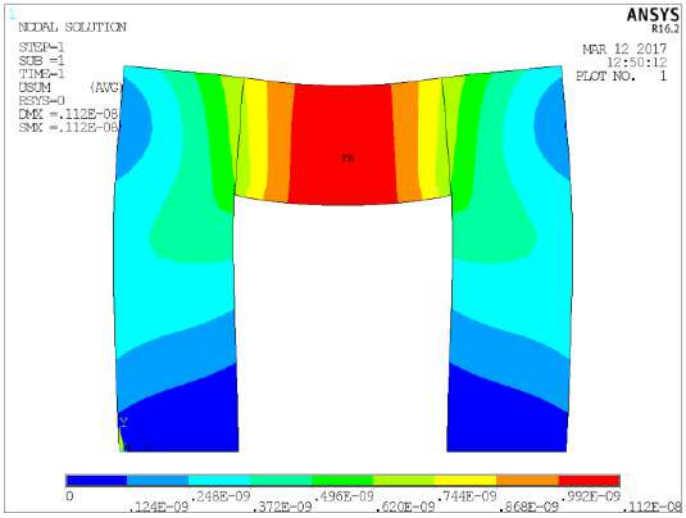

FIGURE 8: TWO-DIMENSIONAL DEFORMED TEST STRUCTURE ALONG LOAD CASE 1

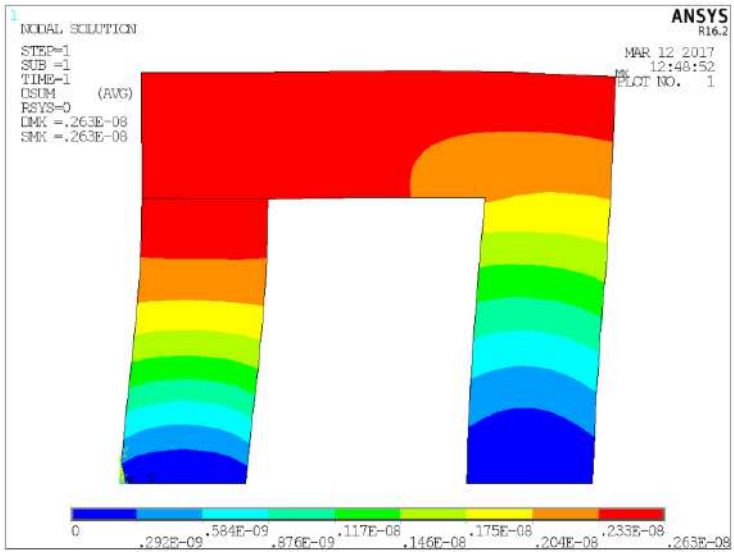

FIGURE 9: TWO-DIMENSIONAL DEFORMED TEST STRUCTURE ALONG LOAD CASE 2

Figures 8 and 9 have similar maps as Figures 5 and 6. The different models are compared using the displacement of 65 points on the central line of the longitudinal symmetrical plan of the structure.

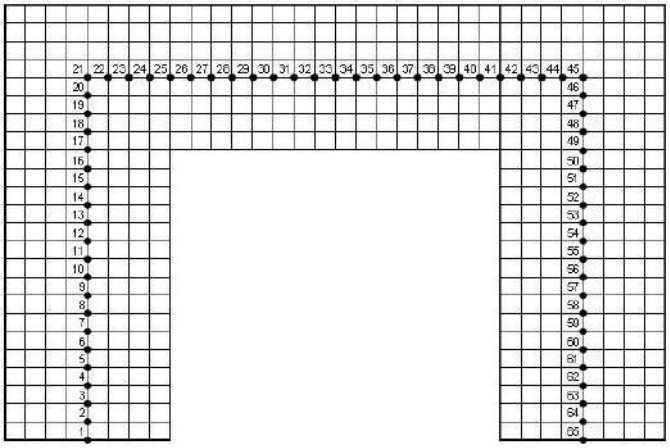

FIGURE 10 : LONGITUDINAL SYMMETRICAL PLAN OF THE STRUCTURE SHOWING THE 65 CENTRAL LINE POINTS

In order to establish a comparison between both FE models and using both load cases, UX and UY displacements of nodes on the central line, along the X and Y axis respectively, are plotted on the same graph (see Figure 11 – 10).

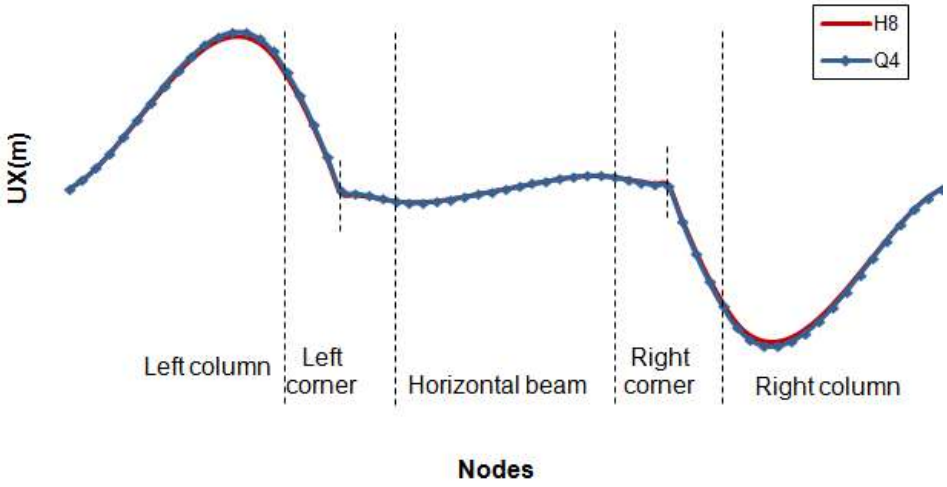

FIGURE 11 : UX (m) CENTRAL LINE DISPLACEMENT ALONG AXE X (LOAD CASE 1)

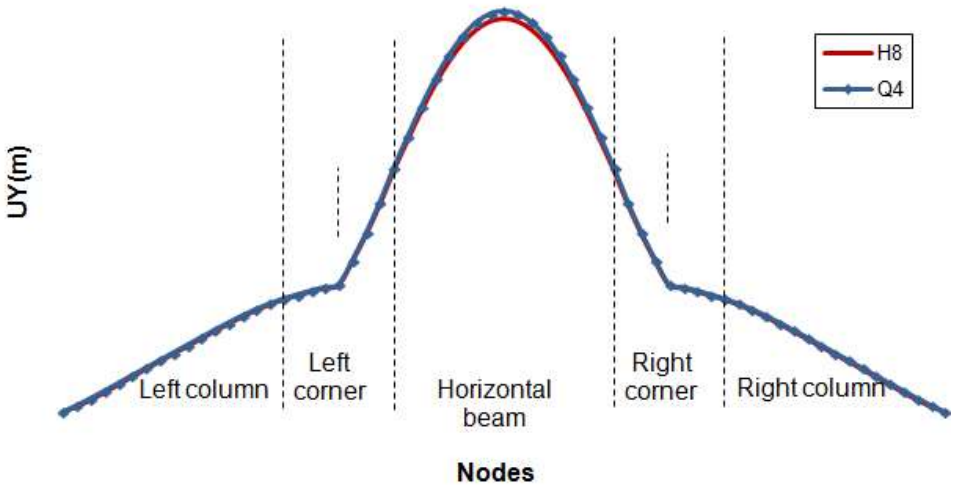

FIGURE 12 : UY (m) CENTRAL LINE DISPLACEMENT ALONG AXE Y (LOAD CASE 1)

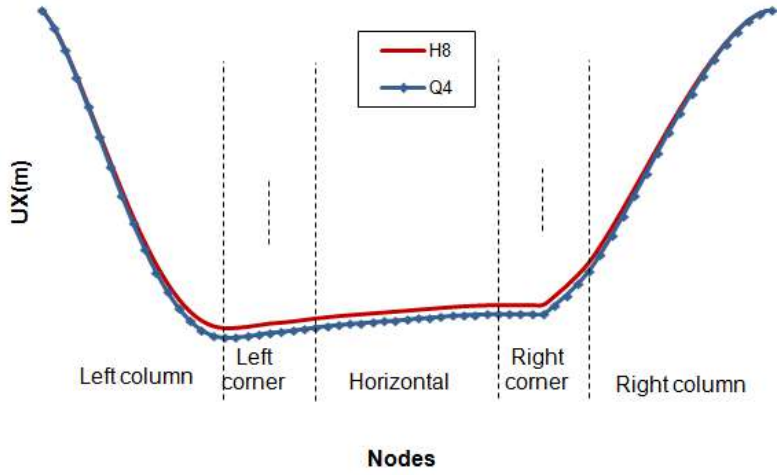

FIGURE 13 : UX (m) CENTRAL LINE DISPLACEMENT ALONG AXE X (LOAD CASE 2)

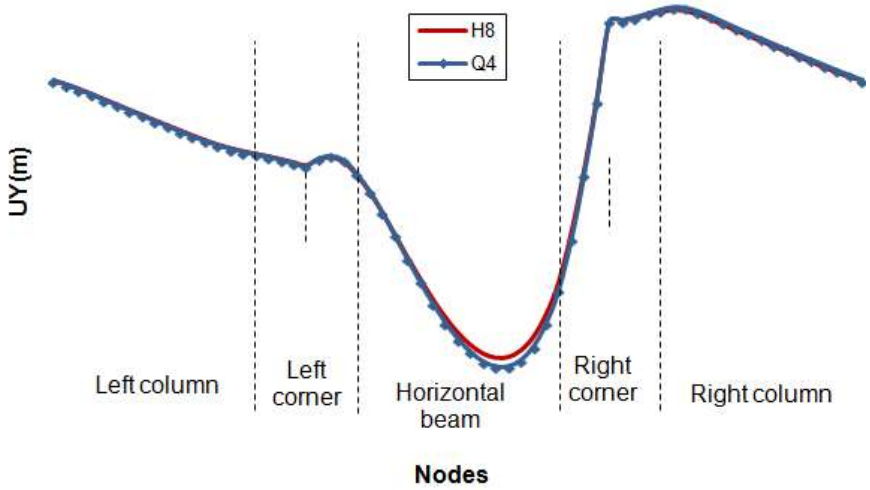

FIGURE 14 : UY (m) CENTRAL LINE DISPLACEMENT ALONG AXE Y (LOAD CASE 2)

Regarding the comparison criteria of the results produced by different models, the following error formula is used:

$$E_{\max} = \max_i \frac{|U_R(i) - U_C(i)|}{\left|\max_j(U_R(j)) - \min_j(U_R(j))\right|}$$

$U_R(i)$ = reference value of a displacement at point i

$U_C(i)$ = calculated value of the same displacement and at the same point i of a new model

The maximum errors for both models H8 and Q4, for both load cases, are listed in Table 1 below:

TABLE 1
COMPARISON BETWEEN H8 AND Q4 MODELS

Load case	Displacement	U_R (m) [H8]	U_C (m) [Q4]	*E*max	Node number (*E*max)
1	UX	-2.6673E-10	-2.7536E-10	1.55%	15 and 51
1	UY	-1.0941E-09	-1.1149E-09	1.90%	33
2	UX	2.4111E-09	2.4842E-09	3.01%	16
2	UY	2.6802E-10	2.7866E-10	2.92%	39

The plane model has produced comparable results to those of the 3-D model. Thus, the reference model is the 2-D model which leads to a reduction in the DOF amount. It will be used to develop the best 1-D element for connection modeling.

IV. ONE-DIMENSIONAL CLASSICAL MODELING

In this section, 1-D elements are used for the test structure. Since the structure is not the slender type, we know that Euler-Bernoulli beams are not adequate. Therefore, we will use Timoshenko beams with 2 nodes per element and 3 DOF per node (Timoshenko model).

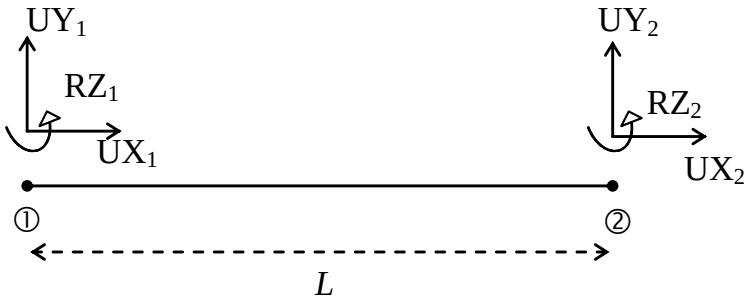

FIGURE 15 : TWO-NODE BEAMS

The transformation from the Q4 model to the 1-D model is shown in Figures 12 and 13. The volumetric charge is transformed into linear charge.

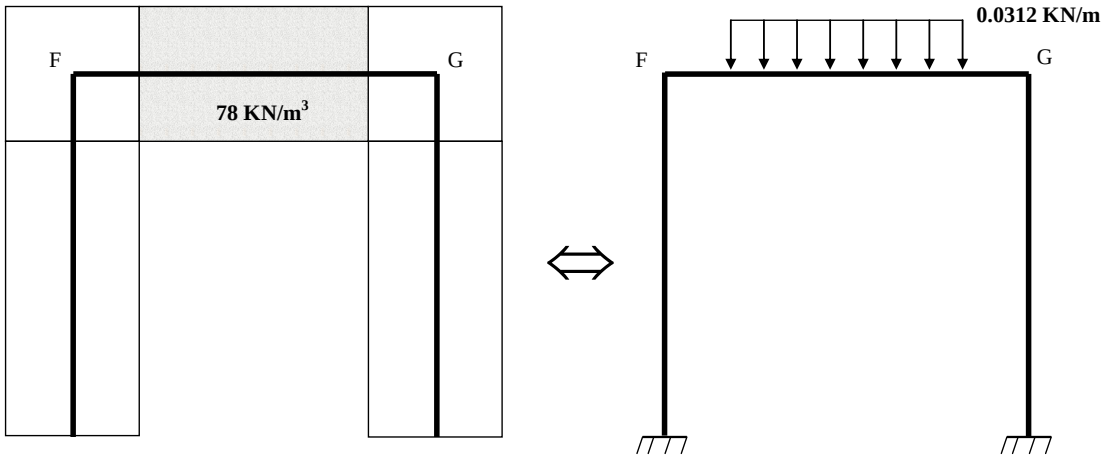

FIGURE 16 : TRANSFORMATION OF THE Q4 MODEL INTO A 1-D MODEL (LOAD CASE 1)

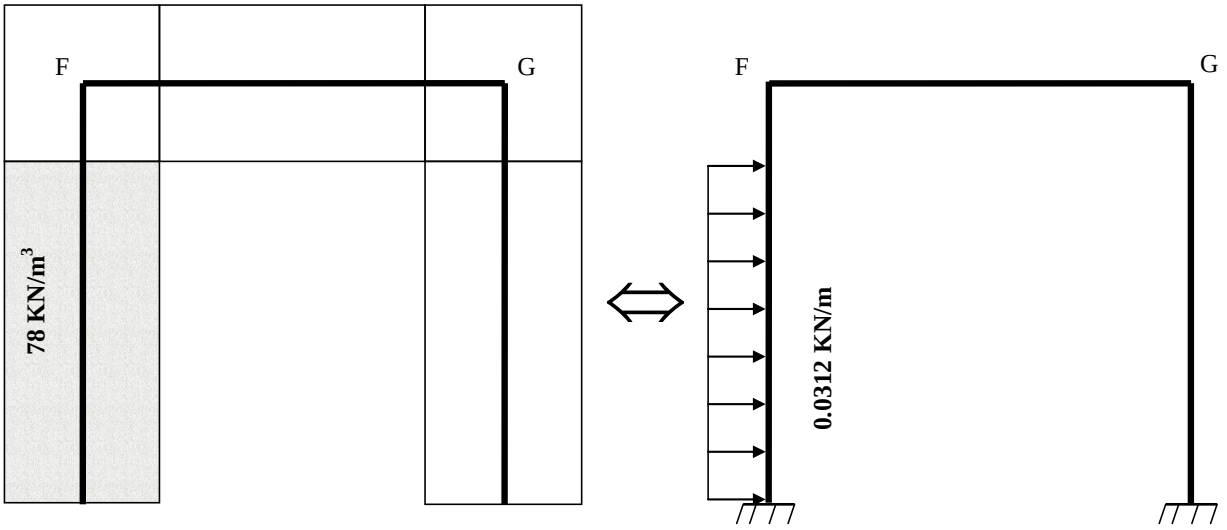

FIGURE 17 : TRANSFORMATION OF THE Q4 MODEL INTO A 1-D MODEL (LOAD CASE 2)

The left and right columns are modeled using 16 elements each. The horizontal beam is also modeled using 16 elements. Both left and right corners are modeled using 4 horizontal linear elements and 4 vertical linear elements, i.e. a total of 64

beam elements. The following figures show the deformed test structure in the 2 load cases as applicable to both models: the reference model Q4 and the Timoshenko model.

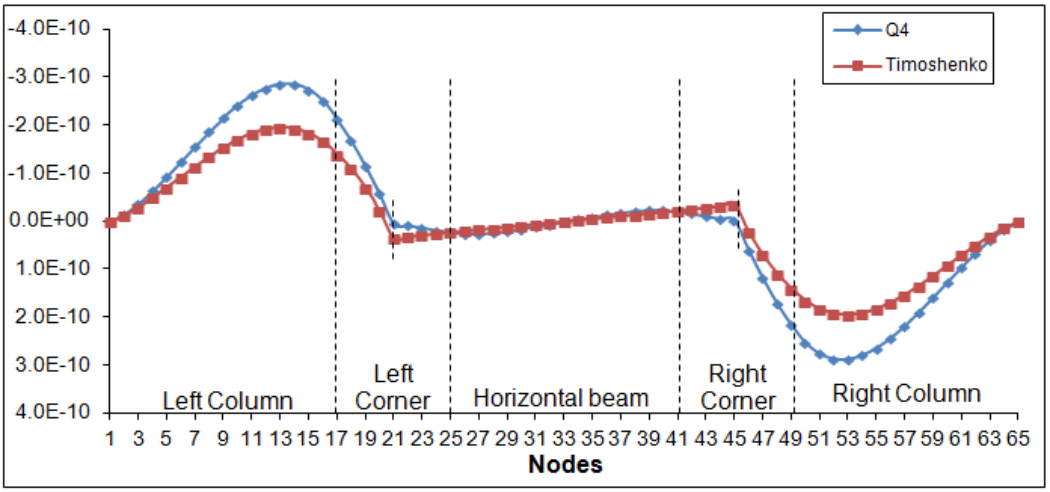

FIGURE 18 : UX (m) DISPLACEMENT OF CENTRAL LINE NODES ALONG X (LOAD CASE 1)

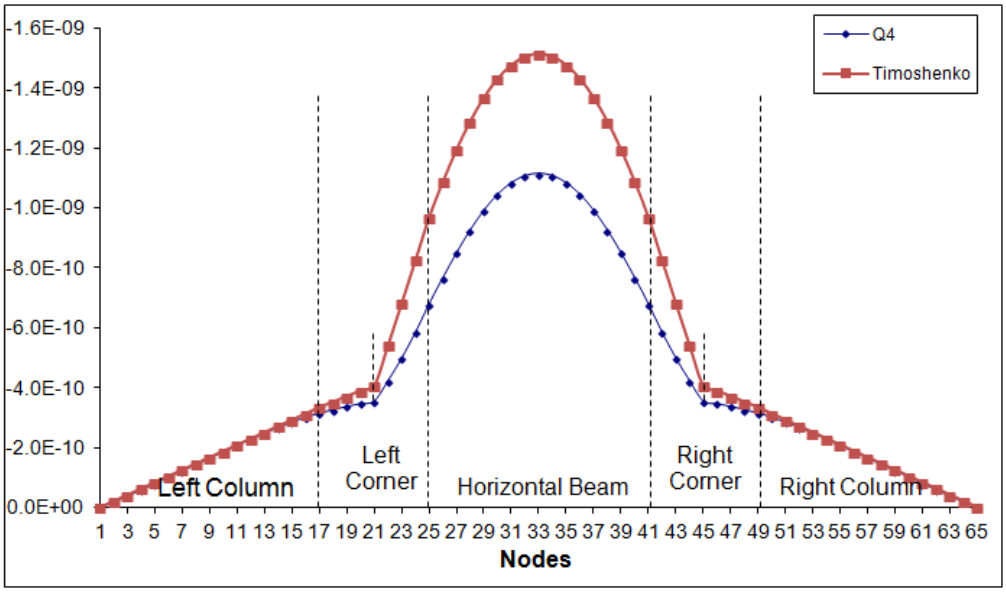

FIGURE 19 : UY (m) DISPLACEMENT OF CENTRAL LINE NODES ALONG Y (LOAD CASE 1)

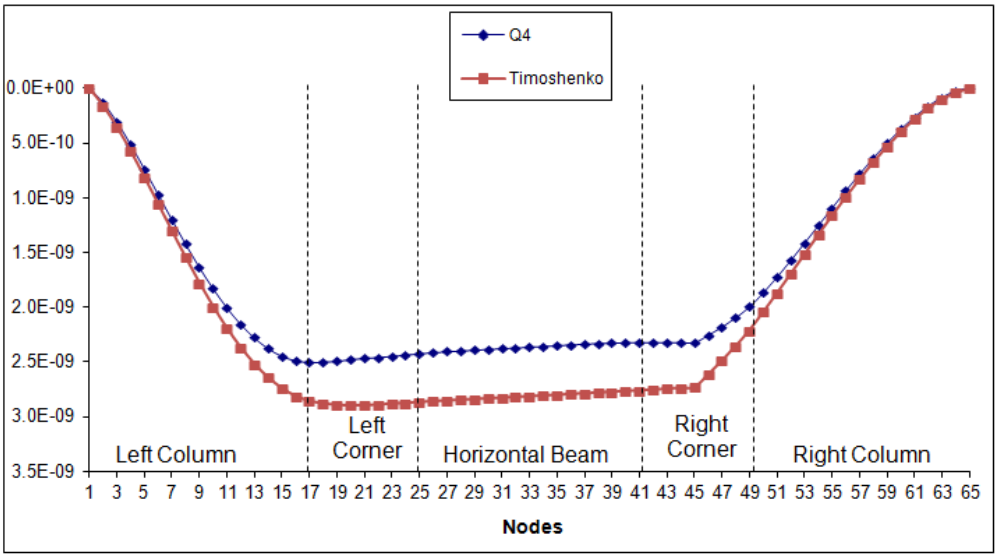

FIGURE 20 : UX (m) DISPLACEMENT OF CENTRAL LINE NODES X (LOAD CASE 2)

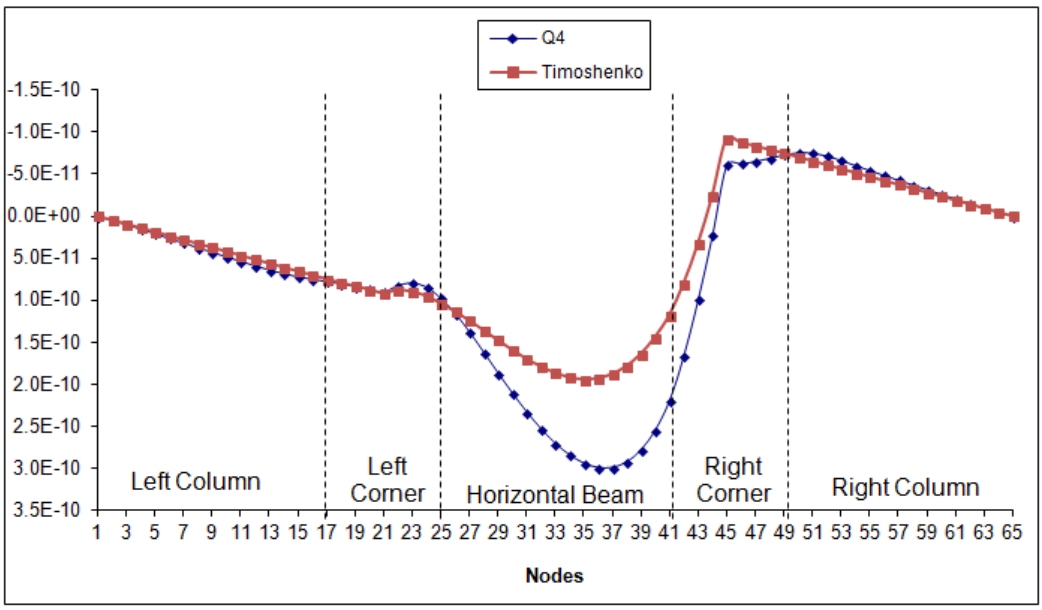

FIGURE 21 : UY (m) DISPLACEMENT OF CENTRAL LINE NODES Y (LOAD CASE 2)

None of the 1-D models produces proximate results in comparison with those given by the Q4 model. Improved models using Timoshenko beams are shown below.

V. FIRST IMPROVED MODEL: CQ CORNER QUAD

A new CQ element is suggested for the corners, based on the utilization of Q4 surface elements since the Q4 modeling and the H8 modeling produce close results. Non-corner elements are still modeled as Timoshenko beams. One way to connect two different meshing types is explained by Dohrmann and al, [4] and [5], and Quiroz and al [9]. Kattner and al [8] explain how modeling joints between frame columns and beams is performed.

The interface between the new CQ element on the one hand and the horizontal and vertical beams on the other hand, is considered rigid in our case. The corner element of 0.02 m × 0.02 m and 0.02 m in thickness is meshed using Q4 elements of 0.02/8 m × 0.02/8 m which produces 64 elements and 81 nodes in total, hence 81×2 DOF: 17 × 2 interface DOF and 64 × 2 non-interface DOF (see next Figure).

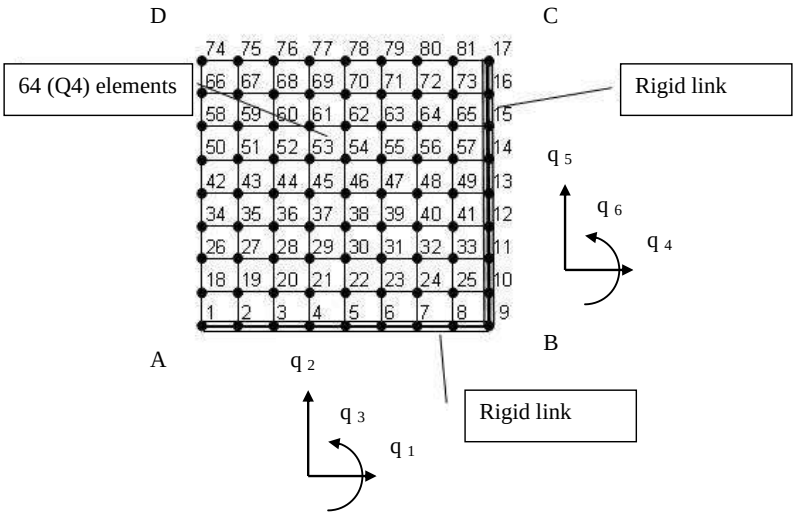

FIGURE 22 : LEFT CORNER WITH RIGID LINKS

The elementary stiffness matrix $k_e(8,8)$ of the Q4 element is mentioned in Cook [2]. By assembling the 64 Q4 elements, the global stiffness matrix of the corner is K(162,162).

Using static condensation, the global stiffness matrix is reduced to $K_c(34,34)$ after elimination of the 128 non-interface DOF [3].

To find matrix Kc(34,34), we use the formula for static condensation. In Matlab code:

```
krr=K(1:34,1:34);
krc=K(1:34,35:162);
kcr=K(35:162,1:34);
kcc=K(35:162,35:162);
Kc=krr-krc*inv(kcc)*kcr;
```

The AB interface is supposed to be rigid. Then, 3 DOF (q_1, q_2, q_3) are enough to determine the DOF of the AB interface:

- q_1: horizontal displacement of the midpoint of segment AB
- q_2: vertical displacement of the midpoint of segment AB
- q_3: rotation of segment AB around its midpoint

The same applies to the BC interface where the DOF (q_4, q_5, q_6) of the midpoint in BC determine the DOF of the rigid interface BC.

The reduced stiffness matrix $K_r(6,6)$ is given by: $K_r = L^T K_c L$, where L(34×6) is the matrix giving the values of the DOF relative to interfaces AB and BC, from degrees q_1, q_2, q_3, q_4, q_5, and q_6.

```
L=[

1  0     0     0     0     0
0  1     -4*a  0     0     0
1  0     0     0     0     0
0  1     -3*a  0     0     0
1  0     0     0     0     0
0  1     -2*a  0     0     0
1  0     0     0     0     0
0  1     -1*a  0     0     0
1  0     0     0     0     0
0  1     0     0     0     0
1  0     0     0     0     0
0  1     1*a   0     0     0
1  0     0     0     0     0
0  1     2*a   0     0     0
1  0     0     0     0     0
0  1     3*a   0     0     0
0  0     0     1     0     4*b
0  1     4*a   0     0     0
0  0     0     1     0     3*b
0  0     0     0     1     0
0  0     0     1     0     2*b
0  0     0     0     1     0
0  0     0     1     0     1*b
0  0     0     0     1     0
0  0     0     1     0     0
0  0     0     0     1     0
0  0     0     1     0     -1*b
0  0     0     0     1     0
0  0     0     1     0     -2*b
0  0     0     0     1     0
0  0     0     1     0     -3*b
0  0     0     0     1     0
0  0     0     1     0     -4*b
0  0     0     0     1     0     ];
```

The stiffness matrix $K_r(6\times6)$ is a function of:

- The length a of side AB
- The length b of side BC

- The elastic modulus E of the material in part ABCD
- The Poisson coefficient *v*
- The thickness of the frame t

The stiffness matrix of the left corner beam of the test structure is given numerically by:

```
kleft=[
  4.6660e+009  1.5022e+009 -5.2058e+006 -4.6660e+009 -1.5022e+009 -2.6432e+007
  1.5022e+009  4.6660e+009  2.6432e+007 -1.5022e+009 -4.6660e+009  5.2058e+006
 -5.2058e+006  2.6432e+007  3.7398e+005  5.2058e+006 -2.6432e+007 -5.7599e+004
 -4.6660e+009 -1.5022e+009  5.2058e+006  4.6660e+009  1.5022e+009  2.6432e+007
 -1.5022e+009 -4.6660e+009 -2.6432e+007  1.5022e+009  4.6660e+009 -5.2058e+006
 -2.6432e+007  5.2058e+006 -5.7599e+004  2.6432e+007 -5.2058e+006  3.7398e+005]
```

With a simple transformation, we can obtain the stiffness matrix of the right corner beam:

```
kright=[
  4.6660e+009 -1.5022e+009 -5.2058e+006 -4.6660e+009  1.5022e+009 -2.6432e+007
 -1.5022e+009  4.6660e+009 -2.6432e+007  1.5022e+009 -4.6660e+009 -5.2058e+006
 -5.2058e+006 -2.6432e+007  3.7398e+005  5.2058e+006  2.6432e+007 -5.7599e+004
 -4.6660e+009  1.5022e+009  5.2058e+006  4.6660e+009 -1.5022e+009  2.6432e+007
  1.5022e+009 -4.6660e+009  2.6432e+007 -1.5022e+009  4.6660e+009  5.2058e+006
 -2.6432e+007 -5.2058e+006 -5.7599e+004  2.6432e+007  5.2058e+006  3.7398e+005]
```

Finally, the CQ model of the constructed frame is as follows:

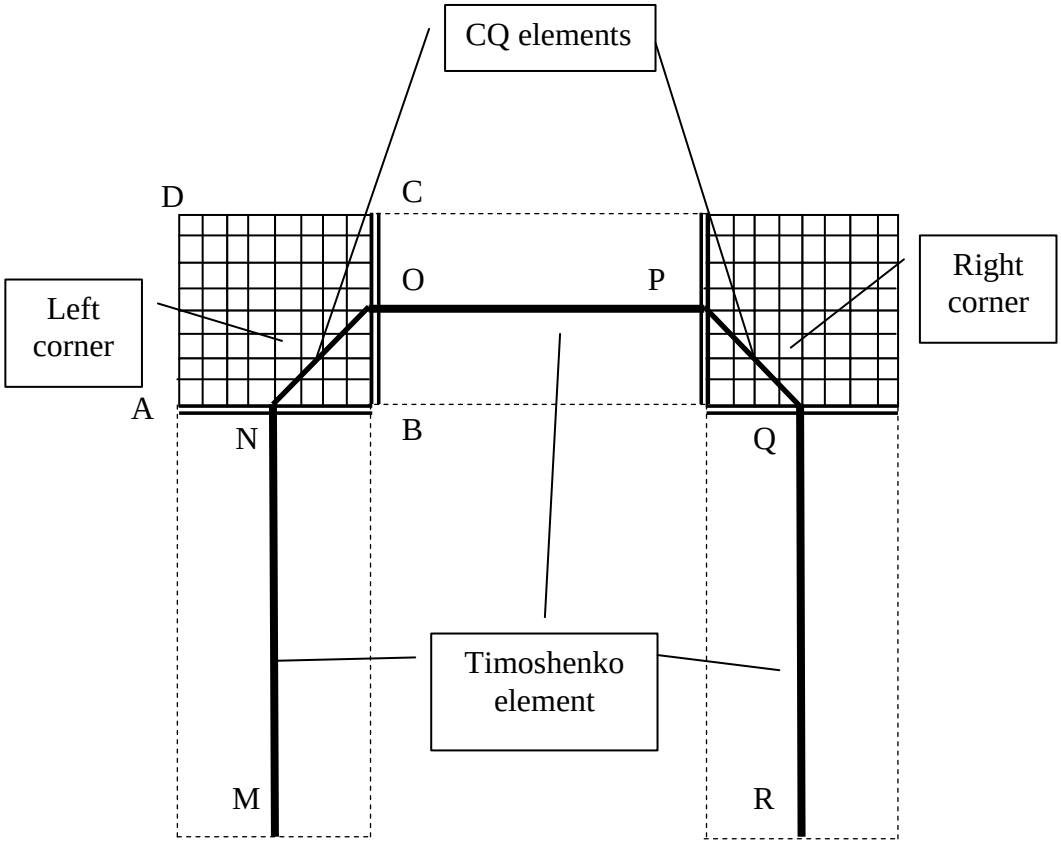

FIGURE 23 : DESCRIPTION OF THE CQ MODEL

- MN, OP and QR are Timoshenko beams
- NO is a CQ element with a $K_{r\ left}(6\times6)$ stiffness matrix
- PQ is a CQ element with a $K_{r\ right}(6\times6)$ stiffness matrix

Figures 24 to 27 show static results under load cases 1 and 2.

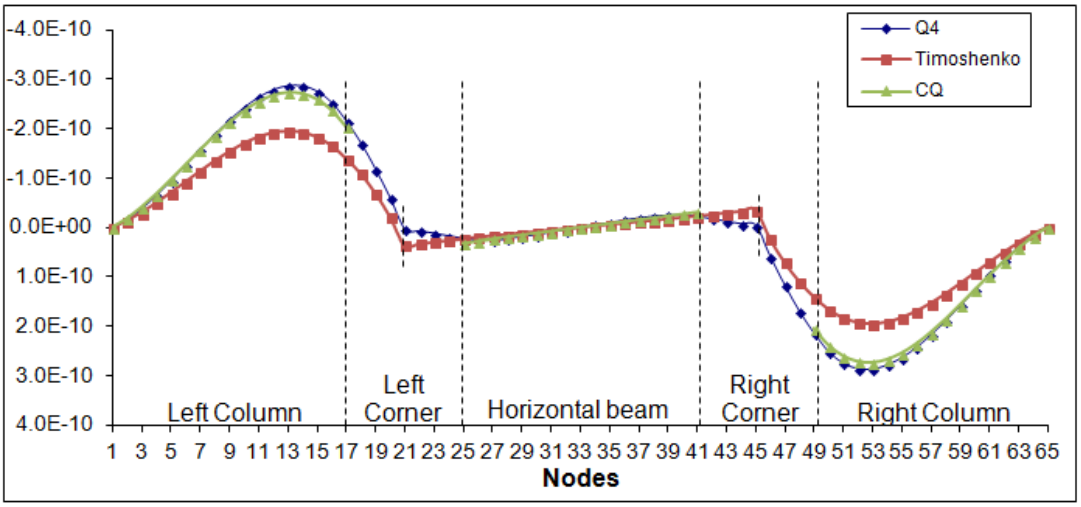

FIGURE 24 : UX (m) DISPLACEMENT OF CENTRAL LINE NODES ALONG X (LOAD CASE 1)

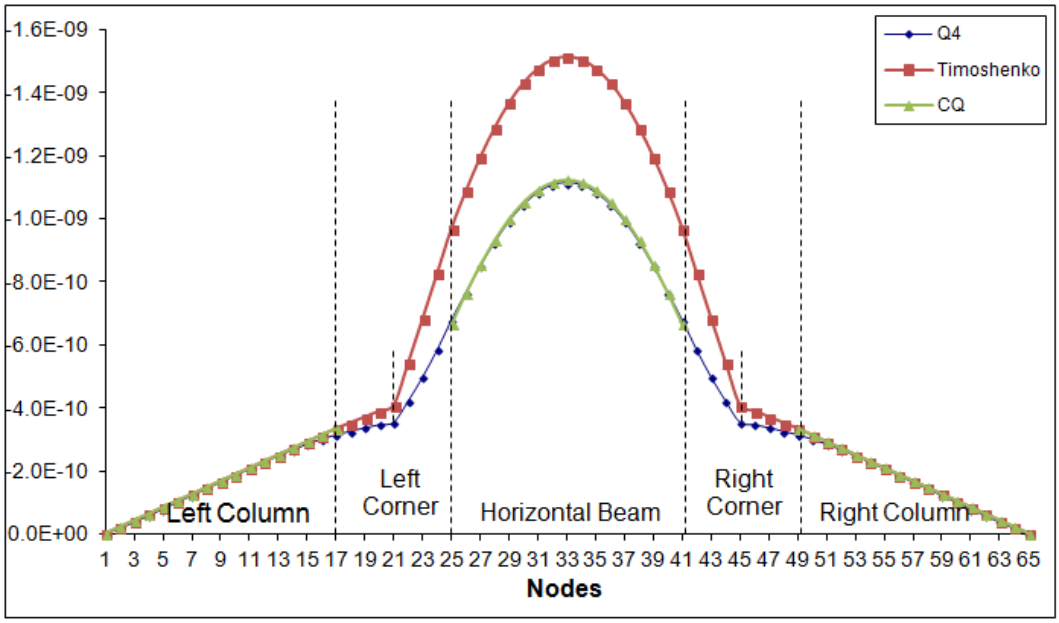

FIGURE 25 : UY (m) DISPLACEMENT OF THE CENTRAL LINE NODES ALONG Y (LOAD CASE 1)

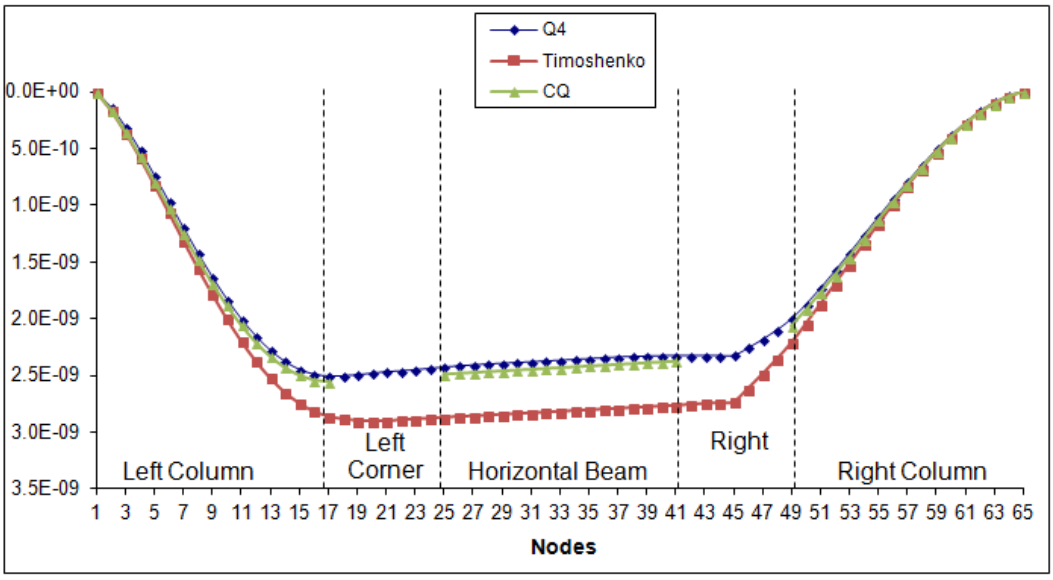

FIGURE 26 : UX (m) DISPLACEMENT OF THE CENTRAL LINE NODES ALONG X (LOAD CASE 2)

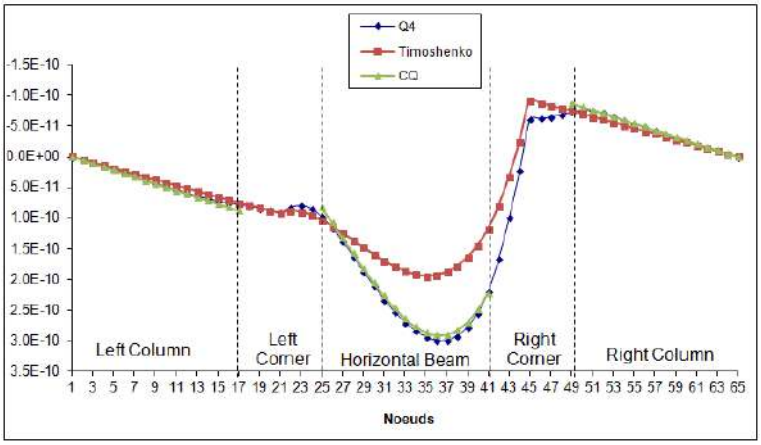

FIGURE 27 : UY (m) DISPLACEMENT OF THE CENTRAL LINE NODES ALONG Y (LOAD CASE 2)

The graphs show that the results of the CQ model are very close to those of the Q4 model. Table 2 shows the results of both models for both load cases. The last column gives the node number corresponding to the highest error value E_{max}.

TABLE 2
COMPARISON OF BOTH MODELS AND ALL LOAD CASES

Load case	Displacement	U_R (m) [Q4]	Model	U_C (m)	E_{max}	Node number (E_{max})
1	UX	2.8613E-10	Timoshenko	1.9284E-10	16.28%	14 or 52
1	UY	-1.1149E-09	Timoshenko	-1.5148E-09	35.87%	33
2	UX	2.3397E-09	Timoshenko	2.7944E-09	18.19%	36 or 37
2	UY	2.7866E-10	Timoshenko	1.645E-10	30.38%	39
1	**UX**	-2.7536E-10	**CQ**	-2.6053E-10	**2.59%**	**15 or 51**
1	**UY**	-3.1495E-10	**CQ**	-3.3374E-10	**1.69%**	**17 or 49**
2	**UX**	2.3947E-09	**CQ**	2.4623E-09	**2.70%**	**28**
2	**UY**	9.7806E-11	**CQ**	8.2391E-11	**4.10%**	**25**

It can be said from the previous table, that the CQ model produces the best approximation to the Q4 model.

VI. SECOND IMPROVED MODEL: RIGID INTERFACE EVERYWHERE (RQ)

In this paragraph, we propose a linear finite element to replace Timoshenko beams in the vertical and horizontal beams. This new element is constructed using the same procedure for the corner elements as in the previous paragraph.
Consider a strip in the beam that is between two consecutive nodes of the midline (see next figure).

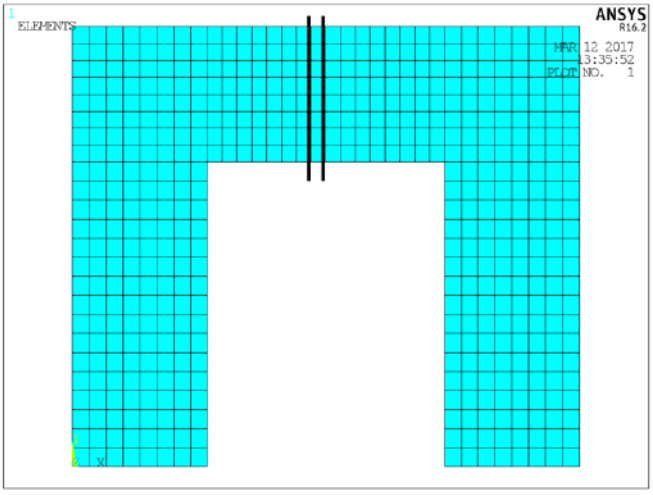

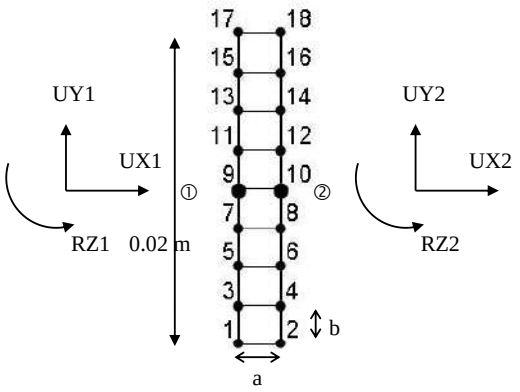

FIGURE 28: RQ ELEMENT

The total length of this element is 0.02 m (from bottom to top). The thickness (along z direction) is always 0.02 m. a = b = 0.045/16 = 0.0028125 m.

The element is discretized in 8 Q4 elements along its length. Therefore, we have a total of 9 nodes and 18 DOF for each interface.

We will assume that plane sections of beams in bending (Timoshenko hypothesis), displacements of nodes that are in the same cut-section are displacements of a rigid body, given by 3 DOFs:

- UX = Displacement along the X axis of the center of the section
- UY = Displacement along the Y axis of the center of the section
- RZ = Rotation around the Z axis

Therefore, the displacements of all the nodes of this element are given by 6 DOFs; 3 DOFs for the left cut-section and 3 DOFs for the right cut-section. This will give us the elementary stiffness matrix ke(6,6). In order to determine ke(6,6), we know that the stiffness matrix for one Q4 element is given by:

The global matrix is K(36,36).

The matrix of the rigid interface is given by:

```
R=[
1   0      4*b    0      0      0
0   1      0      0      0      0
0   0      0      1      0      4*b
0   0      0      0      1      0
1   0      3*b    0      0      0
0   1      0      0      0      0
0   0      0      1      0      3*b
0   0      0      0      1      0
1   0      2*b    0      0      0
0   1      0      0      0      0
0   0      0      1      0      2*b
0   0      0      0      1      0
1   0      1*b    0      0      0
0   1      0      0      0      0
0   0      0      1      0      1*b
0   0      0      0      1      0
1   0      0      0      0      0
0   1      0      0      0      0
0   0      0      1      0      0
0   0      0      0      1      0
1   0      -1*b   0      0      0
0   1      0      0      0      0
0   0      0      1      0      -1*b
0   0      0      0      1      0
1   0      -2*b   0      0      0
0   1      0      0      0      0
0   0      0      1      0      -2*b
0   0      0      0      1      0
1   0      -3*b   0      0      0
0   1      0      0      0      0
0   0      0      1      0      -3*b
0   0      0      0      1      0
1   0      -4*b   0      0      0
0   1      0      0      0      0
0   0      0      1      0      -4*b
0   0      0      0      1      0     ]
```

Therefore, $K = L^T \times Kc \times L$. (Kc is the condensed matrix). We obtain:

```
k=E*t/(v^2-1)*b/a*[
-8,         0,                          0, 8,         0,                          0
 0,     4*v-4,                2*a*(v-1), 0,     -4*v+4,                2*a*(v-1)
 0,2*a*(v-1),-128/3*b^2-4/3*a^2+4/3*a^2*v, 0,-2*a*(v-1), 128/3*b^2-2/3*a^2+2/3*a^2*v
 8,         0,                          0,-8,         0,                          0
 0,    -4*v+4,               -2*a*(v-1), 0,      4*v-4,               -2*a*(v-1)
 0,2*a*(v-1), 128/3*b^2-2/3*a^2+2/3*a^2*v, 0,-2*a*(v-1),-128/3*b^2-4/3*a^2+4/3*a^2*v]
```

Our new modeling is shown in the next figure:

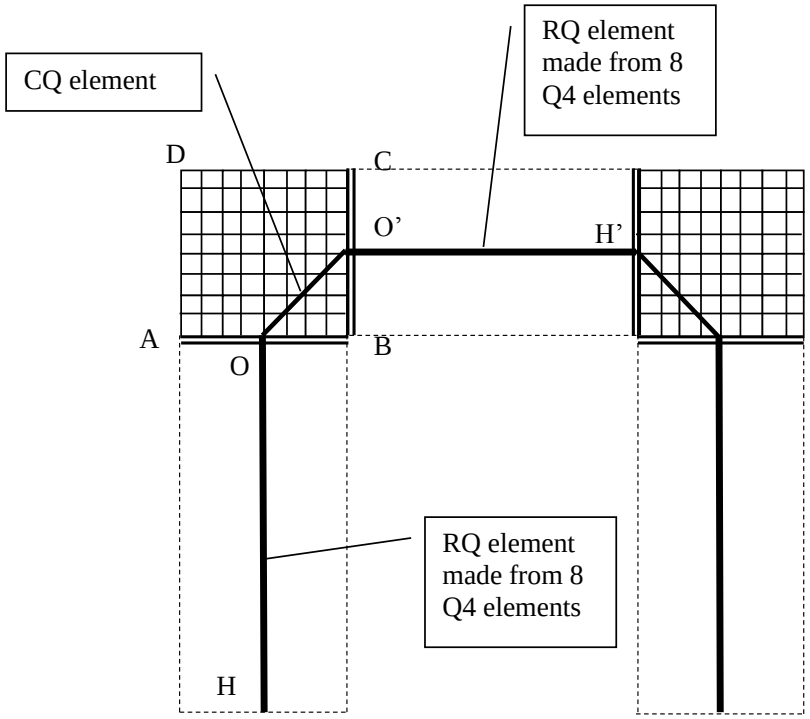

FIGURE 29: RQ MODEL FOR THE HORIZONTAL AND VERTICAL BEAMS WHILE CQ ELEMENT AT THE CORNERS

HO and O'H' are beam elements formed from 8 Q4 elements. OO' is a corner element.

The following graphs show the displacements along X and Y, for the two load cases for all the models that we have considered so far (Q4, Timoshenko, CQ, and RQ):

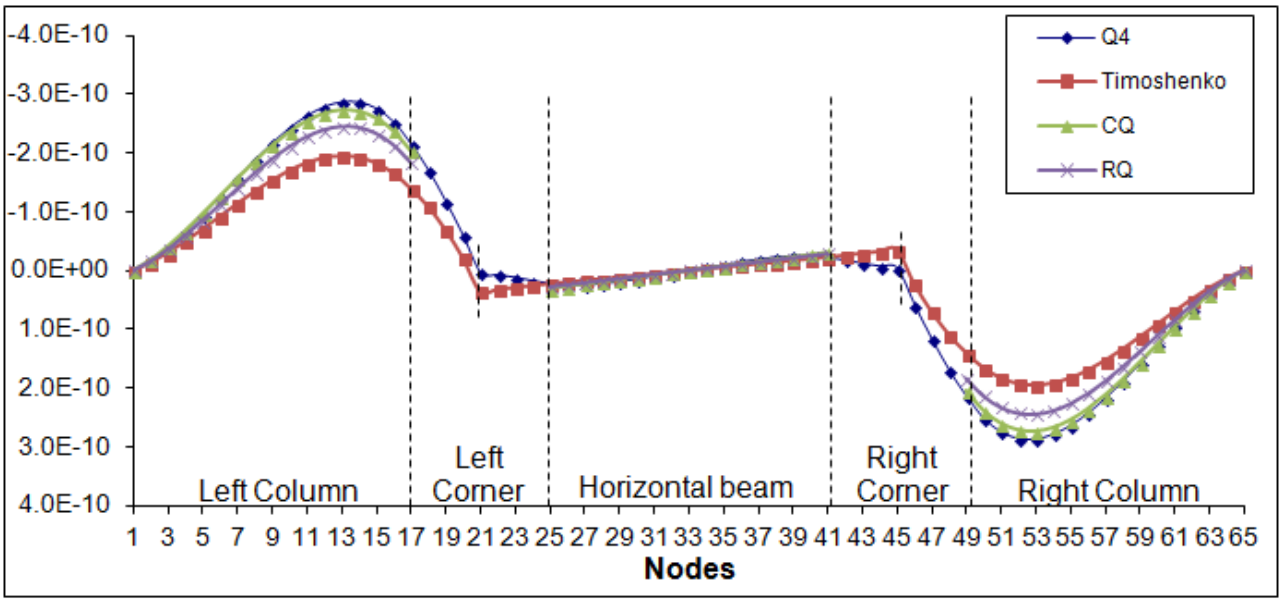

FIGURE 30 : UX (m) DISPLACEMENT OF THE CENTRAL LINE NODES ALONG X (LOAD CASE 1)

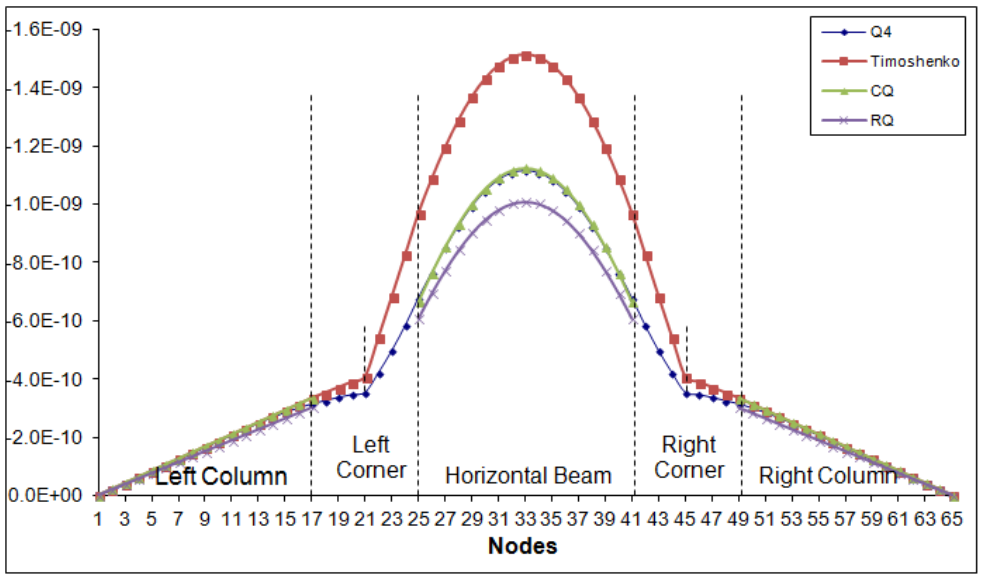

FIGURE 31 : UY (m) DISPLACEMENT OF THE CENTRAL LINE NODES ALONG Y (LOAD CASE 1)

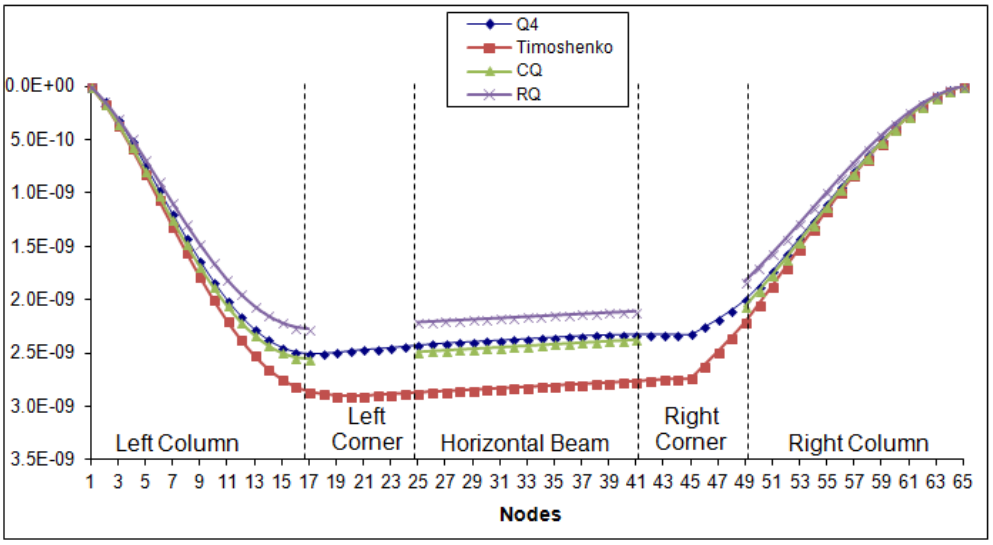

FIGURE 32: UX (m) DISPLACEMENT OF THE CENTRAL LINE NODES ALONG X (LOAD CASE 2)

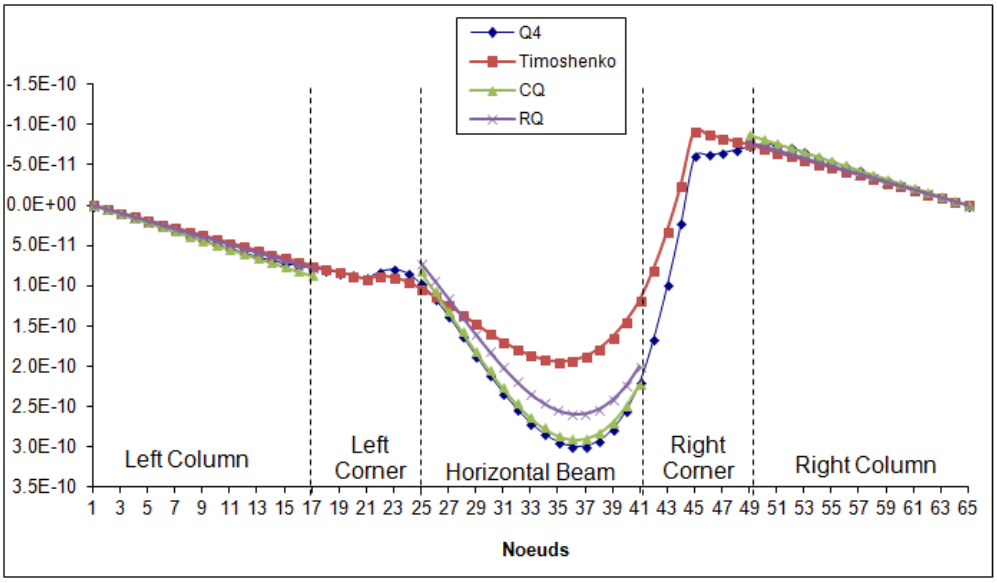

FIGURE 33 : UY (m) DISPLACEMENT OF THE CENTRAL LINE NODES ALONG Y (LOAD CASE 2)

VII. FOURTH IMPROVED MODEL (RQW)

The graphs of the previous paragraph show that the RQ model is a little stiffer than the CQ model. In order to give it a certain flexibility, we will add two DOFs (warping) for every node of the previous paragraph:

A new element is constructed from the RQ model that allows a plane section of a beam to deform a cubic or quadratic deformation after solicitation. Therefore, two DOFs will be added on each node:

A warping (in terms of y^2) that allows a quadratic displacement of the plane section and another warping term (in terms of y^3) that allows a cubic displacement of the plane section. The following figure illustrates the 5 DOFs on each node for the new element.

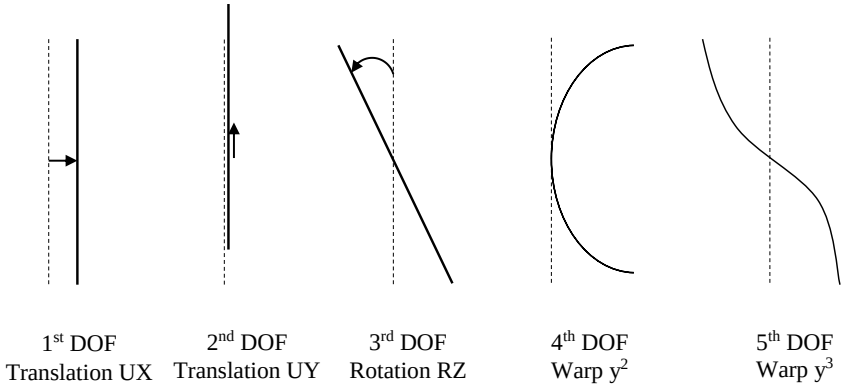

FIGURE 34: THE 5 DOFS FOR THE RQW MODEL

For this element with 5 DOFs per node we expect a stiffness matrix k(10,10). The terms of the 4th and 5th degree of the stiffness degree are calculated as follows:

We find the global matrix K(36,36), then matrix L of the rigid link:

```
L=[
1       0       4*b   -16*b^2          64*b^3  0       0       0       0       0
0       1       0           0          0       0       0       0       0       0
0       0       0           0          0       1       0       4*b     -16*b^2 64*b^3
0       0       0           0          0       0       1       0       0       0
1       0       3*b   -9*b^2           27*b^3  0       0       0       0       0
0       1       0           0          0       0       0       0       0       0
0       0       0           0          0       1       0       3*b     -9*b^2  27*b^3
0       0       0           0          0       0       1       0       0       0
1       0       2*b   -4*b^2           8*b^3   0       0       0       0       0
0       1       0           0          0       0       0       0       0       0
0       0       0           0          0       1       0       2*b     -4*b^2  8*b^3
0       0       0           0          0       0       1       0       0       0
1       0       1*b   -1*b^2           1*b^3   0       0       0       0       0
0       1       0           0          0       0       0       0       0       0
0       0       0           0          0       1       0       1*b     -1*b^2  1*b^3
0       0       0           0          0       0       1       0       0       0
1       0       0           0          0       0       0       0       0       0
0       1       0           0          0       0       0       0       0       0
0       0       0           0          0       1       0       0       0       0
0       0       0           0          0       0       1       0       0       0
1       0       -1*b    -1*b^2         -1*b^3  0       0       0       0       0
0       1       0           0          0       0       0       0       0       0
0       0       0           0          0       1       0       -1*b    -1*b^2  -1*b^3
0       0       0           0          0       0       1       0       0       0
1       0       -2*b -4*b^2            -8*b^3  0       0       0       0       0
0       1       0           0          0       0       0       0       0       0
0       0       0           0          0       1       0       -2*b    -4*b^2  -8*b^3
0       0       0           0          0       0       1       0       0       0
1       0       -3*b    -9*b^2         -27*b^3 0       0       0       0       0
0       1       0           0          0       0       0       0       0       0
0       0       0           0          0       1       0       -3*b    -9*b^2  -27*b^3
0       0       0           0          0       0       1       0       0       0
1       0       -4*b    -16*b^2        -64*b^3 0       0       0       0       0
0       1       0           0          0       0       0       0       0       0
0       0       0           0          0       1       0       -4*b    -16*b^2 -64*b^3
0       0       0           0          0       0       1       0       0       0       ];
```

We can find:

$$k = L^T * K * L$$

the stiffness matrix k for the left corner with (warp) is given numerically by:

kleft =

```
  4.6660e+009  1.5022e+009 -5.2058e+006 -7.3236e+004 -4.3907e+002 -4.6660e+009 -1.5022e+009 -2.6432e+007  2.5186e+005 -1.8964e+003
  1.5022e+009  4.6660e+009  2.6432e+007 -2.5186e+005  1.8964e+003 -1.5022e+009 -4.6660e+009  5.2058e+006  7.3236e+004  4.3907e+002
 -5.2058e+006  2.6432e+007  3.7398e+005 -1.6755e+003  2.7583e+001  5.2058e+006 -2.6432e+007 -5.7599e+004 -1.1072e+002 -4.2280e+000
 -7.3236e+004 -2.5186e+005 -1.6755e+003  2.8150e+001 -1.2750e-001  7.3236e+004  2.5186e+005 -1.1072e+002 -4.7061e+000  8.7138e-005
 -4.3907e+002  1.8964e+003  2.7583e+001 -1.2750e-001  2.6159e-003  4.3907e+002 -1.8964e+003 -4.2280e+000  8.7138e-005 -4.0191e-004
 -4.6660e+009 -1.5022e+009  5.2058e+006  7.3236e+004  4.3907e+002  4.6660e+009  1.5022e+009  2.6432e+007 -2.5186e+005  1.8964e+003
 -1.5022e+009 -4.6660e+009 -2.6432e+007  2.5186e+005 -1.8964e+003  1.5022e+009  4.6660e+009 -5.2058e+006 -7.3236e+004 -4.3907e+002
 -2.6432e+007  5.2058e+006 -5.7599e+004 -1.1072e+002 -4.2280e+000  2.6432e+007 -5.2058e+006  3.7398e+005 -1.6755e+003  2.7583e+001
  2.5186e+005  7.3236e+004 -1.1072e+002 -4.7061e+000  8.7138e-005 -2.5186e+005 -7.3236e+004 -1.6755e+003  2.8150e+001 -1.2750e-001
 -1.8964e+003  4.3907e+002 -4.2280e+000  8.7138e-005 -4.0191e-004  1.8964e+003 -4.3907e+002  2.7583e+001 -1.2750e-001  2.6159e-003
```

With a simple transformation, we can find the stiffness matrix of the right corner of our structure:

kright =

```
  4.6660e+009 -1.5022e+009 -5.2058e+006 -7.3236e+004 -4.3907e+002 -4.6660e+009  1.5022e+009 -2.6432e+007  2.5186e+005 -1.8964e+003
 -1.5022e+009  4.6660e+009 -2.6432e+007  2.5186e+005 -1.8964e+003  1.5022e+009 -4.6660e+009 -5.2058e+006 -7.3236e+004 -4.3907e+002
 -5.2058e+006 -2.6432e+007  3.7398e+005 -1.6755e+003  2.7583e+001  5.2058e+006  2.6432e+007 -5.7599e+004 -1.1072e+002 -4.2280e+000
 -7.3236e+004  2.5186e+005 -1.6755e+003  2.8150e+001 -1.2750e-001  7.3236e+004 -2.5186e+005 -1.1072e+002 -4.7061e+000  8.7138e-005
 -4.3907e+002 -1.8964e+003  2.7583e+001 -1.2750e-001  2.6159e-003  4.3907e+002  1.8964e+003 -4.2280e+000  8.7138e-005 -4.0191e-004
 -4.6660e+009  1.5022e+009  5.2058e+006  7.3236e+004  4.3907e+002  4.6660e+009 -1.5022e+009  2.6432e+007 -2.5186e+005  1.8964e+003
  1.5022e+009 -4.6660e+009  2.6432e+007 -2.5186e+005  1.8964e+003 -1.5022e+009  4.6660e+009  5.2058e+006  7.3236e+004  4.3907e+002
 -2.6432e+007 -5.2058e+006 -5.7599e+004 -1.1072e+002 -4.2280e+000  2.6432e+007  5.2058e+006  3.7398e+005 -1.6755e+003  2.7583e+001
  2.5186e+005 -7.3236e+004 -1.1072e+002 -4.7061e+000  8.7138e-005 -2.5186e+005  7.3236e+004 -1.6755e+003  2.8150e+001 -1.2750e-001
 -1.8964e+003 -4.3907e+002 -4.2280e+000  8.7138e-005 -4.0191e-004  1.8964e+003  4.3907e+002  2.7583e+001 -1.2750e-001  2.6159e-003
```

The following figures show the displacements along X et Y, for both the load cases, for all models (Reference model: Q4 model, Timoshenko model, CQ model, RQ, model and RQw).

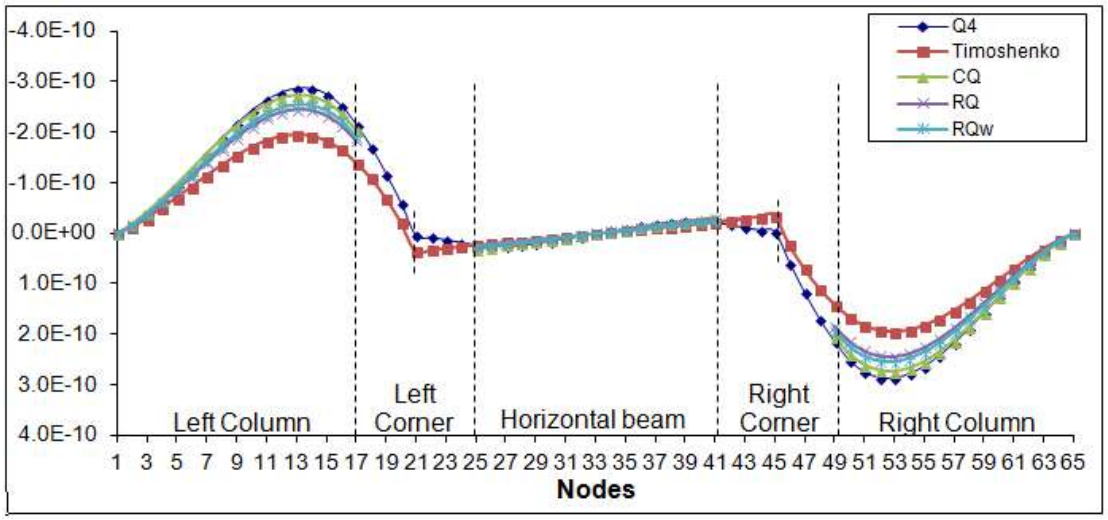

FIGURE 35: UX (m) DISPLACEMENT OF THE CENTRAL LINE NODES ALONG X (LOAD CASE 1)

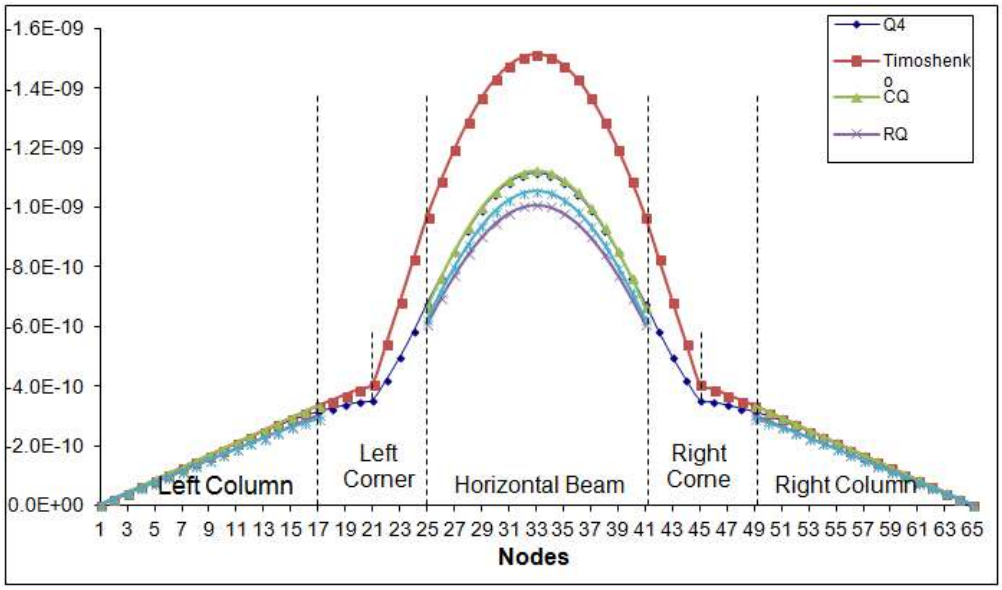

FIGURE 36: UY (m) DISPLACEMENT OF THE CENTRAL LINE NODES ALONG Y (LOAD CASE 1)

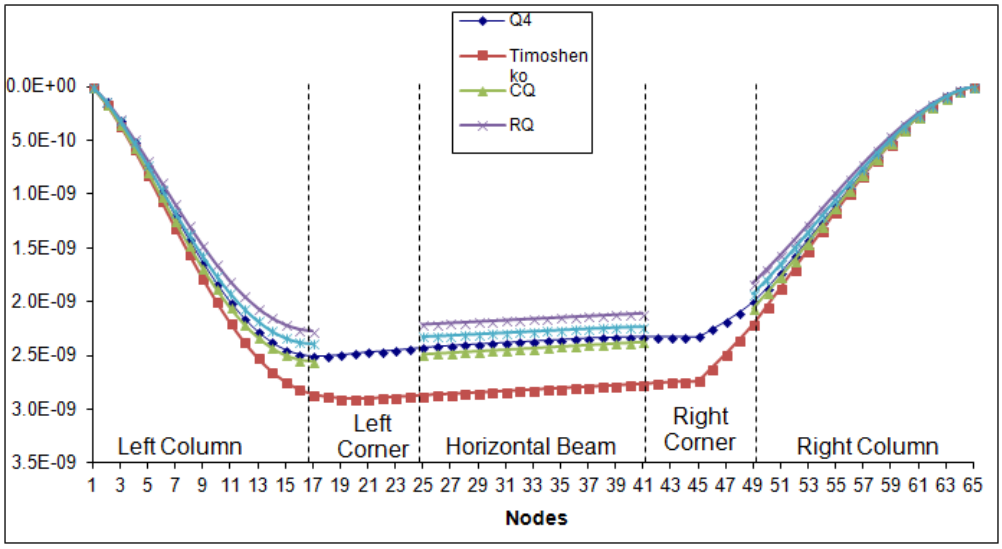

FIGURE 37: UX (m) DISPLACEMENT OF THE CENTRAL LINE NODES ALONG X (LOAD CASE 2)

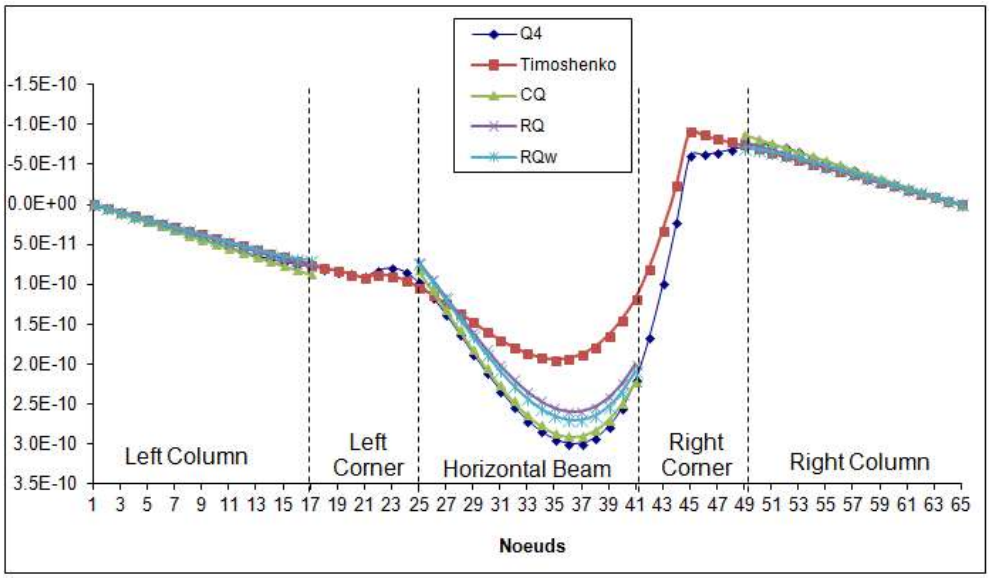

FIGURE 38: UY (m) DISPLACEMENT OF THE CENTRAL LINE NODES ALONG Y (LOAD CASE 2)

The previous graphs show that the RQw is more flexible than RQ, whereas CQ gives best results.

VIII. SUMMARY

The following table summarizes the results coming from all models:

TABLE 3
COMPARISON OF ALL MODELS AND ALL LOAD CASES

Model	Node (where E = E_{max})	Load case	Displacement	E_{max} par rapport à H8	E_{max} par rapport à Q4
H8	15 ou 51	1	UX	0%	1.55%
H8	33	1	UY	0%	1.90%
H8	16	2	UX	0%	3.01%
H8	39	2	UY	0%	2.92%
Q4	15 ou 51	1	UX	1.55%	0%
Q4	33	1	UY	1.90%	0%
Q4	16	2	UX	3.01%	0%
Q4	39	2	UY	2.92%	0%
Timoshenko	14 ou 52	1	UX	15.22%	16.28%
Timoshenko	33	1	UY	38.45%	35.87%
Timoshenko	36 ou 37	2	UX	21.48%	18.19%
Timoshenko	38 ou 39	2	UY	28.44%	30.38%
CQ	**15 ou 51**	**1**	**UX**	1.52%	**2.59%**
CQ	**17 ou 49**	**1**	**UY**	2.74%	**1.69%**
CQ	**28**	**2**	**UX**	5.52%	**2.70%**
CQ	**25**	**2**	**UY**	4.48%	**4.10%**
RQ	14 ou 52	1	UX	6.30%	7.61%
RQ	33	1	UY	7.71%	9.44%
RQ	16	2	UX	6.48%	9.19%
RQ	37	2	UY	8.72%	10.97%
RQw	14 ou 52	1	UX	4.34%	5.71%
RQw	33	1	UY	4.34%	5.37%
RQw	17	2	UX	1.66%	4.52%
RQw	36	2	UY	6.77%	7.84%

It is obvious that the CQ model gives best results when comparing with the Q4 model.

IX. CONCLUSION

Replacing the volumetric modeling of a simple frame by traditional 1-D elements leads to a weak simulation in static analysis. It is found out that the problem arises from corner connections. Modeling these connections by rigid links produces a stiff structure. Using CQ elements at the corners improves the results in the static analysis. Consequently, the number of elements and the number of DOF of the finite element model are dramatically reduced from hundreds of thousands to merely hundreds.

REFERENCES

[1] Alghamdi, S, "Dynamic stiffness matrix and load functions of Timoshenko beam using the transport matrix", Computers and Structures, 79 (2001) 1175-1185.

[2] Cook R. Concepts and applications of finite element analysis. 4th Edition. Wiley 2002.

[3] Craig R. Structural Dynamics – An introduction to computer methods. John Wiley & Sons 1981.

[4] Dohrmann CR, Key SW, Heinstein MW. "A method for connecting dissimilar finite element meshes in two dimensions". International Journal For Numerical Methods In Engineering 2000; **48 (5)**, pp. 655-678.

[5] Dohrmann CR, Key SW, Heinstein MW. "Methods for connecting dissimilar three-dimensional finite element meshes". International Journal For Numerical Methods In Engineering 2000; **47**, pp. 1057-1080.

[6] Hoit M. Computer Assisted Structural Analysis and Modeling. Prentice-Hall 1995.

[7] Kassimali A. Structural Analysis. Second edition. Brooks/Cole 1999.

[8] Kattner M, Crisinel M. "Finite element modeling of semi-rigid composite joints". Computers and Structures 2000; **78**, pp. 341-353.

[9] Quiroz L, Beckers P. "Non-conforming mesh gluing in the finite elements method". International Journal For Numerical Methods In Engineering 1995; **38 (13)**, pp. 2165-2184.

[10] Rao S. Mechanical Vibrations. 4th Edition. Pearson Education 2004.

Preparation of activated carbon from orange peel and its application for phenol removal

Loriane Aparecida de Sousa Ribeiro[1], Liana Alvares Rodrigues[2*], Gilmar Patrocínio Thim[3]

[1,3]Instituto Tecnológico de Aeronáutica-ITA/CTA, Praça Mal. Eduardo Gomes 50, CEP 12228-900, São José dos Campos, São Paulo, Brazil.

[2]Departamento de Engenharia Química, Escola de Engenharia de Lorena-EEL/USP, Estrada Municipal do Campinho S/N, CEP 12602-810, Lorena, São Paulo, Brazil

Abstract— *Activated carbon obtained from orange peel (ACO) was used as a phenol adsorbent. ACO was characterized by X-ray diffraction, Raman spectroscopy, scanning electronic microscopy (SEM) and energy dispersive spectroscopy (EDS). The functional groups present on the sample, were determined by Boehm titration, and it was also determined the point of zero charge (pHpzc). ACO is mainly constituted by micropores, and its structure is turbostratic and lamellar with inorganic impurities. The Boehm titration indicated the basic behavior of the sample. The phenol optimum dosage was 0.1 g/50 cm^3 which was determined by the adsorption study. The maximum adsorption level was in the pH range of 4-8 and its kinetics was described by a pseudo second order model. The equilibrium data have fit very well the Langmuir and Sips isotherms models.*

Keywords— adsorption, agricultural waste, biomass, orange peel, phenol.

I. INTRODUCTION

Brazil is the largest producer of oranges in the world, and it is responsible for about 30% of the world production[1]. Basically, almost all Brazilian´s orange production is used to produce orange juice[2].The European Union is the major consumer of orange juice, being 96% of it imported from Brazil[3]. The fruit is compounded of 50 % (w/w) of juice and the other 50 % of peel, pulp, seeds and membranes[2,4], being its peel, the primary byproduct during the orange juice processing[2]. Part of this waste material is used to produce pet food, fiber (pectin), fuel, essential oils, fertilizers, anti-oxidizing compounds and adsorbents [2,5,6]. However, the major part of the fruit after juice production becomes litter and is discarded to environment by juice industries [5]. Thus, changing the orange peel, which is a low cost agricultural waste, into a useful material, such as adsorbents that can add value to this residue and contribute to the problem of biomass disposal[7].

The phenol molecules and phenol-constituted substances are essential for several industrial processes, such as: rubber, dye, pharmaceutical and pesticide production and oil refining [8,9]. Nevertheless, their presence in water supply poses risks of water quality degradation and aquatic life death, moreover, it can inhibit the microbial community normal activities and cause carcinogenicity in animals [8,10]. Therefore, the discard of this kind of effluent is controlled by environmental offices and the maximum concentration allowed to this effluent is 0.002 mg/L [11]. The industries responsible for phenol contaminated effluent have to remove the phenol before discarding it in the environment in order to comply with the levels demanded by environmental agencies [12].

There are several methods proposed to remove phenol from industrial effluent, such as: biological treatment, adsorption on activated carbon, reverse osmosis, ionic exchange, solvent extraction, ultrasonic degradation and TiO_2 oxidation [13]. Among these methods, the adsorption process is the cheapest, simplest and fastest one for phenol removal [12]. Activated carbon is considered to be an effective method for phenol removal from contaminated effluents due to its elevated surface area, microporosity, and high adsorption capacity [14]. Nonetheless, phenol adsorption is economically unfeasible due to its elevated cost of production [7]. An alternative to reduce the activated carbon production cost is to use an abundant and low cost carbon source, such as agricultural or industrial waste to produce it [15]. Activated carbon from orange peel has been obtained with an elevated surface area and pore volume [16]. Consequently, activated carbon obtained from orange peel has emerged as a potential alternative for activated carbon production.

The main objective of this paper is to study the adsorption process of phenol in the activated carbon obtained from the orange peel. Its goal is to obtain a low cost activated carbon able to remove phenol from industrial effluent and concomitantly enhance the value of an abundant biomass and solve its disposal problem.

II. METHODOLOGY

2.1 Synthesis of the activated carbon from orange peel (citrus sinensis)

The activated carbon was prepared following these seven steps:

1. Rinsing it with deionized water;
2. Drying it in an oven at 100 °C until constant mass;
3. Milling and sieving it (4-8 mesh);
4. Carbonizing it in a tubular furnace under argon flow, from 25 °C to 800 °C at a heating rate of 30 °C/min, which was maintained at 1073K for 1 hour;
5. Turning off the argon flow and turning on CO_2 at 100 cm^3/min. Maintaining the samples under this condition for 3 hours;
6. Turning off the CO_2 flow and turning on the argon at 100 cm^3/min, switching off the heating system;
7. Milling and sieving it (325 mesh). Sample in this stage was called ACO.

2.2 Characterization

The point of zero charge (pHpzc) was determined using the methodology described in several papers [12,17,18]. ACO (0.05 g) was added to several flasks containing 25 cm^3 of KNO_3 (concentrations 10^{-1} and 10^{-2} M) solutions which the initial pH values (pHi) were adjusted in the pH range of 2–8 using 0.1 M of HCl or NaOH. Then, the equilibrium was carried out in a thermostatic linear shaker for 24 h at 298 K. The dispersions were then filtered and the final pH of the solutions (pH_f) was determined. The point of zero charge was found from a plot of ($pH_i - pH_f$) versus pH_i. The Boehm method was used to determine the amount of the oxygenated chemical groups [19], where one gram of ACO was placed in 25 cm^3 of the following aqueous solutions: sodium hydroxide, sodium carbonate, sodium ethoxide, sodium bicarbonate and hydrochloric acid. The vials were sealed, shaken for 24hs and then filtered. The filtrate was titrated with HCl or NaOH to determine the base or acid excess, respectively.

The sample morphology was observed in a Scanning Electron Microscope (SEM), Zeiss model EVO MA 10. Energy dispersive spectroscopy (EDS) measurements were carried out in an Oxford INCA Energy Microanalysis System which was incorporated to SEM. Raman spectroscopy was carried out in a Renishaw 2000 equipment using ionic laser of Ar^+ (λ=514.5 nm). Powders were analyzed in a X ray diffraction equipment, using a PANalytical X'Pert PRO MPD 3060 diffractometer, equipped with a X'celerator detector, operating at 45 kV and 25 mA with CuKα radiation. XRD patterns were collected in the 2θ range from 10 to 90º at scan speed of 0.42 º s^{-1} and step size of 0.017°.

2.3 Adsorption study

Adsorption studies were carried out in amber glass flasks of 100 cm^3, where ACO was mixed to a phenol aqueous solution (50 cm^3), being stirred in a thermostatic shaker. The supernatant solution was separated from the adsorbent by filtration. The phenol concentration in the supernatant was spectrophotometrically determined using UV–VIS absorbance spectrophotometery at 269 nm [20]. Solutions, with higher concentration than the ones detected by the spectrophotometer, were determined by dilution. Adsorption kinetics was performed using 0.1 g of ACO, in a period from 0 to 24 hours, without adjusting its pH, 25 °C and a phenol initial concentration of 1000 mg/dm^3. The pH effect was carried out using 0.1 g of ACO, during 3hs, with a pH range between 2 and 12, at a temperature of 25 °C and a phenol initial concentration of 1000 mg/dm^3. Dosage effect was accomplished using ACO mass range between 0.1 and 0.5 g, bath time of 3 hours, without adjusting its pH, at a temperature of 25 °C and a phenol initial concentration of 1000 mg/dm^3. The isotherm adsorption was obtained using 0.1 g of ACO, bath time of 3 hours, without adjusting its pH, at a temperature of 25 °C and phenol initial concentration ranging from 50 to 1000 mg/L.

III. RESULTS AND DISCUSSION

3.1 Characterization

The pH_{PZC} is the pH in which the surface charge of a material is zero. The surface of an amphoretic material is positively charged if the medium pH is lower than pH_{PZC}. On the other hand, it is negatively charged if the medium pH is higher than pH_{PZC} [7]. The pH_{PZC} of ACO is 10.5, indicating a basic character in water.

The number of basic sites on the ACO surface was determined from the amount of hydrochloric acid that reacted with the activated carbon. The number of acid sites was determined under the following assumptions: a) there are only carboxylic, lactonic, phenolic and carbonyl groups on ACO, b) NaOH neutralizes the carboxylic, lactonic and phenolic groups; c)

Na_2CO_3 neutralizes the carboxylic and lactonic groups; d) $NaHCO_3$ neutralizes only the carboxylic groups; and e) $NaOC_2H_5$ neutralizes the carbonyl (quinoid-type), carboxylic, lactonic and phenolic groups. This procedure is called Boehm titration and is described in several papers [7,19]. Table 1 shows the amount of acid and basic groups present on the ACO surface. The amount of basic groups (3.38) is higher than the acid groups (1.19). Therefore, the sample is predominantly basic.

TABLE 1
SURFACE FUNCTIONAL GROUPS FOR ACO

Acid sites				Basic sites (mmol g^{-1})
Carboxyl (mmol g^{-1})	Lactones (mmol g^{-1})	Phenols (mmol g^{-1})	Carbonyl (quinoid-type) (mmol g^{-1})	
0.00	0.00	1.19	0.00	3.38

Fig. 1 shows the Raman spectrum of ACO sample, which shows peaks centered at 1361 and 1583 cm^{-1}. These peaks are attributed to the D band (1200-1400 cm^{-1}) and G band (1500-1600 cm^{-1}), respectively [22].

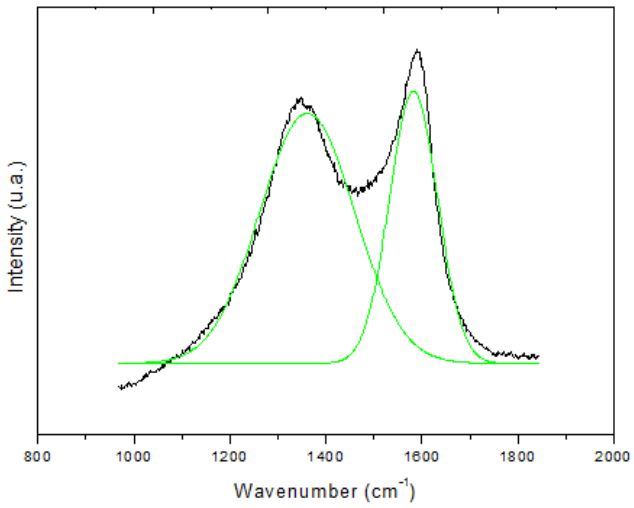

FIGURE 1. RAMAN PROFILE OF THE ACO SAMPLE

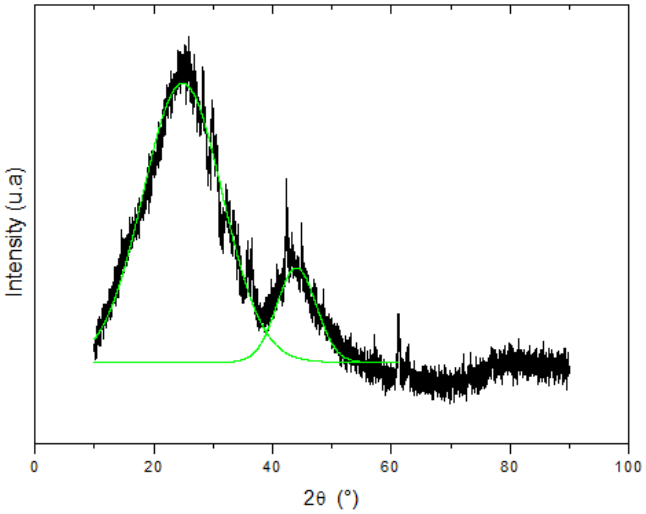

FIGURE 2. X RAY DIFFRACTOGRAM OF THE ACO SAMPLE

A Gaussian deconvolution method was used to obtain the half width of band G (100.5 cm^{-1}), which is much higher than the graphite value (15-23 cm^{-1}), indicating that the crystallinity of the ACO sample is much lower than the graphite [23]. The value of the average lateral sizes (L_a), calculated from Raman data by using Equation 1 [23], is 2.42 nm.

$$L_a = C(\lambda_L)\frac{I_G}{I_D} \quad (1)$$

In equation 1, I_D and I_G are areas of D band and G band, respectively, and $C(\lambda_L)=C_o+\lambda_L C_1$. Where, C_o is equal to -12.6 nm; λ_L is the wavelength and C_1 is equal to 0.033.

Fig. 2 shows the X ray diffraction profile (XRD) of the ACO sample, where one can see broad peaks centered at 24.86 and 44.05 ° (2θ), which are associated to Muller index of (002) and (101) [24]. These peaks are characteristics of a turbostratic structure of graphite micro crystallites and they mean that ACO has an intermediate structure between amorphous carbon and graphite [23].

Using Gaussian deconvolution on XRD data, one could use the peak at 24.86 °to estimate both the spacing of aromatic ring layers (d_{002}) and the crystallite thickness (L_c) [25]. However, the average lateral size ($L_{a\text{-}XRD}$) of the crystallites was determined using the peak at (101) [25]. The d_{002} (0.352 nm) was calculated using Bragg's law and the crystallite size L_c (0.601 nm) and $L_{a\text{-}XRD}$ (2.60 nm) were determined using Scherrer's equation [25]. The value of d_{002} (0.352 nm) was higher than the one of pure graphite (0.336-0.337 nm), due to a lower crystalline degree of the ACO sample in relation to the graphite [23]. It can be observed several sharp and less intense peaks besides peaks at 24.86 and 44.05 ° (2θ), which may be related to inorganic materials that were already present in the biomass. Comparing the value of L_a previously determined by

Raman spectroscopy (2.42) with that determined by XRD (2.60), it can be concluded that they are very close. Nevertheless, the L_a determination by XRD is considered much more accurate than the Raman spectroscopy one [23].

The morphology of the ACO sample can be observed in Fig. 3A and 3B.

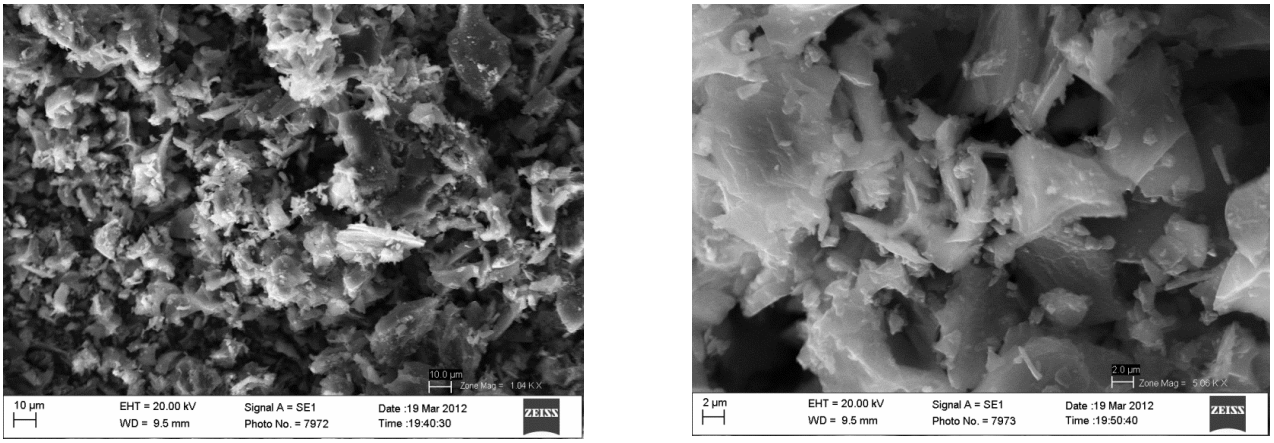

(A) (B)

FIGURE 3. SEM IMAGES OF THE ACO AT DIFFERENT ENLARGEMENTS

These Figures show that the particles are non-uniform, i.e. without a predominant form. In addition, Fig. 3B shows that the ACO has a lamellar structure.

Energy dispersive spectroscopy (EDS) was used to determine the chemical composition of the ACO sample and its results are shown in Table 2.

TABLE 2
RESULTS OF ENERGY DISPERSIVE SPECTROSCOPY (EDS) MEASUREMENTS

	Element								
	C	O	Mg	P	S	Cl	K	Ca	Fe
% Weight	65.0	18.0	0.4	1.2	0.5	0.2	7.8	6.6	0.3
% Atomic	77.5	16.0	0.3	0.5	0.2	0.1	2.9	2.4	0.1

This table shows that the ACO is constituted of several elements, such as: magnesium, phosphorus, surfer, chlorine, potassium, calcium, and iron. According to [26] and [27], most of these elements are a characteristic of the orange peel composition. The concentration of potassium (2.9 %) and calcium (2.4 %) is much higher than the others, but their concentrations are considered normal in Brazilian oranges. The presence of oxygen is an indication that the ACO had a lot of oxygenated groups on its surface.

3.2 Adsorption

The kinetic data of phenol adsorption onto the ACO are shown in Fig. 4.

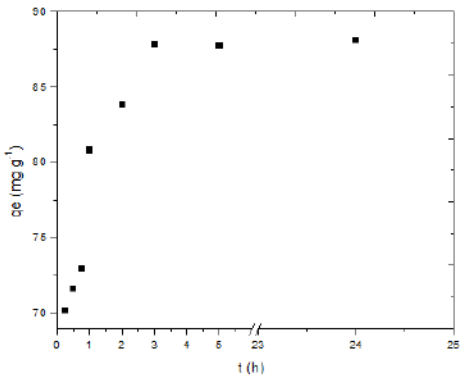

FIGURE 4. CONTACT TIME EFFECT ON ADSORBED PHENOL CONCENTRATION

For the ACO, the contact time of 3 hs is needed to establish the phenol adsorption equilibrium. At this stage, the adsorbed phenol amount is 88 mg g^{-1}, i.e. 19 % of the initial amount. The kinetic data were fitted using pseudo first-order and pseudo second-order kinetic models [28]. The kinetic results are shown in Table 3. It can be observed from Table 3 that the correlation coefficient (R^2) for pseudo first-order kinetic model (0.88) was much lower than R^2 for the pseudo-second order model (1.00), indicating that the kinetic of adsorption process is more accurately represented by the pseudo second-order kinetic model. In addition, the comparison between the equilibrium concentration obtained from Fig. 4 (qe = 88 mg g^{-1}) and that one from pseudo-first order (qe = 23.60 mg g^{-1}) and from pseudo-second order (qe = 87.64 mg g^{-1}) reinforces that the adsorption kinetic process of phenol onto the ACO can be described by a pseudo-second order model.

TABLE 3
KINETIC PARAMETERS OF PHENOL ADSORPTION ON THE ACO

C_0 (mg L^{-1})	Pseudo first-order			Pseudo second-order		
	K_1 (h^{-1})	q_e (mg g^{-1})	R^2	K_2 (h^{-1})	q_e (mg g^{-1})	R^2
1000	0.92	23.60	0.88	0.11	87.64	1.00

Fig. 5 shows the adsorption percentage (%) and adsorption capacity (q_e) of the phenol as a function of the ACO dosage, where the ACO dosage ranged from 0.01 to 0.5 g.

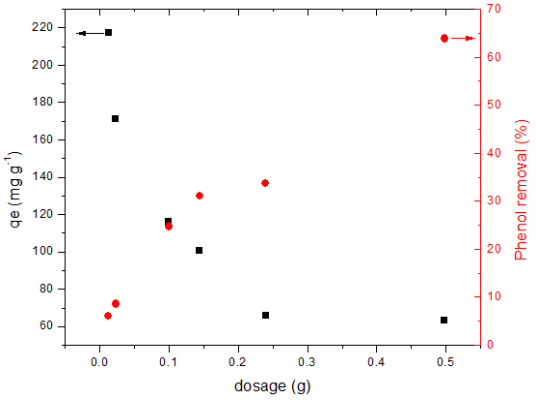

FIGURE 5. EFFECT OF ADSORBENT DOSE ON THE ADSORPTION OF PHENOL ONTO THE ACO

It can be observed that the phenol removal (%) and the phenol adsorption capacity (qe) depend strongly on the ACO dosage. However, these two properties have distinct dependence on the ACO dosage, i.e. the removal efficiency increased with the dosage while the adsorption capacity decreased. The former may happen due to an increase in the adsorption sites with an increase in the ACO dosage [29]. Nevertheless, a higher adsorbent dose results in a lower adsorption capacity due to overcrowding of adsorbent particles, resulting in a decrease in the availability of adsorption sites [7]. In order to carry out further studies we have to choose a "work dosage", in which both the equilibrium concentration and the removal amount have meaningful values. Consequently, in the next studies, an ACO dosage of 0.1 mg g^{-1} will be used.

The effect of pH on phenol adsorption is showed in Fig. 6.

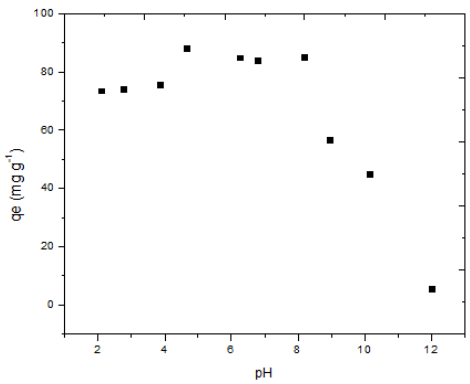

FIGURE 6. EFFECT OF SOLUTION PH ON THE ADSORPTION OF PHENOL ONTO THE ACO

It can be observed that the value of qe is almost the same in the pH range from 2 to 4. After that, i.e. pH > 4, the phenol adsorption increases with an increase in pH up to 4.5, then the phenol adsorption remains constant until pH ~ 8 and thereafter the phenol adsorption decreases. The increase in the phenol adsorption after pH 4 results from the decrease in hydrogen ion concentration in solution [8]. These ions are adsorbed in basic sites, resulting in a decrease in the basic site interactions of the ACO surface with phenol molecules [8]. In other words, the decrease in hydrogen ion concentration in a solution with a pH increase, results in an increase in the site number available for phenol adsorption. The phenol adsorption reaches its maximum value at a pH range from 4.5 to 8 because phenol is undissociated and the dispersion interaction is predominant [14].The decrease in qe value between pH 8 and 10 is given by an increase in OH^- ions quantity [30]. The OH^- ions in the solution are adsorbed on the positively charged ACO surface (pH_{pzc} = 10.5), which reduces the undissociated phenol-ACO surface interaction. At pH >10.5 the phenol adsorption decreases abruptly, probably, due to electrostatic repulsion between the negatively charged ACO surface and the anionic form of the phenol molecules (pK_a = 9.9) in the solution [30,31].

Fig. 7 and Table 4 shows the results of fitted experimental data to Langmuir and Langmuir-Freundlich (Sips) equations [32].

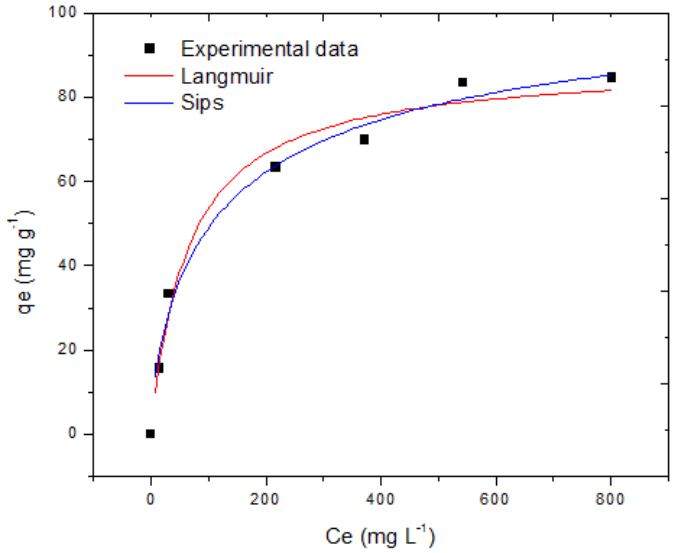

FIGURE 7. ADSORPTION ISOTHERM OF PHENOL ONTO THE ACO

It can be seen that the R^2 related to Langmuir and Langmuir-Freundlich model is quite high and the same. Considering that the adsorption process follows the Langmuir model (the simplest one), the maximum phenol adsorption capacity of ACO is 88 mg g^{-1} and the adsorption occurs in a monolayer [33].

TABLE 4
ADSORPTION ISOTHERM CONSTANTS FOR PHENOL ONTO THE ACO

Langmuir isotherm			Langmuir-Freundlich (Sips) isotherm			
b (L mg^{-1})	Q_m (mg g^{-1})	R^2	b (L mg^{-1})	Q_m (mg g^{-1})	α	R^2
0,02	88	0.97	0.03	111	0.69	0.97

Thus, orange peels must be considered an excellent source of biomass to produce the phenol adsorbent, taking into account their great availability, their environmental disposal problems and their considerable phenol adsorption capacity.

IV. CONCLUSION

The ACO has a turbostratic structure and is mainly constituted by micropores. The sample presents inorganic impurities in its composition and has a basic character in water. The optimum dosage was 0.1 g/50 cm^3 of phenol solution and the optimum pH range was between 4 and 8. The phenol adsorption onto the ACO followed a pseudo second order model and its monolayer adsorption capacity was 88 mg g^{-1}.

ACKNOWLEDGEMENTS

The authors gratefully acknowledge CNPq, Fapesp andCAPES for financial support.

REFERENCES

[1] J.J.T. Gama, C.M. Sylos, Major carotenoid composition of Brazilian Valencia orange juice: Identification and quantification by HPLC, Food Res. Int. 38 (2005) 899–903.

[2] H.R.M. Barros, T.A.P.C. Ferreira, M.I. Genovese, Antioxidant capacity and mineral content of pulp and peel from commercial cultivars of citrus from Brazil, Food Chem. 134 (2012) 1892–1898.

[3] M.T.P.S. Clerici, Nutritional bioactive compounds and technological aspects of minor fruits grown in Brazil, Food Res. Int. 44 (2011) 1658–1670.

[4] L.D. Fiorentin, B.T. Menon, S.T.D. Barros, N.C. Pereira, O.C.M. Lima, A.N. Modenes, Isotermas de sorção do resíduo agroindustrial bagaço de laranja, Rev. Bras. Eng. Agrícola E Ambient. 14 (2010) 653–659.

[5] A.M. Alexandrino, H.G. De Faria, C. Giatti, M. De Souza, R.M. Peralta, Aproveitamento do resíduo de laranja para a produção de enzimas lignocelulolíticas por Pleurotus ostreatus (Jack : Fr), Ciência E Tecnol. Aliment. 27 (2007) 364–368.

[6] M.E.R. Cantu, Journal of Analytical and Applied Pyrolysis Pyrolysis of sweet orange (Citrus sinensis) dry peel, 86 (2009) 245–251.

[7] L.A. Rodrigues, M.L.C.P. da Silva, M.O. Alvarez-Mendes, A.R. Coutinho, G.P. Thim, Phenol removal from aqueous solution by activated carbon produced from avocado kernel seeds, Chem. Eng. J. 174 (2011) 49–57.

[8] Q.-S. Liu, T. Zheng, P. Wang, J.-P. Jiang, N. Li, Adsorption isotherm, kinetic and mechanism studies of some substituted phenols on activated carbon fibers, Chem. Eng. J. 157 (2010) 348–356.

[9] L.A. Rodrigues, T.M.B. Campos, M.O. Alvarez-Mendes, A.R. Coutinho, K.K. Sakane, G.P. Thim, Phenol removal from aqueous solution by carbon xerogel, J. Sol-Gel Sci. Technol. (2012).

[10] K. Lin, J. Pan, Y. Chen, R. Cheng, X. Xu, Study the adsorption of phenol from aqueous solution on hydroxyapatite nanopowders., J. Hazard. Mater. 161 (2009) 231–40.

[11] X. Zeng, Y. Fan, G. Wu, C. Wang, R. Shi, Enhanced adsorption of phenol from water by a novel polar post-crosslinked polymeric adsorbent., J. Hazard. Mater. 169 (2009) 1022–8.

[12] L.A. Rodrigues, L.A. Sousa Ribeiro, G.P. Thim, R.R. Ferreira, M.O. Alvarez-Mendez, A.D.R. Coutinho, Activated carbon derived from macadamia nut shells: an effective adsorbent for phenol removal, J. Porous Mater. (2012).

[13] G. Dursun, H. Ciçek, A.Y. Dursun, Adsorption of phenol from aqueous solution by using carbonised beet pulp., J. Hazard. Mater. 125 (2005) 175–82.

[14] B.H. Hameed, a a Rahman, Removal of phenol from aqueous solutions by adsorption onto activated carbon prepared from biomass material., J. Hazard. Mater. 160 (2008) 576–81.

[15] A. Bhatnagar, M. Sillanpää, Utilization of agro-industrial and municipal waste materials as potential adsorbents for water treatment—A review, Chem. Eng. J. 157 (2010) 277–296.

[16] J.C. Moreno-Piraján, L. Giraldo, Heavy Metal Ions Adsorption from Wastewater Using Activated Carbon from Orange Peel, E-Journal Chem. 9 (2012) 926–937.

[17] L. Wang, J. Zhang, A. Wang, Removal of methylene blue from aqueous solution using chitosan-g-poly(acrylic acid)/montmorillonite superadsorbent nanocomposite, Colloids Surfaces A Physicochem. Eng. Asp. 322 (2008) 47–53.

[18] L.A. Rodrigues, L.J. Maschio, R.E. da Silva, M.L.C.P. da Silva, Adsorption of Cr(VI) from aqueous solution by hydrous zirconium oxide., J. Hazard. Mater. 173 (2010) 630–6.

[19] H. Boehm, Some aspects of the surface chemistry of carbon blacks and other carbons, Carbon N. Y. 32 (1994) 759–769.

[20] L. Zhu, Y. Deng, J. Zhang, J. Chen, Adsorption of phenol from water by N-butylimidazolium functionalized strongly basic anion exchange resin., J. Colloid Interface Sci. 364 (2011) 462–8.

[21] K.S.W. Sing, D.H. Everett, R.A.W. Haul, L. Moscou, R.A. Pierotti, J. Rouquérol, T. Siemieniewska, Reporting physisorption data for gas/solid systems with special reference to the determination of surface area and porosity (Recommendations 1984), Pure Appl. Chem. 57 (1985) 603–619.

[22] C.M.L. Barbosa, M.T.C. Sansiviero, Decomposição térmica de complexos de Zn e Cd com isomaleonitriladitiolato (imnt), Quim. Nova. 28 (2005) 761–765.

[23] O.O. Sonibare, T. Haeger, S.F. Foley, Structural characterization of Nigerian coals by X-ray diffraction, Raman and FTIR spectroscopy, Energy. 35 (2010) 5347–5353.

[24] S.-S. Tzeng, K.-H. Hung, T.-H. Ko, Growth of carbon nanofibers on activated carbon fiber fabrics, Carbon N. Y. 44 (2006) 859–865.

[25] D. Li, H. Wang, X. Wang, Effect of microstructure on the modulus of PAN-based carbon fibers during high temperature treatment and hot stretching graphitization, J. Mater. Sci. 42 (2007) 4642–4649.

[26] A. K. Bejar, N. B. Mihoubi, N. Kechaou, Moisture sorption isotherms – Experimental and mathematical investigations of orange (Citrus sinensis) peel and leaves, Food Chem. 132 (2012) 1728–1735.

[27] A.U. Mahmood, J. Greenman, A.H. Scragg, Orange and potato peel extracts: Analysis and use as Bacillus substrates for the production of extracellular enzymes in continuous culture, Enzyme Microb. Technol. 22 (1998) 130–137.

[28] L.A. Rodrigues, M.L.C.P. da Silva, Thermodynamic and kinetic investigations of phosphate adsorption onto hydrous niobium oxide prepared by homogeneous solution method, Desalination. 263 (2010) 29–35.

[29] A. Shukla, Y.-H. Zhang, P. Dubey, J.L. Margrave, S.S. Shukla, The role of sawdust in the removal of unwanted materials from water., J. Hazard. Mater. 95 (2002) 137–52.

[30] H.B. Senturk, D. Ozdes, A. Gundogdu, C. Duran, M. Soylak, Removal of phenol from aqueous solutions by adsorption onto organomodified Tirebolu bentonite: equilibrium, kinetic and thermodynamic study., J. Hazard. Mater. 172 (2009) 353–62.

[31] M.H. El-Naas, S. a Al-Muhtaseb, S. Makhlouf, Biodegradation of phenol by Pseudomonas putida immobilized in polyvinyl alcohol (PVA) gel., J. Hazard. Mater. 164 (2009) 720–5.

[32] V.V.S. Guilarduci, J.P. Mesquita, P.B. Martelli, H.F. Gorgulho, Adsorção de fenol sobre carvão ativado em meio alcalino, Quim. Nova. 29 (2006) 1226–1232.

[33] L.A. Rodrigues, M.L.C.P. Silva, Adsorption kinetic, thermodynamic and desorption studies of phosphate onto hydrous niobium oxide prepared by reverse microemulsion method, Adsorption. 16 (2010) 173–181.

Mechanical properties of thermoset-metal composite prepared under different process conditions

Gean Vitor Salmoria[1*], Felix Yañez-Villamizar[2], Aurelio Sabino-Netto[3]

CIMJECT, Department of Mechanical Engineering, Federal University of Santa Catarina, 88040-900 Florianopolis, Santa Catarina, Brazil

Abstract— *This paper reports a study on the morphology and mechanical behavior of a thermoset-metal composite used in prototype molds as a function of the process conditions. The investigation of the mechanical properties of epoxy-aluminum specimens post-cured using different routines showed that they are related to the self-controlled diffusion characteristic of thermoset polymeric systems. A high-temperature post-cure routine resulted in higher values for the modulus, stiffness and glass transition temperature, Tg, for the specimens. The fracture surfaces analysis showed the presence of defects, which appeared as empty spaces in the epoxy matrix, due to the mixing and casting process. The defect size and the specimen strength showed a direct correlation. The Weibull modulus was 7.95 for the epoxy specimens characterizing low toughness and the presence of defects in the material, as revealed by fractography. The probability of failure increased rapidly to 50% for applied stress greater than 38 MPa.*

Keywords— Thermoset-metal, mechanical properties, process conditions.

I. INTRODUCTION

Thermoset resin curing permits the rapid manufacturing of parts and objects by casting. The main applications of thermoset curing are the production of prototypes and parts used in the automobile, electrical, biomedical and aerospace industries. Thermoset curing is also applied in the manufacture of functional prototypes, such as prototype tools [1-7]. The thermal and mechanical properties are of great importance for prototype tools such as molds for the injection of thermoplastics, since these tools are subjected to particular work conditions, with temperature variations and mechanical requirements [7-12].

The mechanical properties of parts or tools manufactured by thermoset curing are dependent on the degree of cure of the resin. Manufacturing parameters, such as mixing, curing, post-curing and resin characteristics (monomers, oligomers and curing agent composition), maximum density of cross-linking, photosensitivity, rate and degree of cure, and post-cure method are very important in relation to the structure and properties of the part or tool [10-17]. Knowledge of the relationship between the thermoset resin structure and properties is useful in the manufacturing process, application and quality control of tools. Prototype molds with molding blocks produced by thermoset polymer resins have low mechanical properties compared to conventional steel tools. Prototype molds produced by casting of a thermoset-metal composite are commonly used to produce a small series of polymeric parts [5, 7 12, 14-17]. During injection molding, the mold is subjected to several types of loading, either static or dynamic. This means that the composite in the molding blocks needs to have good mechanical performance to avoid premature failure of the prototype mold. This paper reports a study on the morphology and mechanical behavior of an epoxy-aluminum composite used in prototype molds as a function of the post-cure process conditions.

II. MATERIALS AND METHODS

2.1 Materials

An epoxy polymer containing 30% aluminum by weight, supplied by Hunstman as RenCast 436, was mixed with the appropriate curing agent, Ren HY 150, obtained from the same company. The material is an epoxy system base in bisphenol A and phenol novolac derivatives.

2.2 Mixture Procedure

In order to determine the effect of the post-cure process on the mechanical properties of the epoxy-aluminum composite, the mixture of epoxy pre-polymer with aluminum particles and curing agent was prepared applying mechanical stirring (85 rpm) for 2 min at 20 mmHg. The mixture was poured into silicone rubber models to fabricate the test specimens.

2.3 Cure and Post-cure Procedure

Experiments were carried out to evaluate the influence of the post-cure on the tensile strength and the dynamic mechanical properties of the material. Specimens were cured at room temperature for 24 h, according to the procedure suggested by the supplier, and post-cured in a conventional thermal oven using the post-cure routines shown in Table 1.

TABLE 1
POST-CURE ROUTINES APPLIED TO THE CASTING EPOXY SPECIMENS

Specimens	Post-cure routine
A	2 h at 70ºC ; 2 h at 90ºC; 2 h at 120ºC; 2h at 150ºC
B	4 h at 90ºC ; 4 h at 150ºC
C	4 h at 70ºC ; 4 h at 150ºC

2.4 Tensile Tests

Tensile test specimens were obtained, according to the standard ASTM D638 type I, using the epoxy-aluminum composite. Five specimens were tested for each post-cure cycle, at uniaxial tension and at room temperature, using an EMIC universal testing machine with a displacement rate of 5mm/min. The Young's modulus was determined through the stress–strain correlation considering the linear region (Table 2). The strain was measured using an incremental extensometer.

2.5 Fractography

Fracture surfaces of the tensile specimens were observed with a scanning electron microscope (Philips XL30) in order to investigate the fracture topography. Each specimen was coated with gold in a Bal-Tec Sputter Coater SCD005. Fracture image analysis was carried out using Analysis Pro 2.11.002©Soft-imaging Software GmbH in order to investigate the failure.

2.6 Dynamic Mechanical Analysis (DMA)

Dynamic mechanical analysis was carried out on specimens with dimensions of 10 mm x 40 mm x 3.5 mm over a temperature range of -70ºC to 200 °C using a DMTA analyzer (Elkin-Palmer Instruments) in the three bending point mode geometry, according to the standard ASTM D5023. The specimens were scanned isochronally at 3 °C/min. The damping factor (Tan □) and storage modulus (Log E') were recorded at 1 Hz.

III. RESULTS AND DISCUSSION

Figure 1 presents the stress-strain curves for the post-cured specimens. Table 2 shows the main values for the elastic modulus and the tensile strength for the post-cured specimens and it can be observed that specimens post–cured using routine A presented higher tensile strength values.

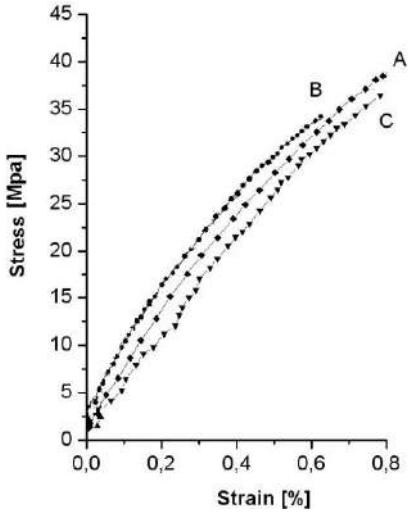

FIGURE 1. STRESS VERSUS STRAIN CURVES FOR THE EPOXY SPECIMENS POST-CURED USING DIFFERENT ROUTINES.

TABLE 2
ELASTIC MODULUS AND TENSILE STRENGTH VALUES FOR SPECIMENS POST-CURED USING DIFFERENT ROUTINES.

Post-cure routine	Elastic Modulus [MPa]	Tensile strength [MPa]
A	6270 (±200)	37 (±3)
B	6350 (±300)	33 (±3)
C	6220 (±300)	35 (±3)

These results are related to the self-controlled diffusion characteristic of the thermoset polymeric systems, leading to a greater improvement in the crosslink density when gradual thermo-curing ramp routines are applied, i.e. in A routine.

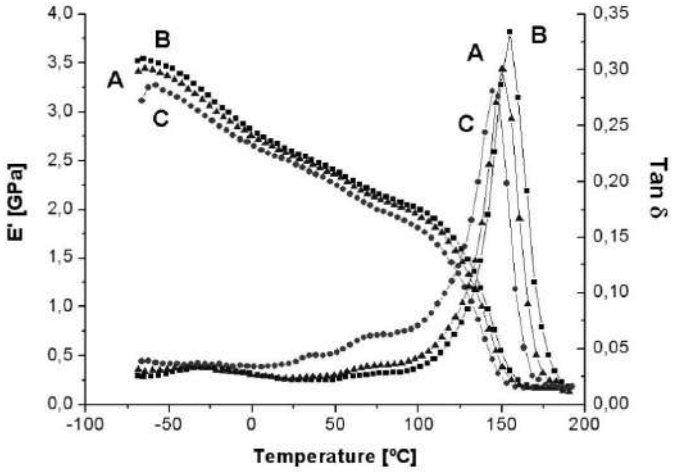

FIGURE 2. STORAGE MODULUS E´ AND TAN δ CURVES FOR THE EPOXY SPECIMENS POST-CURED USING DIFFERENT ROUTINES.

The storage modulus E´ and Tan δ are properties related to the stiffness and toughness of epoxy systems. Post-cure routine B resulted in higher modulus and stiffness values for the specimens. The glass transition temperature, Tg, is obtained when Tan δ is maximum and higher Tg values were obtained for the B specimens confirming a higher cure degree.

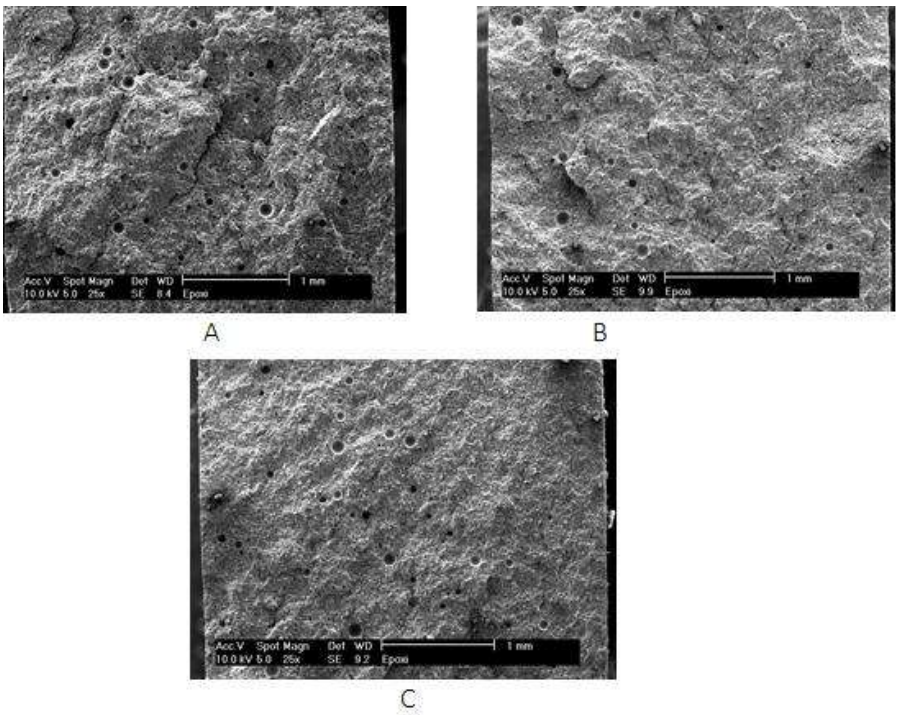

FIGURE 3. FRACTURE SURFACES OF SPECIMENS POST-CURED USING DIFFERENT ROUTINES.

The fracture surface analysis showed the presence of small defects which appeared as empty spaces (bubbles) in the epoxy matrix, probably due to the mixing and casting process. The investigation of the relationship between the defect size and the specimen strength showed a direct correlation, as observed in Figure 4.

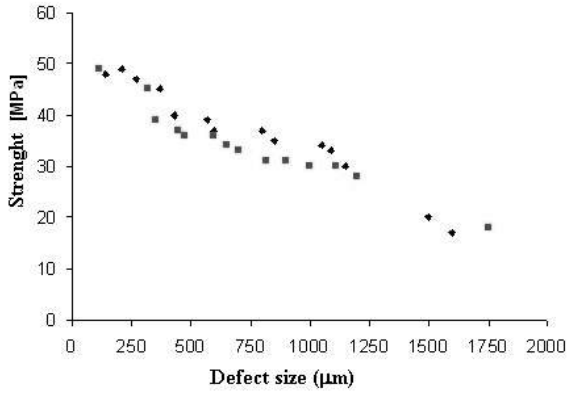

FIGURE 4. RELATIONSHIP BETWEEN DEFECT SIZE AND STRENGTH FOR EPOXY SPECIMENS.

The Weibull modulus characterizes the material friability and the influence of defects. Figure 5 shows the slope of the curve for the Weibull modulus, with a value of 7.95 for the epoxy specimens, characterizing low toughness and defects in the material, as shown in the fractography analysis, independent of the post-cure process applied.

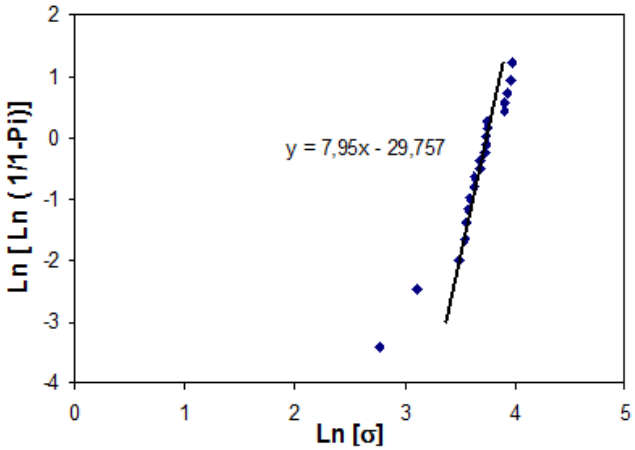

FIGURE 5. THE WEIBULL MODULUS CHARACTERIZING THE MATERIAL FRIABILITY

Figure 6 shows the probability of failure as a function of the applied stress. For an applied stress higher than 30 MPa the failure probability increases rapidly reaching 50% and 80% when the stress is close to 38 and 42 MPa, respectively.

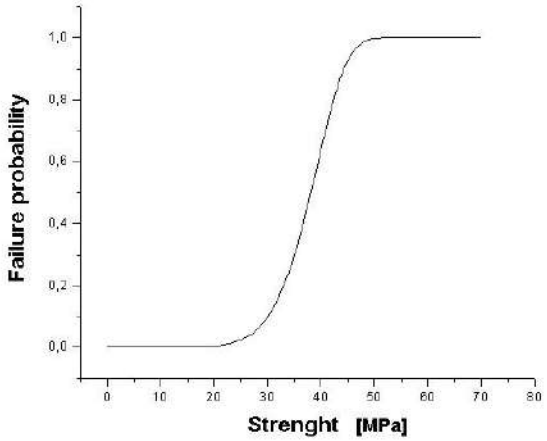

FIGURE 6. THE FAILURE PROBABILITY FOR EPOXY SPECIMENS.

IV. CONCLUSIONS

The relationship between the resin structure and properties provides useful information for the casting manufacturing, application and quality control of tools. The mechanical properties of epoxy-aluminum specimens post-cured by different routines were found to be related to self-controlled diffusion, which is characteristic of thermoset polymeric systems. A greater improvement in the crosslink density occurred when gradual thermo-curing ramp routines were applied, reaching higher tensile strength values and a lower number of defects due to a more homogenous cure. A high-temperature post-cure routine resulted in higher values for the modulus, stiffness and glass transition temperature, Tg, for the specimens. The fracture surface analysis showed the presence of defects due to the mixing and casting process, which appeared as empty spaces in the epoxy matrix. The defect size and the specimen strength showed a direct correlation. The Weibull modulus was 7.95 for the epoxy specimens, characterizing low toughness and defects in the material, as observed by fractography. For applied stress higher than 38 MPa the failure probability increased rapidly to 50%. The results demonstrate that epoxy-aluminum composites show interesting thermal and mechanical properties for tools manufacturing. However, the aluminum content and manufacturing defects can limit their use under critical conditions such as specific geometries and in high stress molding.

V. ACKNOWLEDGMENTS

The authors would like to thank FAPESC-PRONEX, CNPq and AEB (Brazilian Aerospace Agency) for financial support.

REFERENCES

[1] Jacob P.F. (1999) From Rapid Prototyping to Rapid Tooling, ASME, New York.

[2] Salmoria G.V., Gonzalez V.J, Ahrens C.H, Soldi V, Pires A.T.N. (2005). Stereolithography Somos 7110 photosensitive resin: study of curing kinetic and thermal degradation. Journal of Material Processing Technology. 168 (11), 164–71. doi:10.1016/j.jmatprotec.2004.11.012

[3] Salmoria G.V., Ahrens C.H., Fredel M., Soldi V, Pires A.T.N. (2005). Stereolithography Somos 7110 resin: mechanical behaviour and fractography of parts post-cured by different methods. Polymer Testing 24, 157–62. doi:10.1016/j.polymertesting.2004.09.008

[4] Westphal M.G., Pouzada A.S., Salmoria G.V., Ahrens C.H. (2006). Performance and Friction Properties of Injection Hybrid Molds with Stereolitography Molding Zones. Materials Science Forum. 514, 1673-1677. doi:10.4028/www.scientific.net/MSF.514-516.1673

[5] Gonçalves M.W., Salmoria G.V., Pouzada A.S. (2007). Study of tribological properties of molds obtained by stereolithography. Virtual and Physical Prototyping. 2, 29-36. doi:10.1080/17452750701295765

[6] Salmoria G.V., Lafratta F.H., Biava M.M., Ahrens C.H. (2008) Rapid Manufacturing and Rapid Tooling of Polymer Miniaturized Parts Using Stereolithography. Journal of the Brazilian Society of Mechanical Sciences and Engineering. 30 (1), 7-10. http://dx.doi.org/10.1590/S1678-58782008000100002

[7] Salmoria, G.V., Ahrens .C.H., Villamizar F.A.Y., Sabino-Netto A.C. (2008). Influência do Desempenho Térmico de Moldes Fabricados com Compósito Epóxi/Alumínio nas Propriedades de PP Moldado por Injeção. Polímeros. 18 (3), 262-269. http://dx.doi.org/10.1590/S0104-14282008000300013

[8] Sabino Netto, A.C., Salmoria, G.V., Ahrens, C.H., Pouzada, A.S.(2008). Fritction Properties of Steel Fibre Reinforced Epoxy Composites used in Molding Blocks of Hybrid Molds, Materials Science Forum, 587, 217-221. doi:10.4028/www.scientific.net/MSF.587-588.217

[9] Salmoria G.V., Klauss P., Pires A.T.N. (2008). Investigations on cure kinetics and thermal degradation of stereolithography Renshape 5260 photosensitive resin. Polymer Testing. 27, 698–704. doi:10.1016/j.polymertesting.2008.05.008

[10] Sabino Netto, A.C., Salmoria, G.V., Ahrens, C.H., Pouzada, A.S. (2008). Mechanical properties of epoxy composites filled with short steel fibres for hybrid injection molds, Advanced Materials Forum, 587, 217-221. doi: 10.4028/www.scientific.net/MSF.587-588.222

[11] Salmoria, G.V., Ahrens .C.H., Beal V.E., Soldi V., Pires A.T.N. (2009). Evaluation of post-curing and laser manufacturing parameters on the properties of SOMOS 7110 photosensitive resin used in stereolithography. Materials and Design. 30, 758-763. doi:10.1016/j.matdes.2008.05.016

[12] Leite J.L., Rasteiro M.G., Salmoria G.V., Ahrens C.H., Pouzada, A.S. (2010). Epoxy/steel fiber composites-A simple model to predict the fiber sedimentation. Polymer Composites. 31, 1378-1386. doi:10.1002/pc.20923

[13] Martinho P.G., Sabino-Netto A.C., Salmoria G.V., Pouzada A.S, (2011). Hybrid Molds with Epoxy-Based Composites – Effects of Materials and Processing on Molding Shrinkage and Warpage. Internatinal Polymer Processing., 26 (3) 256-264. doi: 10.3139/217.2435

[14] Souza C.F.M., Leite J.L., Salmoria G.V., Pouzada A.S. (2013). Influence of graphite and carbon nanotubes on the mechanical and electrical properties of cast epoxy composites. Materials Science Forum. 730, 909-914.

doi:10.4028/www.scientific.net/MSF.730-732.909

[15] Neves A.F., Salmoria G.V., Ahrens C.H., Pouzada A.S., Silva M.A. (2013). Assessment of Injection Molded Parts of PP/Nanoclay Produced with Hybrid Molds. Materials Science Forum. 730, 963-968. doi:10.4028/www.scientific.net/MSF.730-732.963

[16] Leite J.L., Salmoria G.V., Ahrens C.H., Pouzada A.S. (2013). Characterization of epoxy/steel fibres composites for hybrid injection molds. Materials Science Forum. 730, 277-282. doi:10.4028/www.scientific.net/MSF.730-732.277

[17] Leite Howarth J.L., Pouzada A.S., Maia J.M., Salmoria G.V., Ahrens C.H. (2013). A study on fiber sedimentation velocity in epoxy/steel fiber composites used for hybrid injection molds. Journal of Composite Materials 47, 2436-2447. doi: 10.1177/0021998313509861

Design, Analysis & Performance Check of A Multi-Story (G+23) RCC Building by Pushover Analysis using Sap 2000

Shahana Rahman[1], Mr. Ashish Yadav[2], Dr. Vinubhai R. Patel[3]

[1]M.tech Student: Structural Engineering with Specialization in offshore Structures, UPES, Dehradun, India
[2]Assistant Professor (SS) Civil Engg Department, UPES, Dehradun, India
[3]Ph. D. Structural Engg, Zarna Associate, Vadodara, Gujarat, India

Abstract— *Pushover analysis is one of the most-used nonlinear static procedures for the seismic assessment of structures, due to its simplicity, efficiency in modeling and low computational time. The previous studies about pushover analysis are almost based on symmetric building structures and unidirectional earthquake excitation. This analysis is conducted to evaluate the seismic capacities of a asymmetric-plan building. The seismic response of RC building frame in terms of performance point and the effect of earthquake forces on multi storey building frame with the help of pushover analysis is carried out in this paper. In the present study the building frame is designed as per IS 456:2000 and IS 1893:2002. The main objective of this study is to check the kind of performance a building can give when designed as per Indian Standards. The pushover analysis of the building frame is carried out by using structural analysis and design software SAP 2000 (version 14).*

Keywords— Capacity Curve, Performance Point, Pushover analysis, RC building.

I. INTRODUCTION

Pushover analysis is stated as a nonlinear analysis in which, the nonlinear load-deformation characteristics are determined directly by incorporating the mathematical model of the building frame. The response of individual components and elements of buildings can be calculated separately. Each element shall be exposed to monotonically increasing lateral loads. During an earthquake, the inertia forces generated act as the lateral loads. As the intensity of the load increases, the structure is pushed. Due this, cracks are generated at various locations. When it exceeds the elastic limit, yielding occurs and it leads to plastic hinge formations along the span of the member. The deformations are recorded as a function of the increasing lateral load up to the failure of various structural components. This load incremental process is discontinued when the target displacement is reached at the roof level. Target displacement is the maximum expected displacement by combining both elastic and inelastic responses of the building under selected earthquake ground motion. Pushover analysis evaluates the structural performance by computing the force, drift capacity and seismic demand by a nonlinear static analysis algorithm. The analysis accounts for material inelasticity, geometrical nonlinearity and the redistribution of internal forces. The seismic demand parameters are component deformations, component forces, global displacements (at roof or any other reference points), storey drifts and storey forces.

The static pushover analysis is mainly based on the assumption that the response of the structure is regulated by the first mode of vibration and mode shape, or by the first few modes of vibration, and that this shape remains constant throughout the elastic and inelastic response of the structure. This provides the basis for transforming a dynamic problem into a static problem.

Capacity spectrum method is another approach for getting the target displacement. The basic assumption is that, for the nonlinear SDOF system, the maximum inelastic deformation can be approximated from corresponding value of the linear elastic SDOF system with an equivalent period and damping, and it is same as the displacement coefficient method. In this method the term ductility is incorporated in calculation of effective period and damping. In the capacity spectrum method the pushover curve is considered in the form of acceleration-displacement response spectrum (ADRS) format, and is termed as capacity spectrum. The Figure.1 shows the ADRS format for the capacity spectrum method.

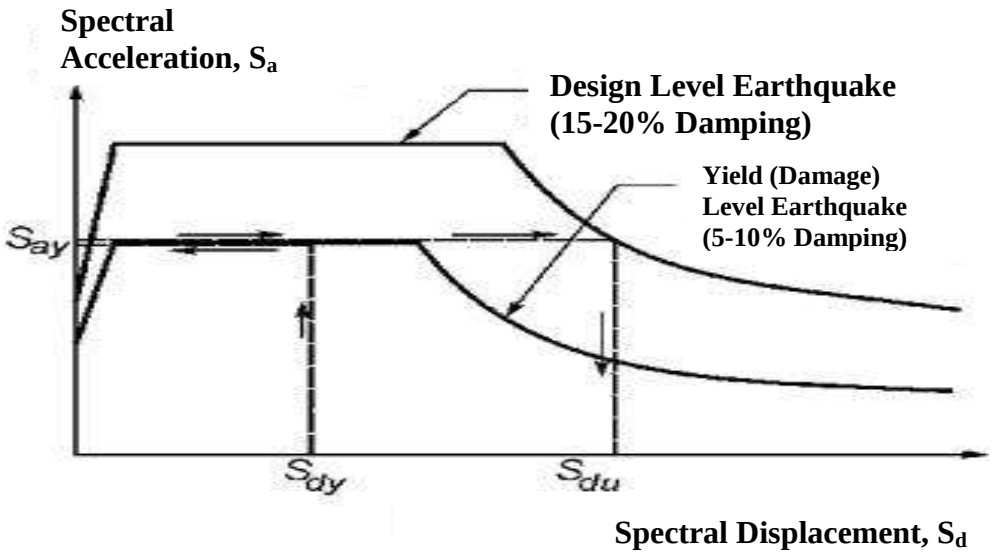

FIG. 1 ADRS FORMAT

II. MATERIALS AND METHODS

TABLE 1
MATERIALS

Material/Section	Grade/Size	Unit	Material/Section	Grade/Size	Unit
Concrete grade	M30		**slab thickness**	0.15	M
Steel grade	Fe500		**wall thickness**	0.23	M
E (concrete)	27386.12788	N/mm^2	**Density of concrete**	25	kN/m^3
E (steel)	210000	N/mm^2	**Density of brick work**	20	kN/m^3
Beam	0.4 x 0.6	m	**live Load**	3	KN/m^2
Column	0.6 x 0.6	m			

Software Used: *SAP2000 V.14.00 and all the analysis (i.e. base shear) have done by using IS 1893.*

2.1 Analysis In SAP2000

The 23 storey residential building is in seismic zone III (Location Vadodara). For the analysis of the building, the basic computer model in the usual manner was created. The figure (2) shows the 3-D model of the building Frame for the pushover analysis of the building the properties of the various plastic hinges such as flexural, shear, torsional and joint hinges are defined. For every beam and column the hinge length is calculated as half of their effective depth. Shear failure mostly occur in beams and columns owing to inadequate shear design. There are a lot of existing buildings which are not detailed as per IS 13920: 1993. Also, poor construction practice may lead to shear failure in framed building in the event of severe earthquakes. This residential building was designed as per IS 456:2000 and detailed as per IS 13920:1993, for adequate main and shear reinforcements, corresponding to the ultimate moment capacity level. When there is no prior failure in shear, flexural plastic hinges will be developed along with the predicted values of ultimate moment capacity. Therefore, it is obvious for a code designed building to fail in flexure and not in shear and there is no need of shear hinge modeling.

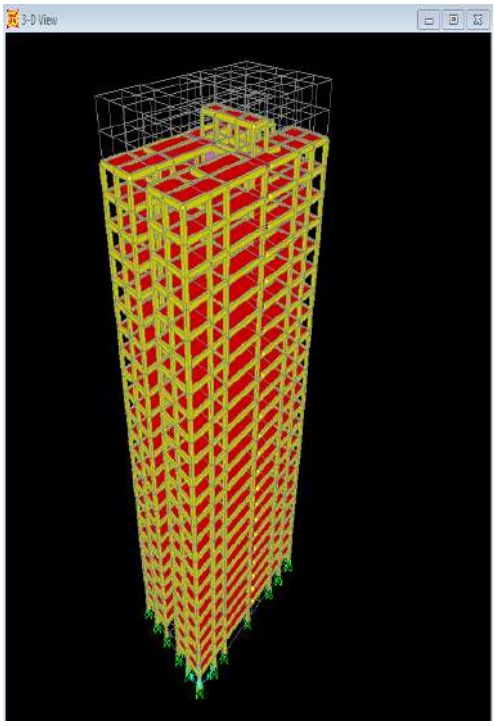

3D MODEL

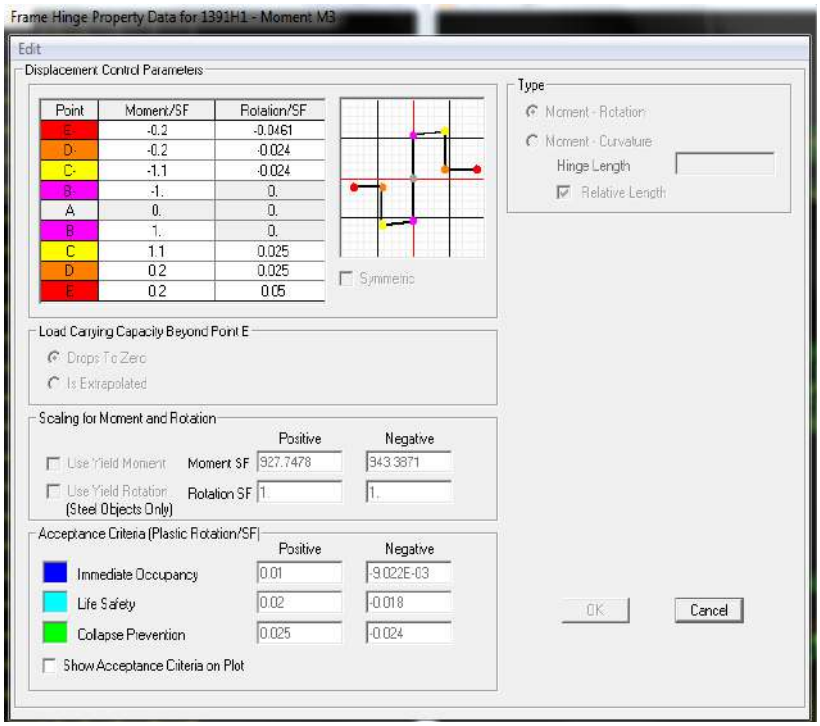

PLASTIC HINGE MODELING

FIGURE 2

III. RESULT AND DISCUSSION

A static non-linear (pushover) analysis of the residential building was carried out using SAP2000. The maximum roof displacement of 0.64 m was chosen to be applied. For pushover analysis the various pushover cases are considered such as push gravity, push X (i.e. loads are applied in X direction), push Y (i.e. loads are applied in Y direction). The various load combinations are also used for this purpose. On the above residential building frame the non-linear static pushover analysis was performed to investigate the performance point of the building frame in terms of base shear and displacement. After pushover analysis the demand curve and capacity curves are plotted to get the performance point of the structure. The performance point is obtained as per ATC 40 capacity spectrum method. The base shear for PUSH X load case is 10202.70 KN and for PUSH Y base shear at performance point is at 13505.90 KN as shown in figure 3 and 4.

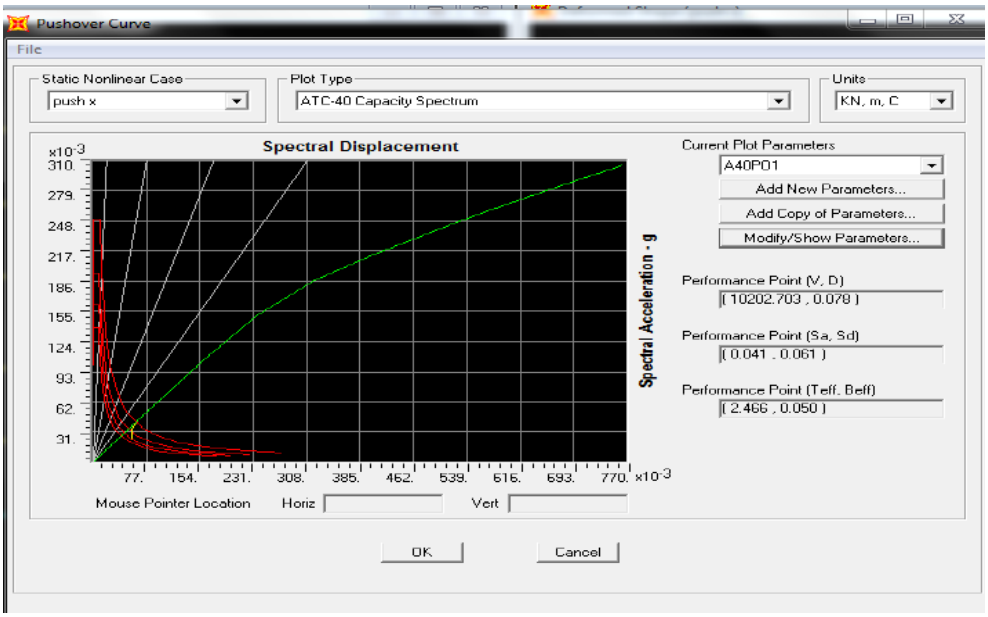

FIGURE 3 CAPACITY CURVE IN X-DIRECTION

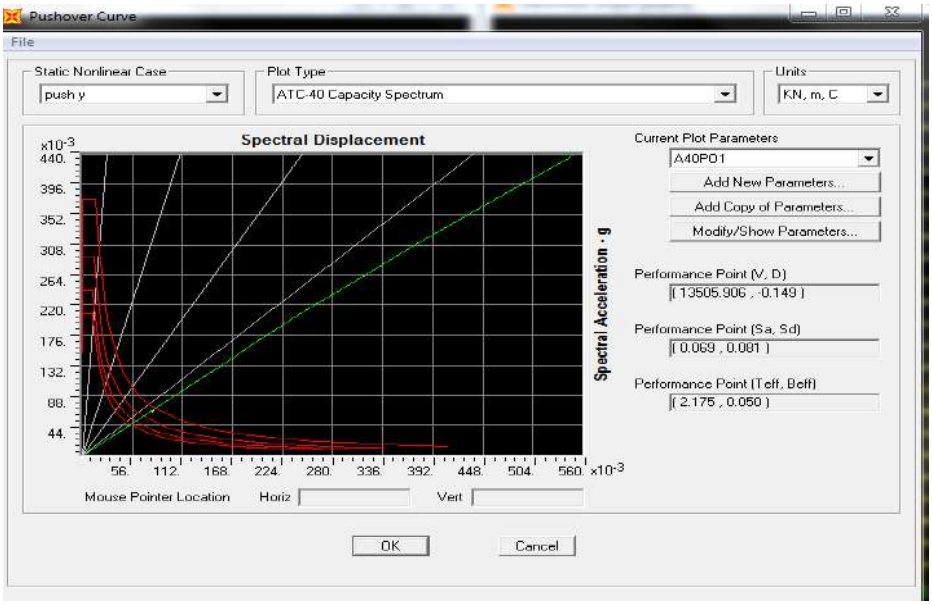

FIGURE 4 CAPACITY CURVE IN Y-DIRECTION

The design base shear of the building frame is found to be 2300 KN as per calculation. After performing the analysis the base shear at performance point is found to be 10202.70 KN for X directional loading and 13505.90 KN for Y directional loading, which is greater than design base shear. Since at the performance point base shear is greater than the design base shear the building frame is safe under the earthquake loading. Both the pushover curves show no decrease in the load carrying capacity of buildings suggesting good structural behavior. Also due to the demand curve intersects the capacity curve near the elastic range, the structure has a good resistance.

TABLE 2
DISTRIBUTION OF DESIGN BASE SHEAR

Story/Floor i	Height From Ground h_i(Meter)	Lumped Mass W_i(KN)	$W_i * h_i$^2	Distribution Of Base Shear (KN)	Shear (KN)
23(roof)	69	3352.6	15961728.6	210.8625534	210.862553
22	66	4630.13	20168846.28	266.4407178	477.303271
21	63	4630.13	18376985.97	242.7693317	720.072603
20	60	4630.13	16668468	220.1989404	940.271543
19	57	4630.13	15043292.37	198.7295437	1139.00108
18	54	4630.13	13501459.08	178.3611417	1317.36222
17	51	4630.13	12042968.13	159.0937344	1476.45596
16	48	4630.13	10667819.52	140.9273218	1617.38328
15	45	4630.13	9376013.25	123.8619039	1741.24518
14	42	4630.13	8167549.32	107.8974808	1849.14267
13	39	4630.13	7042427.73	93.0340523	1942.17672
12	36	4630.13	6000648.48	79.27161853	2021.44834
11	33	4630.13	5042211.57	66.61017946	2088.05852
10	30	4630.13	4167117	55.04973509	2143.10825
9	27	4630.13	3375364.77	44.59028542	2187.69854
8	24	4630.13	2666954.88	35.23183046	2222.93037
7	21	4630.13	2041887.33	26.97437019	2249.90474
6	18	4630.13	1500162.12	19.81790463	2269.72264
5	15	4630.13	1041779.25	13.76243377	2283.48507
4	12	4630.13	666738.72	8.807957614	2292.29303
3	9	4630.13	375040.53	4.954476158	2297.24751
2	6	4630.13	166684.68	2.201989404	2299.449503
1	3	4630.13	41671.17	0.550497351	2300
0(Ground)	0	0	0	0	2300
VB(KN)	2300				
∑Wihi^2	174103818.8				

Design Base shear = 2300 KN (Calculated as per IS 1893 guidelines)

IV. CONCLUSION

The performance of reinforced concrete frames was investigated using the pushover analysis. As a result of the work that was completed in this study, the following conclusions were made:

1. It is concluded that the residential building frame used for pushover analysis is seismically safe, because of the performance point base shear is greater than design base shear.
2. Since the demand curve intersects the capacity curve near the elastic range, the structure has a good resistance and high safety against collapse.
3. The behavior of properly detailed reinforced concrete frame building is adequate as indicated by the intersection of the demand and capacity curves.

REFERENCES

[1] Applied Technology Council (ATC-40), "Seismic Evaluation and Retrofit of Concrete Buildings", Vol- 1 and 2,1996.

[2] Neena Panandikar Hede, K. S. Babunarayan, "Effect of Variation of Plastic Hinge Length on the Results of Non-Linear Analysis", IJRET: International Journal of Research in Engineering and Technology, Vol- nov, pp-439–443, 2013.

[3] Federal Emergency Management Agency - FEMA 356 "Prestandard and Commentary for Seismic Rehabilitation of Buildings", Department of Homeland Security Federal Emergency Management Agency, Washington, 2000.

[4] Durgesh C. Rai, "Guidelines on Seismic Evaluation and Strengthening of Existing Buildings", Indian Institute of Technology Kanpur, 2005.

[5] Freeman S.A, "Prediction of Response of Concrete Buildings to Severe Earthquake Motion", Douglas McHenry International Symposium on Concrete and Concrete Structures, SP-55, American Concrete Institute, pp. 589- 605, 1978.

[6] Anil K. Chopra and Rakesh K. Goel, "A Modal Pushover Analysis Procedure for Estimating Seismic Demands for Buildings", Earthquake Engineering and Structural Dynamics, Vol -31(3), pp 561 -582, 2002.

[7] Emrah Erduran, and Ahmet Yakut, "Vulnerability Assessment of Reinforced Concrete Moment Resisting Frame Buildings", Journals of Structural Engineering, ASCE, Vol- 133, pp- 576-586, 2007.

[8] Akanshu Sharma, G. R. Reddy, K. K. Vaze, R. Eligehausen, "Pushover Experiment and Analysis of a Full Scale Non-seismically Detailed RC Structures", Engineering Structures, Vol- 46, pp.218-233, 2014.

[9] Federal Emergency Management Agency - FEMA 440,"Improvement of Nonlinear Static Seismic Analysis Procedures", Department of Homeland Security Federal Emergency Management Agency, Washington, 2005.

[10] Federal Emergency Management Agency - FEMA 273,"Guidelines for the seismic rehabilitation of buildings", Washington (DC): Building Seismic Safety Council; 1997.

[11] SAP User Manual, version 15, Berkeley (CA, USA): Computer and Structures, Inc., 2000.

[12] IS 456: 2000, "Plain and Reinforced Concrete - Indian Standard Code of Practice", Bureau of Indian Standards, New Delhi, India.

Nonlinear Dynamic Time History Analysis of Multistoried RCC Residential G+23 Building for Different Seismic Intensities

Pruthviraj N Juni[1], S.C. Gupta[2], Dr. Vinubhai R. Patel[3]

[1]M.tech Student: Structural Engineering With Specialization In offshore Structures, UPES, Dehradun , India
[2]Associate Dean (COES), UPES, Dehradun, India
[3]Ph. D. Structural Engg, Zarna Associate, Vadodara, Gujarat, India

Abstract— *In this paper study of nonlinear dynamic time history analysis of Twenty three storied RCC residential building considering different seismic/earthquake intensities is carried out and response of such building due to earthquake is studied. The building under consideration is modeled with the help of SAP2000V.14.00 software. Five different time histories have been used considering seismic intensities V, VI, VII, VIII, IX and X on Modified Mercalli's Intensity scale (MMI) for developing the relationship between seismic intensities and seismic responses. The outcome of the study shows similar variation pattern in Seismic responses i.e. base shear and storey displacements with intensities V to X. From the study it is recommended that analysis of multistoried RCC building using Time History method became necessary to ensure safety against earthquake force.*

Keywords— Multistoried buildings, Scaling, Seismic responses, Time history analysis.

I. INTRODUCTION

All over the world, there is a high demand for construction of tall buildings due to increasing urbanization and spiraling population, and earthquakes have the potential for causing the greatest damages to those high rise structures. Since earthquake forces are random in nature and unpredictable, the engineering tools need to be sharpened for analyzing structures under the action of these forces. Earthquake loads are required to be carefully modeled so as to assess the real behavior of structure with a clear understanding that damage is expected but it should be regulated. Analyzing the structure for various earthquake intensities and checking for multiple criteria at each level has become an essential exercise for the last couple of decades (Romy and Prabha, 2011).

Earthquake causes different shaking intensities at different locations and the damage induced in buildings at various locations is also different. Therefore, it is necessary to construct a structure which is earthquake resistance at a particular intensity of shaking a structure, and not so much the magnitude of an earthquake. Even though same magnitudes of earthquakes are occurring due to its varying intensity, it results into dissimilar damaging effects in different regions. Therefore, it is necessary to study variations in seismic behavior of multistoried RCC frame building for different seismic intensities in terms of various responses such as lateral displacement and base shear. It is necessary to understand the seismic behavior of buildings having similar layout under different intensities of earthquake. For determination of seismic response it is necessary to carry out seismic analysis of the structure using different available methods (Duggal, 2010).

II. STRUCTURAL MODELING AND ANALYSIS

The finite element analysis software SAP 2000 Nonlinear is utilized to create 3D model and run all analyses. The software is able to predict the geometric nonlinear behavior of space frames under static or dynamic loadings, taking into account both geometric nonlinearity and material inelasticity.

2.1 Problem Statements

2.1.1 Structural plan:

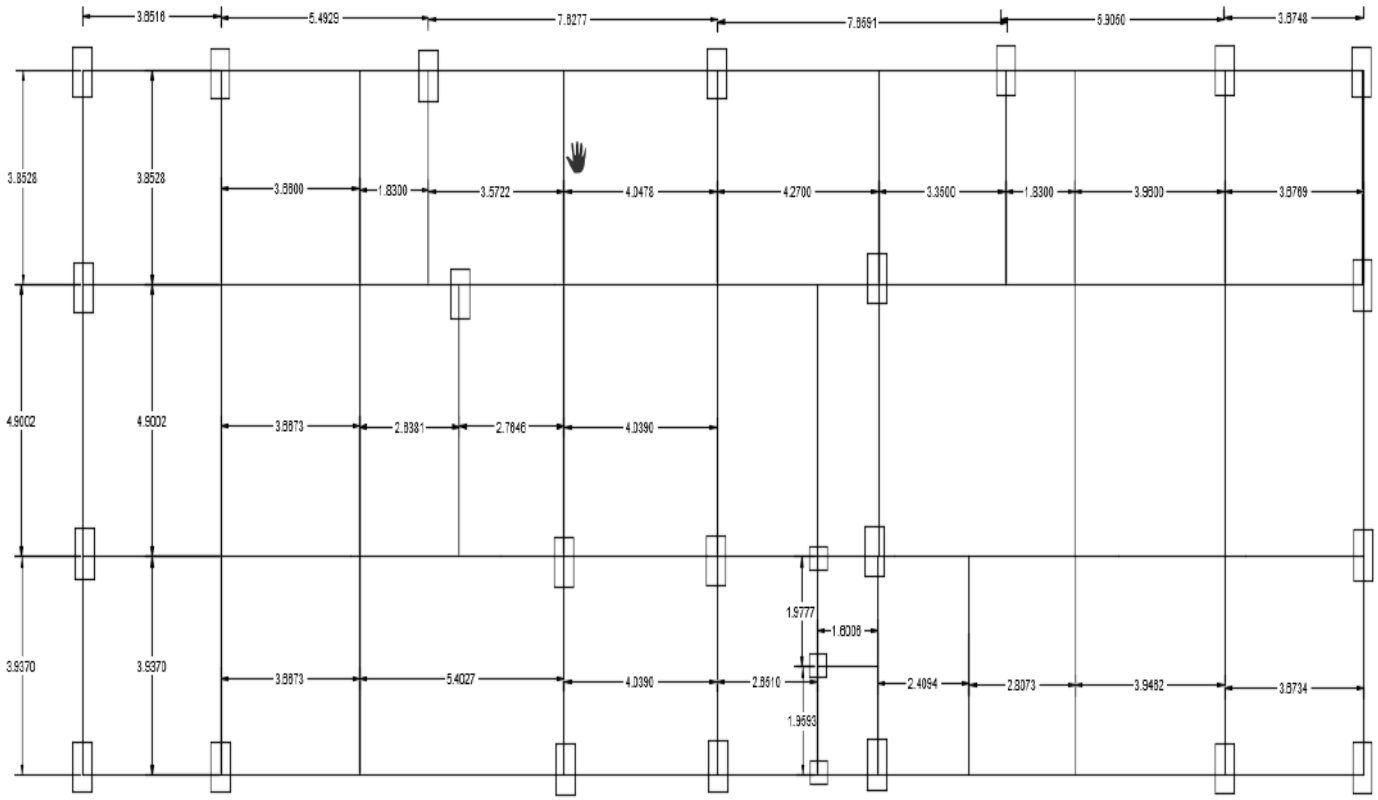

FIGURE 1: STRUCTURAL PLAN

2.1.2 Architectural Plan

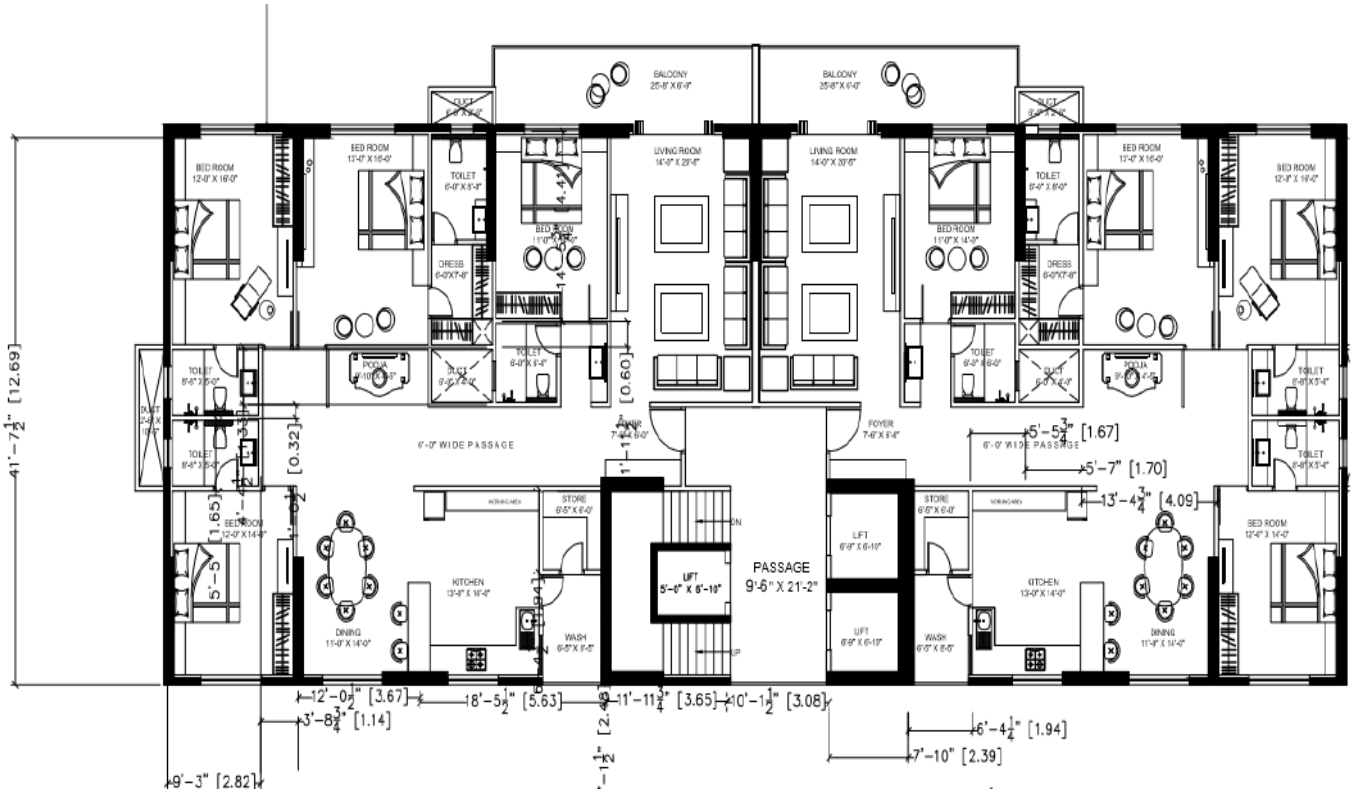

FIGURE 2: ARCHITECTURAL PLAN

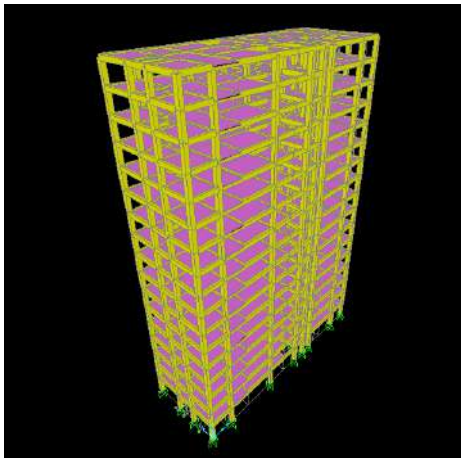

3 D MODEL IN SAP

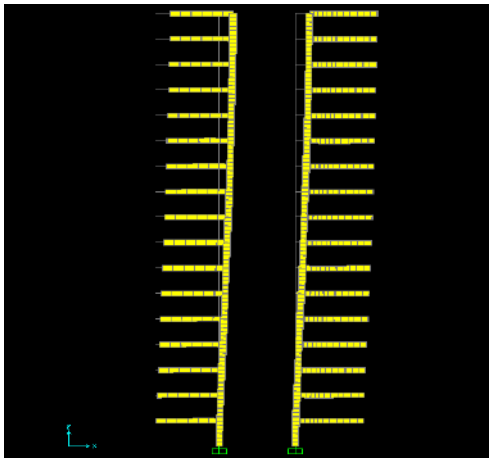

DISPLACEMENT MODEL IN SAP

FIGURE 3

TABLE 1
DIFFERENT TIME HISTORY CONSIDERED FOR STUDY

S.No.	EQ	Date	Magnitude Richter Scale	P.G.A.G
1	Bhuj, India	26-Jan-01	6.9	0.11
2	Koyana, India	11-Dec-64	6.5	0.489
3	Anza, USA	25-Feb-80	4.7	0.11
4	Nahanni, Canada	23-Dec-85	6.9	0.489
5	Northbridge, USA	17-Jan-94	6.7	0.489

III. MATERIALS AND METHODS

TABLE 2
MATERIALS

Material/Section	Grade/Size	Unit	Material/Section	Grade/Size	Unit
Concrete grade	M30		**slab thickness**	0.15	m
Steel grade	Fe500		**wall thickness**	0.23	m
E (concrete)	27386.12788	N/mm2	**Density of concrete**	25	kN/m3
E (steel)	210000	N/mm2	**Density of brick work**	20	kN/m3
Beam	0.4 x 0.6	m	**live Load**	3	KN/m2
Column	0.6 x 0.6	m			

Software : *SAP2000 V.14.00*

IV. RESULTS AND DISCUSSION

Results obtained from the analysis are tabulated in below Tables .Graphical representations of variations in results are shown in Figures. The graph shows that similar variations in seismic responses namely base shear and displacement with intensities V to X.

TABLE 3
VARIATIONS IN BASE SHEAR FOR X DIRECTION

S.No.	Intensity MMI	Base Shears (kN)				
		Bhuj	Koyana	Anza	Nahanni	Northbridge
1	V	666.48	866.424	904.38	1011.48	904.93
2	VI	1666.4	1948.38	2004.48	2211.43	2103.49
3	VII	2665.954	3004.98	3218.32	3400.59	3411.98
4	VIII	3998.391	4108.4	4900.32	5109.66	5003.4
5	IX	5998.39	6211.389	6811.43	7098.42	6911.3
6	X	8331.1065	9013.42	10004.39	11049.61	10940.11

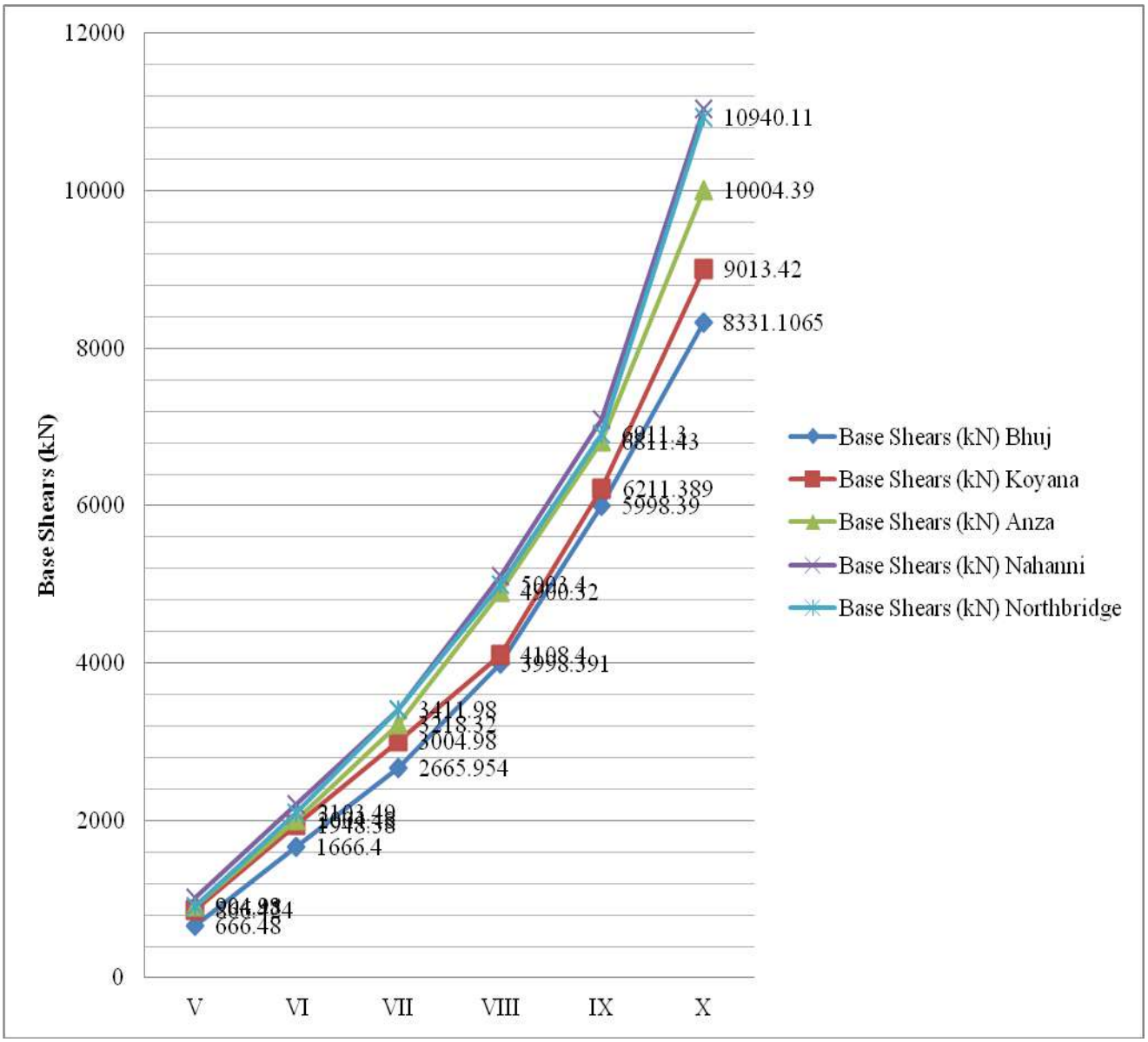

FIGURE 4: VARIATIONS IN BASE SHEAR FOR X DIRECTION

TABLE 4
VARIATIONS IN BASE SHEAR FOR Y DIRECTION

S.No.	Intensity MMI	Base Shears(kN)				
		Bhuj	Koyana	Anza	Nahanni	Northbridge
1	V	888.651	920.44	1102.43	1390.11	1750.39
2	VI	2221.62	2444.92	2780.44	3001.29	3640.11
3	VII	3554.62	3842.46	4100.39	4400.41	4711.39
4	VIII	5331.9	5711.39	6008.82	6344.92	6748.31
5	IX	7997.86	8211.79	8411.99	8791.79	9124.48
6	X	11108.142	11209.4	11600.11	12001.92	12409.18

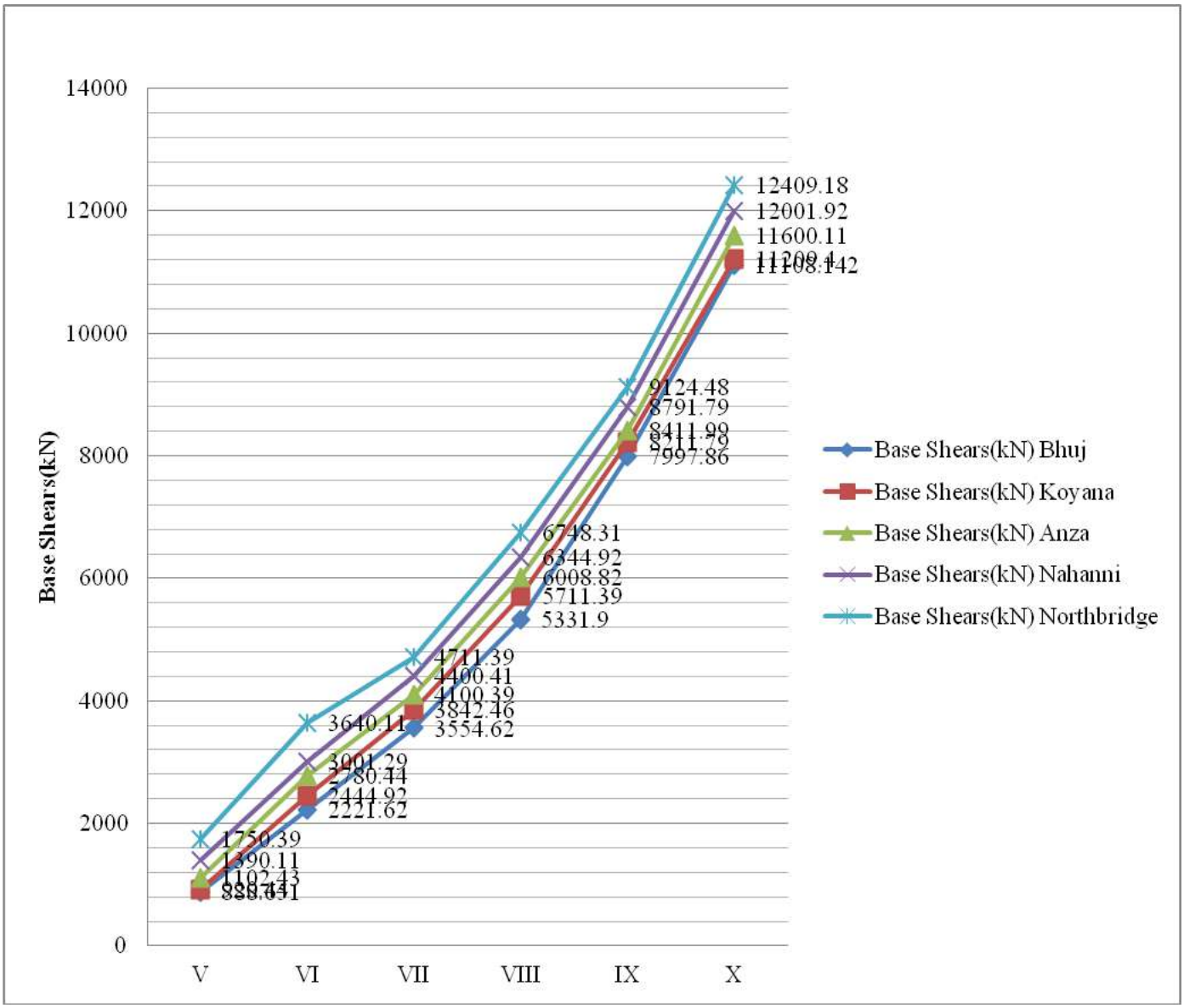

FIGURE 5: VARIATIONS IN BASE SHEAR FOR Y DIRECTION

TABLE 5
VARIATIONS IN ROOF DISPLACEMENT FOR Y DIRECTION

S.No.	Intensity MMI	Displacement (mm)				
		Bhuj	Koyana	Anza	Nahanni	Northbridge
1	V	0.28	0.31	0.51	0.59	0.52
2	VI	0.6	0.68	0.8	0.83	0.78
3	VII	1	1.69	2.1	2.92	2.5
4	VIII	3.1	3.61	3.92	4.52	4.11
5	IX	5.9	6.11	7.28	7.99	7.48
6	X	6.8	7.21	8.11	9.78	9.22

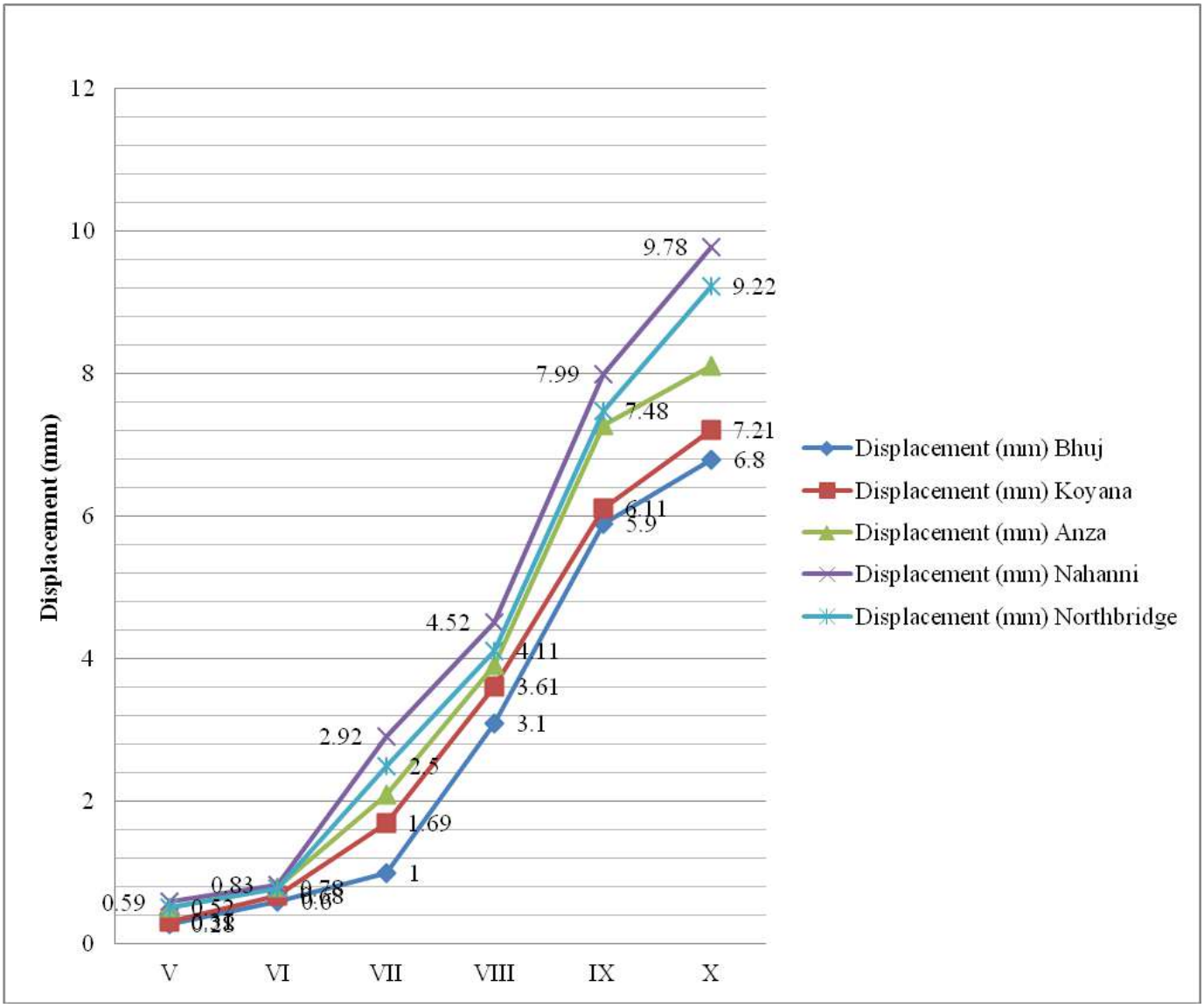

FIGURE 6: VARIATIONS IN ROOF DISPLACEMENT FOR Y DIRECTION

TABLE 6
VARIATIONS IN ROOF DISPLACEMENT FOR X DIRECTION

S.No.	Intensity MMI	Displacement (mm)				
		Bhuj	Koyana	Anza	Nahanni	Northbridge
1	V	0.53	0.629	0.739	0.811	0.844
2	VI	1.02	1.24	1.439	1.591	1.433
3	VII	2.06	2.93	2.811	3.318	3.12
4	VIII	4.09	4.5	4.426	6.019	5.811
5	IX	8.92	9.21	8.298	12.48	11.129
6	X	9.2	10.03	12.37	14.11	13.482

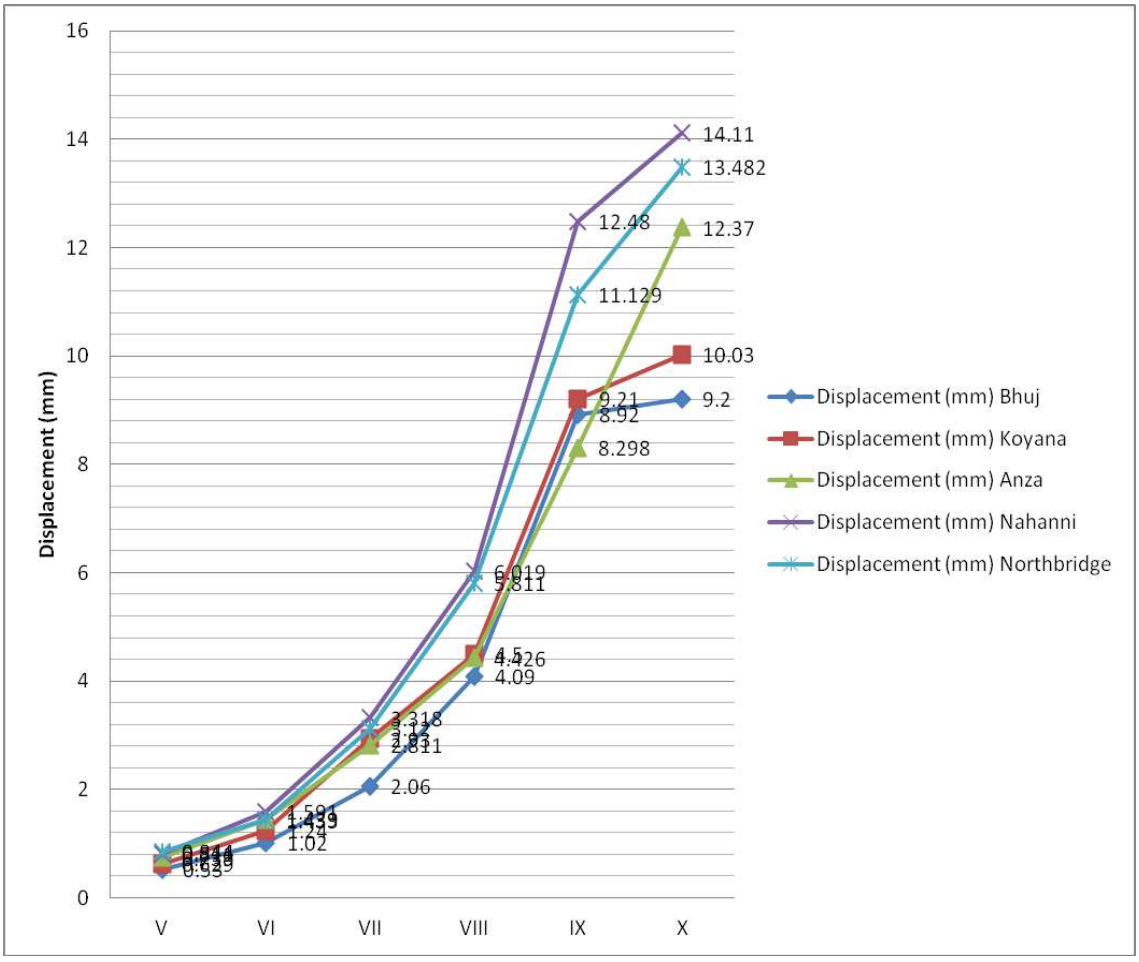

FIGURE 7: VARIATIONS IN ROOF DISPLACEMENT FOR X DIRECTION

V. CONCLUSION

1. The seismic responses namely base shear, storey displacements and storey drifts in both the directions are found to vary in similar pattern with intensities (V to X) for all the Time Histories and both the models considered for the study.
2. The values of seismic responses namely base shear, storey displacement and storey drifts for all the Time Histories and both the models are found to be of increased order for seismic intensities varying from V to X.

3. The maximum value of base shear, storey displacement and storey drift (X and Y directions) for seismic intensities of VI, VII, VIII, IX and X are found to be nearly more by 2.50, 4.005, 7.56, 16.83, and 17.35 times, respectively as compared to seismic intensity of V for both the models (i.e., with and without soft story) and for all the time histories.
4. As Time History Analysis is a realistic method used for seismic analysis, it provides a better check to the safety of structures analyzed and designed bythe method specified in IS code.

REFERENCES

[1] Duggal S K (2010), "Earthquake Resistance Design of Structure", Fourth Edition, Oxford University Press, New Delhi.

[2] Haselton C B and Whittaker A S (2012), "Selecting and Scaling Earthquake Ground Motions for Performing Response-History Analyses", The 15th World Conference on Earthquake Engineering.

[3] Romy M and Prabha C (2011), "Dynamic Analysis of RCC Buildings with Shear Wall", *International Journal of EarthSciences and Engineering*, ISSN 0974-5904, Vol. 04, 659-662.

[4] Shaha V and Karve S (2010), "Illustrated Design of Reinforced Concrete Buildings", Sixth Edition, Structures Publication, Pune.

[5] Wilkinson S and Hiley R (2006), "A Non-Linear Response History Model for the Seismic Analysis of High-Rise Framed Buildings", *Computers and Structures*, Vol. 84.

Sequential Famous Route Analysis Based on Multisource Social Media

D.Sugapriya[1], B.Pavithra[2], G.Suganya[3], M.Antony Robert Raj[4]

[1,2,3]U.G. Students, Dept of CSE, Alpha College of Engineering, Chennai.
[4]Asst.prof.Dept of CSE, Alpha College of Engineering, Chennai.

Abstract— *As an infrastructural and profitable industry, tourism is vital in present day economy and incorporates distinctive extensions and capacities. In the event that it is created suitably, social relations and monetary improvement of nations will be developed and given. Web advancement as a associated tool within the web assumes an extremely deciding part in tourism achievement and appropriate misuse of it can prepare for greater improvement and accomplishment of this industry. Then again, the measure of information in the present world has been expanded and investigation of substantial arrangements of information that is alluded to as large information has been changed over into a key way to deal with upgrade rivalry and set up new strategies meant for improvement, development, advancement, and upgrade of the quantity of clients. Today, huge in sequence is vital issues of statistics supervision in computerized age and one of the primary open doors in tourism industry for ideal misuse of most extreme data. Huge information can shape encounters of keen travel. Surprising development of these information sources has enlivened new Strategies to comprehend the financial marvel in various fields. The systematic approach of huge information underscores the limit of information accumulation and investigation with a phenomenal degree, profundity and scale for taking care of the issues of genuine and utilizations it. In fact, enormous information examinations open the ways to different open doors for building up the present day learning or changing our comprehension of this extension and bolster basic leadership in tourism industry. The reason for this review is to show accommodation of huge information examination to find behavioral examples in tourism industry and propose a model for utilizing information in tourism.*

Keywords— Travel proposal, geo-labeled photographs, online networking, sight and sound data recovery.

I. INTRODUCTION

Programmed travel suggestion is an imperative issue in both research and industry. Enormous media, particularly the twist of web-based social networking (e.g., Facebook, Flick, Twitter and so forth.) offers awesome chances to address numerous testing issues, for example, GPS estimation [1], [2] also, travel suggestion [3]. Travelog sites (e.g., www.igougo.com) offer rich portrayals about historic points also, voyaging background composed by clients. Moreover, group contributed photographs with metadata (e.g., labels, date taken, scope and so on.) via web-based networking media record clients' day by day life and travel involvement. These information are not just helpful for solid POIs (purposes of enthusiasm) ming [4], travel courses ming, yet give a chance to prescribe customized travel POIs and courses in light of client's advantage. There are two principle challenges for programmed travel suggestion. To begin with, the prescribed POIs ought to be customized to client enthusiasm since various clients may lean toward distinctive sorts of POIs. Take New York City for instance. A few people may incline toward social spots like the Metropolitan Museum, while others may incline toward the cityscape like the Central Park. Other than travel topical intrigue, different qualities including utilization capacity (i.e., extravagance, economy), favored going by season (i.e., summer, pre-winter) and favored going by time (i.e., morning, night) may likewise be useful to give customized travel proposal.

Consequently, it is not steady to suggest a progressive travel course (i.e., a gathering of POIs) rather than individual POI. It is extensively extra wearisome and additionally dreary for customers to organize travel game plan than individual POIs. In perspective of the way that the alliance between the zones in addition to opening time of different POIs should be considered. For example, it may regardless not be a nice recommendation if each one of the POIs endorsed for one day are in four corners of the conurbation, instead of the way that the customer may be excited about all the individual POIs.

In disconnected module, the topical bundle space is mined from online networking consolidating travelogs and community contributed photographs. Four travel conveyances (i.e., topical intrigue, time, season and cost) of every point are portrayed in topical bundle space. Taking the upside of the complementation of the two online networking.

Online module concentrates on mining client bundle and prescribing customized POI arrangement in view of client bundle. To start with, labels of client's photograph set are mapped to topical bundle space to get client's topical intrigue dispersion. It

is hard to get client's utilization ability specifically from the printed portrayals of photographs. In any case, the subjects client intrigued in could some way or another mirror these traits.

Existing reviews on travel suggestion mining celebrated travel POIs and courses are predominantly from four sorts of enormous web-based social networking, GPS direction [5], However, general travel course arranging can't well meet clients' close to home prerequisites. Customized travel proposal suggests the POIs and courses by mining client's travel records [6], [7], [8].

II. PROBLEM STATEMENT

Development and success of organizations rely on upon having reasonable data about clients, providers and their exhibitions. The broad volume of multi-media frameworks has assumed a noteworthy part being developed and development of enormous information. Social sites, advanced mobile phones, and different types of gear of clients including PCs and portable workstations have permitted billions of individuals over the world to take part in information conception. In nearby prospect this is normal that enormous information investigation will be utilized broadly in promoting and in addition interpersonal organizations. Without a doubt, enormous information ought to impact all divisions particularly the modern ones; this is done through joining the information from various areas of financial association with outer information.

III. LITERATURE SURVEY

3.1 TITLE: Smart Tourism Destinations

AUTHOR: Buhalis, D., & Amaranggana, A.

DESCRIPTION:

The quick change of developments familiarizes cleverness with all affiliations and gatherings. The Stylish Visiting the appeal intention thought ascends out of the change of Smart Cities. With development being introduced on all affiliations and substances, objectives will abuse coordinated efforts between general identifying advancement and their social portions to reinforce the change of guest experiences. By applying insightful thought to address pioneers' needs some time as of late, in the midst of and after their trek, objectives could assemble their clout level. These paper provision to abuse from the revolutionize of elegant Cities by intangible configuration for stylish sightseeing target through researching tourism applications in objective and tending to both open entryways and troubles it had.

3.2 TITLE: Personalized travel package recommendation

AUTHOR: Q. Liu, Y. Ge, Z. Li, E. Chen, and H. Xiong

DESCRIPTION:

As the universes of trade, amusement, travel, and Internet innovation turn out to be all the more inseparably connected, new sorts of business information get to be distinctly accessible for imaginative utilize and formal examination. To be sure, this paper gives an investigation of abusing on the web travel data for customized travel bundle suggestion. A basic test along this line is to address the extraordinary qualities of travel information, which recognize travel bundles from customary things for suggestion. To this end, first break down the qualities of the travel bundles and build up a Tourist-Area-Season Topic show, which can separate the subjects adapted on both the voyagers and the natural elements (i.e. areas, travel seasons) of the scenes? In view of this TAST show, a mixed drink approach on customized travel bundle proposal. Finally, evaluation of this model and the mixed drink approach on certifiable travel bundle information. The exploratory outcomes demonstrate that the model can viably catch the one of a variety superiority of the travel information and the mixed drink approach is subsequently considerably more viable than conventional suggestion strategies for travel bundle proposal.

3.3 TITLE: Recommending friends and locations based on individual location history

AUTHOR: Y. Zheng, L. Zhang, Z. Ma, X. Xie

DESCRIPTION:

The expanding accessibility of subject securing improvements (GPS, GSM programs, etc.) empowers contributors to log the discipline histories with spatio-transient know-how. Such actual subject histories suggest, to a couple measure, customers' pursuits in spots, and convey us chances to realise the relationship amongst clients in addition to spot. This paper depicts , transporting in the direction of this track along through afford an report of a bespoke accessory as well as pasture

recommender on behalf of the ecological information frameworks on the web. Within the original circumstances, on this advocated framework, a distinctive persons stopover to a geospatial locale on this present fact are utilized as their understood appraisals on that subject. Later, measure the likeness between purchasers regarding their area histories and prescribe to every client a gathering of potential companions in a GIS individual's team. 1/3, we verify an man or woman's benefits in an association of unvisited locales by using including his/her area historical past and those of exclusive consumers. Some unvisited areas that can coordinate their tastes can be prescribed to the man or woman.

IV. SYSTEM ARCHITECTURE

Proposed concept deals with providing database by using hadoop tool able to analyze no limitation of data in addition to simple add number of machines to the cluster and getting results with less time, high throughput and maintain cost is very cheap as well as by using joins , partitions and bucketing techniques in hadoop see in Fig. 1.

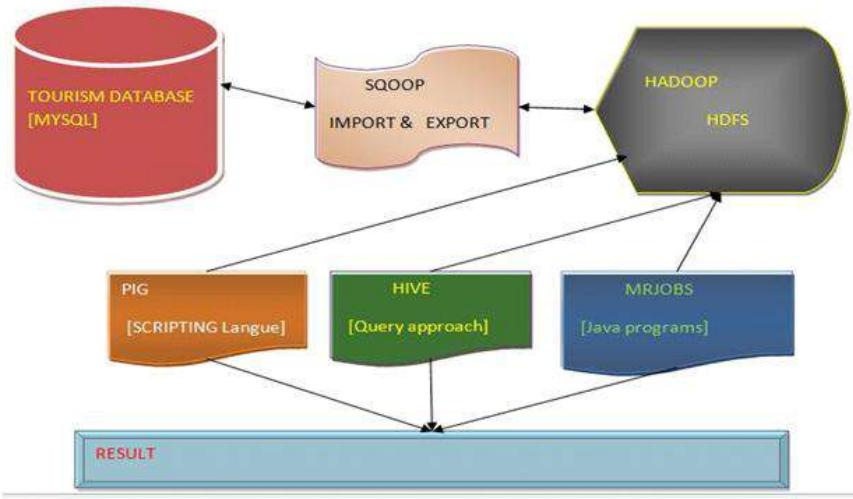

FIG.1. ARCHITECTURE OF THE SYSTEM

To enhance the effectiveness in the terns of bringing the information quick. By methods for when existing or dynamic information required getting concerning examination reason whether information expectation is unrealistic there are chances it is organized or might be unstructured else it would have semi structured information. So on assortment of information investigation is must. So first information preprocessing will go too happened.

V. MODELS AND DESIGN GOALS

5.1 Data Preprocessing Module:

While mining the information, to gather information from various source frameworks notwithstanding in different record designs, for instance level documents with delimiters (CSV) and additionally XML files. To accumulate information from different frameworks that development information in clandestine configurations nobody too utilizes for long haul. The changing over stride may include different information controls, assume moving, part and interpreting and additionally combining, sorting turning and in addition more. For example, a client name may be part into first and additionally last names or else dates may be changed to the standard ISO format.At next stride stacking information into information stockroom should be possible in group forms or else push by line.

5.2 Data Intake via Sqoop

Apache Sqoop is an apparatus intended to exchange information amongst Hadoop and social databases. Sqoop can import information from a RDBMS such MySQL as well as Oracle Database dependent on HDFS and also then fare the information invert later than information has been adjusted utilizing MapReduce. Sqoop interfaces with a relational database (RDBMS) all the way through its java database connection (JDBC) connector along with depends on the database to depict the database blueprint for information to be transported in. Both import and fare use MapReduce, which furnishes parallel operation with adaptation to internal failure. All through import, Sqoop peruses the table, push by line, into HDFS sees in Fig.2.

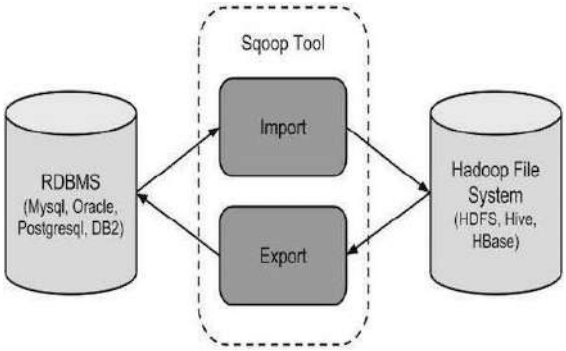

FIG. 2. SQOOP ARCHITECTURE

5.3 Data Analytic With Hive

Hive is an open-source data warehousing illumination will going to harps on pinnacle of Hadoop. Hive ropes problem elucidate in a SQL-like as an authoritative lingo - HiveQL, that are going to masterminded into guide decrease occupations which executed on Hadoop. What's more, HiveQL supports tradition portrays scripts to be piece into inquiries. The lingo consists of a species system with hold up for table's enclosed primitive sorts moreover congregation like assemblage as well as above and beyond maps, and in addition established associations of the same. The significant IO libraries can be wide to request data in custom configurations. Hive additionally involves a framework index, Hive-Metastore, holding patterns notwithstanding insights, which is valuable in information.

5.4 Data Analytic Module with pig

It is an impossible to miss state data managing vernacular which will gives a full rich system of amassed data sorts and in addition over the navigate of execute a substitute traits of proceed ahead the data chiefs. The tongue for Pig can't keep away from being pig Latin. Pig handles each structure and unstructured tongue. It's thinking about all things high of the guide diminish technique running establishment. The scriptt generally used for investigating the data in Hadoop by means of Pig utilization is recognized as Pig Latin. Recalling a conclusive focus to play out a particular undertaking Programmers using Pig and when programming engineers require to make a Pig script by making utilization of the Pig Latin script moreover implement them in the midst of any of the implementation instruments (Grunt Shell as well as UDFs). Functioning as anticipated to implementation, these scripts will get ahead of by methods for an upgrading of revolutionize which leaving to related by the Pig Framework, intention of most obligatory yield. Inside, Apache Pig change these scripts into a get-together of MapReduce associations, likewise, it will make the thing sketcher's occupation coordinate.

5.5 Data Analytic With Mapreduce

The MapReduce encoding sculpt is made out of two primitive capacities that is Map and in addition Reduce. The info information for a MapReduce program is a rundown of <key, value> matches notwithstanding along these lines the Map() capacity is helpful to each combine and furthermore create an arrangement of halfway combines, e.g. <key, list(value)>. After that the Reduce() capacity is utilitarian to each middle of the road combine, prepare estimations of the rundown, and in addition deliver aggregate last outcomes. Moreover, there are additional capacities in the MapReduce execution display for instance rearrange and sort, for dealing with middle information. On the Map side the rearrange capacity will be connected, and also execute information trade by key after Map(). Along these lines, information among a similar key will be communicate to a solitary Reduce work. The sort capacity be propelled on the Reduce side later than information trade. By utilizing key information going to sort field to gathering every one of the sets by methods for a similar key for further handling.

The mapper discharges a halfway key-esteem combine for each word in an archive. The reducer aggregates up all means each word

Algorithm 1. MapReduce Execution

1. Class MAPPER
2. method Map(prid a, prname d)
3. For all term t $\in$ doc d do
4. Emit(term t, count 1)

class Reducer

i. method Reduce(term t, counts [c1, c2, . . .])
ii. method Reduce(term t, counts [c1, c2, . . .])
iii. sum ← 0
iv. for all count c ∈ counts [c1, c2, . . .] do
v. sum ← sum + c
vi. Emit(term t, count sum)

This reckoning determines the live of event of every word in an exceedingly substance assemblage, that is that the underlying stage certain instance, structure a unigram tongue depiction (i.e., chance dissemination in more than words in Associate in Nursing amassing). Input key qualities sets secure the type of (prid, prname) sets that top off on high of the scattered record structure, some place the past could be a choose symbol for the report, and likewise the primary duplicate of the document itself. The clerk get Associate in Nursing info key-regard be part of, tokenizes the report, and what is more unleash a middle key-regard coordinate for every word: the prid itself fills in because the key, and also the entire favored fills in because the regard (hint that we have seen the prid once). The MapReduce execution framework ensured that each one qualities connected with the much identical key area unit gotten in lightweight of current circumstances the reducer. Henceforth, in our guide decrease count, merely need to combination all numbers (ones) connected with every word. The reducer will properly this, and likewise unleash last key-regard sets with the prid because the key, and also the contemplate the regard.

VI. RESULTS AND EVALUATION

By and huge for graphical portrayal in hadoop R accent for the foremost half utilizes. R is code likewise as condition used as a district of enlargement to planned exceptionally to work out functions and factual. it's divergent from completely different insights instruments and to boot different process accent as an example S as R is totally develop expected for measurable data[10]. R is Associate in Nursing open supply and free factual program which may use for each measurable would like and calculations. As of currently contains informational assortment in hadoop cluster but for analyazation that has to speak to in graphical organization in Fig.4. demonstrates the vital development within the amount of specific MapReduce programs registered with our essential ASCII text file administration framework the MapReduce library logs measurements regarding the procedure assets used by the folks for many of the tuime in keeping with ratings thatis that the real followable path by most of the folks will conclude once analyzation

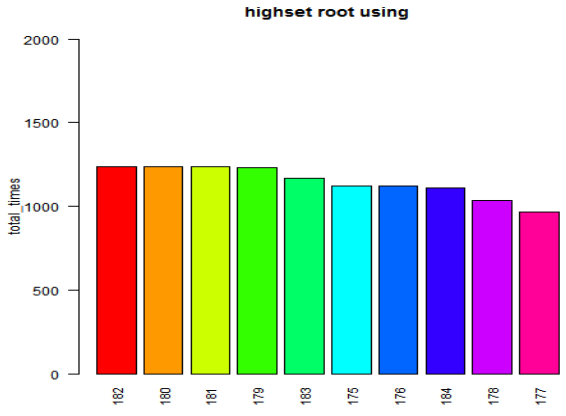

FIG.4. ANALYZATION FOR HIGHEST ROOT

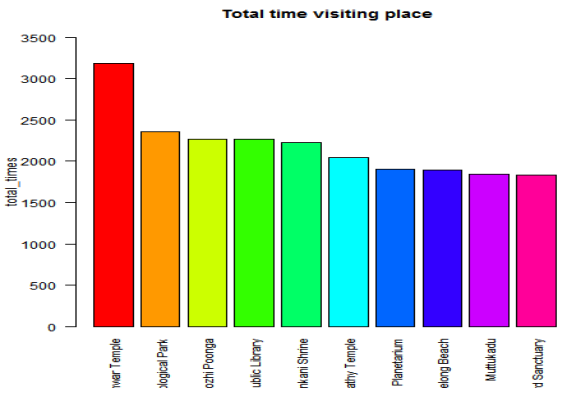

FIG.5. ANALYZATION FOR TOTAL TIME VISITING PLACE

In Fig.5. depicts the graphical similarly as applied mathematics illustration once analyzing each path booth with reference to time by means that of ato reach at explicit destination by that root can take less time to. thus for all destination purpose there ar some root which is able to go via directly or indirectly until to it purpose.So that root can take shortest time to achieve there.

VII. CONCLUSION

Huge information alludes to an extraordinary open door for all travel foundations and tourism. It considerably affects enter forms in tourism industry however its impact is certainly in essential stages. A few segments and organizations are presently trying or utilizing huge information in sight of establishment up till now a bulky amount of them have not even now made any move in such manner. All organizations that were examined in this report had no restriction with the theory that enormous information can possibly change the business altogether. The vital point is moving from potential to reality at any rate in a little scale.

Suitability of endeavors is comprehensive through the make utilize of of colossal data; along these lines, remarkable affiliations are by and by focusing on securing and surveying the data related to customers that has been secured in lodgings or customers' information and in addition collaborations amidst an exact ultimate objective to abuse their required models and data. Colossal data is to a great degree basic in light emission snippet of data that it delicate a proper information about business. In this comportment, it has been seen as a progression hotspot for tourism affiliations and tourism industry. Capacity of colossal data in tourism industry is greatly uncommon and the related affiliations should not disregard the criticalness of this degree.

A portion of the headings for future work is we can utilize start offers taking after future extension:

1. Computation will be In-Memory
2. Dynamic spilling information conceivable to examine

REFERENCES

[1] H. Liu, T. Mei, J. Luo, H. Li, and S. Li, "Finding perfect rendezvous on the go: Accurate mobile visual localization and its applications to routing," in Proc. 20thACMInt. Conf. Multimedia, 2012, pp. 9–18.

[2] J. Li, X. Qian, Y. Y. Tang, L. Yang, and T. Mei, "GPS estimation for places of interest from social users' uploaded photos," IEEE Trans. Multimedia, vol. 15, no. 8, pp. 2058–2071, Dec. 2013.

[3] S. Jiang, X. Qian, J. Shen, Y. Fu, and T. Mei, "Author topic model based collaborative filtering for personalized POI recommendation," IEEE Trans.Multimedia, vol. 17, no. 6, pp. 907–918, Jun. 2015.

[4] J. Sang, T. Mei, T. J. Sun, S. Li, and C. Xu, "Probabilistic sequential POIs recommendation via check-in data," in Proc. ACM SIGSPATIAL Int. Conf. Adv. Geographic Inform. Syst., 2012, pp. 402–405.

[5] Y. Zheng, L. Zhang, Z. Ma, X. Xie, and W. Ma, "Recommending friends and locations based on individual location history," ACM Trans. Web, vol. 5, no. 1, p. 5, 2011.

[6] Y. Shi, P. Serdyukov, A. Hanjalic, and M. Larson, "Personalized landmark recommendation based on geo-tags from photo sharing sites," in Proc. 5th AAAI Conf. Weblogs Social Media, 2011, vol. 11, pp. 622–625.

[7] M. Clements, P. Serdyukov, A. de Vries, and M. Reinders, "Personalised travel recommendation based on location cooccurrence," arXiv preprint arXiv:1106.5213, 2011.

[8] X. Lu, C. Wang, J. Yang, Y. Pang, and L. Zhang, "Photo2trip: Generating travel routes from geo-tagged photos for trip planning," in Proc. Int. Conf. Multimedia, 2010, pp. 143–152.

[9] Marine-Roig, E., & Clavé, S. A. (2015). Tourism analytics with massive user-generated content: A case study of Barcelona. Journal of Destination Marketing & Management, 4(3), 162-172.

[10] https://www.statsoft.com/Portals/0/.../WhitePapers/R_Integration_White_Paper.pdf

Gene Expression Chromosomal Correlations in Tumors of Mesodermal Origin: The Case of Rhabdomyosarcoma and Acute Lymphoblastic Leukemia

Viktoria Papadimitriou[1], George I. Lambrou[*]

[1,2]Graduate Program "Metabolic Bones Diseases", National and Kapodistrian University of Athens, Medical School, Mikras Asias 75, 11527, Goudi, Athens, Greece

[2]First Department of Pediatrics, Choremeio Research Laboratory, National and Kapodistrian University of Athens, Thivon & Levadeias, 11527, Goudi, Athens, Greece

Abstract-*since the advent of high throughput methodologies, like microarrays, the load of genomic data has increased geometrically and along with that the need for computational methods which will interpret these data. In the present work we have studied the common gene expression patterns between two tumor cell types of mesodermal origin. In particular, we have attempted to find causal relations between gene expression levels with respect to chromosomal location. We have found that several genes manifested significant relations, using regression analysis and as such they could pose interesting targets for further investigations. This type of analysis can lead to the understanding of the common mechanisms that transform physiological cells to malignant, as well as it reveals a new holistic way to understand the dynamics of tumor onset as well as the mechanistic of oncogenic drivers. Such approaches could prove to be useful in the prediction of genomic targets that could be further studied in order to unravel the mechanics of tumor ontogenesis.*

Keywords-Acute Lymphoblastic Leukemia, Chromosomal correlations, Mesoderm, Microarrays, Rhabdomyosarcoma.

I. INTRODUCTION

Acute lymphoblastic leukemia (ALL) and rhabdomyosarcoma (RMS) are two type of tumors, which originate from the embryonic mesoderm. ALL is the most frequent malignancy, which appears during childhood. Acute leukemia originates from the undifferentiated lymphoblast, which does not develop into the mature lymphoid cell, giving rise to a tumor. RMS is a rare cancer in childhood. This represents 5-8% of all tumors in childhood, but the sarcomas of head and neck are 12% of all neoplasias in childhood. RMS originates from myoblast or cells that will form the skeletal muscle. These are different from the smooth cells. RMS can be created at any part of the body, which has skeletal muscle but frequently appears in the head and neck. The embryonal form of RMS is most common at birth, which consists of spindle cells and botryoid form with better prognosis, but the alveolar form mainly appears in childhood and adolescence. ALL and RMS consist of cells that are undifferentiated, immortal and with the potential to divide infinitely. Myoblasts originate from the dorsal (paraxial) mesoderm, while blood cells derive from the lateral mesoderm that gives rise to the splachnic mesoderm and this to the hemangioblastic tissue. ALL and many alveolar RMS in childhood present chromosomal translocations, like the PAX3-FKHR, that is an indicator of poor prognosis and associated with metastasis [1].

During embryogenesis, blood cells originate from two sites. From the ventral mesoderm near the yolk sac, which gives rise to the intra-embryonic hematopoietic precursors, but the hematopoietic cells that last throughout the entire life time of an organism are derived from the mesodermal area surrounding the aorta. This differentiation is regulated with a network of various genes, which leads to two similar cell types with others functions and roles in the body. There are several factors that affect gene regulation, which means that aberrations in the regulatory network would lead to tumor cells.

Further on, it has been previously reported that correlation in gene expression and in particular, chromosomal correlation implies common gene regulation [1, 2]. Yet, it is also known that correlation does not imply causality. In that sense, it is of great importance if we would be able to infer gene regulatory mechanisms from chromosomal expression levels.

The present study concerns the extension of a previous work, where gene expression analysis was extensively investigated in two cell lines. The T-cell acute lymphoblastic leukemia CCRF-CEM cell line and the rhabdomyosarcoma TE-671 cell line. We used these cell lines to investigate common patterns of cellular function between the two systems. These two cell types would normally had differentiated into cells of blood and muscle cells but in an unknown stage this normal differentiation stopped and began an informal, uncontrolled proliferation which created the malignancy. The intervening stages and led in tumor genesis are unknown.

Thus, in the present work we attempted to investigate common gene regulation based on chromosomal correlations. Yet, we have tried to move a step forward and find probable etiological relations in gene expression patterns. The present work focuses towards approaches that utilize biological along with mathematical tools, in order to unravel mechanisms in gene expression patterns. Further on, it moves towards a direction that attempts to interpret gene regulation not from the differential point of view but from common gene expression patterns.

II. MATERIALS AND METHODS

2.1 Cell Cultures

The CCRF-CEM (ALL) and the TE-671 (RMS) cell lines were used as the model, both obtained from the European Collection of Cell Cultures (ECACC). The CCRF-CEM cell line, a $CD4^+$ [3] and $CD34^+$ presenting cell line [4], was initially obtained from the peripheral blood of a 2 year old Caucasian female. It was diagnosed as lymphosarcoma which progressed later on to acute leukemia [5]. The child was undergone irradiation therapy and chemotherapy prior to obtaining the cell line. Although remission was achieved at various stages, the disease progressed rapidly [5]. The cell line was observed to have undergone minor changes after long-term culture, except for the presence of dense granules in the nucleoli [6]. Finally, the CCRF-CEM cell line has been reported to manifest autocrine catalase activity which participates to its mechanisms of growth and progression [7].The TE-671 cell line was initially reported to have been obtained from a cerebellar medulloblastoma, before irradiation therapy, of a six-year old Caucasian female [8] and characterized later on [9]. However, it is today known that this cell line is parental if not identical to the RD [10] rhabdomyosarcoma cell line. However, several reports still refer to this cell line as medulloblastoma [11, 12]. The experimental process of cell treatment has been described previously [1].

2.2 Experimental Procedures

Experimental procedures have been described previously in detail by our group [1]. In brief, factors estimated, included cell proliferation, cell cycle distribution and microarray experimentation. For the assay of mRNA levels two sets of microarray chips were used: cDNA microarray chips (4.8k genes) obtained from TAKARA (IntelliGene™ II Human CHIP 1) [13] and microarray chips (9.6k genes) from the Institut fuer Molekularbiologie und Tumorforschung, Microarray Core Facility of the Philipps-Universitaet, Marburg Germany (IMT9.6k). Microarray experimentation has been previously described in our previous work [1]. The microarray data have been submitted to the GEO Database under the Accession Number GSE34522.

2.3 Microarray Data Analysis

Microarray data pre-processing analysis was performed with ImaGene®v.6.0Software (BioDiscovery Inc, CA) and ARMADA software (National Hellenic Research Foundation, Athens Greece) [14]. Data were collected from exported text file and data pre-processing was performed using the Microsoft Excel® environment. Background correction has been performed by using the robust loess-based background correction(rLsBC) approach, as proposed by *Sifakis et al.* (2011) [15]. The background corrected signal intensities were further normalized in order to mitigate the effect of extraneous, non-biological variation in the measured gene expression levels. Genes were tested for their significance in differential expression using a z-test. Genes were considered to be significantly differentially expressed if they obtained a *p*-value <0.05. The False Discovery Rate (FDR) was calculated as previously described [16-18]. There was a FDR of 1% for $p<0.05$ for the IntelliGene microarray chip, and a FDR of 9% for $p<0.01$ for the IMT 9.6k microarray chip. Calculating the FDR for the combination of both platforms gives a FDR of 6% for $p<0.01$.

2.4 Chromosomal Regressions and Data Analysis

Chromosome mapping was performed with Genesis 1.7.2 (Technische Universitaet-Graz, Austria) using Pearson's correlation, Spearman's rank order correlation [2, 19, 20] and WebGestalt web-tool (Vanderbilt University, The Netherlands, http://bioinfo.vanderbilt.edu/gotm/) [21].2D Chromosomal regressions have been performed among the similarly expressed genes between RMS (TE-671) and ALL (CCRF-CEM). 3D chromosomal regressions were performed between similarly expressed genes of RMS and ALL as well as we added the third dimension, which was the log_2 transformed ratio of the respective genes. Regressions and data analysis were performed with the Matlab® computational environment (The Mathworksm Inc. Natick, MA). For linear 2D regressions the binomial equation was used of the form $f(x)=y=ax^2+bx+c$, while for the 3D regressions the equation of the form $f(x,y)=z=ay+bx+c$.

III. RESULTS

Regression analysis was performed in order to find probable causal relations in gene expression with respect to cell type and chromosomal distribution. In particular, we have used genes that manifested similar expression levels, meaning that they were those that were not differentially expressed. We have performed two different kinds of regression analysis. One included a 2D regression of the form $y=ax^2+bx+c$ and the second of the form $z=ay+bx+c$. 2D regressions manifested significant relations between the two cell types and in particular for chromosome 1 with an R^2=0.82 (**Fig. 1A**), chromosome 3 with an R^2=0.82 (**Fig. 1B**), chromosome 8 with an R^2=0.89 (**Fig. 1C**), chromosome 13 with an R^2=0.71 (**Fig. 1D**), chromosome 14 with an R^2=0.91 (**Fig. 1E**), chromosome 15 with an R^2=0.69 (**Fig. 1F**), chromosome 16 with an R^2=0.89 (**Fig. 1G**), chromosome 17 with an R^2=0.81 (**Fig. 1H**), chromosome 21 with an R^2=0.88 (**Fig. 1I**), chromosome 22 with an R^2=0.97 (**Fig. 1J**) and chromosome X with an R^2=0.71 (**Fig. 1K**).

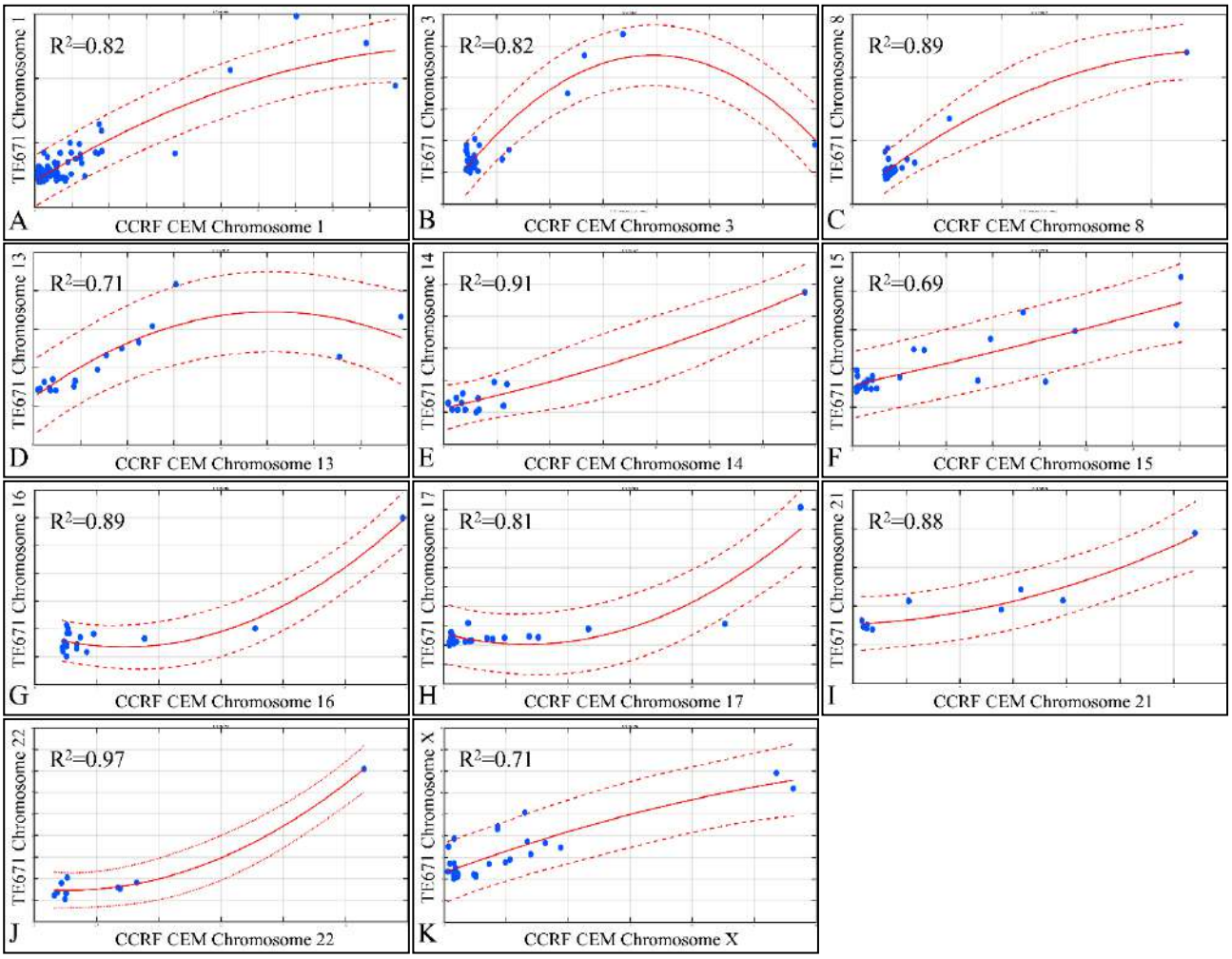

FIGURE 1. REGRESSIONS OF GENE EXPRESSION DATA BETWEEN CCRF-CEM AND TE-671 CELLS, WITH RESPECT TO CHROMOSOMAL EXPRESSION. SIGNIFICANT RELATIONS WERE FOUND FOR CHROMOSOMES 1 (**A**), 3 (**B**), 8 (**C**), 13 (**D**), 14 (**E**), 15 (**F**), 16 (**G**), 17 (**H**), 21 (**I**), 22 (**J**) and X (**K**).

Although 2D regressions manifested significant relations with regard to gene expression, still the revealed functions did not have the complete set of the definition of a function. In other words, for every $x \in D(f)$, there are two y, which can be described as $\exists\, x_1, x_2 \in D(f)$: $x_1 \neq x_2 \Rightarrow f(x_1)=f(x_2)$, *or* $y_1=y_2$, where $D(f)$ is the definition domain of f, and x, y are the expression levels of each gene. The question that came up from this observation, was that the manifested correlations could provide more information if another dimension could be added to the calculations. The solution to this question came from the observation that the log_2 transformed ratio of TE-671 gene expression levels over the CCRF-CEM gene expression levels, could be added as the third dimension. Thus, we have formulated a new relation $z=ay+bx+c$ or $f(x,y)=ay+bx+c$, wherez can

be formulated as $z = \log_2\left(\frac{x}{y}\right)$. Thus, the aforementioned equations become $\log_2\left(\frac{x}{y}\right) = ay + bx + c$. The results of the 3D regression are presented in **Fig. 2**.

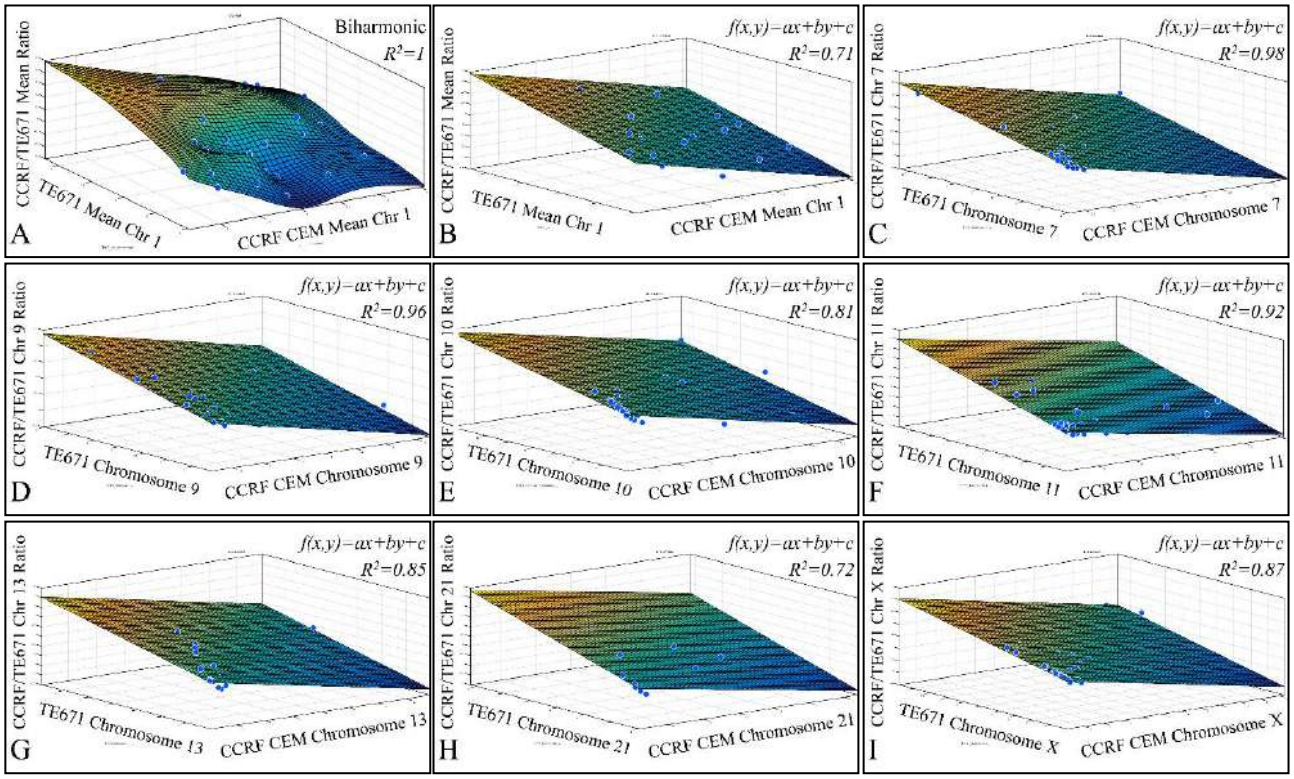

FIGURE 2. 3D REGRESSIONS OF GENE EXPRESSION DATA BETWEEN CCRF-CEM AND TE-671 CELLS AND THEIR RESPECTIVE LOG2 TRANSFORMED RATIO WITH RESPECT TO CHROMOSOMAL EXPRESSION. SIGNIFICANT RELATIONS WERE FOUND FOR CHROMOSOMES 1 (A) WITH BIHARMONIC FUNCTION, 1 (B) WITH A LINEAR FUNCTION, 7 (C), 9 (D), 10 (E), 11 (F), 13 (G), 21 (H) andX (I).

In particular, 3D regression analysis manifested significant relations between the two cell types and their ratio, and in particular for chromosome 1 with an R^2=1 (**Fig. 2A**) and with the use of the biharmonic function, chromosome 1 with an R^2=0.71 (**Fig. 2B**) with the use of the aforementioned linear function, chromosome 7 with an R^2=0.98 (**Fig. 2C**), chromosome 9 with an R^2=0.96 (**Fig. 2D**), chromosome 10 with an R^2=0.81 (**Fig. 2E**), chromosome 11 with an R^2=0.92 (**Fig. 2F**), chromosome 13 with an R^2=0.85 (**Fig. 2G**), chromosome 21 with an R^2=0.72 (**Fig. 2H**) and chromosome X with an R^2=0.87 (**Fig. 2I**).

It appeared that relations in three dimensions manifested better results for the specified chromosomes as compared to two dimensional regressions. This observation, shows that probably a third dimension is necessary in order to comprehend gene regulatory mechanisms.

IV. DISCUSSION

In the present study we used computational and mathematical approaches in order to answer the question whether, a causal relation between gene expression levels of two cell types, could be found based on their chromosomal distribution. We have found that such significant relations could be found both using 2D as well as 3D regression methods. Especially, 2D regressions manifested very good relations among cell types with respect to chromosomes, yet without manifesting a clear causal relation. On the other hand, 3D regressions manifested better results suggesting that causal multi-dimensional relations probably exist. At the same time, the fact that certain genes and chromosomes manifest significant correlations between two different cell types, yet of similar origin, implies that they could probably consist common regulatory mechanisms of tumor ontogenesis. In our previous work we have reported that ANXA4 (Chromosome 2), NP25 (Chromosome 3), VEGFC (Chromosome 4), PDLIM7 and THBS4 (Chromosome 5), CUL7 (Chromosome 6), CD36 (Chromosome 7), BNIP3L

(Chromosome 8), CDC2 and IL2RA (Chromosome 10), MAB21L1 and FOXO1 (Chromosome 13), TCL1A (Chromosome 14), FEM1B (Chromosome 15), CFDP1 and MMP2 (Chromosome 16), RTTN (Chromosome 18), PDCD5 (Chromosome 19), , NNAT and ZNF313 (Chromosome 20), MBNL3, PLAC1, RPS6KA3 and CD40LG (Chromosome X) were genes found to participate in cell differentiation and embryonal processes[1]. These genes were found to manifest significant correlations both in the 2D as well as in 3D regressions. This finding consist of an important observation since it is probable that these genes could possess a common machinery, either through their gene regulation or aberrations, that drives tumor ontogenesis for the two cell types under investigation.

V. CONCLUSION

The present approach attempted to find common regulatory mechanisms in gene expression patterns of two cell types. In particular, we have attempted to discover possible causal relations in gene expression patterns. We have found evidence that such correlations could exist and it is probable that certain genes could be of great significance in tumor ontogenesis. Such approaches could prove to be useful in the prediction of genomic targets that could be further studied in order to unravel the mechanics of tumor ontogenesis.

ACKNOWLEDGEMENTS

VP: This work was funded in part by the National and Kapodistrian University of Athens, Medical School.**GIL**: This work was funded in part by the National and Kapodistrian University of Athens, Medical School. **Authors' Contributions**: **VP**: performed computational experiments, drafted the manuscript, proof-read the manuscript. **GIL**: conceived the idea, performed computational experiments, wrote Matlab code, performed data analysis and drafted the manuscript, gave final permission for submission.

COMPETING INTEREST, DISCLOSURES AND CONFLICT OF INTEREST

The authors have nothing to disclose and no conflict of interest

REFERENCES

[1] G. I. Lambrou, A. Zaravinos, M. Adamaki, D. A. Spandidos, F. Tzortzatou-Stathopoulou, and S. Vlachopoulos, "Pathway simulations in common oncogenic drivers of leukemic and rhabdomyosarcoma cells: a systems biology approach," Int J Oncol, vol. 40, pp. 1365-90, May 2012.

[2] B. A. Cohen, R. D. Mitra, J. D. Hughes, and G. M. Church, "A computational analysis of whole-genome expression data reveals chromosomal domains of gene expression," Nat Genet, vol. 26, pp. 183-6, Oct 2000.

[3] L. Miranda, J. Wolf, S. Pichuantes, R. Duke, and A. Franzusoff, "Isolation of the human PC6 gene encoding the putative host protease for HIV-1 gp160 processing in CD4+ T lymphocytes," Proc Natl Acad Sci U S A, vol. 93, pp. 7695-700, Jul 23 1996.

[4] C. Naujokat, O. Sezer, H. Zinke, A. Leclere, S. Hauptmann, and K. Possinger, "Proteasome inhibitors induced caspase-dependent apoptosis and accumulation of p21WAF1/Cip1 in human immature leukemic cells," Eur J Haematol, vol. 65, pp. 221-36, Oct 2000.

[5] G. E. Foley, H. Lazarus, S. Farber, B. G. Uzman, B. A. Boone, and R. E. McCarthy, "Continuous Culture of Human Lymphoblasts from Peripheral Blood of a Child with Acute Leukemia," Cancer, vol. 18, pp. 522-9, Apr 1965.

[6] B. G. Uzman, G. E. Foley, S. Farber, and H. Lazarus, "Morphologic variations in human leukemic lymphoblasts (CCRF-CEM cells) after long-term culture and exposure to chemotherapeutic agents. A study with the electron microscope," Cancer, vol. 19, pp. 1725-42, Nov 1966.

[7] P. A. Sandstrom and T. M. Buttke, "Autocrine production of extracellular catalase prevents apoptosis of the human CEM T-cell line in serum-free medium," Proc Natl Acad Sci U S A, vol. 90, pp. 4708-12, May 15 1993.

[8] R. M. McAllister, H. Isaacs, R. Rongey, M. Peer, W. Au, S. W. Soukup, *et al.*, "Establishment of a human medulloblastoma cell line," Int J Cancer, vol. 20, pp. 206-12, Aug 15 1977.

[9] H. S. Friedman, S. H. Bigner, R. D. McComb, S. C. Schold, Jr., J. F. Pasternak, D. R. Groothuis, *et al.*, "A model for human medulloblastoma. Growth, morphology, and chromosomal analysis in vitro and in athymic mice," J Neuropathol Exp Neurol, vol. 42, pp. 485-503, Sep 1983.

[10] R. M. McAllister, J. Melnyk, J. Z. Finkelstein, E. C. Adams, Jr., and M. B. Gardner, "Cultivation in vitro of cells derived from a human rhabdomyosarcoma," Cancer, vol. 24, pp. 520-6, Sep 1969.

[11] C. M. Yeung, B. S. An, C. K. Cheng, B. K. Chow, and P. C. Leung, "Expression and transcriptional regulation of the GnRH receptor gene in human neuronal cells," Mol Hum Reprod, vol. 11, pp. 837-42, Nov 2005.

[12] E. S. Chu, T. K. Wong, and C. M. Yow, "Photodynamic effect in medulloblastoma: downregulation of matrix metalloproteinases and human telomerase reverse transcriptase expressions," Photochem Photobiol Sci, vol. 7, pp. 76-83, Jan 2008.

[13] H. W. Chung, S. W. Park, J. B. Chung, J. K. Kang, J. W. Kim, H. S. Kim, *et al.*, "Differences in genetic expression profiles between young-age and old-age gastric adenocarcinoma using cDNA microarray for endocrine disruptor study," Oncol Rep, vol. 12, pp. 33-9, Jul 2004.

[14] A. Chatziioannou, P. Moulos, and F. N. Kolisis, "Gene ARMADA: an integrated multi-analysis platform for microarray data implemented in MATLAB," BMC Bioinformatics, vol. 10, p. 354, 2009.

[15] E. G. Sifakis, A. Prentza, D. Koutsouris, and A. A. Chatziioannou, "Evaluating the effect of various background correction methods regarding noise reduction, in two-channel microarray data," Comput Biol Med, Nov 8.
[16] Y. Klipper-Aurbach, M. Wasserman, N. Braunspiegel-Weintrob, D. Borstein, S. Peleg, S. Assa, *et al.*, "Mathematical formulae for the prediction of the residual beta cell function during the first two years of disease in children and adolescents with insulin-dependent diabetes mellitus," Med Hypotheses, vol. 45, pp. 486-90, Nov 1995.
[17] J. D. Storey and R. Tibshirani, "Statistical significance for genomewide studies," Proc Natl Acad Sci U S A, vol. 100, pp. 9440-5, Aug 5 2003.
[18] J. D. Storey and R. Tibshirani, "Statistical methods for identifying differentially expressed genes in DNA microarrays," Methods Mol Biol, vol. 224, pp. 149-57, 2003.
[19] A. Sturn, J. Quackenbush, and Z. Trajanoski, "Genesis: cluster analysis of microarray data," Bioinformatics, vol. 18, pp. 207-8, Jan 2002.
[20] F. Reyal, N. Stransky, I. Bernard-Pierrot, A. Vincent-Salomon, Y. de Rycke, P. Elvin, *et al.*, "Visualizing chromosomes as transcriptome correlation maps: evidence of chromosomal domains containing co-expressed genes--a study of 130 invasive ductal breast carcinomas," Cancer Res, vol. 65, pp. 1376-83, Feb 15 2005.
[21] B. Zhang, D. Schmoyer, S. Kirov, and J. Snoddy, "GOTree Machine (GOTM): a web-based platform for interpreting sets of interesting genes using Gene Ontology hierarchies," BMC Bioinformatics, vol. 5, p. 16, Feb 18 2004.

Innovation and development of air transport in Slovakia

Darina MATISKOVÁ

Technical University in Košice, Faculty of Manufacturing Technologies with seat in Prešov, Bayerova 1, 080 01 Prešov, Slovakia

Abstract— *This contribution is theory disassemble potential, innovation and development of air transport in Slovakia. The paper deals with the possibilities of aviation production in Slovakia that has currently been going through recession mainly caused by dynamic changes in aviation infrastructure in the country. Rapid development of new technologies in aviation reflects continual pressure on producers of aircrafts and aircraft components in Slovakia aiming to succeed with the production not only in the country but in the world as well. On the contrary, it all is conditioned by complicated legislation that is reflected in the insecurity of the Slovak aviation industry.*

Keywords— Potential, effectivity, aviation technology, production of aircrafts, aviation.

I. INTRODUCTION

Slovakia's aerospace sector, as a part of the aerospace and defence (A&D) sector, must be seen in context of both Europe and the entire world. This sector always includes both civil and defence/military elements. On the civil side this sector and its market is cyclical depending on the acquisition plans of airlines, which fluctuate considerably, especially in a period of uncertain economic expectations and global security concerns. On the defence side, demand depends on the defence budgets and procurement policies of governments, which in turn depend on geopolitical developments and the changing perception of threats.[3]

The main trends and the position of the sector should be understood in the context of the following aspects.[3]

Disunity in aviation legislation and the competition within the category of ultralight aircrafts („ULA“) production in surrounding states causes producers of aviation technology significant problems. The advantage is high individual strong-mindedness of such producers to conquer the difficulties. That is why they have been looking for opportunities on such aviation market where they are currently able to find the customer base for their products also in abroad.

Aviation production potential of Slovakia used to have a long tradition during the epoch of the Czecho-Slovak Republic despite the fact it found its way in the production of aircraft components and supportive logistics. In the domain of aviation, Slovakia used to be respected industrial country with advanced development base. For example, development and production of aircraft engines in Považská Bystrica used to be one of the top ones in the world. In present, after having separated the industry of the former republic and because of the impact of the world-wide economical depression the possibilities of demand in aviation have been limited. In the last decade, many companies have been trying to restructure their production because while operating as assistance producers in favour of foreign aviation producers their share was insignificant.

In European aviation industry, Slovakia acts as a country making use of foreign support. Many Slovak aviation companies have been looking for investors that could be offered their advantages and professional man-power despite the competitive environment of surrounding states. Aviation industry is dependant on acquisition plans of aviation companies of which many have terminated (for example Sky Europe, Slovair) because of economic reasons. Reduction in aviation has recently been evident also in the army corps that consequently causes the increase in number of pilots and aviation professionals on the labour market.

Presently, aviation transport in Slovakia has found its way in acquirement of low cost air transporters with full operating support. Slovak aviation production specializes in the production of reliable smaller engine and motor less aircrafts (ULA aircrafts and sport aircrafts) and their components. Produced aircrafts are equipped by modern avionics and their production is on high-quality technological level.

II. AIRCRAFT PRODUCTION IN SLOVAKIA

Economy laws apply within aviation industry in the same way as in other branches of industry. Especially security and stability in aviation industry determine tendency and ways to achieve high material and development level in aviation and

consequently by that also the attention of investors dealing with development of regional air transport and the production of ULA aircrafts to aviation.

As for the legislation in Slovakia, security standards are given by the Civil Aviation Authority of the Slovak Republic that by establishment of the regulations enables to apply progressive opportunities to ULA producers. Many types of aircrafts are certified more easily abroad than in the country and that is reflected in the attitude of many foreign investors.

In present, there are several ULA producers that directly produce aircrafts or unit components. These are such as:

- AEROSPOOL s.r.o., Prievidza – deals with production of sport aircrafts, type sailplane WT 3 and ULA aircrafts WT 9 Dynamic. The WT 9 Dynamic reaches high quality namely due to its advanced construction, precise hand-work and using the latest aviation materials. The vision of the company to the future is orientation to the production of four-seat aircraft and using the latest technologies.
- AEROPRO s.r.o., Nitra – produces ULA aircrafts EUROFOX 2K and 3K. The aircrafts are constructed as concora high-wing monoplane. Double-beam wing contains Junker´s flap that functions as a flaperon. The fuselage is of truss construction made of steel tubes. The tail parts of the aircraft are made as a tube flat truss construction. The undercraft of EUROFOX-2K is classic with back stern wheel and as for the EUROFOX -3K, there is the undercraft of 3-wheels type operated by the front wheel.
- COMP-LET s.r.o., Senica – produces ULA aircraft type SHARK and deals with serial production of composite components for ultralight aircrafts.
- TOMARK s.r.o., Prešov – specializes in the production of Viper SD-4 ultralight aircraft that is highly appreciated for its equipment and its flying abilities. The aircraft is made for sport an recreational flying and uses modern display systems „Glass cockpit".
- AVAMA s.r.o., Poprad – specializes in the production of ULA aircrafts type Stylux X2 and X3 which are unite-type and components for such an aircraft.

In Slovakia, there are other companies dealing with production of components for aircrafts and aviation. These are: DMD Group, a.s., Trenčín, KINEX – KLF a.s., Kysucké Nové Mesto, Way Industries a.s., Krupina, VRM a.s., Trenčín and Ales a.s., Trenčín.

III. SLOVAK AVIATION ASSOCIATIONS

In the effort to prevent certain marginal discordances while trying to keep safety rules, producers of aviation technology also follow the programmes of other associations that are able to resolve their problems. Following associations can be mentioned:

- **The Slovak Federation of Ultralight Flying (SFUL)** – creates conditions for the development of recreational and sport flying by flying sport mechanisms, their safe utilization for personal need as well their development and construction. We can say the SFUL is the connection between administration, laws, regulations, restrictions and bans on one side and wish-to-fly subjects on the other side. It has been trying to eliminate restricting pressure on wish-to-fly subjects and so that favourable conditions for flying with lower costs and good feeling from recreational and sport flying be created. It is subordinated to the Civil Aviation Authority of the Slovak Republic.
- **Association of Aviation Producers of the Slovak Republic (ZLV SR)** – is independent, non-political and open professional organisation that joins legal and personal entities with the subject of enterprise within the production of aviation and space industry and other associated activities in the domain of army, civil and sport aviation industry or other legal and personal entity in connected domains with the seat in the Slovak Republic. By its effective activity it has been trying to enforce interests of the Slovak aviation industry and to gain support to establish conditions for its stabilization and further development on all the levels of management.

Work results of the organisations should be reflected in the support of creation national legislation that would effectively utilize international obligations and rights of the state, highly qualified and effective organisation that would act in civil aviation and that would make conditions in educational system and development in the favour of aviation development.

IV. LEGISLATIVE AND PRODUCTION PROBLEMS IN PRODUCTION OF ULA AIRCRAFTS IN SLOVAKIA

In present, the legislation in the production process of ULA aircrafts is subordinated to the EASA agency and that causes several problems. In present, aircraft producers are under pressure not only to respect criteria of exact procedures in production but also on the production of harmful emissions, noise and safety rules. Current legislation puts small producers under pressure to keep the same rules that must be kept when producing big transport aircrafts. That is why the statutory text of legislation laws for the production and certification of the ULA aircrafts is just a clear obstacle. Slovak producers try to fight the problem. Many documents and audit reports that double-check conformity of certifications of aircraft components producers used in certain type of ULA aircrafts are obstacle as well. [4]

Cooperation of auditors is difficult and not easy to overcome without economic impact on an aircraft producer and on the total price of aviation mechanism. When producing aircrafts in Slovakia, design system in flying and technology guidebooks for control and certification of produced aircrafts is poorly specified. Producers have to complete various guidebooks and respect another complicated legislation and that consequently increases the price of a produced aircraft.[1,4]

Every used component must be certified when used within an aircraft whether it is construction, dense or composite material. Aviation wiring material has probational-certified values that are given by their producers. Even in this case there may be discordancies when applying during the production of an aircraft.

Producers of aviation mechanisms in Slovakia positively appreciate knowledge ability of Slovak aviation specialists who apply in their companies. But in consideration of abovementioned limitations our aviation specialists look for options to self-full fill in surrounding countries mainly in the Czech Republic.[5]

The importance of ULA aircrafts production in Slovakia is supported by the fact, that there is quality labour potential that is able to overcome obstructions given to the Slovak producers. It is necessary to mention that disunity of legislation is also in Europe itself as the meaning of regulations for each EU country is individually adjusted by regional authorities in order to make it advantageous on the aviation market. (see the conditions for flying ULA aircraft in France) Many skilled professionals support the idea to conceptually resolve ambiguity in legislation according to the model of the USA legislation that is elaborated in detail and on high level.

V. MARKET CONDITIONS, PRODUCTION AND PROMOTION OF ULA AIRCRAFTS

Producers of ULA aircrafts in Slovakia are dependent on conditions of essential material components supply, wiring material and other components mainly from the countries where aviation industry is highly developed. That is why producers expect the same conditions when selling an aircraft as for the other competitive producers from other countries have. This ability to compete should be reflected in the presentation of final product – an aircraft – where quality level of the product is shown in compliance with its price. This is how the support of developed aviation countries is possible to be appreciated so that Slovakia finds respectable place on the international aviation market.[3]

Current governmental support of aviation research and development is significantly limited because economic base and efficiency of repayment time of invested money depends on unbelievable determination of individuals and torso of Slovak aviation educational institutions dealing with aviation studies and research. The possibility to improve this situation is to have higher amount of financial resources to develop national sport flying with the impact on development of good skills also in other aviation disciplines.

To prove competent, it is necessary for small producers of aviation technology in the country to look for the options to participate in European projects dealing with production of small and middle aircrafts within the territory of surrounding states. Of course, provided the quality production and using developed technologies. Presently, the dominant sales places are northern European countries and Germany, France, Belgium and England. Direction of the EU requires strict export licences issued by the country of origin that are nowadays very difficult to obtain.[5]

Promotion and presentation of Slovak aviation products are mainly done at various home and foreign workshops and public flying performances where they win admiration.

VI. CONCLUSION

Transition of the Slovak aviation industry to partial stagnation was influenced by many factors whether it was the historical background of the country, economic situation or dependency of our aviation on countries with developed aviation base. Support for development of aviation production must be oriented also towards further education to support and develop

education in technical and aviation branches as well as to the support of Slovak aviation associations and aero clubs where there is the very first contact of people with aviation technology. It is necessary to improve and look for compromise solutions in legislation so that there is no difference between our and other EU countries. Last but not least, it is necessary to preserve aviation traditions in production and reparation of aviation technology, in aviation research and education and in organizing various aviation events that end in not only verbal agreements but in concrete realisation team resolutions as well.

REFERENCES

[1] Čiesko, J.: Production of Aviation Technology in Slovakia in Present and its Perspectives. Košice : Almanac of International Scientific Conference Aeronautics 07, 24. – 25.10. 2007.

[2] Matisková, D., Pavelenko, S.: Strategy of Choosing Technologies to Cut Materials. In: Management of Manufacturing Systems. Prešov. FVT TU 2004, s. 151 – 155, ISBN 8080732094

[3] Slovak Agency for Development of Investments and Busines. Aviation Industry; www.sario.sk

[4] Zákon č. 143/1998 Z. z. Zákon o civilnom letectve (letecký zákon) a o zmene a doplnení niektorých zákonov

[5] Čapek , J, Klíma, R, Zbíralová, J. : Civilní letectví ve světle práva, ISBN 80-86199-95-3, 2014.

Design and Implementation of a Smart Security System Using GSM Technologies Via Short Message Service(SMS) and Calling Function

Prof. Yogesh.S.Kale[1], Siddhant Sakhare[2], Sanket Bokade[3], Nikhil Nandkar[4], Kaustubh Goswami[5]

Yeshwantrao Chavan College of Engineering, Wanadongri, Nagpur, India

Abstract— *This paper proposes the development of a GSM – based smart security system. It is a combination of electronic devices /equipment working together to detect a fire and any human moment. GSM SIM-300, Microcontroller, Sensors have been used to realize this system. This is a cost effective system that detects fire or smoke or human presence and sends alert information to a registered mobile phone for quick and immediate action thereby, avoiding unnecessary and costly industrial and domestic breakdown. A Short Message Service (SMS) and a Calling function is used as a method of wireless connection in the designed system.*

Keywords— GSM SIM-300, Microcontroller, cost effective, SMS, Calling function, wireless connection.

I. INTRODUCTION

What is a security system? Security is the degree of protection against damages, danger, loss and crime. A security system provides a form of protection that ensures the safety and security of the assets and the threat but is not limited to the elimination of either the asset or the threat. Now a day's wireless technology is used instead of wired topological connection. GSM (Global System for Mobile Communication) technology makes used to communicate input signal from appliances to output message on device. That means after detection of any intrusion GSM Modem sends the appropriate message to registered phone. The signals or data which is comes from sensors or other equipment digitize it by GSM module and send it to receiver. The wireless communication is increasing day by day [2]. This has motivated us to use mobile phones to identify the problem and to receive a feedback SMS about the security and safety. The system operates with the help of sensors installed in this system.

Existing systems

1. Wired System,
2. RF Based Security System,
3. Web enabled Security System.

Disadvantage of Existing Systems

1. Difficult to maintain
2. Need internet access
3. Distance.

Proposed System

The proposed system uses GSM module which enables us to know the security status when we are away.

II. ARCHITECTURE OF THE SYSTEM

It can be implemented to any levels of the security system. The architecture of the system mainly consists of three components the GSM MODEM and the interface circuit that include the different sensors used. The function of the GSM MODEM is the remote communication between the user and the controller through the RS232 serial communication standard. The function of the controller is to continuously check the inputs coming from the different sensor and send message through the GSM network in case of emergency. The microcontroller is connected to different devices like smoke detector, stepper motor, PIR motion detector sensor. The GSM is connected with the user, police station, and fire brigade

through the mobile cellular network [1], [3]. An interface circuit has been designed which includes sensors as input devices. Then the programmed microcontroller has been connected to the interface circuit and the GSM MODEM through the serial port of the GSM MODEM.

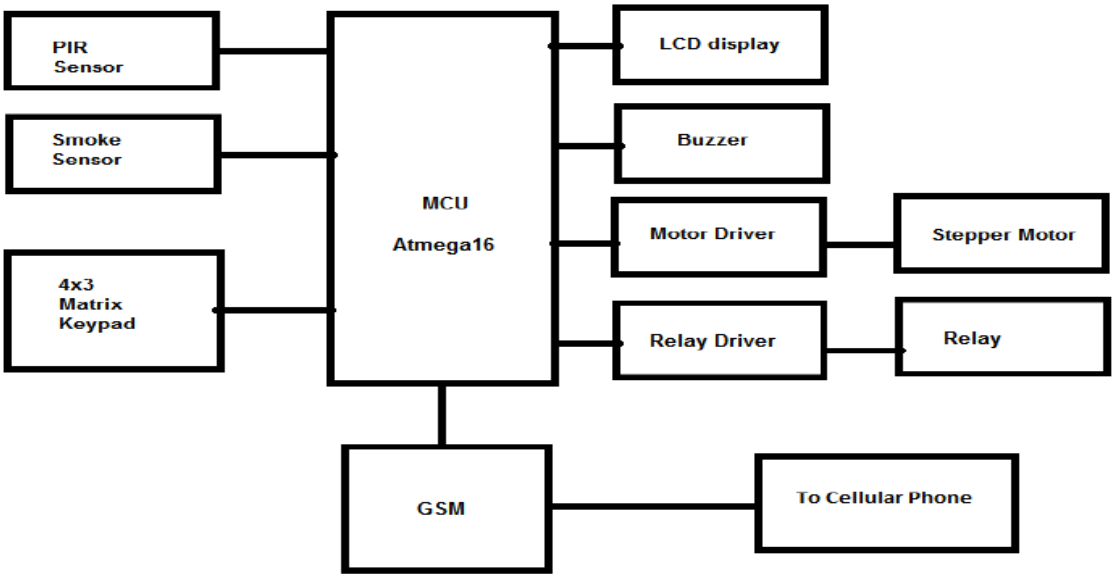

FIG 1: BLOCK DIAGRAM OF CIRCUIT

2.1 Sensing Devices

2.1.1 PIR Sensor

A Pyroelectric Infrared Sensor (PIR sensor) is an electronic sensor, in that type of sensor measures the infrared (IR) light radiating from objects or human in its field of view. The normal sensor emits the radiation but in this sensor detect the radiation. The PIR Sensor has a range of approximately 20 feet (6 meters). The sensor is designed to identify the slowly changing conditions that would happen normally as the daily progresses and the environmental condition changes, but it responds by making its output when sudden changes occur, such as when there is motion. This device is designed mainly for indoor use. Operation outside or in very high temperatures may affect stability negatively [1]. Due to the high sensitivity of PIR sensor device, it is not recommended to use the same condition like rapid environmental changes and strong shock or vibration and also not working in direct sun light or direct wind from a heater or air condition.

FIG 2: PIR SENSOR

2.1.2 Gas and Smoke Sensor:

A gas detector is a device that detects the presence of gases in an area, often as part of a safety system. This type of equipment is used to detect a gas leak and interface with a control system so a process can be automatically shut down. A gas detector can sound an alarm to operators in the area where the leak is occurring, giving them the opportunity to leave. This type of device is important because there are many gases that can be harmful to organic life, such as humans or animals.

FIG 3: GAS SENSOR

2.2 GSM Modem:

GSM (Global System for Mobile Communication) is a wireless network system that uses a mobile operator and functions just like a mobile phone. The GSM modem has a SIM card slot, thus giving the modem a mobile number of its own and enabling it to activate communication over the network. The user can send or receive an SMS as well as make or receive voice calls over the modem interface. The GSM modem may be connected to a computer directly through the serial port or to a microcontroller using RS232. Thus the modem can be used to develop embedded applications. There are a set of AT commands that are used to establish communication between the microcontroller and the GSM modem. The GSM modem used in this security system uses SIM300 module. It has a power and network LED making it convenient to debug. There is also a wire antenna on the modem to provide better reception. SIM300 has an adjustable baud rate of 1200-115200bps. However, in this system it is set to 9600bps [3]. The GSM modem consumes only 0.25A during normal operation and about 1A during transmission.

FIG 4: GSM MODEM USING SIM300 MODULE

TABLE 1
AT COMMANDS

AT Command	Meaning
AT+CMGS	Send message
AT+CMSS	Send message from storage
AT+CMGF=1	To set in text format
AT+CMGD	Delete message
ATD	Dial command
ATH	Hold command

2.3 ATMEGA16 Microcontroller:

ATmega16 is an 8-bit microcontroller which delivers high performance at a low power consumption rate. It has an advanced RISC (Reduced Instruction Set Computing) architecture. The maximum frequency of operation is 16MHz at 4.5V. It has 16KB of in-system self-programmable flash program memory, 1KB of internal static RAM and 512 bytes of internal EEPROM. The microcontroller is a 40 pin IC out of which 32 pins are programmable I/O ports. These ports are divided into four groups of 8 pins each called PORTA, PORTB, PORTC and PORTD [2], [5]. The IC and its pin configuration are shown in Figure.

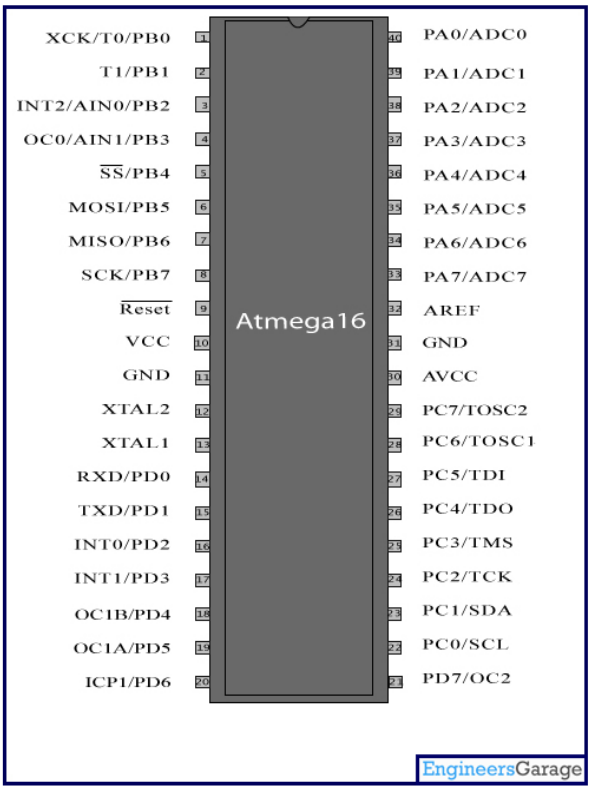

FIG 5: PIN CONFIGURATION OF ATmega16

2.4 Relay Driver Circuit:

Relays are components which allow a low-power circuit to switch a relatively high current on and off, or to control signals that must be electrically isolated from the controlling circuit itself. Newcomers to electronics sometimes want to use a relay for this type of application, but are unsure about the details of doing so. To make a relay operate, you have to pass a suitable 'pull-in' and 'holding' current (DC) through its energizing coil [5]. And generally relay coils are designed to operate from a particular supply voltage often 12V or 5V.

FIG. 6: RELAY

2.5 LCD Display

LCD (Liquid Crystal Display) screen is an electronic display module and find a wide range of applications. A 16x2 LCD display is very basic module and is very commonly used in various devices and circuits. These modules are preferred over seven-segments and other multi segment LEDs. The reasons being: LCDs are economical; easily programmable; have no limitation of displaying special & even custom characters (unlike in seven segments), animations and so on. A 16x2 LCD means it can display 16 characters per line and there are 2 such lines. This LCD has two registers, namely, Command and Data. The command register stores the command instructions given to the LCD. The data register stores the data to be displayed on the LCD [4].

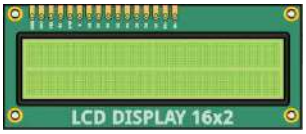

FIG. 7: LCD DISPLAY

2.6 Working Control and Interface Circuit

Nowadays, microcontrollers are so cheap and easily available that it is common to use them instead of simple logic circuits like counters for the sole purpose of gaining some design flexibility and saving some space. Some machines and robots will even rely on a multitude of microcontrollers, each one dedicated to a certain task. each one dedicated to a certain task [5]. Most recent microcontrollers are "In System Programmable", meaning that you can modify the program being executed, without removing the microcontroller from its place.

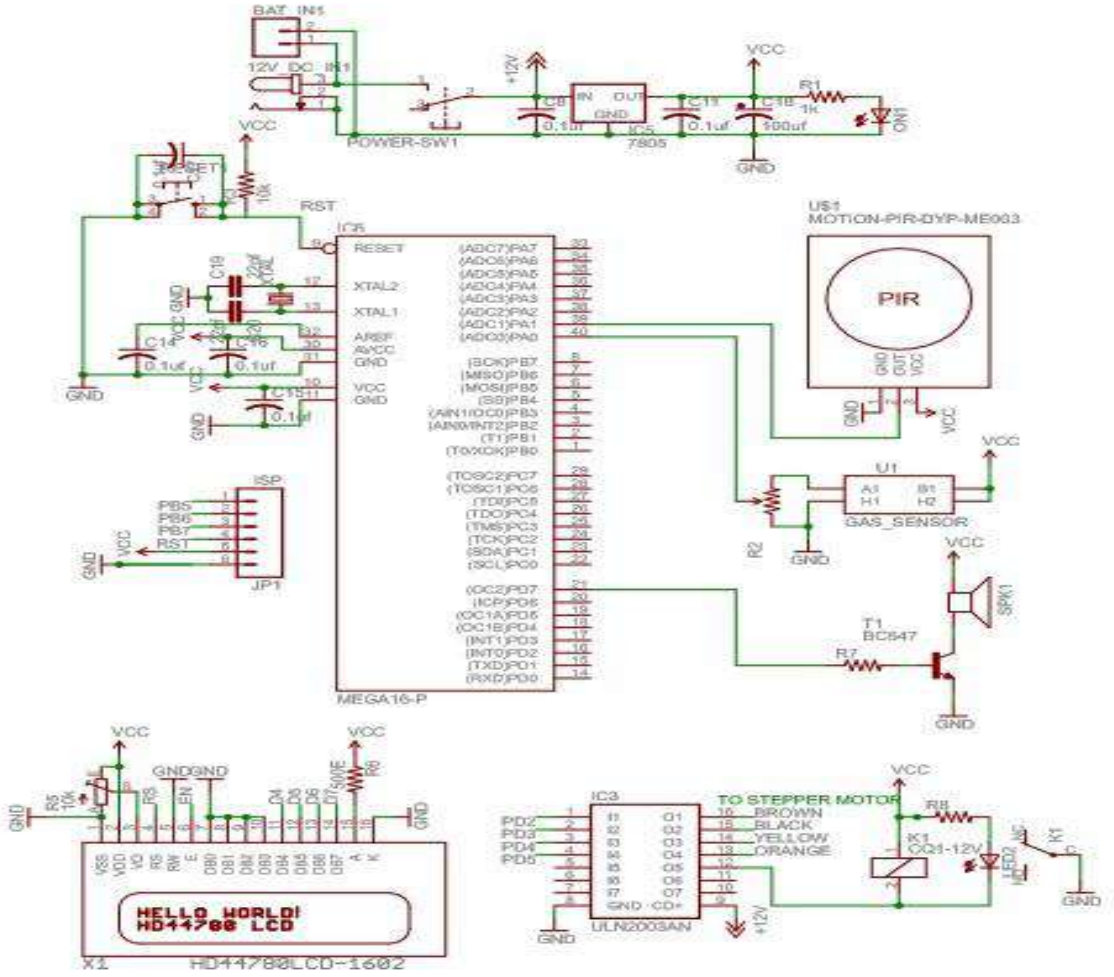

FIG. 8: SCHEMATIC OF THE CIRCUIT

2.7 Working of The System:

The system is fully controlled by the microcontroller and the microcontroller will continuously monitor the sensors, detector and GSM modem. If the voltage level of sensor input pins goes to one (1) then it will send the "AT + CMGS =USER MOBILE NUMBER" to GSM modem through serial port. The GSM modems will response with the character ">". After receiving ">" character microcontroller again send the type of security problem SMS + CTRL Z to GSM Modem. GSM modem will send the type of problem to user [4], [6]. For example any moment detected in security area at the time microcontroller pin number 39 goes to logical one (1). Microcontroller sensed the change and immediately send AT + CMGS = "+88888888888" to GSM modem, GSM modem give ">"character to microcontroller. After receiving ">" Character microcontroller again sends the "MOMENT DETECTED" SMS to GSM Modem. GSM modem sends the SMS to user. After the SMS has been sent a call is being initiated. "ATD USER MOBILE NUMBER" this command can be used to request a call to a registered number. A maximum of five inputs are given on a temporary basis and more number of inputs can be given as per the requirement [6].

III. RESULTS

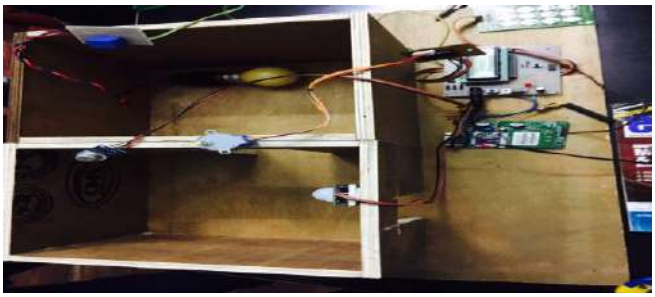

FIG. 9: WORKING MODEL

FIG. 10: SMS FEATURE

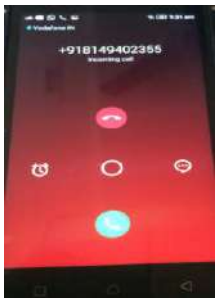

FIG. 11: CALL FEATURE

IV. CONCLUSION

In this project, a low cost, user-friendly, simple, secure and universally acceptable solution for security has been introduced. This approach has achieved the target to control the device remotely using an GSM-based system satisfying user needs and requirements. The system is cost-effective as compared to the previously existing systems in the market and can be easily implemented with high reliability and security. The basic level of security control and remote monitoring has been implemented. The system is extendible and more levels can be further developed. Hence, we can conclude that the required goals and objectives have been achieved.

REFERENCES

[1] Anurag Kumar,, Bharadwaj Amrutur ―Wireless sensor networks for human intruder detection‖ ,Journal of the Indian Institute of Science ,VOL 90:3 Jul–Sep 2010.

[2] Arulogn,o.t.,Adigun,a.Okedirn o ―Design and Development of a Security Surveillance System based on Wireless Sensor Network" International Journal of Innovative Science, Engineering & Technology, Vol. 1 Issue 4, march 2014.

[3] M.Sravan Kumar, M.Mounika, L.Ramya Pavani, E.Ranadeep, B.Siddhartha, K.B.V.S.R.Subramanyam "GSM BASED INDUSTRIAL SECURITY SYSTEM" INTERNATIONAL JOURNAL OF CURRENT ENGINEERING AND SCIENTIFIC RESEARCH (IJCESR) 2394-0697, VOLUME-2, ISSUE-5, 2015.

[4] Nikhil Agarwal, G.Subramanya Nayak "Microcontroller based Home Security System with Remote Monitoring" Special Issue of International Journal of Computer Applications (0975 – 8887) International Conference on Electronic Design and Signal Processing (ICEDSP) 2012.

[5] Hwang, I.-K., Lee, D.-S. and Baek, J.-W. (2009) Home Network Configuring Scheme for All Electric Appliances using ZigBee-Based Integrated Remote Controller. IEEE Transactions on Consumer Electronics, 55, 1300-1307.

[6] Lee, H.-B., Park, J.-L., Park, S.-W., Chung, T.-Y. and Moon, J.-H. (2010) Interactive Remote Control of Legacy Home Appliances through a Virtually Wired Sensor Network. IEEE Transactions on Consumer Electronics, 56, 2241-2248.

Solar Power Satellite by Wireless Power Transmission

Shuchi Shukla[1], Navin Kumar[2]

Abstract— *A immense anxiety has been voiced in latest years over the general use of energy, the partial supply of resources, and the pollution of the environment from the use of current energy conversion systems. Electrical power accounts for much of the energy consumed. Much of this power is wasted during transmission from power plant generators to the consumer. The resistance of the wire used in the electrical grid distribution system causes a loss of 26-30% of the energy generated. This loss implies that our current system of electrical distribution is only 70-74% efficient.*

Nikola Tesla is greatest known for his remarkable statement concerning the wireless transmission of electrical power. His first efforts towards this end started in 1891 and were future to simply "disturb the electrical equilibrium in the nearby portions of the earth... to bring into operation in any way some instrument." In other words the entity of his experiments was simply to create effects locally and detect them at a distance.

Keywords— Power Transmission, Nikola Tesla, Electrical Power, Electrical Distribution.

I. INTRODUCTION

It is recognized that electromagnetic energy is linked with the propagation of electromagnetic waves. In theory, we can utilize all electromagnetic waves for a wireless power transmission (WPT). The distinction between the WPT and communication systems is only efficiency. Maxwell's Equations show that the electromagnetic field and its power diffuse to all directions. Though we transmit energy in a communication system, the transmitted energy is diffused to all directions. Though the conventional power is adequate for a transmission of information, the efficiency from the transmitter to receiver is quiet low. Therefore, we do not call it the WPT system.

WPT is a point-to-point power transmission. For the WPT, we had enhanced concentrate power to receiver. It was prove that the power transmission efficiency can approach close to 100%. We can added concentrate the transmitted microwave power to the receiver aperture areas with taper technique of the transmitting antenna power distribution. Renowned power tapers of the transmitting antenna are Gaussian taper, Taylor distribution, and Chepachet distribution. Such taper of the transmitting antenna is usually used for suppression of side lobes. It correspond to increase in the power transmission efficiency. Concerning the power transmission efficiency of the WPT, there are some good optical approaches in Russia.

Future appropriate and major application of the WPT via microwave is a Space Solar Power Satellite (SPS). The SPS is a gigantic satellite considered as an electric power plant orbiting the Geostationary Earth Orbit (GEO). It consists of mainly three segments; solar energy collector to convert the solar energy into DC (direct current) electricity, DC-to-microwave converter, and large antenna array to beam down the microwave power to the ground. The first solar collector can be moreover photovoltaic cells or else solar thermal turbine. The second DC-to-microwave converter of the SPS can be either microwave tube system and/or semiconductor system. It may be their combination. The third segment is a gigantic antenna array.

Table 1.1 shows some characteristic parameters of the transmitting antenna of the SPS. An amplitude taper on the transmitting antenna is adopt in order to amplify the beam collection efficiency and to reduce side lobe level in almost all SPS design. A characteristic amplitude taper is called 10 dB Gaussian in which the power density in the center of the transmitting antenna is ten times larger than that on the edge of the transmitting antenna.

The SPS is anticipated to be operational around 2030. Before understanding of the SPS, we can think about other applications of WPT. In recent years, mobile devices advanced considerably and have need of decreasing power consumption. It means that we can utilize the diffused weak microwave power as power source of the mobile devices with low power consumption such as RF-ID. The RF-ID is radio IC-tug with wireless power transmission and wireless information. This is a new WPT application like broadcasting.

TABLE 1
TYPICAL PARAMETERS OF TRANSMITTING ANTENNA OF THE SPS [7]

Model	Old JAXA model	JAXA1 model	JAXA2 Model	NASA/DOE model
Frequency	5.8 GHz	5.8 GHz	5.8 GHz	2.45 GHz
Diameter of transmitting antenna	2.6 kmϕ	1 kmϕ	1.93 kmϕ	1 kmϕ
Amplitude taper	10 dB Gaussian	10 dB Gaussian	10 dB Gaussian	10 dB Gaussian
Output power (beamed to earth)	1.3 GW	1.3 GW	1.3 GW	6.72 GW
Maximum power density at center	63 mW/ cm^2	420 mW/cm^2	114 mW/cm^2	2.2 W/ cm^2
Minimum power density at edge	6.3 mW/ cm^2	42 mW/ cm^2	11.4 mW/cm^2	0.22 W/ cm^2
Antenna spacing	0.75 λ	0.75 λ	0.75 λ	0.75 λ
Power per one antenna (Number of elements)	Max. 0.95 W (3.54 billion)	Max. 6.1W (540 million)	Max. 1.7 W (1,950 million)	Max. 185 W (97 million)
Rectenna Diameter	2.0 kmϕ	3.4 kmϕ	2.45 kmϕ	1 kmϕ
Maximum Power Density	180 mW/cm^2	26 mW/cm^2	100 mW/cm2	23 mW/cm^2
Collection Efficiency	96.5 %	86 %	87 %	89 %

JAXA: Japan Aerospace Exploration Agency, NASA: National Aeronautics and Space Administration, DOE: US Department of Energy

II. HISTORY OF WIRELESS POWER TRANSMISSION

In 1864, James C. Maxwell predict the survival of radio waves by means of mathematical model. In 1884, John H. Poynting realize that the Poynting vector would play an significant role in quantify the electromagnetic energy. In 1888, bolstered by Maxwell's theory, Heinrich Hertz succeed in performance new evidence of radio waves by his spark-gap radio transmitter. The forecast and evidence of the radio wave in the end of 19th century was initiate of the wireless power transmission.

During the identical period of Marchese G. Marconi and Reginald Fessenden who are pioneer of communication via radio waves, Nicola Tesla suggested an idea of the wireless power transmission and carried out the first WPT experiment in 1899[1][2]. He said "This energy will be composed all over the globe rather in small amounts, ranging from a fraction of one to a few horse-powers. One of its chief use will be the illumination of isolated homes". He actually built a gigantic coil which was connected to a high mast of 200-ft with a 3 ft-diameter ball at its top. He fed 300 Kw power to the Tesla coil resonated at 150 kHz. The RF potential at the top sphere reach 100 MV.

Unfortunately, he abortive because the transmitted power was diffused to all directions with 150 kHz radio waves whose wave length was 21 km.

To deliberate the transmitted power and to enlarge transmission efficiency, we have to use higher frequency than that used by Tesla. In 1930s, much progress in generating high-power microwaves, namely 1-10 GHz radio waves, was achieved by invention of the magnetron and the klystron. After World War II, high power and high efficiency microwave tubes were advanced by expansion of radar technology. We can concentrate a power to receiver with microwaves. We call the wireless power transmission with microwaves as microwave power transmission (MPT). Based on the development of the microwave tubes during the World War II, W. C. Brown started the First MPT research and development in 1960.

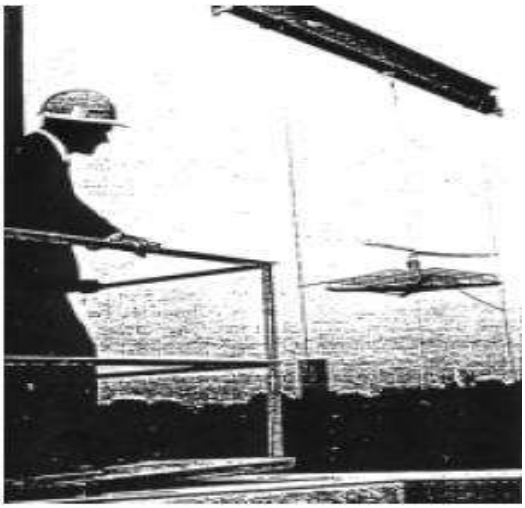

FIGURE 1 MPT DEMONSTRATION WITH HELICOPTER BY W.C. .BROWN

First of all, he made a retina, rectifying antenna which he named, for receiving and rectifying microwaves. The efficiency of the first rectenna developed in 1963 was 50 % at output 4WDC and 40% at output 7WDC, respectively [3].

With the rectenna, he succeeds in MPT experiments to wired helicopter in 1964 and to free-flied helicopter in1968 (Fig. 1). In 1970s; he tried to increase DC-RF-transmission-RF-DC total efficiency with 2.45 GHz microwave. In 1970, overall DC-DC total efficiency was only 26.5 % at 39WDC in Marshall Space Flight Center.

In parallel, he and his team succeed in the major MPT demonstration in 1975 at the Venus Site of JPL Goldstone Facility (fig 2). Distance between a transmitting parabolic antennas, whose diameter was 26m, and a rectenna array, whose size was 3.4 m x 7.2 m, was 1 mile.

FIG. 2: FIRST GROUND-TO-GROUND MPT EXPERIMENT IN 1975 AT THE VENUS SITE OF JPL GOLDSTONE FACILITY

FIG.3: STATIONARY HIGH ALTITUDE RELAY PLATFORM.

After 1990s, many MPT laboratory and field experiments were carried out in the world. We often use 2.45 GHz or 5.8 GHz of the ISM band (ISM=Industry, Science, and Medical) for the MPT system. A Canadian group demonstrated fuel-free airplane flight experiment with MPT in 1987 which was called SHARP (Stationary High Altitude Relay Platform) with 2.45 GHz.

In USA, there were many MPT investigated and growth projects after W. C. Brown: for instance, retro directive microwave transmitters, rectenna, new devices and microwave circuit technologies.

In Japan, there were a lot of field MPT experiments such as fuel-free airplane flight experiment with MPT phased array with 2.411 GHz in 1992, ground-to-ground MPT experiment with Power Company and universities in 1994-95.

FIG. 4 . GROUND-TO-GROUND MPT EXPERIMENT IN JAPAN IN 1994-95

III. RECENT TRENDS

Antennas for Microwave Power Transmission: All antennas can be practical for both the MPT system and communication systems, for example, Yagi-Uda antenna, horn antenna, parabolic antenna, micro strip antenna, phased array antenna or any extra type of antenna.

To predetermined target of the MPT system, we typically select a large parabolic antenna, for example, in MPT demonstration in 1975 at the Venus Site of JPL Goldstone Facility and in ground-to-ground MPT experiment in 1994-95 in Japan. In the fuel-free airship light experiment with MPT in 1995 in Japan, they changed a direction of the parabolic antenna to pursue the moving airship.

However, we have to employ a phased array antenna for the MPT from/to moving transmitter/receiver which comprise the SPS because we have to control a microwave beam direction exactly and quickly. The phased array is a directive antenna which generates a beam form whose shape and direction by the relative phases and amplitudes of the waves at the individual antenna elements.

It is likely to guide the direction of the microwave beam. The antenna elements might be dipoles [1], slot antennas, or any other type of antenna, even parabolic antennas [2, 3]. In some MPT experiments in Japan, the phased array antenna was adopted to steer a direction of the microwave beam (Fig.5).

All SPS is designed with the phased array antenna.

FIG.5. PHASED ARRAY USED IN JAPANESE FIELD MPT EXPERIMENT

Recent Technologies for Transmitters: The knowledge working for generation of microwave radiation is an vital topic for the MPT system. We require higher efficient generator/amplifier for the MPT system than that for the wireless communication

system. For highly efficient beam collection on rectenna array, we require highly stabilized and precise phase and amplitude of microwaves for phased array system for the MPT.

There are two types of microwave generators/amplifiers. One is a microwave tube and the other is semiconductor amplifier.

Magnetron: Magnetron is a cross field tube in which electrons emitted from the cathode take cyclical path to the anode. The magnetron is self-oscillatory device in which the anode contains a resonant RF structure. The magnetron has long history from invention by A. W. Hull in 1921.

The sensible and well-organized magnetron tube attracted worldwide attention only after K. Okabe proposed divided anode-type magnetron in 1928. Magnetron technologies received a boost during the World War II, especially with the Japanese Army. The magnetrons were also useful for microwave ovens. As a result, the magnetron of 500 – 1,000 W is widely in use for microwave ovens in 2.45 GHz, and is a relatively inexpensive oscillator (below $5). There is a net global capacity of 45.5GW/year for all magnetrons used in microwave ovens whose production is 50– 55 millions. It was W. C. Brown who invented a voltage controlled oscillator with a cooker-type magnetron in PLL.

Semiconductor Amplifier: After 1980s, semiconductor devices became leading in microwave world in its place of the microwave tubes. This was driven by advances in mobile phone networks. The semiconductor device is expected to expand microwave applications, for example, phased array and active included antenna (AIA), because of its manageability and mass productivity. After 1990s, some MPT experiments were approved out in Japan with phased array of semiconductor amplifiers.

Typical semiconductor devices for microwave circuits are FET (Field Effect Transistor), HBT (Hetero junction Bipolar Transistor), and HEMT (High Electron Mobility Transistor). Present materials for the semiconductor devices are Si for lower frequency below a few GHz and GaAs for higher frequency.. It is simple to control phase and amplitude through the microwave circuits with semiconductor devices, for example, amplifiers, phase shifters, modulators, and so on.

At present, new materials are underneath development to allow semiconductor devices yield increased output power and efficiency.

Transmitter Issues and Answers for Space Use: Largest MPT application is a SPS in which over GW microwave will be transmitted from space to ground at distance of 36,000km. In the SPS, we will use microwave transmitters in space. For space use, the microwave transmitter will be required lightness to reduce launch cost and higher efficiency to reduce heat problem.

A weight of the microwave tube is lighter than that of the semiconductor amplifier when we compare the weight by power-weight ratio (kg/kW). The microwave tube can generate/amplify higher power microwave than that by the semiconductor amplifier. Kyoto University's groups have developed a light weight phase controlled magnetron called COMET, Compact Microwave Energy Transmitter with a power-weight ratio below 25g/W (fig.6.)

FIG. 6 COMPACT MICROWAVE ENERGY TRANSMITTER WITH THE PCM (COMET)

The COMET includes DC/Converters, a control circuit of the phase controlled magnetron with 5.8 GHz, a heat radiation circuit, a wave guide, and an antenna [4]. The power-weight ratio of the COMET is lightest weight in all microwave generators and amplifiers. TWTA for satellite use has lighter power weight ratio: 220Wat 2.45GHz at 2.65 kg (the TWTA weighs 1.5kg, the power supply weighs 1.15kg). 130W at 5.8 GHz at 2.15 kg (the TWTA weighs 0.8kg, the power supply weighs 1.35kg). Hence, they can deliver12g/W and 16.5g/W, respectively. They do not include a heat radiation circuit, a wave guide, and an antenna.

IV. RECENT TECHNOLOGICAL TRENDS

Retro directive Beam Control: A microwave power transmission is suitable for a power transmission from/to moving transmitters/targets. Therefore, accurate target detection and high efficient beam forming are important. Retro directive system is always used for SPS.

A corner reflector is most basic retro directive system. The corner reflectors consist of perpendicular metal sheets, which meet at an apex. Incoming signals are reflected back in the direction of arrival through multiple reflections off the wall of the reflector. Van Atta array is also a basic technique of the retro directive system. This array is made up of pairs of antennas spaced equidistant from the center of the array, and connected with equal length transmission lines. The signal received by an antenna is re-radiated by its pair, thus the order of re-radiating elements are inverted with respect to the center of the array, achieving the proper phasing for retro directivity.

Usual retro directive system have phase conjugate circuits in each receiving/transmitting antenna, which play same role as pairs of antennas spaced equidistant from the center of the array in Van Atta array. The signal is called a pilot signal. We do not need any phase shifters for beam forming. The retro-directive system is usually used for satellite communication, wireless LAN, military, and so on.

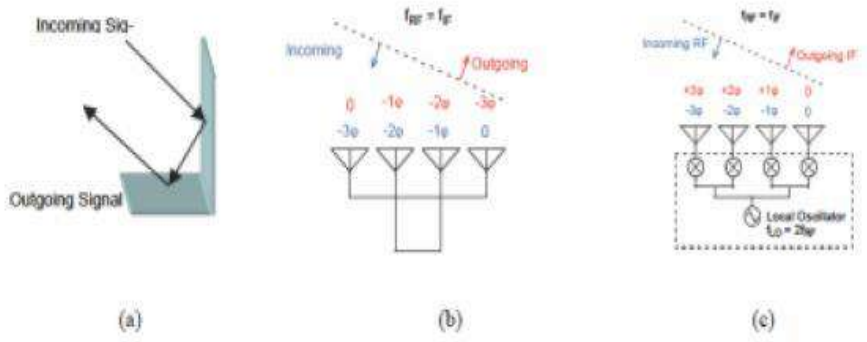

(A) TWO-SIDED CORNER REFLECTOR, (B) VAN ATTA ARRAY, (C) RETRODIRECTIVE ARRAY WITH PHASE CONJUGATE CIRCUITS.

Environmental Issues: One of the characteristics of the MPT is to use more intense microwave than that in wireless communication systems. Therefore, we have to consider MPT safety for humans.

Interaction with Atmosphere: In general, effect of atmosphere on microwaves is quite small. There are absorption and scatter by air, rain, and irregularity of air refraction ratio. In 2.45 GHz and 5.8 GHz, the absorption by water vapor and oxygen dominate the effect in the air. Especially, it is enough to consider only absorption by the oxygen in the microwave frequency. It is approximately 0.007 dB/km. In the SPS case, the amount of total absorption through the air from space is approximately 0.035 dB.

Interaction with Space Plasmas: When microwaves from SPS propagate through ionospheric plasmas, some interaction between microwaves and the ionospheric plasmas occurs. It is well known that refraction, Faraday rotation, scintillation, and absorption occur between weak microwave used for satellite communication and the plasmas. However, influence on the MPT system is negligible. It is nonlinear interaction between intense microwave and the space plasmas that we have to investigate before the commercial SPS. We theoretically predict that the following may occur: heating of the plasmas, plasma hall effect, thermal self-focusing effect of the microwave beam, and three-wave interactions and excitation of electrostatic waves in MHz bands. These interactions don't not occur in existent satellite communication systems because microwave power is very weak.

V. RECENT TRENDS: WIRELESS POWER TRANSMISSION–RECEIVERS AND RECTIFIERS

Point-to-point MPT system needs a large receiving area with a rectenna array because one rectenna element receives and creates only a few W. Especially for the SPS, we need a huge rectenna site and a power network connected to the existing power networks on the ground. On contrary, there are some MPT applications with one small rectenna element such as RF-ID.

Recent Technologies of Rectenna: The word "rectenna" is composed of "rectifying circuit" and "antenna". The rectenna can receive and rectify a microwave power to DC. The rectenna is passive element with a rectifying diode, operated without any power source. The circuit, especially diode, mainly determines the RF-DC conversion efficiency. Silicon Schottky barrier diodes were usually used for earlier rectenna. New devices like SiC and GaN are expected to increase the efficiency. The rectenna with FET or HEMT appear ed recently. The single shunt full-wave rectifier is always used for the rectenna. It consists of a diode inserted in the circuit in parallel, a λ/4 distributed line, and a capacitor inserted in parallel. In an ideal situation, 100% of the received microwave power should be converted into DC power.

Recent Technologies of Rectenna Array: The rectenna will be used as an array for high power MPT because one rectenna element rectifies a few W only. For usual phased array antenna, mutual coupling and phase distribution are problems to solve. For the rectenna array, problem is different from that of the array antenna because the rectenna array is connected not in microwave phase but in DC phase.

When we connect two rectenna in series or in parallel, they will not operate at their optimum power output and their combined power output will be less than that if operated independently. This is theoretical prediction.

VI. EFFICIENCY

We classify the MPT efficiency roughly into three stages; DC-RF conversion efficiency which includes losses caused by beam forming, beam collection efficiency which means ratio of all radiated power to collected power on a receiving antenna, and RF-DC conversion efficiency.

RF-DC Conversion Efficiency: The RF-DC conversion efficiency of the rectenna or the CWC is over 80 % of experimental results as shown. Decline of the efficiency is caused by array connection loss, change of optimum operation point of the rectenna array caused by change of connected load, trouble of the rectenna, and any losses on the systems, for example, DC/AC conversion, cables, etc. [6] However, it is easier to realize higher efficiency than that on the other two stages.

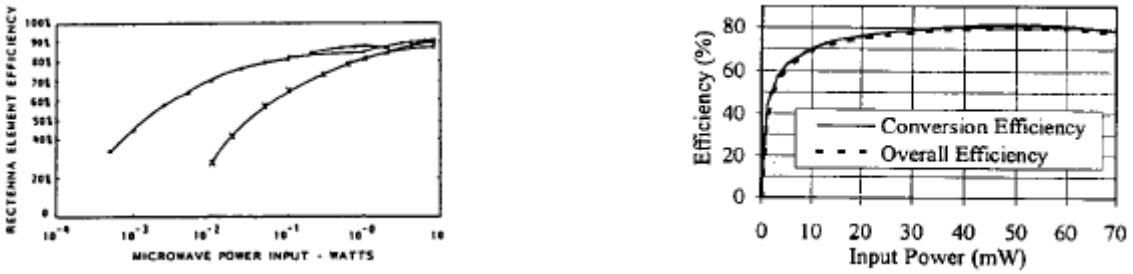

(A)EFFECIENCY OF 2.45 GHZ RECTENNA **(B)EFFECIENCY OF 5.8 GHZ RECTENNA[2]**

FIG. 7 EFFICIENCY OF RECTENNA ELEMENT

Beam Collection Efficiency: The beam collection efficiency depends on the transmitter and receiver aperture areas, the wavelength, and the separation distance between the two antennas.

VII. CONCLUSION

Electrical energy can be reasonably transmitted without wires to any terrestrial distance. The monetary transmission of power without wires is of vital importance to man.

This knowledge opened up the possibility of constructing power stations on the moon. These power stations will be able of transmitting power to earth using microwave energy. Such microwave energy would then be changed into electricity using a huge array of rectenna receivers on the earth.

However with all the challenge that face wide-scale consumption of this new technology wireless power transmission for solar power satellite is still measured as a next-generation power transmission system.

REFERENCES

[1] Tesla, N., "The transmission of electric energy without wires", *Electrical World*, March 5, 1904

[2] Brown, W. C., "Beamed microwave power transmission and its application to space", *IEEE Trans. Microwave Theory Tech.*, vol. 40, no. 6, 1992, pp.1239-1250

[3] Kaya, N., S. Ida, Y. Fujino, and M. Fujita, "Transmitting antenna system for airship demonstration of Space Energy and Transportation" *IEEE* Vol.1, No.4, 1996, pp.237-245

[4] Fujiwara, E., Y. Takahashi, N. Tanaka, K. Saga, "Compact Microwave Energy Transmitter (COMET)", Proc. of Japan-US Joint Workshop on SSPS (JUSPS), 2003, pp.183-185.

[5] Hatsuda, T., K. Ueno, M. Inoue, "Solar power satellite interference assessment", *IEEE*, Vol. 3, No. 4, Dec. 2002, pp.65-70

[6] McSpadden, J. O., L. Fun, and K. Chang, "A High Conversion Efficiency 5.8 GHz Rectenna", *IEEE MTT-S Digest*, 1997, pp.547-550

AD Publications
Sector-3, MP Nagar, Bikaner,
Rajasthan, India
www.adpublications.org, info@adpublications.org